Search for resonant Higgs boson pair production in the $b\bar{b}WW^*$ decay channel in the boosted 1-lepton final state using the full Run 2 ATLAS dataset

Dissertation

zur Erlangung des mathematisch-naturwissenschaftlichen Doktorgrades
„Doctor rerum naturalium“
der Georg-August-Universität Göttingen

im Promotionsprogramm Physik
der Georg-August University School of Science (GAUSS)

vorgelegt von

Kira Abeling

aus Twistringen

Göttingen, 2022

Betreuungsausschuss

Prof. Dr. Stanley Lai
Prof. Dr. Ariane Frey
PD Dr. Jörn Große-Knetter

Mitglieder der Prüfungskommission:

Referent:	Prof. Dr. Stanley Lai II. Physikalisches Institut, Georg-August-Universität Göttingen
Koreferentin:	Prof. Dr. Ariane Frey II. Physikalisches Institut, Georg-August-Universität Göttingen

Weitere Mitglieder der Prüfungskommission:

PD Dr. Jörn Große-Knetter
II. Physikalisches Institut, Georg-August-Universität Göttingen

Prof. Dr. Steffen Schumann
Institut für Theoretische Physik, Georg-August-Universität Göttingen

Prof. Dr. Laura Covi
Institut für Theoretische Physik, Georg-August-Universität Göttingen

Prof. Dr. David Marsh
Theoretical Particle Physics and Cosmology, King's College London

Tag der mündlichen Prüfung: 01. April 2022

Referenz: II.Physik-UniGö-Diss-2022/01

Search for resonant Higgs boson pair production in the $b\bar{b}WW^*$ decay channel in the boosted 1-lepton final state using the full Run 2 ATLAS dataset

Abstract

Despite the great success of the Standard Model of Particle Physics in explaining physics phenomena over a wide range of energy scales, many open questions remain and it is known that this model of nature is incomplete. The Higgs boson as the most recent discovered particle has completed the Standard Model. With its coupling to mass, it is an excellent candidate to shed light on physics beyond the Standard Model.

This thesis presents the search for resonant Higgs boson pair (HH) production as well as resonant production of a Higgs boson in association with another additional scalar particle (SH) in the $b\bar{b}WW^{(*)}$ decay channel with one charged lepton in the final state using the full Run 2 dataset recorded by ATLAS. This decay channel combines the advantages of a high branching ratio with a reasonable background level due to the lepton in the final state.

The mass of the scalar resonance considered ranges between $m_X = 800\,\text{GeV}$ and $m_X = 5\,\text{TeV}$ for HH production and between $m_X = 750\,\text{GeV}$ and $m_X = 3\,\text{TeV}$ for SH production. The latter introduces a second mass scale m_S which covers the range between $m_S = 170\,\text{GeV}$ and $m_S = 2.5\,\text{TeV}$ where $m_S < m_X - m_H$ is required. Assuming the scalar particle has couplings similar to the Higgs boson, the decay $S \to WW$ will be dominant for the entire considered mass range. Due to the high mass of the heavy scalar resonance, the boosted topology is exploited where the decay products of the Higgs boson decaying to a $b\bar{b}$-pair as well as the decay products of the hadronically decaying W boson cannot be resolved. They are therefore reconstructed as single hadronic objects called large-R jets. Furthermore, one of the large-R jets is expected to overlap with the charged lepton making this topology not only unique but challenging to reconstruct.

This dense environment requires the use of new approaches such as track assisted reclustered jets which profit from the excellent spatial resolution of tracks to describe the large-R jets. Moreover, only muons will be considered as charged leptons in the final state of this search since they are less sensitive to hadronic energy deposits close by.

Since no significant excess of data over the expected backgrounds is expected in the ATLAS Run 2 dataset, expected 95% CL_s upper limits are evaluated on the respective cross sections. The limits become more stringent for higher values of m_X due to the reduced amount of background in this phase space, and smaller m_S due to the more boosted topology. Therefore, the best expected limits without considering systematic uncertainties are $\sigma(pp \to X \to HH) = 2.8\,\text{fb}$ at $m_X = 5\,\text{TeV}$ and $\sigma(pp \to X \to SH) \times \mathcal{BR}(SH \to b\bar{b}WW) = 0.87\,\text{fb}$ at $m_X = 3\,\text{TeV}$ and $m_S = 240\,\text{GeV}$.

Suche nach resonanter Higgsboson-Paarproduktion im $b\bar{b}WW^*$ Zerfallskanal im „boosted“ 1-Lepton Endzustand unter Benutzung des vollen Run 2 ATLAS Datensatzes

Zusammenfassung

Trotz des beachtlichen Erfolgs des Standardmodells der Teilchenphysik, Physikphänomene über viele Energiebereiche hinweg zu beschreiben, bleiben viele Fragen unbeantwortet und es ist bekannt, dass dieses Modell unvollständig ist. Das Higgsboson, als zuletzt entdecktes Teilchen, hat das Standardmodell vervollständigt. Mit seiner Kopplung an die Teilchenmasse ist es ein exzellenter Kandidat für die Suche nach Physik jenseits des Standardmodells.

Diese Arbeit präsentiert die Suche nach resonanter Higgsboson-Paarproduktion (HH) sowie nach resonanter Produktion eines Higgsbosons in Verbindung mit einem weiteren skalaren Teilchen (SH) im $b\bar{b}WW^{(*)}$ Zerfallskanal mit einem geladenen Lepton im Endzustand unter der Verwendung des kompletten Run 2 Datensatzes, der von Atlas aufgenommen wurde. Dieser kombiniert die Vorteile eines hohen Verzweigungsverhältnisses mit angemessenen Untergrundbeiträgen aufgrund des Leptons im Endzustand.

Die Masse der betrachteten skalaren Resonanz liegt zwischen $m_X = 800\,\text{GeV}$ und $m_X = 5\,\text{TeV}$ für die HH-Produktion und zwischen $m_X = 750\,\text{GeV}$ und $m_X = 3\,\text{TeV}$ für die SH-Produktion. Letztere führt eine weitere Massenskala ein, die den Bereich zwischen $m_S = 170\,\text{GeV}$ und $m_S = 2.5\,\text{TeV}$ abdeckt, wobei $m_S < m_X - m_H$ verlangt wird. Wird angenommen, dass das skalare Teilchen ähnliche Kopplungen wie das Higgsboson besitzt, dann dominiert der Zerfall $S \to WW$ den ganzen betrachteten Massenbereich. Aufgrund der hohen Masse der schweren skalaren Resonanz wird die „boosted“ Topologie verfolgt. Diese zeichnet sich dadurch aus, dass die Zerfallsprodukte des Higgsbosons, welches in ein $b\bar{b}$-Paar zerfällt, sowie die Zerfallsprodukte des hadronisch zerfallenden W-Bosons nicht mehr auflösbar sind. Daher werden sie in einem hadronischen Objekt, genannt large-R Jet, zusammengefasst. Darüber hinaus wird erwartet, dass einer der large-R Jets mit dem Lepton überlappt, was in einer schwierigen aber ebenso einzigartigen Topologie resultiert.

Diese dicht besiedelte Umgebung verlangt nach neuen Ansätzen wie „trackassisted reclustered Jets“, die von der hervorragenden räumlichen Spurauflösung profitieren, zur Rekonstruktion der large-R Jets. Weiterhin werden lediglich Myonen als Leptonen in dieser Suche in Betracht gezogen, da diese weniger von nahen hadronischen Energiesignalen beeinflusst werden.

Da kein signifikanter Überschuss von Daten verglichen mit dem Untergrund für den Atlas Run 2 Datensatz abzusehen ist, werden 95% CL_s erwartete obere Grenzen auf den Wirkungsquerschnitt gesetzt. Die Grenzen werden stringenter für höhere m_X Werte, da in dieser Region weniger Untergrund zu finden ist, und für kleinere m_S Werte, weil hier die Topologie mehr geboostet ist. Daher sind die stärksten zu erwartetenden Grenzen ohne Einberechnung systematischer Unsicherheiten erreicht mit $\sigma(pp \to X \to HH) = 2.8\,\text{fb}$ für $m_X = 5\,\text{TeV}$ und mit $\sigma(pp \to X \to HH) \times \mathcal{BR}(SH \to b\bar{b}WW) = 0.87\,\text{fb}$ für $m_X = 3\,\text{TeV}$ und $m_S = 240\,\text{GeV}$.

Contents

CHAPTER 1

Introduction

It has always been in human desire to understand how nature works. Already the ancient Greeks attempted to explain physics phenomena by using elements. Until today, the understanding of these elements has evolved to elementary particles but the idea is still the same and summarised in the Standard Model of particle physics (SM).

The discovery of the Higgs boson in 2012 [1,2] opened a complete new field of research. At present, many measurements of and with the Higgs boson have been made and confirmed its SM like nature [3]. The search for Higgs boson pair production is seen as the ultimate test of the SM, as it allows a direct measurement of the self-coupling of Higgs bosons from which the self-coupling strength can be extracted, which in turn defines the shape of the Higgs potential. However, due to destructive interference, the SM predicted cross section $\sigma_{HH}^{\mathrm{SM}} = 31.05\,\mathrm{fb}$ [4–11] is very small, but this value can be enhanced by theories beyond the SM (BSM).

The ATLAS and CMS experiments at CERN have searched for Higgs boson pair production in the $b\bar{b}b\bar{b}$, $b\bar{b}W^+W^-$, $b\bar{b}\tau^+\tau^-$, $b\bar{b}\gamma\gamma$, $W^+W^-W^+W^-$ and $W^+W^-\gamma\gamma$ channels [12–23] with at least $\int\mathcal{L}dt = 36\ \mathrm{fb}^{-1}$ of $\sqrt{s} = 13$ TeV data without finding any significant evidence for either SM or BSM Higgs boson pair production in the combination of all channels [24,25].

The analysis presented in this thesis belongs to a new approach and extension [26] of the previous Atlas analysis performed on the dataset recorded in 2015 and 2016 corresponding to $\int\mathcal{L}dt = 36\ \mathrm{fb}^{-1}$ [13]. Due to the Higgs boson's coupling to mass, the Higgs boson decay with the highest branching ratio is the decay to a $b\bar{b}$-pair and the second highest branching ratio is provided by the decay into two W bosons of which at least one is virtual [27]. The decay of $HH \to b\bar{b}W^+W^-$ offers the second highest Higgs boson pair branching ratio with around 25%. Since the W bosons themselves are not stable, they can either decay into a pair of quarks or a charged lepton in conjunction with the corresponding neutrino.

Since the presence of leptons cause differences in the analysis requirements and background compositions, analysis strategies quite often depend on the lepton multiplicity in the final state. Three possible channels arise in the $b\bar{b}WW^{(*)}$ final state, where τ-leptons are only counted as charged leptons if they decay leptonically:

- **0-lepton channel** where both W bosons decay hadronically,
- **1-lepton channel** where one W boson decays hadronically, while the other decays leptonically and
- **2-lepton channel** where both W bosons decay leptonically. This channel is not covered in this thesis due to its small branching ratio and overlap with other Higgs boson pair decay modes.

Many BSM theories predict additional, massive scalar resonances, X, which can either decay to two SM-like Higgs bosons, H, or another scalar particle, S, in conjunction with a SM-like Higgs boson. In the general approach, X is only required to allow the decay to SH and S is assumed to have Higgs boson like couplings. Since the masses of X and S are not predicted by a single theoretical model in this approach, a wide range of masses, m_X and m_S, is scanned where only

$$m_X > m_S + m_H \text{ and } m_S > 2m_W$$

is required. This allows that both S and H are produced as real particles and that S can decay into two real W bosons. Thus, the decay of S is restricted to a pair of W bosons leaving H to exclusively decay into a $b\bar{b}$-pair.

This results in various topologies, where the final state particles can either be resolvable and reconstructed as individual objects or boosted and reconstructed as combined objects. A unique case is the split-boosted topology in which the W bosons are separated but its respective decay products are boosted.

In this thesis, the focus lays on the boosted 1-lepton channel and is structured as follows. Chapter 2 provides more details on the nature of the Higgs boson in the SM as well as examples of BSM theories that introduce one or more additional scalar particles. An overview of the experimental setup is given in Chapter 3 and of the analysis in Chapter 4. Chapter 5 discusses studies related to the boosted 1-lepton channel in more detail. In Chapter 6, the various systematic uncertainties are elaborated upon and Chapter 7 describes the statistical analyses performed in the boosted 1-lepton channel including the results obtained. The thesis is concluded in Chapter 8.

CHAPTER 2

Phenomenology of the Standard Model and Beyond

This chapter provides an overview of the particle physics phenomenology backgrounds of interest. The Standard Model of particle physics is briefly discussed including its particle content and its interactions. Due to the relevance for this thesis, the Brout-Englert-Higgs mechanism as well as the production and decays of the resulting Higgs boson are covered in more detail. The known limitations of the Standard Model are described as well. The second part then discusses Higgs boson pair production not only in the Standard Model but also in beyond Standard Model theories. Finally, the extension to resonant Higgs boson production in conjunction with another scalar particle is reviewed.

Throughout this thesis, natural units will be used in calculations and particle quantities. This means, that units are expressed in terms of the speed of light c and of the reduced Planck constant $\hbar$ without writing them down explicitly.

2.1. The Standard Model of Particle Physics

The Standard Model of particle physics (SM) is very successful theory that is able to explain many physics phenomena up to large energy scales by a limited number of elementary particles and interactions. More detailed explanations can be found in Refs. [28–30].

Quantum field theories and the Lagrange formalism [31, 32] are used to derive the equations of motions for the respective fields and, thus, kinematic properties of the particles representing the fields and mediating the interactions. The particles correspond to either matter fields ψ (spin-$\frac{1}{2}$, fermions), gauge fields W (spin-1, vector bosons) or scalar fields ϕ (spin-0, scalar bosons). The starting point is to calculate the Lagrangian $\mathcal{L}$ by subtracting the potential energy V from the kinetic energy T

$$\mathcal{L} = T - V \tag{2.1}$$

which is then integrated over time to obtain the action, a quantity necessary to derive the equations of motions for the fields. In 1949, Richard Feynman developed a graphical representation together with a set of rules simplifying the calculations of processes significantly [33, 34].

Another important concept of the SM is the use of symmetries under which the Lagrangian is invariant. Consequently, Noether's theorem [35] implies conserved quantities of the theory due to these symmetries.

Interactions in particle physics always relate to charge conservations, since these interactions correspond to local gauge symmetries represented by special Lie groups. For a free theory of N complex fields, the $\mathrm{U}(1) \times \mathrm{SU}(N)$ symmetry is conserved, where $\mathrm{U}(1)$ denotes the unitary group of size 1 and $\mathrm{SU}(N)$ denotes the special unitary group of size N, respectively. As Lie groups, any of the group elements can be written as

$$U = e^{i\theta_a T^a} \tag{2.2}$$

with θ_a being real parameters of the group and T^a being called the generators of the group. The dimension a of θ and T depends on N. For $N = 2$, three generators and parameters exist while for $N = 3$, there are eight generators and parameters. The Lagrangian must then be invariant under transformations of the fields by this symmetry

$$\mathcal{L}(\psi) = \mathcal{L}(\psi') \text{ with } \psi(x) \to \psi' = e^{i\theta_a T^a}\psi. \tag{2.3}$$

This is called global gauge invariance. It is also possible to require a local gauge invariance by making the parameters depending on the space-time

$$\theta_a \to \theta_a(x).$$

Concrete examples will follow later in this section.

2.1.1. Particle Content

The particle content of the SM includes 17 predicted particles of which all have been discovered in the past 130 years [1, 2, 36–57]. An overview of these is displayed in Figure 2.1. There are three types of particles:

- **fermions** which are spin-$\frac{1}{2}$ particles and are considered as the building blocks of the visible matter in the universe,
- **vector bosons** or gauge bosons which are spin-1 particles and are associated to an interaction and
- **the Higgs boson** which is a spin-0 particle and the only scalar particle in the SM.

Not shown are antiparticles, which can be interpreted as the particles moving backwards in time with an inverted sign on all charges. The most prominent antiparticle is the

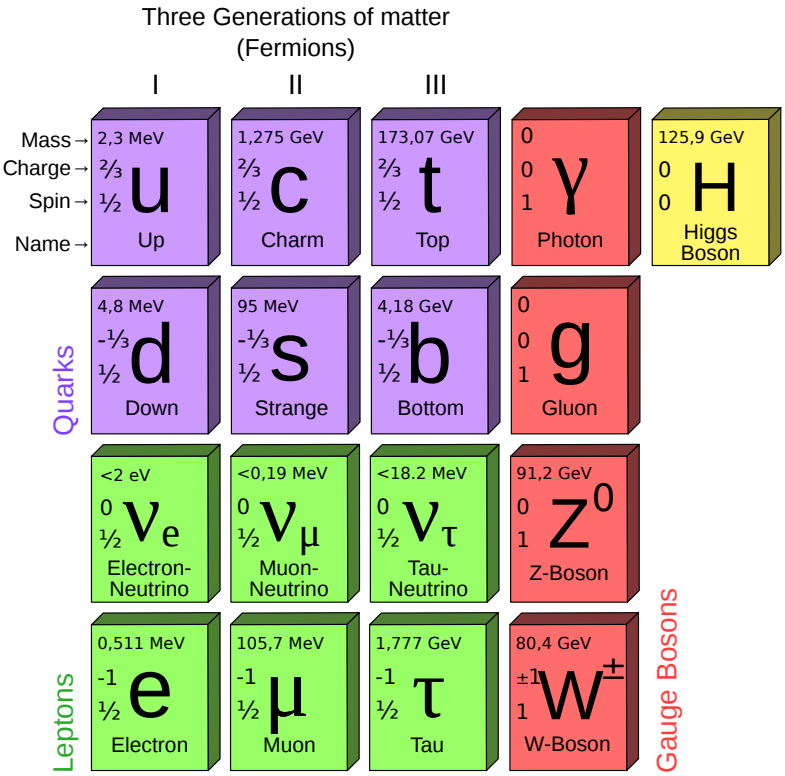

Figure 2.1.: Summary of all particles in the SM including their mass, charge and spin values. They are ordered by type and generation. ©Wikimedia Commons

positron as the antielectron and was the first to be discovered in 1933 [58]. The photon, the Z boson and the Higgs boson are their own antiparticles.

Furthermore, the SM includes three of the four fundamental interactions, namely the electromagnetic, the weak and the strong interaction where each has one or more gauge bosons associated to it. In general, all interactions correspond to a non-abelian gauge symmetry which can be described by Yang-Mills theory [59] and are renormalizable as shown by 't Hooft [60]. The non-abelian nature of the group results in a non-zero commutator relation between its generators which causes self-couplings between the gauge bosons.

The electromagnetic interaction is mediated by the photon, γ, which couples to the electrical charge. This means that only charged particles can participate in electromagnetic interactions, and the coupling is stronger the larger the charge is. The gluon, g, is the mediator of the strong force and couples to colour charge. In contrast to the electrical charge, colour charge only has three discrete values: red, green and blue. The weak interaction is special because its mediators the W and Z bosons cause charged and neutral currents, respectively. While the W boson's coupling depends on the chirality of a particle, the Z boson also couples to the hypercharge where both properties depend on the third component of the weak isospin. The Higgs boson has a special role in the SM

as it is not a gauge boson but still a mediator of interactions between massive particles in the SM and the Higgs field by coupling to the particle's mass. More details on the mathematical representation of the interactions are given in Sections 2.1.2–2.1.7.

The fermions are distinguished by their ability to interact strongly into quarks, which carry a colour charge, and leptons, which are colour neutral. Within these groups, the fermions can be further sorted by their electrical charge into up-type quarks with a charge of $+2/3$, down-type quarks with a charge of $-1/3$, neutrinos which are electrically neutral or charged leptons with a charge of -1. Based on their mass, quarks and charged leptons can be arranged in three generations where the first generation corresponds to the lightest mass and the third generation to the heaviest mass. Since neutrinos are considered to be massless in the SM despite measurements suggesting very small masses (see Section 2.1.8), they are sorted to match the flavour of the charged lepton. Each generation of quarks and leptons forms a weak isospin doublet where up-type quarks and neutrinos have a weak isospin of $+1/2$ while down-type quarks and charged leptons have a weak isospin of $-1/2$.

Stable matter is only made of the first generation of fermions, namely, the up-quarks, down-quarks and electrons. Particles from higher generations are not stable and decay after a certain time into a lighter generation. Since neutrinos only interact weakly, they do not form bound states.

2.1.2. Quantum Electrodynamics

One of the most successful theories in physics is quantum electrodynamics (QED) [33,61–69]. It describes interactions between electrically charged particles mediated by photons.

Using Einstein notation, the electromagnetic Lagrangian for a massive fermion ψ and a massless spin-1 photon field A^μ can be expressed as

$$\begin{aligned}\mathcal{L}_{\mathrm{EM}} &= \overline{\psi}(x)(i\gamma^\mu D_\mu - m)\psi(x) - \tfrac{1}{4}F^{\mu\nu}F_{\mu\nu} \text{ with } D_\mu = \partial_\mu - ig_e A_\mu \\ &= \underbrace{\overline{\psi}(x)(i\gamma^\mu \partial_\mu - m)\psi(x)}_{\text{free fermion field}} + \underbrace{g_e\overline{\psi}\gamma^\mu\psi A_\mu}_{\text{fermion-photon interaction}} - \underbrace{\tfrac{1}{4}F^{\mu\nu}F_{\mu\nu}}_{\text{free photon field}} ,\end{aligned} \tag{2.4}$$

where $\overline{\psi} = \psi^\dagger\gamma^0$ denotes the adjoint spinor, γ^μ denote the gamma matrices, D_μ denotes the covariant derivative, m denotes the particles mass and

$$F_{\mu\nu} = \partial_\mu A_\nu - \partial_\nu A_\nu \tag{2.5}$$

represents the field strength tensor. The covariant derivative introduces interactions between the photon and the fermion with a coupling strength of g_e.

This Lagrangian is invariant under local U(1) transformations with a phase $\alpha(x)$

$$\psi(x) \to \psi'(x) = e^{i\alpha(x)}\psi(x) \text{ and } A_\mu \to A'_\mu = A_\mu + \frac{1}{g_e}\partial_\mu\alpha. \tag{2.6}$$

2.1.3. Quantum Flavourdynamics

Weak interactions were first observed in β decays of radio active atoms, where a down-quark is converted into an up-quark, while radiating an electron and an antielectron-neutrino [70,71]. These interactions are mediated by the $W^{\pm}$ bosons, which only couple to left-handed particles and right-handed antiparticles corresponding to the third component of the weak isospin being $I_3 = \pm\frac{1}{2}$ [72]. Consequently, these fermions are placed in isospin doublets, and while no coupling to right-handed particles corresponds to $I_3 = 0$, right-handed fermions only exist in isospin singlets. Neutrinos have been found to only exist as left-handed particles and right-handed antiparticles [73].

Usually, weak interactions occur within the same doublet, but "strange" hadron decays with unusual long lifetimes can be explained by the strange quark in the second generation decaying via a charged current to the up quark of the first generation (GIM mechanism) [74]. Consequently, the mass eigenstates that are observed in experiments are not identical to the flavour eigenstates participating in the weak interaction. For three generations of quarks, the CKM matrix (V_{CKM}) named after Cabibbo, Kobayashi and Maskawa transforms the flavour eigenstates to the mass eigenstates

$$\begin{pmatrix} d \\ s \\ b \end{pmatrix} = V_{\mathrm{CKM}} \begin{pmatrix} d' \\ s' \\ b' \end{pmatrix} \tag{2.7}$$

where V_{CKM} is unitary and $|V^{ij}_{\mathrm{CKM}}|^2$ describes the transition probability from a up-type quark of the ith generation to an down-type quark of the jth generation [75].

The charged current Lagrangian can then be written as [76,77]

$$\begin{aligned} \mathcal{L}_{CC} = & -\frac{g_2}{\sqrt{2}}\left[\overline{d}_j\gamma^\mu\frac{1-\gamma^5}{2}V^{ij}_{\mathrm{CKM}}u_i + \overline{\nu}_i\gamma^\mu\frac{1-\gamma^5}{2}\ell_i\right]W^+_\mu \\ & -\frac{g_2}{\sqrt{2}}\left[\overline{u}_i\gamma^\mu\frac{1-\gamma^5}{2}V^{ij}_{\mathrm{CKM}}d_j + \overline{\ell}_i\gamma^\mu\frac{1-\gamma^5}{2}\nu_i\right]W^-_\mu \end{aligned} \tag{2.8}$$

with $\gamma^5 = i\gamma^0\gamma^1\gamma^2\gamma^3$ and g_2 being the coupling strength, d and u denoting the down-type and up-type quarks, respectively, and ℓ and ν denoting the charged leptons and neutrinos of the generations i and j.

In contrast to the charged current of the weak interaction, the neutral current mediated by the Z boson not only couples to the weak isospin but also to the electrical charge of the particle. Furthermore, no flavour changing neutral currents at tree level have been observed so far, such that no CKM matrix modifications are necessary. The Lagrangian

$$\mathcal{L}_{NC} = \frac{g_2}{\cos\theta_W}\left[\overline{\psi}\gamma^\mu\frac{1-\gamma^5}{2}\psi - \sin^2\theta_W Q\overline{\psi}\gamma^\mu\psi\right]Z_\mu \tag{2.9}$$

with Q being the electrical charge of the fermion and θ_W being the weak mixing angle.

2.1.4. Electroweak Unification

The idea of unifying the electromagnetic and weak interaction arises from the similarity of the electromagnetic and weak neutral currents [78–80]. By introducing the hypercharge as

$$Y = 2(Q - I_3) \tag{2.10}$$

and writing W^a_μ with $a = 1, 2, 3$ as the weak isospin fields and B_μ as the hypercharge field, the photon and Z boson fields can be expressed through the weak mixing angle as

$$\begin{pmatrix} A \\ Z \end{pmatrix} = \begin{pmatrix} \cos\theta_W & \sin\theta_W \\ -\sin\theta_W & \cos\theta_W \end{pmatrix} \begin{pmatrix} B \\ W^3 \end{pmatrix} \tag{2.11}$$

and the fields of the observed $W^\pm$ bosons as

$$W^\pm = \tfrac{1}{\sqrt{2}}(W^1 \mp iW^2). \tag{2.12}$$

Using these representation of the fields, W^a_μ respect the $\mathrm{SU}(2)_L$ symmetry where the index L indicates that only particles with left-handed chirality carry a weak isospin. The generators of this group are the Pauli matrices σ_a. The remaining field B_μ respects the $\mathrm{U}(1)_Y$ symmetry with the hypercharge Y being the generator of this field. Asserting the unification means that the Lagrangian is invariant under local $\mathrm{SU}(2)_L \times \mathrm{U}(1)_Y$ symmetry.

Considering that the right handed neutrino isospin singlet does not exist in the SM, the contributions of leptons (l) and quarks (q) need to be evaluated independently in the Lagrangian. As discussed in detail for QED, to preserve invariance of the Lagrangian under local gauge transformations, the derivative needs to be replaced by the covariant derivative

$$\partial_\mu \to D_\mu = \partial_\mu - ig_2\frac{\sigma_a}{2}W^a_\mu - ig_1\frac{Y_L}{2}B_\mu \tag{2.13}$$

in the case of left-handed doublets and

$$\partial_\mu \to D^R_\mu = \partial_\mu - ig_1\frac{Y_R}{2}B_\mu \tag{2.14}$$

in the case of right-handed singlets. The electroweak Lagrangian can then be written as

$$\mathcal{L}_{\mathrm{EW}} = \mathcal{L}_l + \mathcal{L}_q + \mathcal{L}_{\mathrm{fields}} \tag{2.15}$$

where

$$\mathcal{L}_l = i\bar{l}_L\gamma^\mu D_\mu l_L + i\bar{\ell}_R\gamma^\mu D^R_\mu \ell_R \tag{2.16}$$

is the contribution for leptons,

$$\mathcal{L}_q = i\bar{q}_L\gamma^\mu D_\mu q_L + i\bar{u}_R\gamma^\mu D^R_\mu u_R + i\bar{d}_R\gamma^\mu D^R_\mu d_R \tag{2.17}$$

is the contribution for quarks, and

$$\mathcal{L}_{\text{fields}} = -\tfrac{1}{4}W_a^{\mu\nu}W_{\mu\nu}^a - \tfrac{1}{4}B^{\mu\nu}B_{\mu\nu} \tag{2.18}$$

is the contribution from the kinematic terms of the W_μ^a and B_μ fields with

$$\begin{aligned} W_{\mu\nu}^a &= \partial_\mu W_\nu^a - \partial_\nu W_\mu^a + g_2 \varepsilon^{abc} W_\mu^b W_\nu^c \text{ and} \\ B_{\mu\nu} &= \partial_\mu B_\nu - \partial_\nu B_\mu. \end{aligned} \tag{2.19}$$

The last term for $W_{\mu\nu}^a$ results from their commutation relations, whereby g_2 denotes the coupling constant and ε^{abc} is the totally antisymmetric tensor that ensures the correct structure of the commutator. These terms then yield self-couplings of the bosons resulting from the non-abelian nature of the $\mathrm{SU}(2)_L$ symmetry group.

It should be noted that to preserve the invariance of the Lagrangian, no mass terms have been added. This contradicts experimental observations which show that the fermions as well as the weak bosons are massive. This problem is addressed by the Brout-Englert-Higgs mechanism explained in Section 2.1.6.

2.1.5. Quantum Chromodynamics

The strong interaction is mediated by the gluon which couples to the colour charge that takes three discrete values: red, blue and green. Therefore, the corresponding quantum field theory is called quantum chromodynamics (QCD) [81–88].

Mathematically, the QCD is expressed through the $\mathrm{SU}(3)_C$ symmetry group where C stands for colour. Analogous to QED, the Lagrangian can be written as

$$\mathcal{L}_{\text{QCD}} = \overline{q}_i \left(i\gamma^\mu (D_\mu)_{ij}\right) q_j - \tfrac{1}{4}G^{\mu\nu}G_{\mu\nu} \tag{2.20}$$

with

$$G_{\mu\nu}^a = \partial_\mu G_\nu^a - \partial_\nu G_\mu^a + g_s f^{abc} G_\mu^b G_\nu^c \text{ and } (D_\mu)_{ij} = \partial_\mu \delta_{ij} - i g_s (T_a)_{ij} G_\mu^a \tag{2.21}$$

representing the kinematic terms of the eight gluon fields G_μ^a and the covariant derivative in context of the $\mathrm{SU}(3)_C$ symmetry. The coupling strength is denoted by g_s and the structure constants f^{abc} enforces the correct commutation rules. The generators $T_a = \frac{1}{2}\lambda_a$ correspond to the Gell-Mann matrices λ_a. The indices i and j represent the colour state of the respective quark spinor q. These definitions ensure invariance of the Lagrangian $\mathcal{L}_{\text{QCD}}$ under local $\mathrm{SU}(3)_C$ gauge transformations.

Within the SM, the QCD is unique in many aspects. The gluon can undergo an infinite number of self-interactions resulting in the coupling constant becoming larger with smaller energies. Therefore, at high energy scales, quarks or gluons can be considered asymptotically free, allowing the use of perturbation theory while, for lower energy scales, strong interactions become quickly non-perturbative.

It also means that increasing the distance between quarks increases the energy stored in the gauge field such that a new $q\bar{q}$-pair can be created. This process is called hadronisation and takes place on the timescale of $\mathcal{O}(10^{-24}\,\mathrm{s})$.

Another consequence of QCD is colour confinement. It implies that hadronising quarks only exist in bound states called hadrons. These are colour neutral, either by three differently coloured quarks forming a bound state called a baryon, or by a quark and an antiquark with the same colour forming a bound state called a meson.

2.1.6. The Brout-Englert-Higgs Mechanism

The combined Lagrangian of the SM

$$\mathcal{L}_{\text{SM}} = \underbrace{-\tfrac{1}{4}G^a_{\mu\nu}G^{\mu\nu}_a - \tfrac{1}{4}W^a_{\mu\nu}W^{\mu\nu}_a - \tfrac{1}{4}B_{\mu\nu}B^{\mu\nu}}_{\text{kinematics of gauge fields}} + \underbrace{\overline{\psi}^f_L i\gamma^\mu D_\mu \psi^f_L + \overline{\psi}^f_R i\gamma^\mu D_\mu \psi^f_R}_{\text{kinematics and interactions of fermions}} \tag{2.22}$$

with

$$D_\mu \psi = \Big(\partial_\mu - \underbrace{ig_s T_a G^a_\mu}_{SU(3)_C} - \underbrace{ig_2 T_a W^a_\mu}_{SU(2)_L} - \underbrace{ig_1 T B_\mu}_{U(1)_Y}\Big)\psi \tag{2.23}$$

is invariant under $\text{SU}(3)_C \times \text{SU}(2)_L \times \text{U}(1)_Y$ gauge transformations. It does not include any mass terms since a fermion mass term would mix the left-handed and right-handed spinors which is forbidden within the $\text{SU}(2)_L$ symmetry. A gauge boson mass term on the other hand would break the invariance of the Lagrangian. However, fermion as well as gauge boson masses have been experimentally observed.

A solution to the limitation of massive gauge bosons has been proposed simultaneously by Guralnik, Hagen, Kibble, Brout, Englert and Higgs in the 1960's [89–94] where Higgs was the first to predict the Higgs boson itself. The theory is called Brout-Englert-Higgs (BEH) mechanism. Today, the BEH mechanism is considered as the mechanism that completed the SM, although not all phenomena in the universe can be explained within the SM.

The idea is quite simple. While the full symmetry of the Lagrangian should be preserved in general, specific states such as the lowest energy state (vacuum state) do not need to be invariant under the full symmetry. As soon as the system reaches this state, the symmetry is spontaneously broken. For the electroweak theory, this can be achieved by introducing two complex scalar fields placed in an isospin doublet

$$\Phi = \begin{pmatrix} \phi^+ \\ \phi^0 \end{pmatrix} = \frac{1}{\sqrt{2}} \begin{pmatrix} \phi_1 + i\phi_2 \\ \phi_3 + i\phi_4 \end{pmatrix} \tag{2.24}$$

with a hypercharge of $Y_\Phi = +1$, ϕ^+ being electrically charged and ϕ^0 electrically neutral. This extra field contributes another term

$$\mathcal{L}_H = (D_\mu \Phi)^\dagger (D^\mu \Phi) - V(\Phi) \text{ with } V(\Phi) = \mu^2 \Phi^\dagger \Phi + \lambda \left(\Phi^\dagger \Phi\right)^2 \tag{2.25}$$

to the Lagrangian, where $V(\Phi)$ denotes the Higgs potential. The use of the covariant derivative of the form

$$D_\mu = \partial_\mu - i\frac{g_2 \sigma_a}{2} W^a_\mu - i\frac{g_1 Y_\Phi}{2} B_\mu \tag{2.26}$$

ensures that the Lagrangian is invariant under the $\mathrm{SU}(2)_L \times \mathrm{U}(1)_Y$ gauge transformations representing the electroweak sector of the SM.

The two free parameters of the Higgs potential, λ and μ^2, are real and can take either positive or negative values. Restricting $\lambda > 0$, ensures that the potential is bounded from below such that the vacuum state is stable. The remaining parameter μ^2 determines the form of the Higgs potential. Figure 2.2 shows the two different possibilities for μ^2 using a simpler example of a complex scalar singlet $\phi = \phi_1 + i\phi_2$ for display reasons. The conclusions hold when using a doublet with four degrees of freedom.

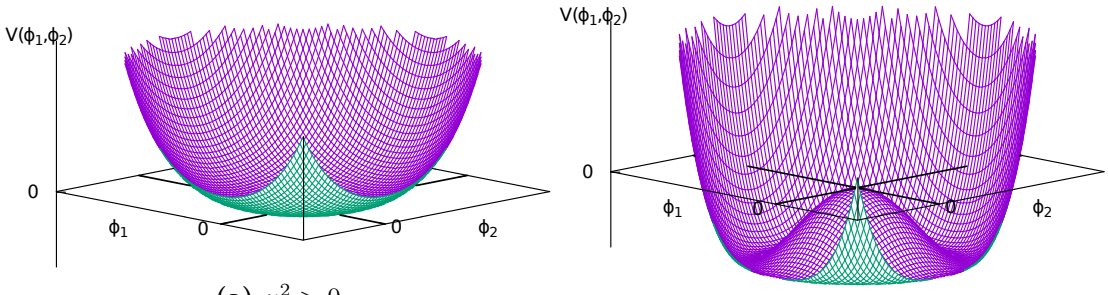

(a) $\mu^2 > 0$ **(b)** $\mu^2 < 0$

Figure 2.2.: Sketch of a simplified Higgs potential $V(\phi) = \lambda(\phi\phi^*)^2 + \mu^2(\phi\phi^*)$ for a complex scalar field $\phi = \phi_1 + i\phi_2$ with $\lambda > 0$ and different values of μ^2.

If μ^2 is positive, the potential has one minimum at $\phi_1 = \phi_2 = \phi_3 = \phi_4 = 0$ resulting in the vacuum state being invariant under the $\mathrm{SU}(2)_L \times \mathrm{U}(1)_Y$ symmetry. If, however, μ^2 is negative, the minimum turns into a local maximum surrounded by an infinite set of equivalent minima satisfying

$$\sum_i \phi_i^2 = \frac{-\mu^2}{\lambda} = v^2, \tag{2.27}$$

where v is called vacuum expectation value.

At some point the field spontaneously chooses one of these minima as its vacuum state and, thus, breaks the symmetry of the Lagrangian in the vacuum state while the potential itself still respects it. As per convention, the minimum is assumed to be real, and must be in the uncharged component of the doublet. This preserves the exact symmetry of quantum electrodynamics $\mathrm{U}(1)_{\mathrm{EM}}$ with its generator, the electrical charge $Q = I_3 + \frac{Y_\Phi}{2}$, and the masslessness of the photon:

$$\langle \Phi^0 \rangle = \begin{pmatrix} 0 \\ v \end{pmatrix}. \tag{2.28}$$

Expanding the fields around the minimum, the resulting doublet

$$\Phi = \frac{1}{\sqrt{2}} \begin{pmatrix} \theta_2(x) + i\theta_1(x) \\ v + H(x) - i\theta_3(x) \end{pmatrix} \tag{2.29}$$

contains three massless, scalar Goldstone bosons $\theta_a(x)$ [95, 96] and one massive Higgs boson $H(x)$ as will be shown in the following. Since the Lagrangian is constructed to be invariant under local gauge transformations of the $\mathrm{SU}(2)_L \times \mathrm{U}(1)_Y$ group, it is possible to absorb the Goldstone bosons in a gauge called the unitary gauge:

$$\Phi = \frac{1}{\sqrt{2}} e^{i\theta_a(x)\sigma^a} \begin{pmatrix} 0 \\ v + H(x) \end{pmatrix}, \tag{2.30}$$

where σ^a refers to the Pauli matrices. Inserting this expression into the Lagrangian from Eq. 2.25, diagonalising the mass matrix and identifying the electroweak bosons as the mass eigenstates:

$$\begin{aligned} W_\mu^\pm &= \frac{1}{\sqrt{2}}(W_\mu^1 \mp i W_\mu^2) \text{ for the } W \text{ bosons} \\ Z_\mu &= \frac{g_2 W_\mu^3 - g_1 B_\mu}{\sqrt{g_2^2 + g_1^2}} \text{ for the } Z \text{ boson and} \\ A_\mu &= \frac{g_2 W_\mu^3 + g_1 B_\mu}{\sqrt{g_2^2 + g_1^2}} \text{ for the photon,} \end{aligned} \tag{2.31}$$

the Lagrangian emerges as

$$\begin{aligned} \mathcal{L}_H = &\underbrace{\frac{1}{2}\partial_\mu H \partial^\mu H - \lambda v^2 H^2}_{\text{massive scalar}} \underbrace{-\lambda v H^3 - \frac{1}{4}\lambda H^4}_{\text{self-interactions}} + \underbrace{\frac{g_2^2 v^2}{4} W_\mu^- W^{+\mu} + \frac{v^2}{8(g_2^2 + g_1^2)} Z_\mu Z^\mu}_{\text{mass terms for gauge bosons}} \\ &\underbrace{+ \frac{g_2^2 v}{2} W_\mu^- W^{+\mu} H + \frac{g_2^2}{4} W_\mu^- W^{+\mu} H^2 + \frac{v}{4(g_2^2 + g_1^2)} Z_\mu Z^\mu H + \frac{1}{8(g_2^2 + g_1^2)} Z_\mu Z^\mu H^2}_{\text{interactions between the scalar and gauge fields}}. \end{aligned} \tag{2.32}$$

While the $W_\mu^\pm$ and Z_μ gauge bosons and the scalar Higgs boson H have mass, the photon remains massless

$$m_H = \sqrt{2\lambda v^2},\ m_W = \frac{g_2 v}{2},\ m_Z = \frac{v}{2\sqrt{g_2^2 + g_1^2}} \text{ and } m_A = 0. \tag{2.33}$$

Therefore, the vacuum expectation value can be inferred to be

$$v = \frac{2 m_W}{g_2} = \sqrt{\frac{1}{\sqrt{2} G_F}} \approx 246\,\mathrm{GeV} \tag{2.34}$$

using the definition of the Fermi constant G_F [97].

While the weak bosons have obtained their mass through this mechanism, the fermion masses have not been considered at this stage. Due to the different transformation of left-handed fermion doublets and right-handed fermion singlets, the Lagrangian does not preserve the $\mathrm{SU}(2)_L \times \mathrm{U}(1)_Y$ symmetry if a fermion mass term

$$-m_f \overline{\psi}\psi = -m_f \left(\overline{\psi}_R \psi_L + \overline{\psi}_L \psi_R\right) \tag{2.35}$$

is present. However, adding the complex scalar doublet to the equation, the Lagrangian becomes invariant under $\mathrm{SU}(2)_L \times \mathrm{U}(1)_Y$ transformations since

$$\left(\overline{\psi}_L \Phi \psi_R\right)^\dagger = \overline{\psi}_R \Phi^\dagger \psi_L. \tag{2.36}$$

Therefore, the Lagrangian term

$$\mathcal{L}_d = -\lambda_f \left(\overline{\psi}_L \Phi \psi_R + \overline{\psi}_R \Phi^\dagger \psi_L\right) \tag{2.37}$$

is invariant. Using the unitary gauge, the Lagrangian can be rewritten as

$$\begin{aligned}\mathcal{L}_d &= -\frac{\lambda_f}{\sqrt{2}} \left(\begin{pmatrix} \overline{U} & \overline{D} \end{pmatrix}_L \begin{pmatrix} 0 \\ v+H \end{pmatrix} (D)_R + (\overline{D})_R \begin{pmatrix} 0 & v+H \end{pmatrix} \begin{pmatrix} U \\ D \end{pmatrix}_L \right) \\ &= -\frac{\lambda_f v}{\sqrt{2}} (\overline{D}_L D_R + \overline{D}_R D_L) - \frac{\lambda_f}{\sqrt{2}} H (\overline{D}_L D_R + \overline{D}_R D_L)\end{aligned} \tag{2.38}$$

resulting in fermion masses of

$$m_f = \frac{\lambda_f v}{\sqrt{2}}, \tag{2.39}$$

where λ_f denotes the Yukawa coupling [79, 82, 83]. It should also be noted that, in addition to the mass term, an interaction term between the fermions and the Higgs boson arises that is proportional to the fermion's mass. However, since the vacuum state of the Higgs potential must be in the neutral component of the doublet, it can only give mass to down-type fermions, namely charged leptons and down-type quarks. To also allow the generation of masses for up-type fermions, a conjugate complex scalar doublet

$$\Phi_C = -i\sigma_2 \Phi^* = \begin{pmatrix} -\phi^{0*} \\ \phi^- \end{pmatrix} = \begin{pmatrix} -\phi_3 + i\phi_4 \\ \phi_1 - i\phi_2 \end{pmatrix} \tag{2.40}$$

is constructed which transforms exactly the same as the normal doublet. Thus, after symmetry breaking, the Lagrangian for up-type fermions reads

$$\begin{aligned}\mathcal{L}_u &= \lambda_f \left(\overline{\psi}_L \Phi_C \psi_R + \overline{\psi}_R \Phi_C^\dagger \psi_R\right) \\ &= -\frac{\lambda_f v}{\sqrt{2}} (\overline{U}_L U_R + \overline{U}_R U_L) - \frac{\lambda_f}{\sqrt{2}} H (\overline{U}_L U_R + \overline{U}_R U_L)\end{aligned} \tag{2.41}$$

yielding the same result for up-type quarks and down-type fermions.

2.1.7. Higgs Boson Production and Decay

The Higgs boson is the only scalar particle in the SM that is elementary. It has a spin-0 and a positive parity. Furthermore, it does not carry an electric charge and is colourless. It couples to massive bosons ($\propto m_V^2$) as well as massive fermions ($\propto m_f$). The mass

of the Higgs boson is not predicted by the SM, which made the search for it extremely challenging.

In 2012, nearly 50 years after the prediction of the Higgs boson, a scalar resonance was observed by ATLAS and CMS [1, 2] with a mass of $m_H = 125.09 \pm 0.24\,\text{GeV}$ [98]. Until today, no significant deviations from the quantities predicted for the SM Higgs boson have been observed [99–104].

Since the LHC collides protons, the initial partons are in general gluons or light quarks. Due to the strong coupling dependence on the mass and the large mass difference between the light quarks ($\mathcal{O}(10\,\text{MeV})$) and the vector bosons and the top quark ($\mathcal{O}(100\,\text{GeV})$), the direct production of Higgs bosons ($q\bar{q} \to H$) is irrelevant at the LHC. Instead the four production modes depicted in Figure 2.3 have the highest relevance [105].

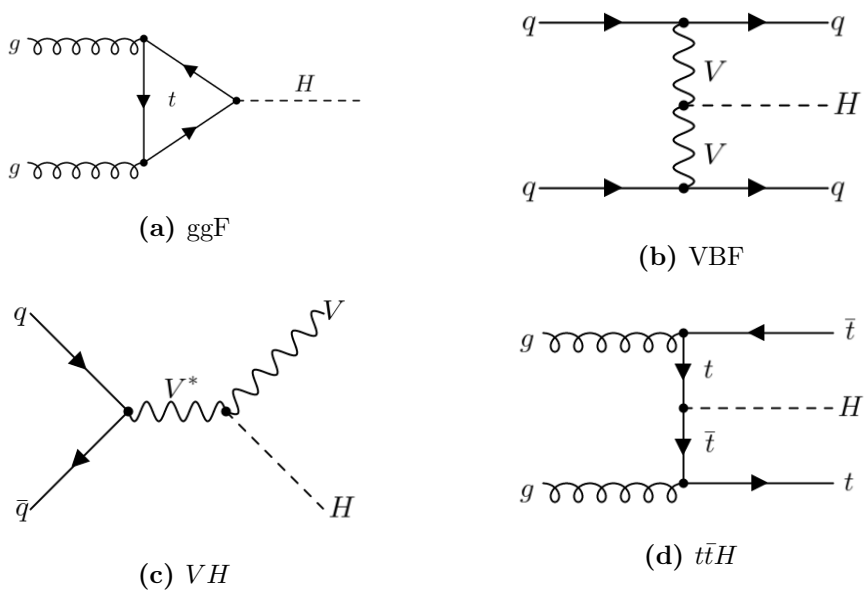

Figure 2.3.: Feynman diagrams of the four main Higgs boson production modes in the SM at the LHC.

The leading production mechanism at the LHC is gluon-gluon fusion (ggf) with a cross section of $\sigma(pp \to H) = 48.52\,\text{pb}$ calculated at N3LO QCD and NLO EW precision [106–110] where two gluons produce a Higgs boson via a quark loop dominated by top quarks as the most massive particles in the standard model.

The cross section of the second leading production mechanism is already an order of magnitude smaller with $\sigma(pp \to qqH) = 3.779\,\text{pb}$ calculated at NNLO QCD and NLO EW precision [109–114] where two quarks each radiate a heavy vector boson that then fuse together to produce the Higgs boson. A special detector signature stems from the residuals of the initial quarks which leave a signal in both forward regions of the detector.

Associated production with a vector boson (VH or Higgs-strahlung) is the third leading production mechanism at the LHC. At tree-level a quark and antiquark form a

virtual massive vector boson which then radiates a Higgs boson before it decays. The cross section for WH is $\sigma(pp \to WH) = 1.369\,\text{pb}$ calculated at NNLO QCD and NLO EW precision [109–114] and $\sigma(pp \to ZH) = 0.8824\,\text{pb}$ for ZH also calculated at NNLO QCD and NLO EW precision [109–114].

The fourth of the main production modes is the Higgs boson production in association with a top quark pair ($t\bar{t}H$) with a cross section of $\sigma(pp \to t\bar{t}H) = 0.5065\,\text{pb}$ calculated at NLO QCD and NLO EW precision [109, 110, 115–117]. Here, two gluons each emit a $t\bar{t}$-pair where the top quark of one gluon fuses with the antitop-quark of the other gluon to produce a Higgs boson resulting in one Higgs boson and one top-quark pair in the final state.

The cross sections of the described scenarios depending on the mass of the Higgs boson at a centre-of-mass energy of $\sqrt{s} = 13\,\text{TeV}$ are also illustrated in Figure 2.4 (a). Since the Higgs boson is not stable, it decays into different pairs of particles where the sum of masses of these particles together must be smaller than the Higgs boson mass. Furthermore, the Higgs boson prefers decays to more massive particles due to its coupling strength being proportional to the particle's mass for fermions and to the particle's mass squared for bosons. The branching ratios for Higgs boson decays into various final states depending the mass of the Higgs boson are shown in Figure 2.4 (b) [105].

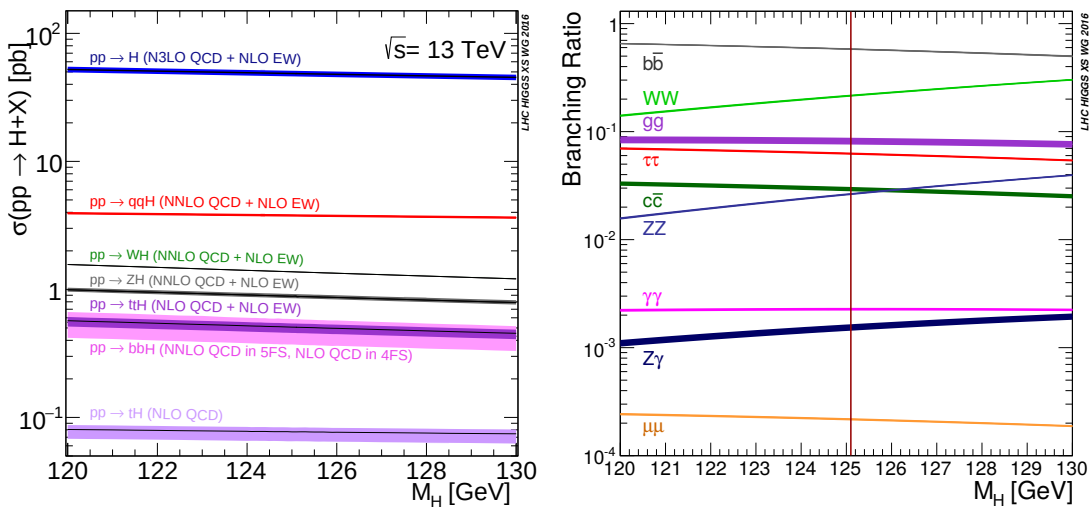

(a) production **(b)** decay

Figure 2.4.: Expected LHC production cross section and decay branching ratios of the Higgs boson depending on its mass [105].

The leading decay mode is the decay into a $b\bar{b}$-pair with a branching ratio of around $\mathcal{BR}(H \to b\bar{b}) = 58\%$ since this is the heaviest particle whose mass is smaller than half of the Higgs mass allowing both particles to be real. Figure 2.5 (a) depicts the Feynman diagram of the Higgs boson decaying into a fermion pair.

However, a decay into particles whose mass is larger than half of the Higgs mass

is possible if the particles themselves are not stable. This allows the particle to exist for a very short period of time as virtual (off-shell) particle before it decays into much lighter real (on-shell) particles. The production of such off-shell particle is quantum mechanically suppressed. An example is the decay to a pair of W bosons. Since $m_W > m_H/2$, at least one of the W bosons needs to be produced off-shell and, therefore, the branching ratio $\mathcal{BR}(H \to WW^*) = 21.52\%$ is a factor of three smaller than the decay into a bottom quark pair. However, since the W boson mass is so much larger than the mass of the other light fermions, it is still the second leading decay mode. The corresponding Feynman diagram can be found in Figure 2.5 (b).

The third leading decay mode is the decay into gluons, which as for the production is not possible directly since the gluons are massless as shown in Figure 2.5 (c). The branching ratio is in the order of 8%.

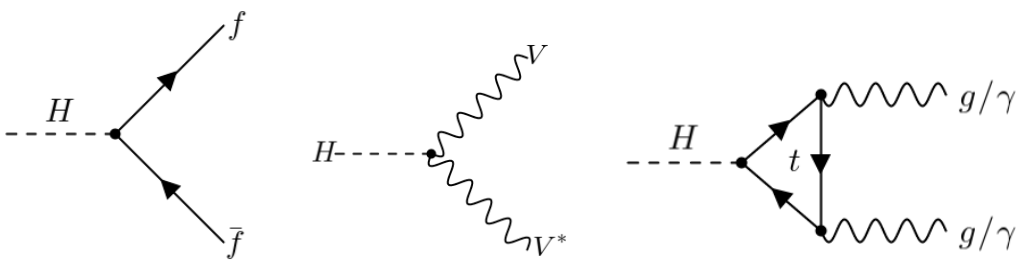

(a) $H \to \bar{f}f$ **(b)** $H \to VV^*$ **(c)** $H \to$ massless bosons

Figure 2.5.: Feynman diagrams of the three general decay modes to fermions, to massive vector bosons and to massless vector bosons via a particle loop.

This is followed by the decay into a $\tau^+\tau^-$-pair (6.256%), a $c\bar{c}$-pair (2.884%), a ZZ^*-pair (2.641%), a $\gamma\gamma$-pair (0.227%) and a photon in conjunction a Z boson (0.1541%).

With $\mathcal{BR}(H \to \mu^+\mu^-) = 0.02171\%$, the decay into a $\mu^+\mu^-$-pair is the decay mode with the smallest branching ratio that is generally searched for [118], since not only the branching ratio is important to detect events but also how easily signal events can be distinguished from events arising from other processes.

2.1.8. Limitations of the Standard Model

Despite the SM being one of the most successful theories in physics, it cannot explain all physics phenomena observed and not all its predictions match the experiment. Due to the large number of limitations of the SM, only the most prominent examples will be briefly discussed in this section.

By construction, gravity is not included in the SM, since on the energy scales relevant for particle physics, the gravitational strength is several orders weaker than of any other interaction. It only becomes dominant when reaching the Planck scale ($\mathcal{O}(10^{19}\,\text{GeV})$). This causes inconsistencies between the extremely successful theory of general relativity [119] and the SM [120–123].

In addition, the microwave background, rotation curves as well as absorption lines of hydrogen suggest that there must be more matter than what is actually visible [124,125]. Since this matter does not or very rarely interact with the particle content of the SM, it is called dark matter and must be a particle beyond the SM [126]. Furthermore, since the accelerated expansion of the universe might not be explained by the vacuum energy of the SM, the concept of dark energy [127,128] appears to be necessary. According to the latest measurements by the Planck telescope in the context of the ΛCDM model, only 5% of the universe consists of visible matter and energy described by the SM, 27% is dark matter and the remaining 68% appear to be dark energy [129].

Another mystery is the existence of matter in a universe without antimatter. Shortly after the Big Bang, matter and antimatter are assumed to have been equally distributed. Later processes with CP violation, baryon number violation and interactions out of thermal equilibrium can cause an excess of matter [130]. So far, only CP violation in weak interactions between quarks has been observed experimentally, but this is not sufficient to explain the amount of matter in the universe today [131–135].

Neutrinos are considered massless in the SM, but oscillations in the neutrino flavour have been observed in solar neutrinos, atmospheric neutrinos, reactor neutrinos and neutrino beams by detecting a deficit in the predicted flavour and an enhancement of other neutrino flavours [136–143]. This is only possible if the mass eigenstates are linear combinations of the flavour eigenstates realised through the PMNS matrix in analogy to the CKM matrix [144,145]. Compared to all other particle masses in the SM, the neutrino masses are tiny, yielding the question if they are generated by the BEH mechanism.

In addition to physics not included in the SM, there are also observed deviations from its predictions with the most prominent example being the measurement of the anomalous magnetic moment of muons, which is predicted by QED to a very high precision and measured with an even higher precision [146]. A deviation of 4.2 standard deviations is observed, indicating that there might be processes in addition to what is known from the SM. Another recent example is the evidence for lepton universality violation in B^0 meson decays by LHCb [147], for which first deviations have been measured by BaBar [148] and Belle [149] before.

There are also a few theoretical shortcomings. Considering the 19 free parameters of the SM, they must be determined by measurements as there is no prediction provided. This also yields the questions why are there exactly 19 free parameters, why are there three generations of matter, and whether there could be more free parameters.

The strong sector as non-perturbative theory also leaves some questions open. For example, no CP violation has been observed [150], although it is not forbidden by theory in principle. Colour confinement has also been observed in every experiment so far but is not analytically proven.

The last example discussed here is the hierarchy problem which appears to be a lucky coincidence of the universe [151]. Corrections to the Higgs boson mass from quantum loops are several orders of magnitudes larger than the Higgs boson mass itself. However, the observed value indicates that these corrections cancel, implying the Higgs boson mass might be fine tuned.

Many of these issues can be overcome by theories beyond the SM. Selected benchmark scenarios using two Higgs bosons as window to "new physics" are given in Sections 2.2.2 and 2.2.3.

2.2. Higgs Boson Pair Production

In this thesis, a search for Higgs boson pairs is conducted. Therefore, the production of Higgs boson pairs as well as their decays are discussed in more detail in this section.

Since the decay of a particle is independent of its production, the branching ratios for a Higgs boson produced alone or in conjunction with any other particle are identical. The branching ratios of final states relevant for searches for Higgs boson pair production are summarised in Table 2.1.

	bb	WW	$\tau\tau$	ZZ	$\gamma\gamma$
bb	34%				
WW	25%	4.6%			
$\tau\tau$	7.3%	2.7%	0.39%		
ZZ	3.1%	1.1%	0.33%	0.07%	
$\gamma\gamma$	0.26%	0.1%	0.02%	0.01%	$< 0.001\%$

Table 2.1.: Branching ratios of a Higgs boson pair with $m_H = 125\,\text{GeV}$ [105]. The rows stand for the decay channel of one Higgs boson while the columns denote the decay of the other Higgs boson. Only decays relevant for searches are listed.

The leading decay channel for Higgs boson pair production is the decay of both Higgs bosons into a bottom quark pair with approximately 34%. This is followed by one Higgs boson decaying into a bottom quark pair while the other decaying into a W boson pair with around 25%. The next relevant decays already have a significantly smaller branching ratio of 7.3% for the decay into a bottom quark pair in conjunction with a τ lepton pair, and of 4.6% with for the decay into two W boson pairs. The lowest listed branching ratio is the decay to two photon pairs with less than 0.001%.

In contrast to the decay, the production of Higgs boson pairs depends on the model considered. While Higgs boson pair production is possible in the SM solely in a non-resonant mode, beyond SM theories allow the production of Higgs boson pairs in a resonant mode by introducing a heavy particle X that can decay into Higgs bosons. Some of these theories can be extended to scenarios where X decays into a Higgs boson in conjunction with another scalar particle whose mass is larger than m_H but smaller than m_X.

2.2.1. Higgs Boson Pair Production in the Standard Model

In the SM Lagrangian that includes the Higgs field (see Eq. 2.32), triple and quartic self-couplings of the Higgs boson arise. While the triple self-coupling is proportional to

$v\lambda$, the quartic self-coupling is proportional to $\lambda/4$ and, therefore, much smaller than the triple coupling , since

$$\lambda = \frac{m_H^2}{2v^2} \approx 0.13. \tag{2.42}$$

Furthermore, the triple coupling can be produced at tree-level, increasing the contribution of this process to Higgs boson pair production even more with respect to the quartic coupling. Thus, the quartic coupling is negligible and will not be considered in the following.

In order to produce two real Higgs bosons via the triple self-coupling, the mediator Higgs boson needs to be virtual with a mass $m_{H^*} \geq 2m_H$. Since the mass of virtual particles is not clearly defined but has a broad range, reconstructing this mass does not result in a resonance peak and this production mode is thus called non-resonant. Although the mediator Higgs boson is virtual, the production modes are identical to the ones of a real single Higgs boson.

The leading production mechanism is the gluon-gluon fusion and the resulting process ($gg \to H^* \to HH$) is shown in Figure 2.6 (a). This allows a direct measurement λ and, hence, of the Higgs potential without assuming a value of the Higgs boson mass. However, the SM also allows other processes that start with two gluons and end with two Higgs bosons as shown in Figure 2.6 (b). Here, the two gluons form a box of (top) quarks which then form the two Higgs bosons and is therefore also a non-resonant process.

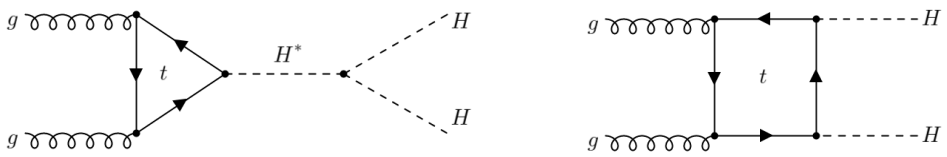

(a) Higgs self-coupling **(b)** top Yukawa-coupling

Figure 2.6.: Main non-resonant production modes of Higgs boson pairs at the LHC.

Due to the destructive interference between these processes, the resulting cross section is $\sigma(gg \to HH) = 31.05\,\text{fb}$ [4–11] which makes a discovery at the LHC difficult. Compared to the single Higgs gluon-gluon fusion cross section, this cross section is three orders of magnitude smaller.

The other single Higgs production mechanisms, vector boson fusion, Higgs-strahlung and Higgs boson production in association with a top quark pair, can also be translated to Higgs boson pair production in the same way as the gluon-gluon fusion but their cross sections are much smaller such that they do not contribute significantly [152].

2.2.2. Higgs Boson Pair Production beyond the Standard Model

Generally, there are two possibilities to approach beyond SM (BSM) theories. The top-down approach starts from well-motivated SM extensions valid up to energy scales

much higher than the electroweak scale while the bottom-up approach on the other hand focuses on the most general form of BSM models at the electroweak scales. For an extended Higgs sector, this translates to studies of complete models such as the Minimal Supersymmetric Standard Model [153–159] that contain an extended Higgs sector (top-down approach) or to look at the most general forms of scalar extensions such as Two Higgs Doublet Models [160] without any model dependence (bottom-up approach). This thesis and, thus, the remaining sections of this chapter follows the model independent bottom-up approach.

While it is possible to modify the Higgs self-coupling strength (κ_λ) or the top-Yukawa coupling (κ_t) to achieve a change in the interference between the Higgs self-coupling and box diagrams (see Figure 2.6) and, therefore, to enhance the Higgs boson pair production cross section of the non-resonant mode [161], another scenario is the resonant production of Higgs boson pairs by a new heavy particles which due to conservation laws can be either spin-0 or spin-2. Since the number of models predicting such particles is too large to be presented in detail in this thesis, only two theories which are most popular and most relevant for the analysis in this thesis are selected. Both theories introduce one or more new heavy scalar resonances X by extending the Higgs sector of the SM resulting in processes as shown in Figure 2.7. The notation used in this section follows Ref. [162] to a large extent.

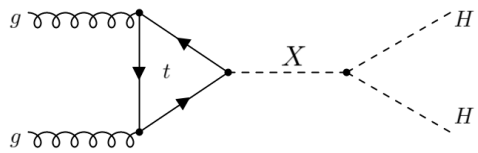

Figure 2.7.: Feynman diagram of resonant Higgs boson pair production where X denotes a heavy scalar.

Real Scalar Singlet Extension

The simplest possibility to obtain a new scalar particle is augmenting the SM by a real scalar singlet (RxSM) with a hypercharge $Y_S = 0$. [163–174]. The most general scalar potential that is renormalizable can be written as

$$V(\Phi, S) = \underbrace{-\mu^2\Phi^\dagger\Phi + \lambda(\Phi^\dagger\Phi)^2}_{\text{SM potential}} + \underbrace{\frac{a_1}{2}\Phi^\dagger\Phi S + \frac{a_2}{2}\Phi^\dagger\Phi S^2}_{\text{interactions}} + \underbrace{b_1 S + \frac{b_2}{2}S^2 + \frac{b_3}{3}S^3 + \frac{b_4}{4}S^4}_{\text{singlet potential}} \tag{2.43}$$

where Φ denotes the SM Higgs doublet and S the singlet extension. This potential includes all interactions between S and the SM particles, i.e. S can only couple to Φ

within the SM. Expanding the fields around their vacuum expectation values v and v_S, respectively, the fields can be expressed by

$$\Phi = \frac{1}{\sqrt{2}} \begin{pmatrix} 0 \\ v + H \end{pmatrix} \text{ and } S = \frac{1}{\sqrt{2}} \left(v_S + \phi_S \right), \tag{2.44}$$

with H being the SM Higgs boson and ϕ_S the new scalar field. In the broken phase, i.e. if $v_S \neq 0$, electroweak symmetry breaking causes ϕ_S and H to mix and to form two new mass eigenstates $h_{1,2}$

$$\begin{pmatrix} h_1 \\ h_2 \end{pmatrix} = \begin{pmatrix} \cos\theta & \sin\theta \\ -\sin\theta & \cos\theta \end{pmatrix} \begin{pmatrix} H \\ S \end{pmatrix} \tag{2.45}$$

through the mixing angle θ. This mixing reduces the couplings of h_1 and h_2 by $\cos\theta$ and $\sin\theta$, respectively, also suppressing the production and decay relative to the SM prediction. The masses $m_{1,2}$ of $h_{1,2}$ are ordered by convention to fulfil $m_2 \geq m_1$. In this thesis, however, the case where $m_1 = 125\,\text{GeV}$ and $m_2 > 2m_1$, thus allowing $h_2 \to h_1 h_1$ decays, is considered.

If $v_S = 0$, no such mixing and no couplings to SM particles exist such that S becomes a dark matter candidate. This phase is called dark matter phase. In this thesis, the primary interest is in the broken phase since it allows resonant Higgs boson pair production.

Some theoretical and experimental constraints limit the available phase space of this model in the broken phase. For one, the model is required to preserve vacuum stability at low and high energy scales, perturbative unitarity as well as perturbative couplings in the scalar potential at low and high energies. Experimentally, the model must respect precision measurements of electroweak observables, the W boson mass and the single Higgs decay rates as well as limits on searches conducted by the LHC experiments.

Imposing a $\mathbb{Z}_2$ symmetry where the fields transform as

$$\Phi \to \Phi \text{ and } S \to -S, \tag{2.46}$$

three parameters vanish with $a_1 = b_1 = b_3 = 0$. If S has a non-zero vacuum expectation value, the $\mathbb{Z}_2$ symmetry is softly broken and the scalar sector can be described by five parameters

$$m_1,\ m_2,\ v,\ \sin\theta \text{ and } \tan\beta = \frac{v}{v_S}. \tag{2.47}$$

Taking into account the aforementioned constraints, the maximum allowed value of $|\sin\theta|$ can be calculated to be approximately 0.2 for various values of m_2 resulting in a minimum Higgs boson pair branching ratio of $\mathcal{BR}(h_2 \to h_1 h_1) \approx 20\% - 25\%$ [162].

Without the $\mathbb{Z}_2$ symmetry, no symmetry is associated to S such that its vacuum expectation value is non-physical and can be set to zero. No further constraints can be set on the parameters of the potential yielding a much more complex vacuum structure. However, since the singlet is not allowed to contribute to the generation of W boson

and Z boson masses, the observed electroweak symmetry breaking pattern can only be achieved when $(v, v_s)_0 = (246\,\text{GeV}, 0)$ is the global minimum of the potential. This puts constraints on the $h_2 - h_1 - h_1$ coupling such that

$$\begin{aligned}\lambda_{211} =& \frac{b_3}{\sqrt{2}} \sin^2\theta \cos\theta + \frac{a_1}{2\sqrt{2}} \cos\theta(\cos^2\theta - 2\sin^2\theta) \\ &+ \frac{a_2}{2} v \sin^\theta(2\cos^2\theta - \sin^2\theta) - 6\lambda v \sin\theta \cos^2\theta.\end{aligned} \tag{2.48}$$

The branching ratio can be $\mathcal{BR}(h_2 \to h_1 h_1) \gtrsim 80\%$ resulting in the Higgs boson pair production cross section that can be larger by one order of magnitude compared to the SM.

These new scalar particles are generally considered to fulfil the narrow-width approximation, where interference effects are negligible around the resonance peak. However, interference effects can occur for $m_{h_1 h_1} \ll m_2$. Furthermore, the self-coupling strength is modified due to the mixing with the scalar such that a further enhancement of the cross section due to interference effects can be expected as shown in Figure 2.8 for a benchmark point of the real scalar singlet extension of the SM. The resonance peak around $m_S = 900\,\text{GeV}$ can be clearly seen as well as the broad distribution of the non-resonant Higgs boson pair production.

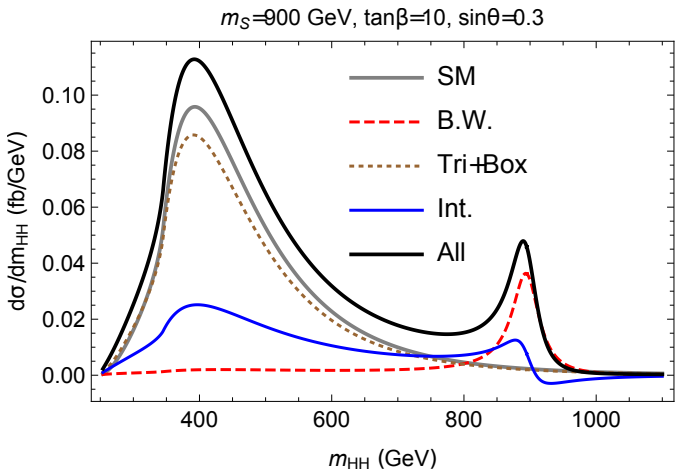

Figure 2.8.: Higgs boson pair production cross section depending on the invariant mass spectrum m_{HH} for a benchmark point of the real scalar singlet extension of the SM with a softly broken $\mathbb{Z}_2$ symmetry imposed. The red dashed line corresponds to the resonance peak, the brown dotted line refers to the diagrams of the non-resonant production without interference, which is shown between non-resonant and resonant production modes in blue and the combination of the three terms in black. The SM production cross section is added as grey line for comparison [174].

Two Higgs Doublet Models

Another model motivated by many BSM theories, such as supersymmetry [157] and axion models [175], or by the baryon asymmetry in the universe [176] is the two Higgs Doublet Model (2HDM) [160] where a second scalar doublet is augmented to the complex scalar doublet present in the SM. The notation in this thesis follows the one of Ref. [177].

In the most general case, a 2HDM potential can have a very complex vacuum state with up to 14 free parameters where the minima can be CP conserving, CP violating or also charge violating. The potential for two complex scalar doublets, Φ_1 and Φ_2, with a hypercharge of $Y = +1$ is

$$\begin{aligned} V = & m_{11}^2 \Phi_1^\dagger \Phi_1 + m_{22}^2 \Phi_2^\dagger \Phi_2 + \frac{\lambda_1}{2}\left(\Phi_1^\dagger \Phi_1\right)^2 + \frac{\lambda_2}{2}\left(\Phi_2^\dagger \Phi_2\right)^2 \\ & - \left[m_{12}^2 \Phi_1^\dagger \Phi_2 + \text{h.c}\right] + \lambda_3 \Phi_1^\dagger \Phi_1 \Phi_2^\dagger \Phi_2 + \lambda_4 \Phi_1^\dagger \Phi_2 \Phi_2^\dagger \Phi_1 \\ & + \left\{\frac{\lambda_5}{2}\left(\Phi_1^\dagger \Phi_2\right)^2 + \left[\lambda_6\left(\Phi_1^\dagger \Phi_1\right) + \lambda_7\left(\Phi_2^\dagger \Phi_2\right)\right]\left(\Phi_1^\dagger \Phi_2\right) + \text{h.c}\right\}, \end{aligned} \tag{2.49}$$

where the parameters m_{12}^2, λ_5, λ_6 and λ_7 can be complex, while the other parameters m_{11}^2, m_{22}^2, λ_1, λ_2, λ_3 and λ_4 are real. Applying spontaneous symmetry breaking from $\mathrm{SU}(2)_L \times \mathrm{U}(1)_Y$ to $\mathrm{U}(1)_{\mathrm{EM}}$ results in minima of the form

$$\langle \Phi_a^0 \rangle = \frac{v_a}{\sqrt{2}} e^{i\xi_a} \text{ with } a = 1, 2 \tag{2.50}$$

where the vacuum expectation values v_a are real and positive by convention. At this stage Φ_1 and Φ_2 are indistinguishable which means that, without changing the physics, a different basis with different parameters can be chosen.

For most BSM theories, it is sufficient to apply simplifications to this general potential. By choosing a basis where all parameters are simultaneously real, the potential becomes CP conserving. However, this real basis still allows for a spontaneous symmetry breaking of the vacuum which can be omitted by requiring that the complex phase of the vacuum $\xi_a = n\pi$ where n can only take integer values.

Expanding the fields around their minima yields

$$\Phi_a = \begin{pmatrix} \phi_a^+ \\ \frac{v_a + \rho_a + i\eta_a}{\sqrt{2}} \end{pmatrix} \text{ with } a = 1, 2 \tag{2.51}$$

where $v = \sqrt{v_1^2 + v_2^2} \approx 246\,\text{GeV}$. Using the definition $\tan\beta = v_2/v_1$ and the mixing angle α, the eight degrees of freedom can be translated to 3 massless Goldstone bosons ($G^\pm$ and G_0) and 5 scalar fields, of which two are charged ($H^\pm$), two are neutral and CP even (light h and heavy H) and one is neutral and CP odd (A). As in the SM, the Goldstone bosons are used to generate the masses of the $W^\pm$ and Z bosons.

The extended Yukawa Lagrangian

$$\mathcal{L}_{\mathrm{Y}}^{\mathrm{2HDM}} = \lambda_{ij}^{(1)} \overline{\psi}_i \Phi_1 \psi_j + \lambda_{ij}^{(2)} \overline{\psi}_i \Phi_2 \psi_j \tag{2.52}$$

yields the mass matrix

$$\mathcal{M}_{ij} = \frac{\lambda_{ij}^{(1)} v_1}{\sqrt{2}} + \frac{\lambda_{ij}^{(2)} v_2}{\sqrt{2}}, \tag{2.53}$$

where $\lambda^{(1)}$ and $\lambda^{(2)}$ are not simultaneously diagonalisable. This means that the mass matrix is not flavour diagonal and allows for flavour changing neutral currents (FCNCs) at tree level which contradicts current observations. The FCNCs can be omitted by enforcing all fermions with the same quantum numbers, i.e. right-handed fermions of the same charge, to couple to the same doublet by applying at least one discrete symmetry.

Since Φ_1 and Φ_2 are indistinguishable, there are four possible 2HDM types based on the coupling of the fermions to the different scalar doublets that forbid FCNCs. These are summarised in Table 2.2 with the discrete symmetries used to enforce the couplings. As per convention, the up-type quarks always couple to Φ_2.

Model	ψ_R^u	ψ_R^d	ψ_R^ℓ	Symmetry
Type I	Φ_2	Φ_2	Φ_2	$\mathbb{Z}_2: \ \Phi_1 \to -\Phi_1$
Type II	Φ_2	Φ_1	Φ_1	$\mathbb{Z}_2: \ \Phi_1 \to -\Phi_1$ & $\psi_R^d \to -\psi_R^d$
Lepton-specific	Φ_2	Φ_2	Φ_1	$\mathbb{Z}_2: \ \Phi_1 \to -\Phi_1$ & $\psi_R^\ell \to -\psi_R^\ell$
Flipped	Φ_2	Φ_1	Φ_2	$\mathbb{Z}_2: \ \Phi_1 \to -\Phi_1$ & $\psi_R^d \to -\psi_R^d$ & $\psi_R^\ell \to -\psi_R^\ell$

Table 2.2.: Types of 2HDMs, which omit FCNC, and the coupling of the Higgs doublets to the different types of fermions. By convention, up-type quarks always couple to Φ_2.

The Yukawa Lagrangian can be rewritten in terms of the observable fields with the couplings ξ_ϕ^f for the scalar ϕ and fermion type f

$$\begin{aligned}\mathcal{L}_{\mathrm{Y}}^{\mathrm{2HDM}} = & \sum_{f=u,d,\ell} \frac{m_f}{v} \left(\xi_h^f \overline{\psi}^f h \psi^f + \xi_H^f \overline{\psi}^f H \psi^f + \xi_A^f \overline{\psi}^f \gamma_5 A \psi^f \right) \\ & \left[\frac{\sqrt{2} V_{ud}}{v} \overline{\psi}^u \left(m_u \xi_A^u P_L + m_d \xi_A^d P_R \right) H^+ \psi^d + \frac{\sqrt{2} m_\ell \xi_A^\ell}{v} \overline{\psi}_L^\nu H^+ \psi_R^\ell + \mathrm{h.c.} \right].\end{aligned} \tag{2.54}$$

The values of the couplings are summarised in Table 2.3 for all four 2HDM types. The coupling to vector bosons is the same for all four models. While the couplings of h and H to vector bosons are suppressed by $\sin(\beta - \alpha)$ and $\cos(\beta - \alpha)$, respectively, compared to the SM couplings, the couplings of A to vector bosons vanishes completely.

In all models, it is also possible that the scalar particles couple to each other as described by the potential in Eq. 2.49, where the coupling strengths are not predicted by the model.

2.2.3. Extensions to SH production

To obtain resonant production of two different scalar particles of which one is the SM-like Higgs boson, another degree of freedom needs to added to the models discussed in

Fermion f	Scalar ϕ	Coupling ξ_ϕ^f in 2HDM			
		Type I	Type II	Lepton-specific	Flipped
ψ^u	h	$\cos\alpha/\sin\beta$	$\cos\alpha/\sin\beta$	$\cos\alpha/\sin\beta$	$\cos\alpha/\sin\beta$
	H	$\sin\alpha/\sin\beta$	$\sin\alpha/\sin\beta$	$\sin\alpha/\sin\beta$	$\sin\alpha/\sin\beta$
	A	$\cot\beta$	$\cot\beta$	$\cot\beta$	$\cot\beta$
ψ^d	h	$\cos\alpha/\sin\beta$	$-\sin\alpha/\cos\beta$	$\cos\alpha/\sin\beta$	$-\sin\alpha/\cos\beta$
	H	$\sin\alpha/\sin\beta$	$\cos\alpha/\cos\beta$	$\sin\alpha/\sin\beta$	$\cos\alpha/\cos\beta$
	A	$-\cot\beta$	$\tan\beta$	$-\cot\beta$	$\tan\beta$
ψ^ℓ	h	$\cos\alpha/\sin\beta$	$-\sin\alpha/\cos\beta$	$-\sin\alpha/\cos\beta$	$\cos\alpha/\sin\beta$
	H	$\sin\alpha/\sin\beta$	$\cos\alpha/\cos\beta$	$\cos\alpha/\cos\beta$	$\sin\alpha/\sin\beta$
	A	$-\cot\beta$	$\tan\beta$	$\tan\beta$	$-\cot\beta$

Table 2.3.: Yukawa couplings ξ_ϕ^f for up-type and down-type quarks and charged leptons to the neutral Higgs bosons h, H and A with respect to the SM in the four 2HDM types. The coupling of $H^\pm$ follows the description in Eq. 2.54 [177].

the previous section. Again, the most simple extension is the extension of the SM by two real scalar singlets or for more complex signatures, the augmentation of the 2HDM by a real scalar singlet.

Two Real Scalar Singlet Extension

Instead of one singlet, N singlets can be added to the SM, yielding the general potential

$$V(\Phi, \phi_i) = V_{\text{SM}}(\Phi) + V_{\text{singlets}}(\Phi, \phi_i) \tag{2.55}$$

where

$$\begin{aligned} V_{\text{singlets}}(\Phi, \phi_i) = a_i\phi_i + m_{ij}\phi_i\phi_j + T_{ijk}\phi_i\phi_j\phi_k + \lambda_{ijkl}\phi_i\phi_j\phi_k\phi_l \\ T_{iHH}\phi_i(\Phi^\dagger\Phi) + \lambda_{ijHH}\phi_i\phi_j(\Phi^\dagger\Phi) \end{aligned} \tag{2.56}$$

with all parameters being real, and V_{SM} being the SM Higgs potential as described in Eq. 2.25. Since ϕ_i are pure gauge singlets, the kinematics are trivial

$$T_{\text{singlets}} = \sum_i \partial^\mu\phi_i\partial_\mu\phi_i, \tag{2.57}$$

meaning that there are no interactions with any SM particles besides the scalar doublet. Therefore, there is no difference in terms of observable phenomenology between N complex singlets or $2N$ real singlets. The extension of the SM by such singlets is thus a theory of CP even scalar particles only.

In the two real singlet model (TRSM) [178], two real singlet fields X and S are added to the SM scalar sector. As for the one singlet extension, a $\mathbb{Z}_2$ symmetry is introduced

for each singlet, transforming the fields as follows

$$\begin{aligned} \mathbb{Z}_2^S &: \; X \to X, \; S \to -S, \; \Phi \to \Phi, \text{ and} \\ \mathbb{Z}_2^X &: \; X \to -X, \; S \to S, \; \Phi \to \Phi. \end{aligned} \tag{2.58}$$

These symmetries simplify the potential to

$$\begin{aligned} V(\Phi, X, S) = \mu_\Phi^2(\Phi^\dagger\Phi) + \lambda_\Phi(\Phi^\dagger\Phi)^2 + \mu_S^2 S^2 + \lambda_S S^4 + \mu_X^2 X^2 + \lambda_X X^4 \\ + \lambda_{\Phi S}(\Phi^\dagger\Phi)S^2 + \lambda_{\Phi X}(\Phi^\dagger\Phi)X^2 + \lambda_{SX} S^2 X^2 \end{aligned} \tag{2.59}$$

where all nine free parameters are real.

Expanding the fields around the minimum after electroweak symmetry breaking, the scalar doublet in the unitary gauge can be expressed as

$$\Phi = \begin{pmatrix} 0 \\ \frac{v+\phi_H}{\sqrt{2}} \end{pmatrix}, \; S = \frac{v_S + \phi_S}{\sqrt{2}} \text{ and } X = \frac{v_X + \phi_X}{\sqrt{2}} \tag{2.60}$$

with $v \approx 246\,\text{GeV}$, v_S and v_X being the respective vacuum expectation values.

As in the extension of the SM by one singlet, there exist two phases. The dark matter phase occurs if v_S or v_X vanish, where the corresponding field does not mix and is stabilised by its $\mathbb{Z}_2$ symmetry. The broken phase denotes the case where both $v_S, v_X \neq 0$, resulting in softly broken $\mathbb{Z}_2$ symmetries. This allows the fields ϕ_H, ϕ_S and ϕ_X to mix and to form observable mass eigenstates h_i with $i = 1, 2, 3$

$$\begin{pmatrix} h_1 \\ h_2 \\ h_3 \end{pmatrix} = \underbrace{\begin{pmatrix} c_1 c_2 & -s_1 c_2 & -s_2 \\ s_1 c_3 - c_1 s_2 s_3 & c_1 c_3 + s_1 s_2 s_3 & -c_2 s_3 \\ c_1 s_2 c_3 + s_1 s_3 & c_1 s_3 - s_1 s_2 c_3 & c_2 c_3 \end{pmatrix}}_{R_{ij}} \begin{pmatrix} \phi_H \\ \phi_S \\ \phi_X \end{pmatrix} \tag{2.61}$$

where

$$\begin{aligned} s_1 = \sin\theta_{HS}, \; s_2 = \sin\theta_{HX}, \; s_3 = \sin\theta_{SX}, \\ c_1 = \cos\theta_{HS}, \; c_2 = \cos\theta_{HX}, \; c_3 = \cos\theta_{SX} \end{aligned}$$

denote the mixing angles θ between the scalar fields. By convention, the fields h_1 to h_3 have increasing masses, i.e. $m_1 \leq m_2 \leq m_3$.

The μ^2 and λ parameters of the potential can then be expressed in terms of the masses (m_1, m_2 and m_3), mixing angles (θ_{HS}, θ_{HX} and θ_{SX}) and vacuum expectation values (v, v_S and v_X). One of the masses and consequently one of the scalar fields must correspond to the discovered Higgs boson with $m_H \approx 125\,\text{GeV}$. In addition, $v \approx 246\,\text{GeV}$ is also set by measurement, leaving seven free parameters in the TRSM. In contrast to other singlet extensions, the TRSM allows for any combination of the parameters covering the full phase space without losing consistency within the model.

Although the singlets themselves cannot couple to SM particles, the mass eigenstate h_a ($a = 1, 2, 3$) contains a fraction of the SM scalar doublet which does couple to SM

particles as described in Section 2.1.7. The production cross section can then be written as

$$\sigma(m_a) = R_{a1}^2 \sigma_{\mathrm{SM}}(m_a). \tag{2.62}$$

The partial decay widths of h_a to any SM particle pair also scale with R_{a1}^2 resulting in the total decay width also being rescaled by R_{a1}^2. Therefore, the branching ratios are the same as the SM ones since the scaling factor cancels in the calculations. However, as can be seen in the potential, self-couplings as well as couplings between ϕ_H, ϕ_S and ϕ_X are allowed and thus, so are (self-)couplings between the mass eigenstates. The coupling strengths can be expressed as

$$\tilde{\lambda}_{aaa} = \tfrac{1}{3}\left(\sum_i \frac{R_{ai}}{v_i}\right) m_a^2$$

$$\tilde{\lambda}_{abb} = \left(\sum_i \frac{R_{ai}R_{bi}^2}{v_i}\right)\left(m_a^2 + 2m_b^2\right) \tag{2.63}$$

$$\tilde{\lambda}_{abc} = \left(\sum_i \frac{R_{ai}R_{bi}R_{ci}}{v_i}\right)\left(\sum_i m_i^2\right) \tag{2.64}$$

and used in the partial decay width

$$\Gamma_{a\to bc} = \frac{\tilde{\lambda}_{abc}^2}{16\pi m_a^3}\sqrt{\sum_i m_i^4 - \sum_{i,\,j\neq i} m_i^2 m_j^2}\,\frac{1}{1+\delta_{bc}}\Theta(m_a - m_b - m_c) \tag{2.65}$$

where the case $b = c$ is explicitly allowed. This implies that scalar pair production is allowed if the mass differences are positive

$$\begin{aligned} &pp \to h_a \to h_b h_b \text{ with } m_a > 2m_b \text{ and} \\ &pp \to h_a \to h_b h_c \text{ with } m_a > m_b + m_c. \end{aligned} \tag{2.66}$$

If $m_b > 2m_c$, cascade decays are allowed where the final state consists of three or even four scalar particles in the final state.

Since there is no equivalent scalar particle to scalar particle decay in the SM, the branching ratio to SM particles needs to be corrected by

$$\mathcal{BR}(h_a \to \mathrm{SM}) = \big(1 - \mathcal{BR}(h_a \to \text{scalars})\big)\mathcal{BR}(H_{\mathrm{SM}} \to \mathrm{SM}). \tag{2.67}$$

This means that the lightest mass eigenstate h_1 has branching ratios identical to the SM Higgs boson. Thus, the benchmark, where the observed Higgs boson corresponds to $h_{125} = h_1$, is the most promising given the current measurements of the discovered Higgs boson. The branching ratios of $\mathcal{BR}(h_2 h_{125} \to \mathrm{SM})$ depending on the mass of h_2 are depicted in Figure 2.9. While $m_2 < 2m_H$, the decay into the $b\bar{b}WW^*$ decay channel dominates. If $m_2 \geq 2m_H$ the decay of $h_2 \to h_{125}h_{125}$ becomes the leading one with around 70%.

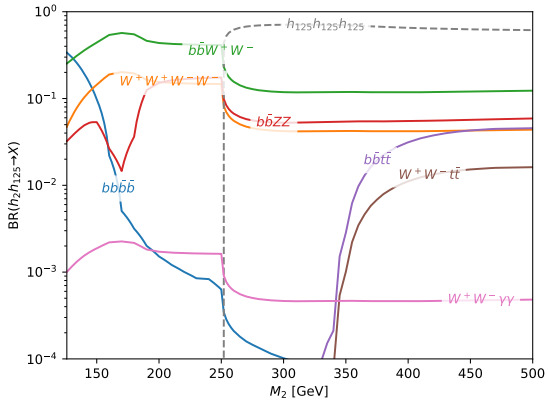

Figure 2.9.: Branching ratios of $h_2 h_1$, where $h_1 = h_{125}$ the observed Higgs boson, and $\theta_{HS} = -0.129$, $\theta_{HX} = 0.226$ and $\theta_{SX} = -0.899$. The vacuum expectation values are set to $v_S = 140\,\text{GeV}$ and $v_X = 100\,\text{GeV}$ [178].

Two-Higgs-Doublet Model with Scalar Singlet

2HDMs result in five spin-0 particles of which only two are neutral and CP even such that it is not possible for a scalar particle to decay to different scalar particles. The simplest solution to allow such decays is by augmenting the 2HDM by a real scalar singlet S (N2HDM) [179]. Starting from a CP conserving 2HDM with a softly broken $\mathbb{Z}_2$ symmetry to forbid FCNCs (see Section 2.2.2), the potential can be expressed as

$$V = V^{\text{2HDM}} + \frac{m_S^2}{2} S^2 + \frac{\lambda_S}{8} S^4 + \frac{\lambda_{S1}}{2} \left(\Phi_1^\dagger \Phi_1\right) S^2 + \frac{\lambda_{S2}}{2} \left(\Phi_2^\dagger \Phi_2\right) S^2 \tag{2.68}$$

with V^{2HDM} being the general 2HDM potential from Eq. 2.49 and the parameters being all real. Following the standard procedure of electroweak symmetry breaking and expanding the field around the minima, the fields are expressed as

$$\Phi_1 = \begin{pmatrix} \phi_1^+ \\ \frac{v_1 + \rho_1 + i\eta_1}{\sqrt{2}} \end{pmatrix}, \; \Phi_2 = \begin{pmatrix} \phi_2^+ \\ \frac{v_2 + \rho_2 + i\eta_2}{\sqrt{2}} \end{pmatrix}, \; S = v_S + \rho_S, \tag{2.69}$$

where v_1, v_2 and v_S are real vacuum expectation values with $v = \sqrt{v_1^2 + v_2^2} \approx 246\,\text{GeV}$ and $\tan\beta = v_2/v_1$.

Two $\mathbb{Z}_2$ symmetries are imposed. The first one is a trivial generalisation of the $\mathbb{Z}_2$ symmetry of the 2HDM to include the scalar singlet as well, expressed by

$$\mathbb{Z}_2 : \; \Phi_1 \to \Phi_1, \; \Phi_2 \to -\Phi_2, S \to S. \tag{2.70}$$

This $\mathbb{Z}_2$ symmetry is softly broken and ensures that there are no FCNCs in the Yukawa coupling terms. The second symmetry

$$\mathbb{Z}_2^S : \; \Phi_1 \to \Phi_1, \; \Phi_2 \to \Phi_2, S \to -S \tag{2.71}$$

can be conserved if $v_S = 0$ making S a candidate for dark matter. It can also be broken if $v_S \neq 0$ causing S to mix with the other CP even scalar particles ρ_i. While the charged and CP odd mass matrices are unchanged compared to the 2HDM, ρ_i form three new mass eigenstates H_i

$$\begin{pmatrix} H_1 \\ H_2 \\ H_3 \end{pmatrix} = \underbrace{\begin{pmatrix} c_1 c_2 & s_1 c_2 & s_2 \\ -s_1 c_3 - c_1 s_2 s_3 & c_1 c_3 - s_1 s_2 s_3 & c_2 s_3 \\ -c_1 s_2 c_3 + s_1 s_3 & -c_1 s_3 - s_1 s_2 c_3 & c_2 c_3 \end{pmatrix}}_{R_{ij}} \begin{pmatrix} \rho_1 \\ \rho_2 \\ \rho_S \end{pmatrix}. \tag{2.72}$$

The H_i are ordered by their masses $m_1 \leq m_2 \leq m_3$ and

$$c_1 = \cos\alpha_1,\ c_2 = \cos\alpha_2,\ c_3 = \cos\alpha_3$$
$$s_1 = \sin\alpha_1,\ s_2 = \sin\alpha_2,\ s_3 = \sin\alpha_3$$

denote the mixing angles α_i. In the limit of $\alpha_{2,3} \to 0$ and $\alpha_1 \to \alpha + \frac{\pi}{2}$, the 2HDM decouples from the singlet.

Compared to the SM, the couplings of H_i are modified by factors depending on the mixing angles α_i and β. The coupling coefficients for a coupling between H_i and the heavy vector bosons are

$$c(H_i VV) = \cos\beta R_{i1} + \sin\beta R_{i2}, \tag{2.73}$$

yielding a reduced coupling than in the SM. The coupling between H_i and fermions is significantly affected by the type of the fermion and the type of the 2HDM under consideration. The coupling coefficients are summarized in Table 2.4. In this case, the couplings can be either enhanced or reduced depending on the mixing angle values. Couplings between H_i and AZ, $H^\pm W^\mp$, AA and $H^\pm H^\mp$ are also possible.

	up-type	down-type	charged leptons
type I	$\frac{R_{i2}}{\sin\beta}$	$\frac{R_{i2}}{\sin\beta}$	$\frac{R_{i2}}{\sin\beta}$
type II	$\frac{R_{i2}}{\sin\beta}$	$\frac{R_{i1}}{\cos\beta}$	$\frac{R_{i1}}{\cos\beta}$
lepton-specific	$\frac{R_{i2}}{\sin\beta}$	$\frac{R_{i2}}{\sin\beta}$	$\frac{R_{i1}}{\cos\beta}$
flipped	$\frac{R_{i2}}{\sin\beta}$	$\frac{R_{i1}}{\cos\beta}$	$\frac{R_{i2}}{\sin\beta}$

Table 2.4.: Coupling coefficients $c(H_i ff)$ of the N2HDM Higgs bosons H_i to fermions depending on the fermion and 2HDM types [179].

As in the TRSM, (self-)couplings between the three scalars H_i can also occur with the

coupling strengths [179]

$$g_{H_iH_iH_i} = \frac{3}{v}\left(-\tilde{\mu}^2\left[R_{i2}^2 c_\beta\left(\frac{R_{i2}c_\beta}{s_\beta} - R_{i1}\right) + R_{i1}^2 s_\beta\left(\frac{R_{i1}s_\beta}{c_\beta} - R_{i2}\right)\right]\right. \tag{2.74}$$
$$\left. + \frac{m_{H_i}^2}{v_S}\left[R_{i3}^3 v + R_{i2}^3\frac{v_S}{s_\beta} + R_{i1}^3\frac{v_S}{c_\beta}\right]\right)$$

$$g_{H_iH_iH_j} = \frac{1}{v}\left(-\frac{1}{2}\tilde{\mu}^2\left(\frac{R_{i2}}{s_\beta} - \frac{R_{i1}}{c_\beta}\right)\left(6R_{i2}R_{j2} + 6R_{i3}R_{j3}s_\beta^2 + \sum_k \epsilon_{ijk}R_{k3}s_{2\beta}\right)\right. \tag{2.75}$$
$$\left. + \frac{2m_{H_i}^2 + m_{H_j}^2}{v_S}\left[R_{i3}^2 R_{j3}v + R_{i2}^2 R_{j2}\frac{v_S}{s_\beta} + R_{i1}^2 R_{j1}\frac{v_S}{c_\beta}\right]\right)$$

$$g_{H_1H_2H_3} = \frac{1}{v}\left(\tilde{\mu}^2\left[(2R_{12}R_{13} + R_{32}R_{33})c_\beta + (R_{31}R_{33} - 3R_{12}R_{23}R_{33} - R_{21}R_{23})s_\beta\right.\right. \tag{2.76}$$
$$\left. + 3R_{12}R_{22}\left(\frac{R_{31}}{c_\beta} - \frac{R_{32}}{s_\beta}\right) + 3R_{13}R_{23}R_{31}\frac{s_\beta^2}{c_\beta}\right]$$
$$\left. + \frac{\sum_i m_{H_i}^2}{v_S}\left[R_{13}R_{23}R_{33}v + R_{12}R_{22}R_{32}\frac{v_S}{s_\beta} - R_{11}(R_{22}R_{32} + R_{23}R_{33})\frac{v_S}{c_\beta}\right]\right),$$

where ϵ_{ijk} denotes the totally antisymmetric tensor, and $s_\beta = \sin\beta$ and $c_\beta = \cos\beta$. The couplings in the N2HDM have a more complex structure than the TRSM but are also more flexible when it comes to interpreting observed results.

CHAPTER 3

Experimental Setup

This chapter describes the experimental setup used to collect the data for the analysis. This includes an overview of the accelerator chain leading to the Large Hadron Collider (LHC) in Section 3.1. The accelerated protons are brought to collision in the ATLAS detector (see Section 3.2) which then records information related to the particles created during the collision. In addition to recorded data, events of various physics processes are simulated using the Monte Carlo technique which is explained in Section 3.3.

3.1. The Large Hadron Collider

The Large Hadron Collider (LHC) [180] is a circular proton-proton and heavy ion synchrotron operated by the European Organisation for Nuclear Research (CERN) in the tunnel originally built for the Large Electron-Positron collider (LEP) [181]. It is located close to Geneva at the Swiss-French border. With a circumference of 27 km, it is the largest collider in operation.

In contrast to LEP, particles accelerated in the LHC do not have opposite charge. To still be able to have particle beams running in opposite directions, nearly all dipole magnets to keep the particles on their circular path follow the design of twin-bore magnets resulting in complicated dipole structures which couples the rings magnetically as well as mechanically, at the cost of reduced flexibility.

With a designed maximum centre-of-mass energy of $\sqrt{s} = 14\,\text{TeV}$ for proton-proton collisions, a strong dipole field of $B = 8\,\text{T}$ is required to keep the particles on their circular track. As in other large accelerators, superconducting electromagnets are used that are constructed out of superconducting cables made of niobium-titanium.

However, this magnetic field strength is not achievable with the hitherto operating temperature of 4.2 K. Instead, superfluid helium cools the magnets down to approximately 2 K. In addition to the dipoles, quadrupole magnets are implemented to (de-)

focus the beam such that the particle losses are minimised and a high particle density is provided at the interaction points. Further sextupole and octupole magnets are used for small corrections to the beam to increase its stability.

Due to the strong dipole field strength necessary, the magnets are designed in a way that does not allow to accelerate the particles from rest to their maximum energy. Thus, the older and smaller accelerators at CERN are reused in an accelerator chain as displayed in Figure 3.1 where each accelerator has its own energy range. All protons start off in the linear accelerator LINAC 2 which guides them into the Proton Synchroton Booster where they are accelerated to an energy of $E \approxeq 1.4\,\text{GeV}$. Then the Proton Synchroton (PS, $E \simeq 25\,\text{GeV}$) and Super Proton Synchroton (SPS, $E \simeq 450\,\text{GeV}$) follow before the protons are injected in opposite directions into the LHC, which then accelerates them to up to $E_{\text{max}} = 7\,\text{TeV}$ to reach the desired centre-of-mass energy of up to $\sqrt{s} = 14\,\text{TeV}$. At this energy the protons are moving with nearly the speed of light. Heavy ions take a similar path but are created at the linear accelerator LINAC 3 and are then injected into LEIR before entering the PS, SPS and finally the LHC.

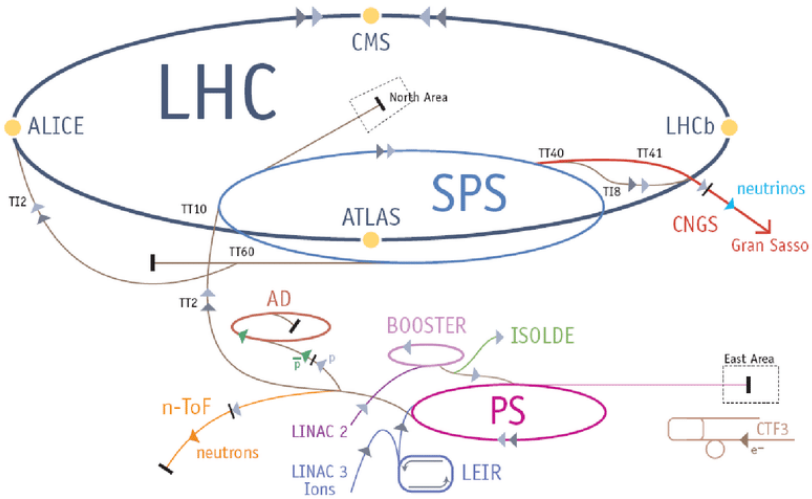

Figure 3.1.: Sketch of the CERN accelerator chain for protons (light grey arrows) and heavy ions (dark grey arrows) to the LHC. Side experiments at different points in the accelerator chain are also included but will not be discussed in detail. ©CERN

In addition to the high centre-of-mass energy, the second performance goal of the LHC is to have a high luminosity. The luminosity is a measure to quantify the amount of collision data, where the event rate relates to the luminosity by

$$\frac{dN}{dt} = \mathcal{L} \cdot \sigma \tag{3.1}$$

with $\mathcal{L}$ being the luminosity and σ being the cross section. While the cross section is a characteristic of the process, the luminosity is purely determined by quantities of the

accelerator.

The aim is to reach a peak luminosity of $\mathcal{L} = 10^{34}\,\mathrm{cm}^{-2}\mathrm{s}^{-1}$ for proton-proton collisions, which is crucial to study processes with small cross sections. The proton beam is not continuous, but consists of many proton packages, called bunches that enable clearly defined and timely separated beam interactions. The bunches each have a large number of protons. In addition, small beam sizes also help increase the luminosity which can be expressed by [180]

$$\mathcal{L} = \frac{N_1 N_2 n_b f R}{2\pi\sqrt{\sigma_{x,1}^2 + \sigma_{x,2}^2}\sqrt{\sigma_{y,1}^2 + \sigma_{y,2}^2}} \tag{3.2}$$

where $N_{1/2}$ is the number of particles in the colliding bunches, n_b is the number of bunches in the accelerator, f is the revolution frequency, R the luminosity reduction factor based on collision angle and finite bunch lengths and $\sigma_{x/y,1/2}$ are the transverse dimensions of the bunches.

At the LHC, there are up to 1.15×10^{11} particles per bunch and 2808 bunches per beam. Consequently, several events are produced during a bunch crossing. The distance between the bunches is also an important design parameter of the LHC. The bunch spacing is so short that it allows collisions every 25 ns. Due to interactions and other small beam losses, the luminosity does not remain constant over time such that a run has a lifetime of approximately 15 h before the luminosity becomes so small that interesting interactions become unlikely.

There are four large experiments located at four beam interaction points at the LHC. The two largest experiments are ATLAS [182] and CMS [183] which both are multi-purpose experiments. They collect the largest amount of data, to test the Standard Model with precision measurements and search for beyond Standard Model phenomena to explain the deviations seen so far. The discovery of the Higgs boson by both experiments simultaneously and independently in 2012 [1, 2] has been the largest success so far. Another experiment is LHCb [184] which focuses on B-physics. In a recent publication, LHCb found hints of violation of lepton universality in B-hadron decays [147]. The fourth large experiment is ALICE [185] which focuses on researching the quark-gluon plasma which was the state of the universe very shortly after the Big Bang.

The LHC started to run in 2010 with a centre-of mass energy of $\sqrt{s} = 7\,\mathrm{TeV}$, which was increased to $\sqrt{s} = 8\,\mathrm{TeV}$ in 2012. This period is referred to as Run 1. After a three year shutdown to upgrade the accelerator as well as the detectors, Run 2 began in 2015. For four years, until the end of 2018, the centre-of-mass energy was constant at $\sqrt{s} = 13\,\mathrm{TeV}$ for proton-proton collisions. The second long shutdown was planned to last until 2021 but is prolonged by one year due to the worldwide COVID pandemic. Run 3 is now aimed to start in the beginning of 2022 at a centre-of-mass energy of $\sqrt{s} = 13.6\,\mathrm{TeV}$ with a planned duration of three years, doubling the current amount of data available, followed by another long shutdown which is used to upgrade the LHC to the High-Luminosity LHC (HL-LHC) which will increase the luminosity by another factor of 10 for Run 4 and beyond [186].

3.2. The ATLAS Detector

Since data taken by the ATLAS experiment is analysed in this thesis, an overview is provided in this section based on Reference [182], which contains much more detailed information that is outside the scope of this thesis.

ATLAS, short for A Toroidal LHC ApparatuS, is a cylindrical multi-purpose detector with a nearly complete 4π coverage placed approximately 100 m below the surface in Geneva, Switzerland, very close to the Swiss-French boarder. With a length of 46 m and a diameter of 25 m, it is the largest of the four main LHC experiments and has a mass of 7000 t. A sketch of the detector is shown in Figure 3.2.

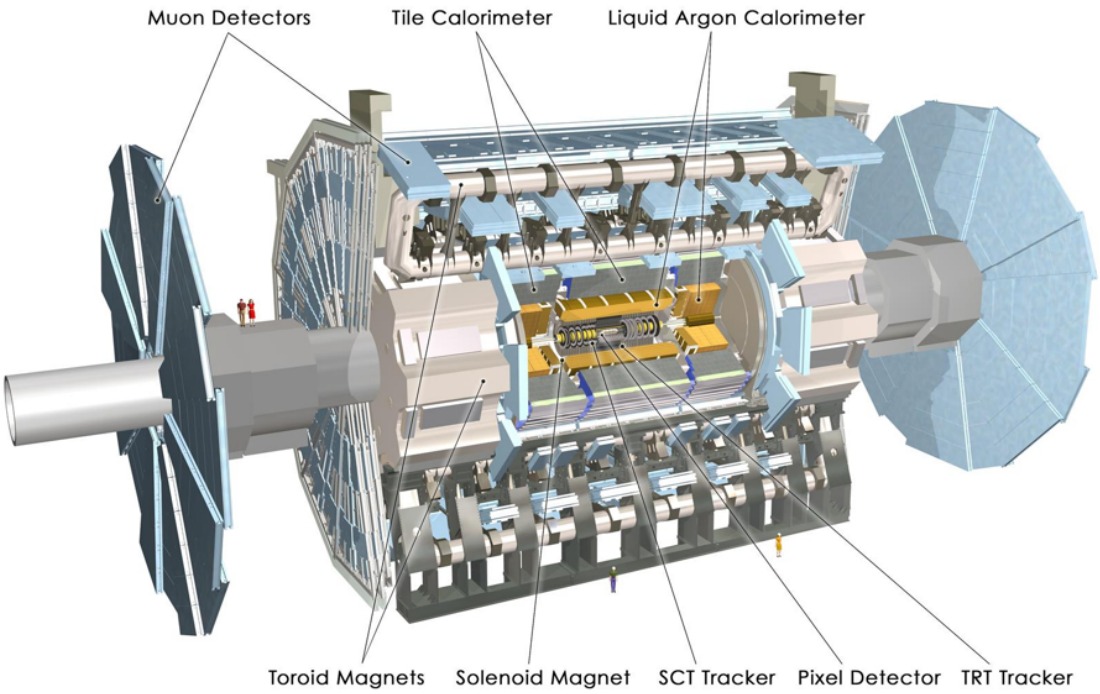

Figure 3.2.: Sketch of the ATLAS detector profile exhibiting the subcomponents: the Inner Detector in the centre surrounded by LAr and Tile calorimeters and the Muon Spectrometer. The persons drawn on the left-hand side of the detector are provided for scale. ©CERN

Built in an onion like structure, each layer of the detector focuses on specific types of particles and measurements. In the centre of the detector, directly around the interaction point, is the Inner Detector, a tracking detector with high spatial resolution. It is followed by two calorimeters, one designed for electromagnetically interacting particles and one designed for strongly interacting hadrons, which have a lower granularity but can measure the energy of both charged and neutral particles by stopping them in their dense material. This is surrounded by the Muon Spectrometer since muons, as minimum

ionising particles, do not deposit enough energy to be stopped and thus, are measured again in this tracking detector component.

The detector is described in more detail in Sections 3.2.1 to 3.2.6. This includes the coordinate system with the most common variable definitions used in the context of this thesis, the individual components of the detector and the trigger system employed to cope with the huge amount data resulting from collisions every 25 ns. The planned upgrades of the ATLAS detector are also discussed.

3.2.1. The Coordinate System

ATLAS uses an orthogonal right-handed coordinate system with the origin being placed at the constructed interaction point as shown in Figure 3.3. While the x-axis points to the centre of the LHC, the y-axis points upwards to the surface. The z-axis lies on the beam axis with the direction obeying the right-handedness of the coordinate system.

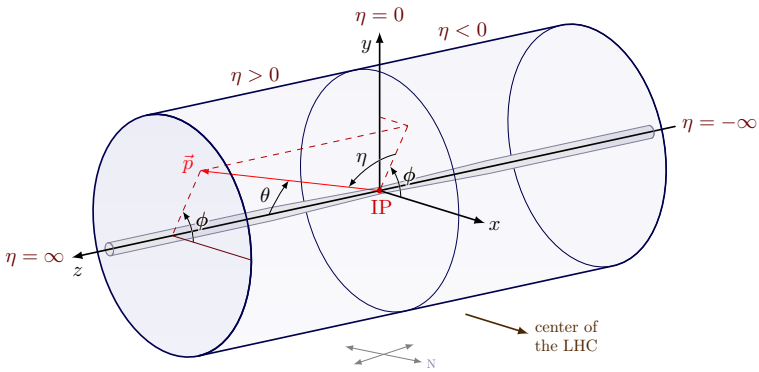

Figure 3.3.: Sketch of the coordinate system used in ATLAS. Both the Cartesian and the cylindrical coordinates including the pseudorapidity η is shown. The blue cylinder symbolises the detector, while the beam pipe is drawn as grey cylinder. The red arrow is an example particle with a momentum $\vec{p}$, that starts at the interaction point (IP) and travels through the detector.

Since ATLAS is a cylindrical detector, spherical coordinates instead of Cartesian coordinates are used in most cases. The azimuthal angle ϕ is the angle around the z-axis in the x-y-plane, starting on the x-axis and taking on values from $-\pi$ to π. The polar angle θ subtends the z-axis and the x-y-plane allowing values between 0 and π.

In contrast to electron-positron colliders, which collide elementary particles, the LHC does not collide the protons directly but the partons inside them. Those, however, only carry a fraction of the energy of the proton, which is also not fixed but randomly distributed. Thus, while the momentum before and after the collision is conserved in all components, only the initial transverse components are known, making transverse variables very valuable due to their invariance of Lorentz-boosts in the z-direction.

One of the most crucial variables is the transverse momentum of a particle defined as

$$p_{\mathrm{T}} = \sqrt{p_{\mathrm{x}}^2 + p_{\mathrm{y}}^2} \tag{3.3}$$

with p_{x} and p_{y} being the momentum component in x- and y-direction, respectively.

Another useful variable at hadron colliders is the pseudorapidity defined as

$$\eta = -\ln\left(\tan\left(\tfrac{\theta}{2}\right)\right) = \tfrac{1}{2}\ln\left(\frac{|\vec{p}| + p_{\mathrm{z}}}{|\vec{p}| - p_{\mathrm{z}}}\right) \tag{3.4}$$

with $\vec{p}$ being the total momentum of the particle and p_{z} the momentum component in z-direction. This variable has the advantage that it is defined in terms of the polar angle and the particle flow per unit pseudorapidity is approximately constant. In the relativistic limit, where the mass is much smaller than the momentum of the particle, and $E \approx |\vec{p}|$ with E denoting the particle's energy, the pseudorapidity equals the rapidity

$$y = \tfrac{1}{2}\ln\left(\frac{E + p_{\mathrm{z}}}{E - p_{\mathrm{z}}}\right). \tag{3.5}$$

Differences in rapidity are Lorentz-invariant under boosts in the z-direction and, thus, the same applies to differences in the pseudorapidity in the relativistic limit.

To describe distances between two particles a and b in the detector the ΔR variable is used which is defined as

$$\Delta R(a,b) = \sqrt{\Delta\eta^2 + \Delta\phi^2} = \sqrt{(\eta_a - \eta_b)^2 + (\phi_a - \phi_b)^2} \tag{3.6}$$

and, in the relativistic limit, is invariant under boosts along the z-direction since its components are invariant.

3.2.2. The Inner Detector

The main idea of a tracking detector is that a particle passes through it and leaves ionisation signals in several layers of active material called hits which are then combined into tracks representing the trajectory of the particle. Since ionisation can only be caused by charged particles, adding a magnetic field to the detector causes the particle's trajectory to bend according to the Lorentz force:

$$R = \frac{p_{\mathrm{T}}}{B \cdot q} \tag{3.7}$$

where R denotes the radius of the trajectory, B denotes the magnetic field strength and q the charge of the particle.The ratio of the p_{T} and charge of the particle can be determined by measuring the radius of curvature of the corresponding track. Since the p_{T} is proportional to the radius, the relative resolution of the p_{T} decreases with increasing p_{T} since the measurement of the radius becomes more imprecise. Having a strong magnetic field to bend the particle's path as much as possible together with a high granularity and a high spatial resolution is important to obtain a good p_{T} resolution.

Considering that the Inner Detector is placed closest to the interaction point, an excellent spatial resolution also helps in identifying which hit belongs to which track and track vertices, which are useful for determining the originating point of particles. More details are given Section 4.2.1.

The Inner Detector has a diameter of 2.1 m and a length of 6.2 m composing of three subcomponents: a pixel detector, a strip detector and a transition radiation tracker (TRT) as shown in Figure 3.4. The spatial resolution worsens towards the more outer parts. To avoid unwanted interactions and, therefore, distortions of the particles, a 4.5 cm thick solenoid made of super conducting cables surrounds the entire Inner Detector immersing it in a magnetic field of $B = 2\,\mathrm{T}$.

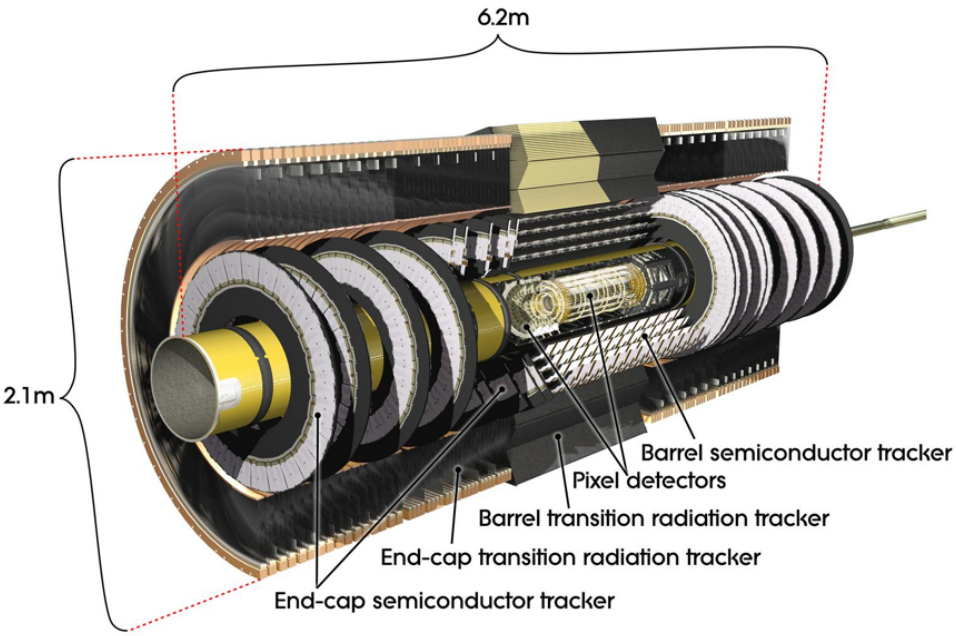

Figure 3.4.: Sketch of the Inner Detector of ATLAS showing the three subcomponents: pixel detector, strip detector and transition radiation tracker. ©CERN

The pixel detector starts only a few centimetres away from the interaction points and consists of approximately 92 million silicon pixels distributed across four barrel layers and three endcap disks on each side of the detector. Shortly before Run 2, an extra pixel layer, the Insertable B-Layer (IBL) [187], with a pixel size of $50 \times 250\,\mu\mathrm{m}^2$ was installed in front of the pixel detector used in Run 1 to refine the detection of the misplaced vertices and improve the identification of B-hadrons. The other pixels all have a size of $50 \times 400\,\mu\mathrm{m}^2$.

Following the pixel detector, a silicon strip detector is inserted. It consists of over 6 million implanted readout strips distributed across four cylindrical barrel layers and nine endcap disks on each side of the detector. Every $80\,\mu\mathrm{m}$, a readout strip is placed with a rotation of 40 mrad resulting in an accuracy of $17\,\mu\mathrm{m}$ in the direction transverse to the

strips. Together with the pixel subsystem, it covers a pseudorapidity range of $|\eta| < 2.5$.

The last subsystem, the TRT, consists of 300 000 straw tubes with a diameter of 4 mm and a very thin gold plated tungsten wire in the centre. 50 000 of these tubes each 144 cm long are placed in the barrel region, and 250 000 tubes with a smaller length of 39 cm in the endcaps cover the $|\eta| < 2.0$ range of the detector. The tubes are filled with a mixture of xenon, carbon dioxide and molecular oxygen and follow the principle of drift tubes, where a passing particle excites the gas mixture which is then transferred to an electrical signal. A special feature of the TRT is that an electron emits transition radiation which then excites the xenon in particular and thus, provides extra information for the particle identification since this does not happen for heavier charged particles. The spatial resolution reaches 170 μm.

Overall the Inner Detector has a momentum resolution of $\sigma_{p_\mathrm{T}}/p_\mathrm{T} = 0.05\% \cdot p_\mathrm{T} \oplus 1.0\%$.

3.2.3. The Calorimeters

In contrast to the tracking detectors, calorimeters can detect particles independently of their charge by stopping the particle by a mechanism called showering. While traversing the dense material of the detector, a particle interacts with the material, emits radiation and undergoes pair-production, which again interacting with the detector material building a particle shower. Since there is a critical energy after which no radiation is emitted or pair production is performed, respectively, the low energetic particles are absorbed by the material and the shower stops.

While electrons and photons shower by electromagnetic processes only, hadrons and gluons mainly interact strongly with the atoms of the calorimeter material. Due to the differences of these interactions, the showers behave differently in the detector. Electromagnetic showers are shorter and narrower than showers from hadrons.

Since the number of particles is Poisson distributed, the uncertainty on N_max is $\sqrt{N_\mathrm{max}}$ and, thus, the uncertainty of the energy which is proportional to the number of particles can be expressed as

$$\sigma_{E_0} \propto \sqrt{E_0} \Leftrightarrow \frac{\sigma_{E_0}}{E_0} \propto \frac{1}{\sqrt{E_0}}. \tag{3.8}$$

This means that with increasing energy, the measurement becomes more precise because there are more shower particles to measure.

Due to limited space in detectors for calorimeters, a short shower depth and, therefore, a small radiation length is desirable. Many such materials, however, are not suitable as active materials submitting electrical or optical signals for shower particles being absorbed. Therefore, ATLAS uses sampling calorimeters which are built of alternating layers of passive material with a very short radiation length and active material with a longer radiation length but the ability to transmit signals. However, the disadvantage is that not all particles of the shower are measured but need to be extrapolated from the measurements in the active material.

The Inner Detector is surrounded by the liquid argon (LAr) calorimeter which is separated into the LAr electromagnetic barrel (length = 6.4 m, thickness = 0.53 m), the

LAr electromagnetic endcaps (radius = 2.077 m, thickness = 0.632 m each), two LAr hadronic endcap (radius = 2.09 m, thickness = 0.8 m and 1.0 m) and three LAr forward (radius = 0.455, thickness = 0.45 m each) calorimeters also for hadronic showers (see Figure 3.5). While LAr is the active medium, either lead, tungsten or copper layers are used as passive material depending on the placement. As the names indicate, the LAr calorimeter mainly measures the energy of photons and electrons but also the energy of hadrons in the endcap and forward parts of the detector. The LAr is ionised by these particles resulting in an electric current which is then measured. Of particular note is the structure of the barrel region, which has an accordion-like design with a honeycomb pattern, such that there is a uniform response for particles from every direction. To keep the argon in its liquid state, it has to be cooled down to $-184°$ C which is too cold for the readout electronics. Therefore, special tubes filled with cables transmit the signals outside the calorimeter to a warmer region where the readout electronics are located.

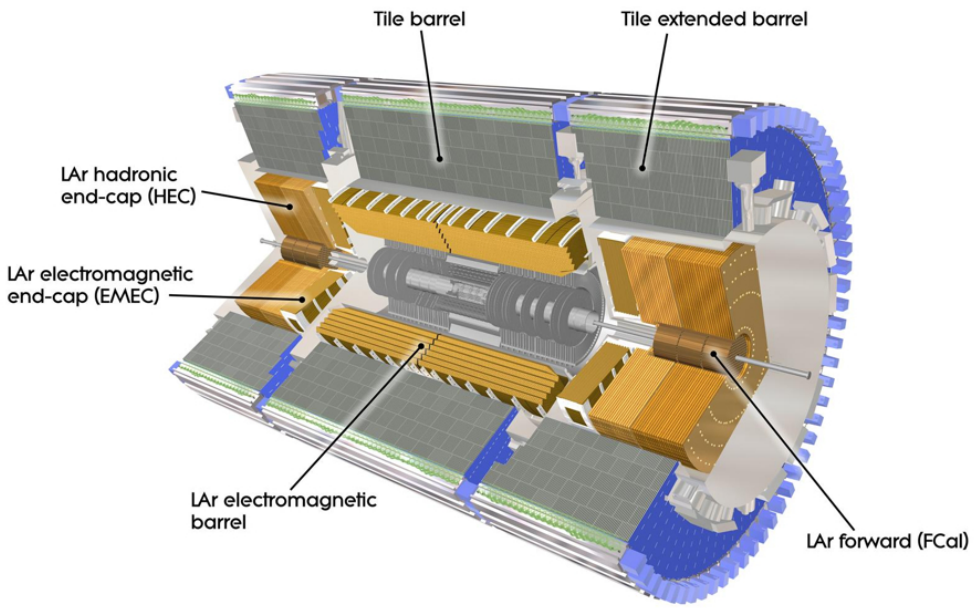

Figure 3.5.: Sketch of the calorimeters built into ATLAS consisting of the LAr and Tile calorimeters. ©CERN

Following the LAr calorimeter, the Tile calorimeter is inserted in ATLAS. Its main purpose is to register hadronic showers that continue to develop beyond the LAr calorimeter. It consists of the Tile barrel and the Tile extended barrel as depicted in Figure 3.5. It is made out of steel as the passive material and 420000 plastic scintillators as the active material. In contrast to the LAr, the plastic scintillators produce photons that are turned into an electric current using 4900 photo multiplier tubes. The current is proportional to the energy of the original particle.

Due to different materials and granularity of the subcomponents, the resolution is not constant across the calorimeter as displayed in Table 3.1. The best resolution is obtained for the LAr electromagnetic calorimeters which profit from their high granularity.

Component	Resolution σ_E/E	Coverage	Particles
LAr em barrel and endcaps	$10\%/\sqrt{E} \oplus 0.7\%$	$\lvert\eta\rvert < 3.2$	electron, photons
LAr hadronic endcaps and Tile	$50\%/\sqrt{E} \oplus 3\%$	$\lvert\eta\rvert < 3.2$	hadrons, gluons
LAr forward	$100\%/\sqrt{E} \oplus 10\%$	$3.1 < \lvert\eta\rvert 4.9$	hadrons, gluons

Table 3.1.: Summary of the relative resolution σ_E/E and the η coverage of the different calorimeter parts of ATLAS and which particles are mostly detected [182].

3.2.4. The Muon Spectrometer

Since muons as minimum ionising particles do not deposit enough energy in the Inner Detector or the calorimeters to be well measured or even stopped, an additional tracking detector, the Muon Spectrometer, encloses the other detector parts as depicted in Figure 3.6. As the magnetic field from the solenoid in the Inner Detector is not sufficient to bend the muons in this outer region of ATLAS, three additional toroid magnets are included in the muon system: one large toroid in the barrel region consisting of 8 coils of 100 km superconducting wire in total, and two smaller toroids with 8 superconducting coils at the endcaps, one on each side, to bend particles leaving the detector very close to the beam axis. In total a magnetic field of 3.5 to 4.0 T is generated.

The Muon Spectrometer consists of 4000 individual muon chambers using various detector technologies. In the barrel region, Monitored Drift Tubes (MDTs) used for measuring the track curvature and Resistive Plate Chambers (RPCs) used for triggering and additional coordinate measurement, are installed. Both are chambers filled with a gas mixture in a strong electric field, where the gas is excited by muons passing through. The freed electrons in the gas are then accelerated to the anode and cause an electron avalanche resulting in a detectable electronic signal. For RPCs, the electric field is parallel between two plates while for MDTs, the electric field is between the wall of the tube and a wire in the centre. Directly after the endcaps of the calorimeter, the muon endcap inner station made of Cathode Strip Chambers (CSCs) is installed to have a precise spatial measurement with a resolution of down to 60 μm. Here, the principle from above is even more refined with alternating several parallel anode wires and 90° rotated cathode strips. While the electrons drift to the anodes, the positively charged ions drift to the cathode strips, yielding a two coordinate measurement.

Following the endcap toroid on each side, four big wheels are installed. These consist of MDTs and Thin-Gap Chambers (TGCs), which follow the principle of the CSCs but with different dimensions between anodes and cathodes. The muon endcap outer station consisting of MDTs cover the forward region.

For muons with $p_{\mathrm{T}} = 1\,\mathrm{TeV}$, The Muon Spectrometer allows a relative resolution of

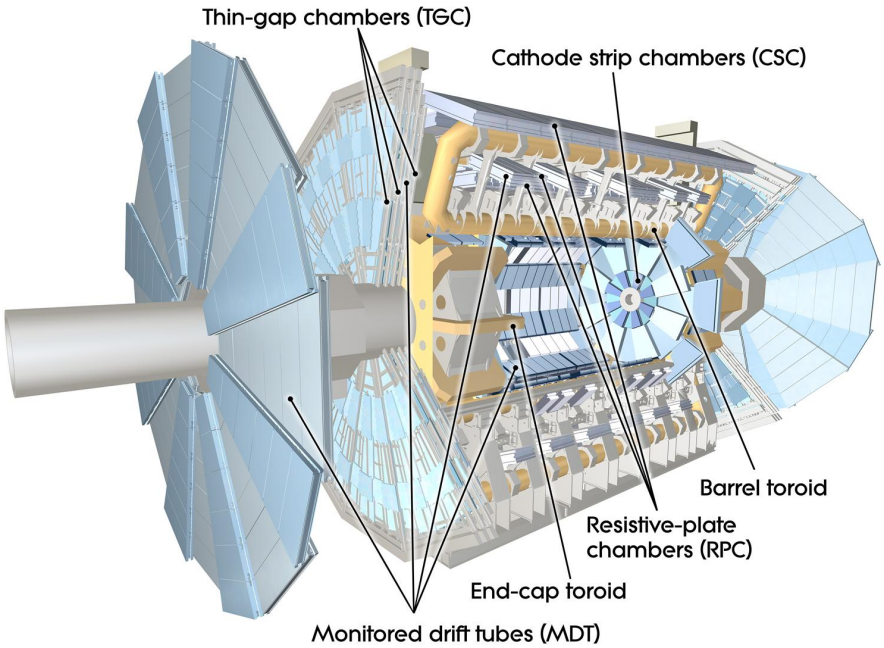

Figure 3.6.: Sketch of the muon spectrometer installed in Atlas. ©CERN

0.05% which is significantly better than what is achieved by the Inner Detector alone.

3.2.5. Trigger System

With bunch crossings every 25 ns and on average 34 inelastic proton-proton scatterings per bunch crossing, a data stream of more than 600 TB/s needs to be processed. Considering the data bandwidths and storage capacity available today, this amount of data is not practically processable. This said, not every event actually contains interesting physics processes. Therefore, Atlas employs a two-level trigger system to reduce the event rate by selecting potentially interesting events and to transfer only a small subset of the collected data to permanent storage [188].

The level-1 trigger (L1) is a hardware based trigger that uses the information provided by the calorimeters and the Muon Spectrometer to select events which have large energy deposits in the calorimeter or where a high energetic muon is present. The collected information is then compared to predefined tigger items and, if the energy matches the requirements, the event is kept, otherwise it is discarded. This simple, fast and purely energy based approach already reduces the event rate from 40 MHz to approximately 100 kHz which is buffered for the second trigger level to refine the selection.

In contrast to L1, the second trigger level is software based and makes decisions based on high-level objects. It is therefore called high-level trigger (HLT). This trigger level makes use of fast reconstruction algorithms taking into account information from the Inner Detector as well. Furthermore, signature analysing algorithms to identify and

to distinguish between the various objects allow to apply p_{T} thresholds tailored to the individual objects. Requirements based upon a combination of objects is possible in order to match the needs of the different analyses. This reduces the event rate by a factor of 100 to approximately 1 kHz. At this rate, events can be stored permanently for physics analyses.

3.2.6. Future Upgrades

Each run of the LHC comes with new challenges for the detector hardware as well as software. While the energy increased significantly between Run 1 and Run 2, future Runs will only feature minimal energy raises. Rather, upgrades focus on increasing instantaneous luminosity and thus, the number of simultaneous collisions along with the density of particles passing through the detector. Therefore, ATLAS must constantly be upgraded to cope with the new requirements. Although ATLAS is designed to be resistant against high energetic radiation from such collisions, there are still degradations in the detector that are to be expected.

ATLAS has two upgrade programs carried out on different timescales. While at the time of writing this thesis, the Phase-I upgrade has been finalised and aims for increased performance of ATLAS in Run 3, the Phase-II upgrade is in the final stage of design and at the beginning of commissioning to provide the tools for successful data taking during the HL-LHC.

The Phase-I upgrade program impacts three parts of ATLAS: the Muon Spectrometer [189], the LAr calorimeter electronics [190] and the trigger system [191]. The Muon Spectrometer has been extended by a 5 m in diameter new small wheel (NSW) placed between the barrel and end-cap regions on both sides of the detector covering a pseudorapidity range of $1.3 < |\eta| < 2.7$. Each wheel consists of two external small strip TGC wedges and two internal micromegas wedges. The aim is to improve the muon triggers by matching the signals of the Big Wheels, which cover a pseudorapidity range of $1.0 < |\eta| < 2.7$, and the NSW. This leaves a gap in the region $1.0 < |\eta| < 1.3$ only covered by the large sectors of the Muon Spectrometer. To reduce the expected muon trigger rate, 16 MTBs in the Barrel Inner Small regions have been replaced by small MTBs and 16 new, thinner RPCs with the corresponding front-end electronics.

The LAr calorimeter has been employed new front-end as well as back-end electronic boards to increase the readout granularity to maintain good trigger performance at low thresholds, even at high instantaneous luminosity. Furthermore, the L1 Calo trigger system has been updated with new Feature Extractor boards to increase the distinction between photons, electrons, τ-leptons and hadronic objects with refined processing of the information provided by the calorimeter.

Lastly, the trigger system itself has been upgraded to include the updates on the Muon Spectrometer and the calorimeter discussed before. The new Sector Logic board, the L1Topo upgrade and the Central Trigger Processor all aim to have more logical resources and a higher data bandwidth while keeping the trigger rate down, especially in the end-cap regions. Furthermore, the readout system has been based on the FELIX system, which is a server based system acting as a router between the different front-end

links using a commercial multi-gigabit network that transfers the data to the desired destination.

The Phase-II upgrade program is relevant to the following parts of ATLAS to cope with the high data rates expected for the HL-LHC: the complete Inner Detector [192–194], the LAr and Tile calorimeters [195, 196], the Muon Spectrometer [197] and the trigger system [198]. After operating ATLAS for so many years, many detector parts already have been damaged and are not designed to resist the radiation exposition from the HL-LHC.

The largest upgrade will be the replacement of the current Inner Detector by an all silicon tracking detector called Inner Tracker (ITk). It consists of a pixel detector in the centre allowing a coverage of $|\eta| < 4.0$ with a high spatial resolution. It is surrounded by a strip detector covering $|\eta| < 2.7$. The system is complemented by a High Granularity Timing Detector (HGTD) in the forward regions to allow a novel measurement of charged particles in time and space. More details on the ITk can be found in Section B.

For the LAr calorimeter, electronics that have not been upgraded during the Phase-I upgrade will be replaced in the Phase-II upgrade to allow the detector to operate with full granularity at 40 MHz. For the Tile calorimeter, a complete replacement of all electronics is also planned. Furthermore, around 10% of the photo-multipliers operating at the most radiation exposed parts of the Tile calorimeter will be exchanged.

In the Muon Spectrometer, the parts of the Inner Barrel System that have not been upgraded during Phase-I are replaced in Phase-II using the same procedure. Furthermore, the Large Barrel Sectors will also be extended by additional RPCs mounted on top of the existing MDTs. In the end-caps, the doublet TGCs will be replaced by triplet TGCs for a more robust alignment algorithm. All these measures should help to control the muon trigger rate at a sufficiently low trigger threshold.

Lastly, the trigger system will be upgraded to a single-level hardware trigger, taking into account all the other updates that are planned for the subsystems. It is composed of the Level-0 calorimeter and muon triggers which are extended by the Global Trigger that partially replaces and extends the processors used in Run 2 and Run 3. These events are then processed in the Event Filter which provides HLT functionality and is accompanied by the Hardware-based Tracking for the Trigger co-processors. This structure can also be evolved into a dual-level based hardware trigger if the data rates in the HL-LHC are higher than expected.

3.3. Monte Carlo Event Simulation

In data, all signal and background processes are unavoidably mixed. Therefore, it is crucial to study the detector response for each process in various scenarios independently. A detailed Monte Carlo (MC) simulation [199, 200] has been developed that starts with generating events of a certain process and carries them through to a format which is identical to the real detector. This software chain is separated into three steps: the generation of the event and immediate decays of unstable particles, the simulation of interactions with the detector and the digitisation of energy deposits in active parts of

the detector into electrical signals similar to the readout of the real ATLAS detector. Thus, the format of the simulated events is equivalent to the format of recorded data events such that both can be processed by the same ATLAS trigger and reconstruction algorithms. An overview of the discussed processes can be found in Figure 3.7.

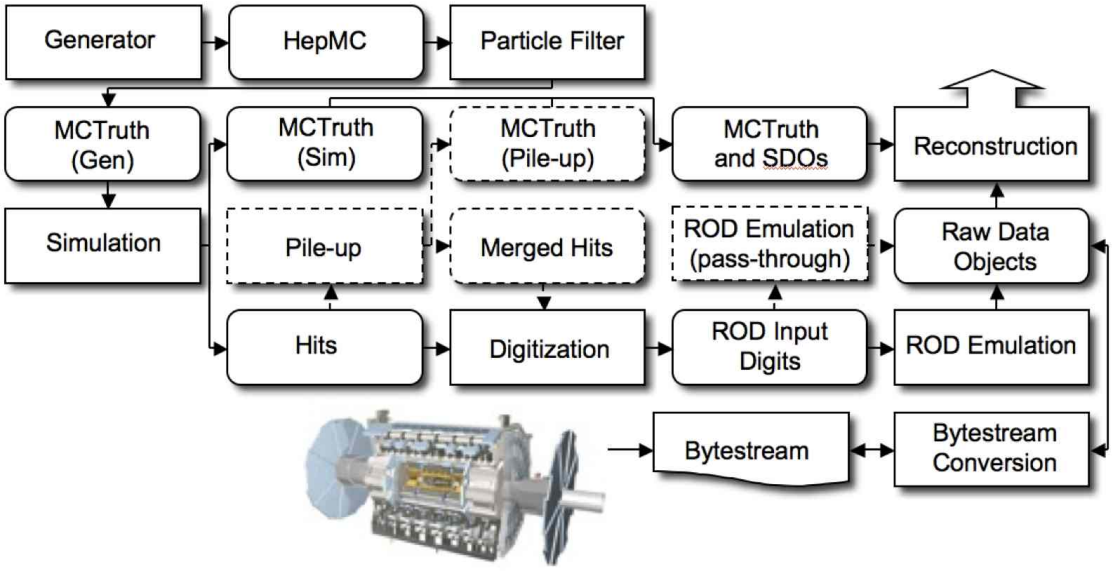

Figure 3.7.: Outline of the steps included in MC event simulation from the generator in the top left corner to the reconstruction in the top right corner. The path of recorded data events is also shown with the recording starting in the bottom. Algorithms and applications are shown with square-cornered boxes, while persistent data formats are shown with round-cornered boxes. Dashed lines on boxes indicate optional steps [199].

Dividing the simulation chain in this way allows to use the resources more effectively by storing the output rather than regenerating it each time. It is also possible to run identical events through different configurations of the simulation or digitisation. Furthermore, the number of events per computing job can be adjusted based on the complexity of the simulation step. While the event generation is comparably fast and many events can be processed in a single job, the detector simulation takes significantly longer, and fewer events are processed in a single job. The digitisation then again collects more events in a single job in order to have fewer output files at the end of the simulation chain.

3.3.1. Event Generation

The first step in the simulation is to generate the events as shown in Figure 3.8. Events in particle physics can be described by quantum field theories and, hence, the cross section of a process and thus, the probability of an event occurring, can be derived by calculating the matrix element. Since quantum field theory is usually a perturbation theory, the matrix element calculation can be performed to a desired order of accuracy.

Current event generators range between leading order (LO) and next-to-next-to-leading order (NNLO) perturbation theory.

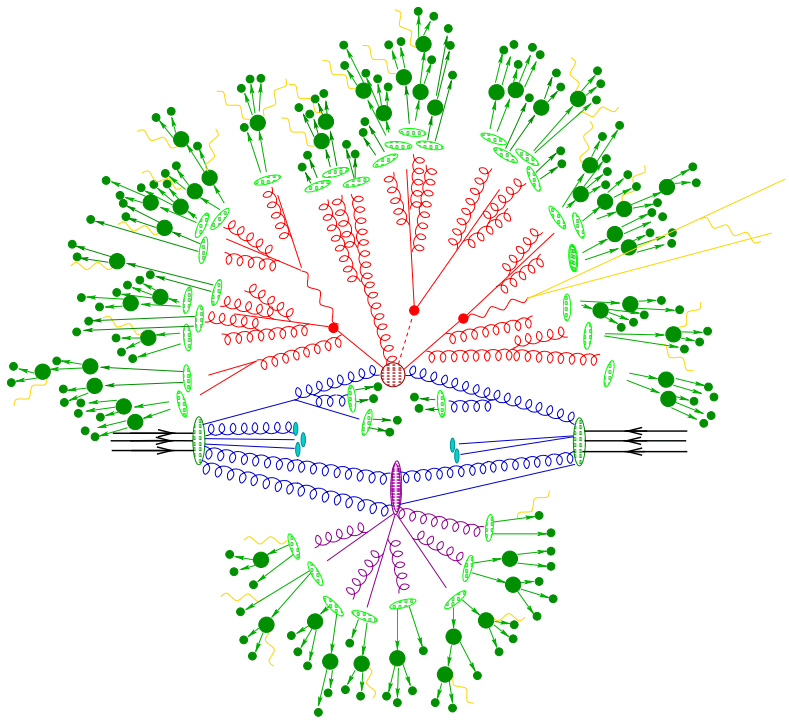

Figure 3.8.: Sketch of a proton-proton collision simulated by an event generator. The incoming protons are drawn as black lines, the interacting partons in blue. The red circle in the centre denotes the hard scattered event surrounded by parton shower. The light green circles represent the transition from partons to colour-neutral hadrons, where the following dark green lines and circles show hadron decays. The yellow lines stand for electromagnetic particles. The purple circle in the bottom half of the sketch shows pileup [201].

The starting point of the generation process are the partons (blue) with energy fractions x_1 and x_2 of the incoming protons (black) derived from parton distribution functions (PDFs) which describe the substructure of the proton. They then form the the hard-scattered event (red circle). Since many particles have a short decay length $c\tau < 10\,\mathrm{mm}$, they are considered as unstable by the generator and decay further. This decay length is chosen because these particles will decay before reaching any part of the detector such that interaction with any detector material as well as with the magnetic field are ignored in the prompt decays. Therefore, no detector geometry is needed in this step of the simulation.

Due to the non-perturbative nature of the strong interaction, special generator algorithms called parton showers are included to calculate this part of the event which is responsible for extra initial and final state radiation (red lines). Afterwards, hadronisa-

tion where colour charged particles, namely gluons and quarks, are combined to form colour-neutral hadrons takes place (light green circles). The hadrons themselves (dark green) could also be considered unstable and further decays are generated. It is also possible to have electroweak radiations in the initial or final state (yellow).

Since a hadron collider as the LHC is a busy environment, not only the hard scattered event takes place, but it can be accompanied by additional events (pileup, purple circle) such as minimum bias events, beam halo events, beam gas events or cavern background events. Since there is no interaction between the particles from pileup events and from the hard-scattered event, it is more efficient to simulate the hard-scattered event and pileup independently and overlay them at the stage of digitisation. Afterwards, the simulated pileup profile is matched to the profile observed in data events called pileup reweighting.

All generators have a default parameter set which may not be optimised for the running conditions at the LHC. Therefore, the parameters can be tuned. These tunes consider minimum bias events and other spectator processes, called underlying events, and are designed to reproduce recorded data.

While only the stable particles need to be processed by the detector simulation and digitisation, having access to the information on the unstable particles in the event may give insights that the reconstructed objects cannot provide. Therefore, the output of the event generator consists of all particles including links of the decay chain. This is called Truth record [202].

Furthermore, information of the interacting partons such as the momentum fractions are saved to allow parton distribution reweighting without rerunning the event generation. Since not all events are of interest for analyses, it is possible to filter events based on the presence or absence of particles or cuts on the energy of certain particles reducing the workload for the next simulation steps.

3.3.2. Detector Simulation

The detector simulation is responsible for the interaction between the stable particles and the detector material using the GEANT4 toolkit [203,204] which provides physics models as well as infrastructure for particle transportation through the detector geometry. After converting the events to the GEANT4 format, cuts and transformations can be applied. For example, the primary vertex position is smeared to account for the luminous range in ATLAS. Furthermore, only particles that satisfy $|\eta| < 6$ are considered to save simulation time.

All surviving particles are then passed through the detector where the interactions are described by numerical models that work well for various particles performing certain interactions with the detector material in a limited energy range. Thus, many models are combined in GEANT4 Physics Lists [205]. The calorimeter part clearly dominates the number of total interactions as well as hits in the active material. To reduce the processing time and file size, neutrons which are created 150 ns after the primary interaction are removed since they do not influence the hadronic shower development nor the energy

scale or energy resolution. Furthermore, neutrinos also are removed from the simulation as soon as they are created since the probability for any interaction practically vanishes.

For an accurate simulation, it is also crucial that the detector geometry matches the real ATLAS detector as much as possible. Therefore, the details of the geometry are preserved in the simulation with only necessary approximations in the detector being used for dead materials such as cable bundles or cooling pipes. The detector structure is described in terms of basic shapes which are arranged in logical volumes with additional properties such as a material. These logical volumes can then be placed in physical volumes that describe the position in the detector. While creating such a dense and complex geometry, any overlaps or touching surfaces must be omitted since otherwise the particle in the detector simulation becomes lost in the volumes.

To maintain all the information needed to describe the ATLAS geometry, a central database, called the ATLAS Geometry Database, contains all fundamental constants such as volume dimensions, rotations and positions as well as element and material properties. Links to external files such as the magnetic field map, can be included as well. Since certain settings can also vary from run to run, the detector can be further configured with conditions such as misalignments or distortions. These conditions are stored in a second database, the ATLAS Conditions Database.

While the stable particles traverse the detector material, they can still decay. The resulting daughter particles are added to the truth record. Since there are many interactions between the particles and the detector material, not every interaction is stored. Instead requirements on the kinetic energy of the incoming and outgoing particles need to be satisfied. All interactions with active parts of the detector are stored as hits containing information on the energy deposited, the position, and time. While the hits in the Inner Detector are spatially well separated and thus, treated independently, a merging of hits is performed for the calorimeters because the number of hits from showers is too large to be stored individually.

The detailed detector description in GEANT4 causes the full simulation to take a very long time which makes it impractical to produce enough events for many physics analyses. Studies show that 80% of the processing time is spent on particles travelling through the calorimeters. With AFII, a faster but more inaccurate simulation is used to provide a large number of events that can be run through the standard ATLAS reconstruction to act as a supplement to full simulation samples. AFII consists of two parts: the Fast ATLAS Tracking Simulation for the Inner Detector and Muon Spectrometer and Fast Colorimeter Simulation (FastCaloSim) [206] yielding an improvement in computing time by a factor of 100 and a factor of 10 using only FastCaloSim. The default setting is to use full simulation for the tracking detectors and fast simulation for the calorimeters.

Instead of simulating the interactions between the particles and the detector material, the energy of particle showers is deposited directly according to parametrisations of the longitudinal and lateral energy profile in FastCaloSim. Respecting the distribution of active and passive material, a fine granularity in the particle energy and pseudorapidity is necessary for the parametrisation. The longitudinal depth of the shower centre also needs to be taken into account. The energy fractions in all calorimeter layers are picked

randomly including Gaussian correlations between the fractions. The lateral energy in each layer is then determined from a symmetric average radial shape function. Events being generated using FastCaloSim can be processed directly by the reconstruction without running digitisation. This means that pileup needs to be added beforehand. Due to the simplifications, fast simulation events differ from full simulation events in quantities that depend on the shower shape such as electron identification or jet energy scale. Furthermore, substructure information inside the showers are lost.

3.3.3. Digitisation

The digitisation step converts the hits produced in the detector simulation to digits through the detector electronics readout drivers (RODs). A digit is created when the signal of an active detector part exceeds a predefined threshold in a certain time window. The digits can either just store that the threshold has been passed or it can also store the signal shape over time, depending on the detector part. The digits are then written out as Raw Data Objects (RDOs) which are convertible to and from bytestream format used to record actual data. In addition, maps from the hits to the truth particles that deposited that energy called Simulated Data Objects (SDOs) are created for the tracking detectors which can be used later to evaluate the performance of track reconstruction.

While pileup events do not influence the event generation and the interaction of the particles with the detector material, it does influence the readout of signals. Therefore, the hits from the hard-scattered event are overlaid with the hits from pileup events. Additionally, due to the long signal integration times, the detector response also contains information from earlier bunch crossings in most components. During this overlay, the run and event numbers of the hard-scattered event are kept, ignoring the information from the pileup events.

As for the detector simulation, it is possible to enable only certain components of the detector. There is also the option to apply the L1 trigger at this stage, which would require most detector parts to be enabled.

To have a consistent geometry layout between the simulation and the digitisation, the same geometry and conditions tags are used. In addition to the conditions relevant in the simulation, conditions affecting the readout such as defect readout channels or general detector noise become relevant in the digitisation.

CHAPTER 4

The $X \to HH/SH \to b\bar{b}WW^{(*)}$ channel

In this analysis, the resonant production of Higgs boson pairs (HH production) and the production of a Higgs boson in conjunction with another scalar particle (SH production) is investigated. By convention, the heavy resonance is denoted as X and is exclusively a scalar resonance. The scalar particle produced in conjunction with the Higgs boson is denoted as S and the Higgs boson as H. The masses are ordered by $m_X > m_S > m_H$, and $m_H = 125\,\text{GeV}$ is the measured mass of the observed Higgs boson. To allow a resonant decay of X, its mass is required to be $m_X > 2m_H$ for HH production and $m_X > m_S + m_H$ for SH production. Following the observed SM-like branching ratios of H, the decay into a $b\bar{b}$-pair and a W boson pair is the second leading decay channel for HH production and, depending on the model and the mass of S, can be the leading decay channel for SH production. By requiring $m_S > 2m_W$, the assumption that S decays exclusively to a W boson pair is made in this thesis leaving H decaying to a $b\bar{b}$ pair.

The first section of this chapter discusses the various topologies arising for different values of m_X and m_S while Section 4.2 then explains the reconstruction of the relevant physics objects. This chapter is concluded by a summary of the used simulated and recorded datasets in Section 4.3.

4.1. Topological Signatures

As already briefly mentioned in Chapter 1, the search for $X \to HH \to b\bar{b}WW^*$ and $X \to SH \to b\bar{b}WW$ production yields various detector topologies. Figure 4.1 shows the all topologies and their appearance in the m_X-m_S plane for the case that both W bosons decay hadronically (0-lepton). The topologies of the 1-lepton channel are similar and can be obtained by exchanging the hadronic decay products of one W boson by a charged lepton and the corresponding neutrino.

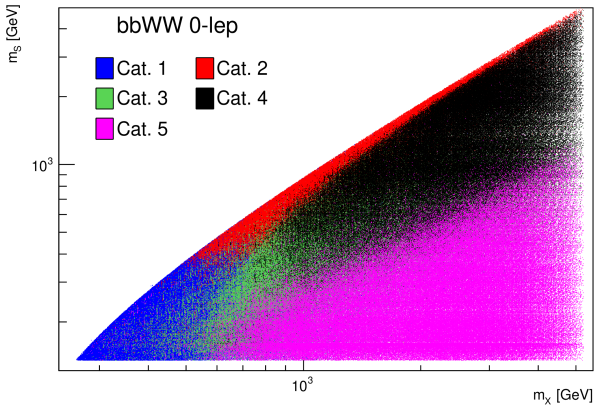

(a) topology categorisation depending on m_X and m_S

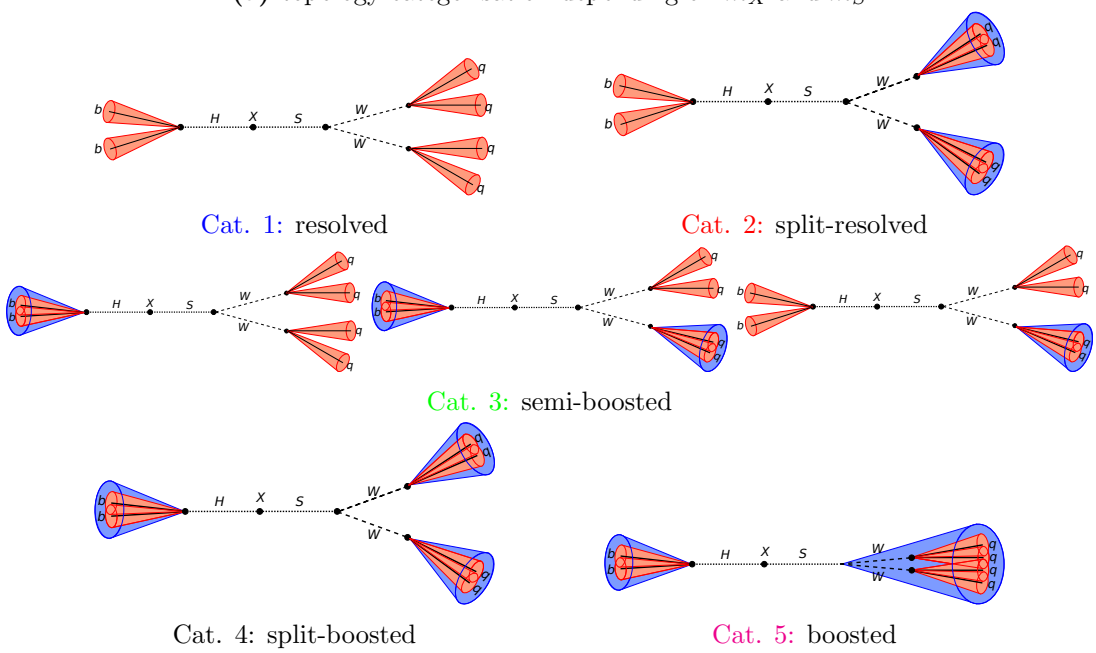

(b) sketches of the topologies in the various categories

Figure 4.1.: Possible topologies for $X \to SH \to b\bar{b}WW$ in the 0-lepton channel. The categorisation in the top plot [26] is determined by the distances between the Higgs boson decay products and between the decay products of both W boson decays and relate to the topologies shown in the bottom detector view sketches. The categories and topologies are similar for the 1-lepton channel if one set of hadronic W boson decay products are exchanged by a lepton and the corresponding neutrino.

Since not all topologies (and channels) offer sensitivity to the signals of interest, the analysis limits itself to five channels:

- resolved 1-lepton channel,
- split boosted 1-lepton channel,
- boosted 1-lepton channel,
- split-boosted 0-lepton channel and
- boosted 0-lepton channel

which are discussed in detail in the following.

4.1.1. Resolved 1-Lepton Channel

The resolved 1-lepton channel [207] focuses on the non-resonant Higgs boson pair production as predicted by the SM. The final state consists of two b-quarks, two light quarks, one charged lepton and one neutrino. As the name suggests, all of these particles are well isolated from each other and can be reconstructed as individual objects as shown in Figure 4.2. While the objects can be reconstructed easily, combining the correct objects in the event is challenging. Backgrounds such as $t\bar{t}$ production yield the same final state, making such a background irreducible. Therefore, advanced analysis techniques such as the usage of a multivariate discriminant are employed as a powerful tool to distinguish between signal and background events.

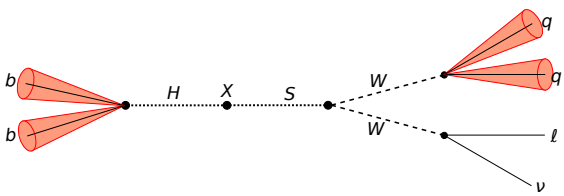

Figure 4.2.: Schematic sketch of the $X \to SH \to b\bar{b}WW$ production in the resolved 1-lepton channel. The S can be replaced by H resulting in one of the W bosons becoming off-shell.

The resonant production topology is dominant for both HH and SH production for low $m_X \lesssim 1\,\text{TeV}$ and correspondingly small m_S. In these cases, most of the event energy is converted into the masses of H and S and they have a relatively small momentum such that their decay products only obtain a Lorentz boost that is at most in the same order as their momentum obtained from the scalar particles' masses.

4.1.2. Boosted 1-Lepton Channel

The other extreme in the 1-lepton channel is the boosted topology. While the final state particles are identical to those in the resolved topology, not all of them are separated

enough such that they can be reconstructed as individual objects due to the detector resolution. This particularly affects the hadronic decay products. However, as depicted in Figure 4.3, the fully boosted topology also features a lepton overlapping with the light quarks from the hadronically decaying W boson. This unique topology is not present in many background processes. The main challenge in this channel is therefore the reconstruction of the charged lepton in this dense environment to fully exploit the uniqueness of the topology. While the topology already offers an obvious distinction between signal and backgrounds, preserving a high signal efficiency during the event reconstruction will be challenging.

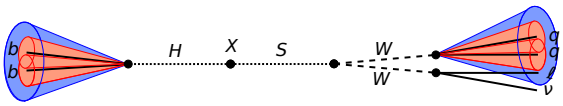

Figure 4.3.: Schematic sketch of the $X \to SH \to b\bar{b}WW$ production in the boosted 1-lepton channel. The S can be replaced by H resulting in one of the W bosons becoming off-shell.

This topology typically occurs in resonant HH or SH production if m_X exceeds 1 TeVand is significantly larger than m_H and m_S, respectively, such that only a fraction of the event energy corresponding to m_X is used to generate the masses of H and S. Therefore, they have a momentum which is considerably larger than their mass resulting in their decay products being highly boosted in their direction of flight. The spatial separation of the final state particles depends of their momentum transverse to the boost. This momentum can only be achieved from m_H and m_S which are significantly smaller than the energy of the boost. Thus, the spatial separation of the final state particles is not large enough to be resolve.

This channel will be covered in greater detail in the later chapters of this thesis.

4.1.3. Split-boosted 1-Lepton Channel

The split-boosted topology has a detector signature between the resolved and boosted topology. While the hadronic decay products of the Higgs boson and the W boson are still too collimated to be resolved by the ATLAS calorimeters, the W bosons themselves are well separated as shown in Figure 4.4.

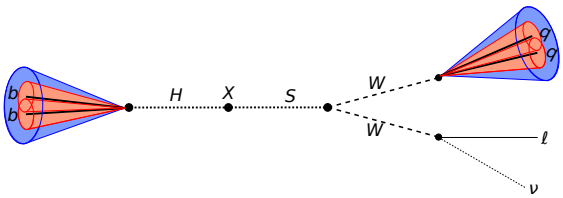

Figure 4.4.: Schematic sketch of the $X \to SH \to b\bar{b}WW$ production in the split-boosted 1-lepton channel.

This topology is dominant in resonant SH production, where $m_X \gtrsim 1\,\text{TeV}$ with a comparably large $m_S \gtrsim 0.3 m_X$ is the typical phase space. This results in a large asymmetry in the energies available for the final state particles. With S becoming more massive, the decay products of the Higgs boson become less boosted until they are resolvable as two separate objects. At the same time, the W bosons become more separated, with their respective decay products still being collimated. In the extreme case, the decay products from one W boson can even overlap with the decay products of the Higgs boson. This topology is therefore very sensitive to the difference between m_X and m_S, but profits from a better lepton reconstruction due to the lepton being isolated.

4.1.4. Split-boosted 0-Lepton Channel

The split-boosted topology in the 0-lepton channel is very similar to the one in the 1-lepton channel. The relevant mass ranges for m_X and m_S are also the same, but the charged lepton and neutrino are replaced by two collimated light quarks such that in the detector, three large hadronic objects are visible as shown in Figure 4.5.

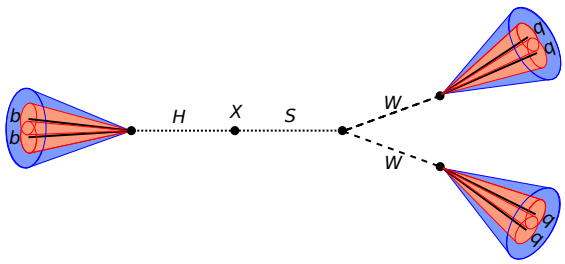

Figure 4.5.: Schematic sketch of the $X \to SH \to b\bar{b}WW$ production in the split-boosted 0-lepton channel. The $b\bar{b}ZZ$ decay channel is achieved by replacing the W bosons by Z bosons with the final state remaining the same.

While in the 1-lepton channels, background processes with a prompt lepton such as $t\bar{t}$ and vector boson production are dominant, the all-hadronic final states are dominated by backgrounds that feature many hadronic objects in the detector such as inelastic proton-proton scattering which has a very high cross section at hadron colliders. Thus, the main difficulty of this channel is to distinguish the hadronic signal from the hadronic background. Since each of the hadronic objects can be associated to either a Higgs boson or a W boson, tagging algorithms to look for specific characteristics of these objects such as their mass or substructure are a crucial part of this analysis [26].

For this topology, not only is the decay $S \to WW$ relevant, but also the decay $S \to ZZ$ can be investigated using the same approach since the final state is identical with the W-tagging needs to be replaced by Z-tagging.

4.1.5. Boosted 0-lepton Channel

As in the split-boosted case, the transition from 1-lepton to 0-lepton is mainly replacing the leptonically decaying W boson by a hadronically decaying W boson while the

mass ranges are still generally valid. The main difference here is the containment of all hadronic W decay products in one single large hadronic object as depicted in Figure 4.6 yielding an extremely dense environment within this hadronic object.

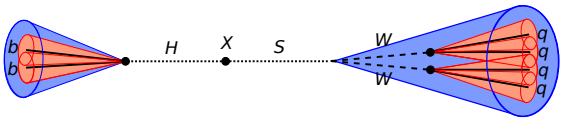

Figure 4.6.: Schematic sketch of the $X \to SH \to b\bar{b}WW$ production in the boosted 0-lepton channel. The S can be replaced by H resulting in one of the W bosons becoming off-shell. The $b\bar{b}ZZ$ decay channel is achieved by replacing the W bosons by Z bosons with the final state remaining the same.

As in the split-boosted 0-lepton channel, a dedicated tagger to identify hadronic objects seeded by four quarks (4-prong objects) has been developed using machine learning algorithms [208]. Since the training of the tagger has been performed on fully boosted $H \to WW^* \to 4q$ events, the tagger assumes the Higgs boson mass value as an important part of the algorithm training, making it unusable for identifying the fully boosted $S \to WW \to 4q$ signature [26]. Thus, the focus is set purely on resonant HH production.

4.2. Object Reconstruction

The signals provided by the ATLAS detector only contain information on the coordinates, on the time and sometimes on the signal amplitudes. In contrast to MC simulations, where the truth record can be used to match detector signals to a certain particle, this is not possible in recorded data. Therefore, specific algorithms are used to interpret the detector signals and identify signatures that are typical for certain particles as shown in Figure 4.7. In addition, energy calibrations are necessary to obtain sensible values for the transverse momentum or mass of a particle. Further corrections are applied to simulated events to account for differences between data and MC simulation. Since the individual algorithms use all signals of the ATLAS detector, an overlap removal between the different objects is necessary to avoid double counting of energies by different objects.

4.2.1. Tracks

Tracks are reconstructed using hits in the Inner Detector and Muon Spectrometer of the ATLAS experiment. The tracking algorithm employed by ATLAS [209] follows the current standard procedure in track reconstruction [210] with adjustments made to account for the dense environment at the LHC [211].

Starting in the pixel and strip components of the ATLAS Inner Detector, cluster space points are formed from the raw signals by a Connected Component Analysis [212]. Using three space points that are compatible with at least one other space point, a track seed is formed allowing a rudimentary momentum estimate without reducing the number of possible combinations. These seeds are fed to a combinatorial Kalman filter [213] which

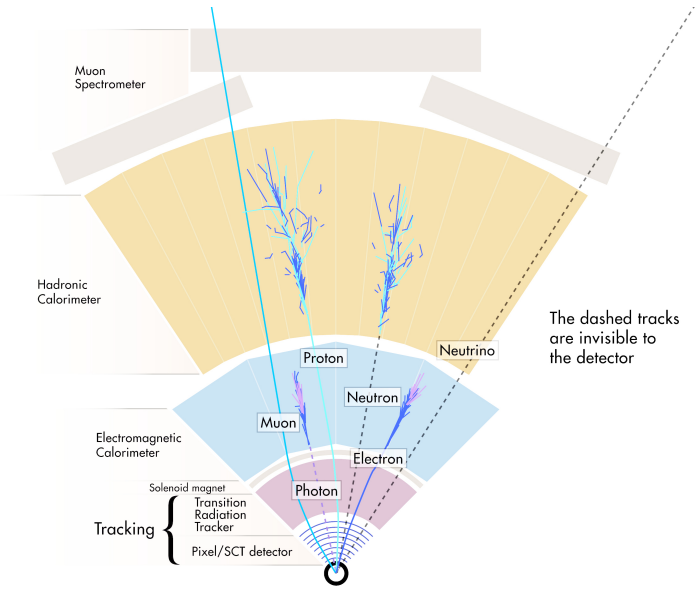

Figure 4.7.: Signatures of various particle types schematically included in a sketch of the ATLAS detector parts. Shown are muons, electrons, photons and neutrinos as well as protons and neutrons as examples for charged and neutral hadrons. Dashed lines only illustrate the path of the respective particle and do not correspond to an actual detector signal. ©CERN (colours inverted)

builds track candidates by probing the compatibility with remaining space points. These track candidates are parametrised by [214]

$$\tau = (d_0, z_0, \phi, \theta, q/p) \tag{4.1}$$

where d_0 and z_0 are the transversal and longitudinal impact parameters, respectively, ϕ is the azimuthal angle, θ is the polar angle and q/p denotes the ratio of electrical charge and momentum. The impact parameters are defined to yield the smallest distance between the interaction point and the track candidate. Additionally, all these track candidates are assigned a track score based on its quality.

The track candidates are rejected if they fail any of the loose selection criteria:

- $p_{\mathrm{T}} > 500\,\mathrm{MeV}$ and $\eta < 2.5$,
- $|d_0| < 2.0\,\mathrm{mm}$ and $|z_0 \sin\theta| < 3.0\,\mathrm{mm}$,
- ≥ 7 pixel and strip cluster with ≤ 2 combined pixel and strip holes of which only one may be in the pixel detector and
- ≤ 1 shared pixel cluster and ≤ 2 shared strip clusters.

At this stage, information from the Transition Radiation Tracker is also included and a high resolution track fit is performed [215, 216]. Fitted tracks without ambiguities are added to the final list of tracks.

These tracks are then used to determine the vertices of the proton-proton collision [217,218]. The starting vertex seed is based on the global maximum of the z_0 distribution of the selected tracks. The tracks are considered to be compatible with the vertex if $|d_0/\sigma_{d_0}| < 7$, otherwise they remain unassociated. These two steps are then repeated for all unassociated tracks until each track is matched to a vertex. The primary vertex (PV) is determined to be the vertex which maximises the sum of the squared transverse momenta of the associated tracks. Other vertices in the bunch crossing area are assigned to pileup events while vertices outside this area are called secondary vertices which result from decays of particles that originate from the PV.

4.2.2. Leptons

At the LHC, there are two possibilities for leptons to be produced. They result either from the decay of heavy bosons or top quarks which are produced during the collision, or from the decay of hadrons. While the first possibility for lepton production occurs within a very short time window after the collision, the decaying particles do not travel much and their decay vertex can be considered identical to the PV. The leptons are therefore called prompt leptons, while the leptons from the second production mode are labelled non-prompt, as these leptons originate from particles which have already travelled a considerable distance within the detector. The decay vertex in this case can in principle be distinguished from the PV.

The only prompt leptons that can be detected, are electrons and muons. Neutrinos do not interact with the ATLAS detector material. τ-leptons, on the other hand, decay quickly such that leptonic decays of prompt τ-leptons are considered to be prompt electrons or muons, respectively. Hadronic decays of τ-leptons are not considered any further in this analysis.

Since this analysis focuses on the boosted 1-lepton decay channel, the main goal is to identify prompt leptons, i.e. prompt electrons and prompt muons, and distinguish them from non-prompt leptons as these mostly occur in background events.

The final selection of electrons and muons in the context of the presented analysis is given in Table 4.1.

Electrons

Electrons [219, 220] are reconstructed by using the tracks of the Inner Detector and the energy deposits in the calorimeters. While the tracks are reconstructed as described in Section 4.2.1 with an additional Gaussian sum filter [223] applied to account for the energy loss of charged particles in material, the energy deposits are collected in topo-clusters [224] using the EM scale which accounts for the energy deposited by electromagnetic showers correctly.

	Electrons	Muons
$p_{\mathrm{T}} >$	10 GeV	10 GeV
$\lvert\eta\rvert <$	2.47	2.5
	excluding $1.37 < \lvert\eta\rvert < 1.52$	
$\lvert d_0/\sigma_{d_0}\rvert <$	5.0	3.0
$\lvert z_0 \sin\theta\rvert <$	0.5 mm	0.5 mm
Identification	Medium	Medium
Isolation	TightTrackOnly	TightTrackOnly
Identification	LooseBL	Loose
Isolation	-	-

Table 4.1.: Selection of the leptons in this analysis, namely electrons and muons. These criteria are split into kinematic selection, the signal (tight) selection and the loose selection derived for the background estimate (see Section 5.7). For identification and isolation, the names of the working points are given which are explained in the respective paragraphs [219–222].

The reconstruction of electrons starts from the topo-clusters whose energy from cells in the EM calorimeter is larger than 400 MeV and contributes at least 50% to the total energy of the cluster. A track is matched to a cluster if $-0.10 < q \cdot \Delta\phi < 0.05$ with q being the charge of the track and $|\Delta\eta| < 0.05$. If multiple tracks are matched to the same cluster, only the highest ranked track is kept. These topo-clusters and tracks then form dynamic, variable size electron superclusters.

Despite energy calibration and position corrections having been applied to the clusters before the tracks were matched, the superclusters are recalibrated to account for the effect of the matched track [220, 225].

A list of variables which offer discrimination power between prompt electrons and hadronic showers, photon showers as well as leptonic decays of heavy flavour quarks is created and can be found in Table 1 in Ref. [220]. This list is used in the construction of likelihood functions to identify electrons stemming from signal (s, isolated prompt) or background (b, non-prompt) processes

$$L_{s(b)}(x) = \prod_{i \in \text{variables}} P_{s(b),i}(x_i), \tag{4.2}$$

where $P_i(x_i)$ denote the probability density functions of the discriminating variable i at a value x_i. The likelihood discriminator is then

$$d'_L = -\frac{1}{15} \ln\left(\frac{L_b}{L_s}\right). \tag{4.3}$$

Four working points namely VeryLoose, Loose, Medium and Tight, are defined corresponding to an increasing threshold of the likelihood discriminant. Additional requirements on the number of hits of the track are made for the Loose, Medium and Tight

working points. For the Medium and Tight working points, the track furthermore needs to have a hit in the innermost pixel layer. This requirement is an optional variation of the Loose working point called LooseBL.

In addition to the identification (ID), the isolation of an electron can be used to determine whether it is a prompt or non-prompt lepton. Isolation refers to the transverse energy surrounding the electron in either the Inner Detector or the calorimeters. The raw calorimeter isolation is built by summing up the transverse energy of all topo-clusters within a cone around the electron. The core energy of the electron is subtracted in a rectangular cluster around the electron centre. Since not all energy is necessarily subtracted, an additional leakage correction is needed. A correction to account for pileup contributions is also included [226]. The isolation is then expressed as [220]

$$E_{\mathrm{T}}^{\mathrm{coneXX}} = E_{\mathrm{T,raw}}^{\mathrm{XX}} - E_{\mathrm{T,core}} - E_{\mathrm{T,leak}}^{\mathrm{XX}}(E_T, \eta) - E_{\mathrm{T}}^{\mathrm{XX}}(\eta) \tag{4.4}$$

where XX refers to the cone size $\Delta R = \mathrm{XX}/100$.

The track isolation variable $\left(p_{\mathrm{T}}^{\mathrm{coneXX}}\right)$ is calculated in a similar way, where the p_{T} of selected tracks in a cone around the electron track are summed up, with the electron track itself being excluded. It is also possible to define the isolation on particle flow objects [227], which basically is a combination of selected tracks and neutral particle flow objects $\left(E_{\mathrm{T,neflow}}^{\mathrm{coneXX}}\right)$ in cones around the electron track and cluster centre.

The selected tracks are required to to have $p_{\mathrm{T}} > 1\,\mathrm{GeV}$, $|\eta| < 2.5$, at least seven silicon hits with at most two silicon holes and at most one shared hit. Additionally, the tracks must be either associated to the PV or not associated to any vertex but satisfying $|z_0 \sin\theta| < 3\,\mathrm{mm}$ with respect to the PV.

Instead of a fixed cone size, it is also possible to define a variable size cone (varcone)

$$\Delta R = \min\left(\frac{10\,\mathrm{GeV}}{p_{\mathrm{T}}}, \frac{\mathrm{XX}}{100}\right). \tag{4.5}$$

Electrons considered in this thesis are required to pass $p_{\mathrm{T}} > 10\,\mathrm{GeV}$ and $|\eta| < 2.47$ excluding $1.37 < |\eta| < 1.52$ which corresponds to the transition region between the LAr barrel and the LAr endcap calorimeters and is poorly instrumented. Furthermore, the electrons need to satisfy $|d_0/\sigma_{d_0}| < 5.0$ and $|z_0 \sin\theta| < 0.5\,\mathrm{mm}$. The optimal ID and isolation working points have been determined in resonant HH production samples in the 1-lepton final state for $m_X = 1, 2, 3\,\mathrm{TeV}$. During the time of these studies no background or further signal samples were available. Thus, the prompt electron efficiency is determined from events in these samples where the true charged signal lepton is an electron, while the non-prompt electron efficiency is roughly estimated by only using events where the true charged lepton is a muon.

The four mentioned working points of the ID have been checked, and the electron ID efficiencies in the different samples are depicted in Figure 4.8. While the kinematic preselection barely effects the electron efficiency in both cases, requiring any ID has a large impact on the reconstruction efficiency. As expected, the efficiencies decrease for stricter ID working points. Furthermore, the prompt electron efficiency also decreases

for increasing m_X since the overlap between the charged lepton and the hadronic decay products of the W boson increases for increasing m_X, making the identification of the electron more difficult. The non-prompt electron efficiency is generally independent of m_X. At the time of these studies, the LooseBL ID working point was chosen, since it offers the best compromise between a high prompt electron efficiency and a low non-prompt electron efficiency. During the progression of the analysis, the ID was tightened to the Medium working point to be usable in the background estimate (see Section 5.7 and Appendix A.9).

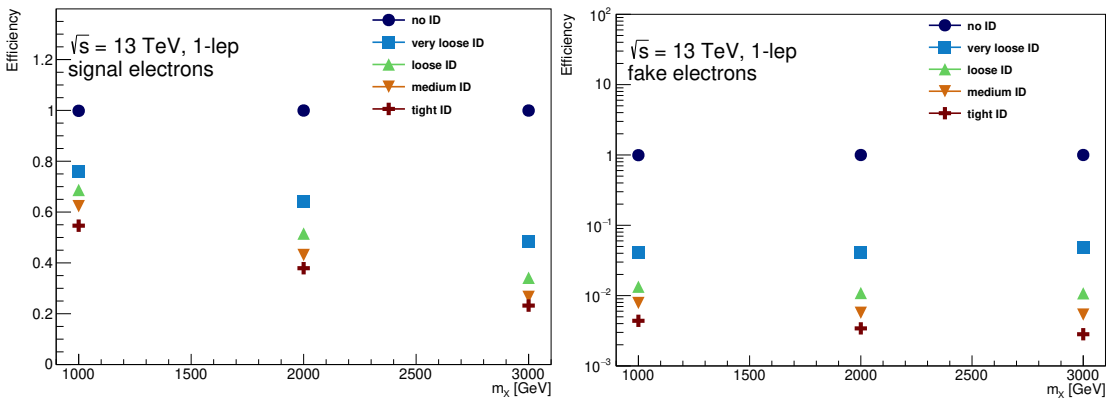

(a) true electron **(b)** true muon

Figure 4.8.: Efficiency of finding a reconstructed electron passing a certain ID in events split in the truth lepton flavour for three different m_X. In this case, loose refers to the LooseBL working point.

Next, various isolation working points whose definitions are summarised in Table 4.2 are checked. The results can be found in Figure 4.9 for electrons passing the LooseBL ID. The best performing isolation working point is the TightTrackOnly isolation, yielding the highest prompt electron efficiency and with the non-prompt electron efficiency being comparable with the Loose or PFlowLoose isolation working points. In particular, for higher m_X, where the environment of the electron is very dense, using only track information in a variable size cone is beneficial.

Working Point	Calorimeter	Track	Track $p_{\mathrm{T}}^{\mathrm{min}}$
Loose	$E_{\mathrm{T}}^{\mathrm{cone20}}/p_{\mathrm{T}}^{e} < 0.2$	$p_{\mathrm{T}}^{\mathrm{varcone30}}/p_{\mathrm{T}}^{e} < 0.15$	1.0 GeV
Tight	$E_{\mathrm{T}}^{\mathrm{cone20}}/p_{\mathrm{T}}^{e} < 0.06$	$p_{\mathrm{T}}^{\mathrm{varcone30}}/p_{\mathrm{T}}^{e} < 0.06$	1.0 GeV
PFlowLoose	$(p_{\mathrm{T}}^{\mathrm{varcone30}} + 0.4E_{\mathrm{T,neflow}}^{\mathrm{cone20}})/p_{\mathrm{T}}^{e} < 0.16$		0.5 GeV
PFlowTight	$(p_{\mathrm{T}}^{\mathrm{varcone30}} + 0.4E_{\mathrm{T,neflow}}^{\mathrm{cone20}})/p_{\mathrm{T}}^{e} < 0.045$		0.5 GeV
TightTrackOnly	-	$p_{\mathrm{T}}^{\mathrm{varcone30}}/p_{\mathrm{T}}^{e} < 0.06$	1.0 GeV
TightTrackOnlyFR	-	if $p_{\mathrm{T}}^{e} < 50$ GeV: $p_{\mathrm{T}}^{\mathrm{varcone30}}/p_{\mathrm{T}}^{e} < 0.06$ else $p_{\mathrm{T}}^{\mathrm{cone20}}/p_{\mathrm{T}}^{e} < 0.06$	1.0 GeV

Table 4.2.: Definitions of isolation working points available for electrons [220].

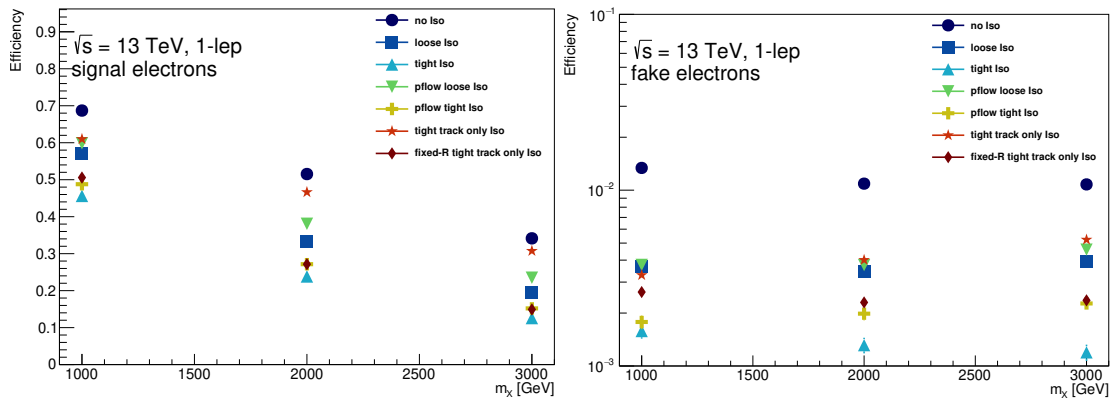

(a) true electron **(b)** true muon

Figure 4.9.: Efficiency of finding a reconstructed electron passing the LooseBL ID and a certain isolation in events split by the truth lepton flavour for three different m_X.

This can also be seen in Figure 4.10 (a) which shows fraction of kinematically preselected and LooseBL identified electrons passing a certain isolation working point depending on the electron p_{T}. For $p_{\mathrm{T}}^{e} \lesssim 50\,\mathrm{GeV}$, all isolation working points feature the same behaviour of more electrons passing the isolation, but only the TightTrackOnly working point continues this trend and reaches full efficiency for $p_{\mathrm{T}}^{e} \gtrsim 100\,\mathrm{GeV}$. Looking at the true electron p_{T} distribution in Figure 4.10 (b), it is evident that a large fraction of electrons are actually expected to have such a high p_{T}, making the TightTrackOnly working point the best isolation working point for this analysis.

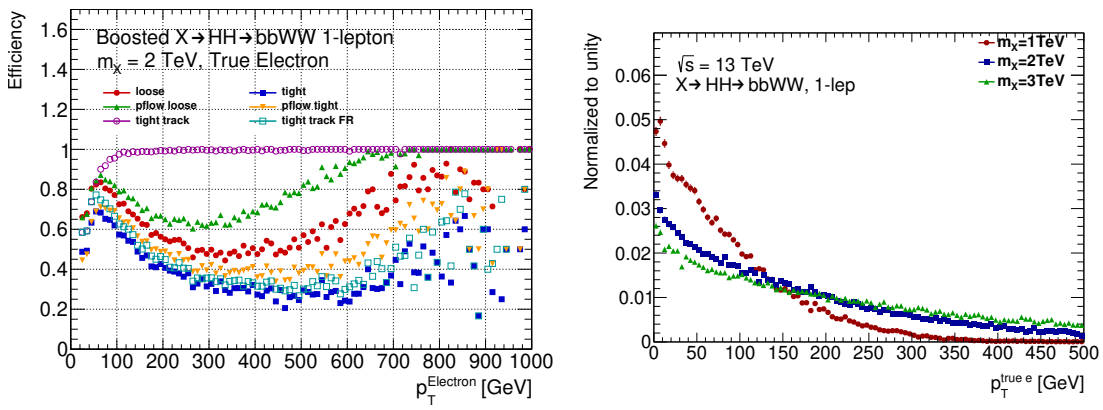

(a) electron isolation efficiency **(b)** true electron p_{T}

Figure 4.10.: Fraction of reconstructed electrons passing the isolation depending on their p_{T} using $m_X = 2$ TeV signal events where the true lepton is an electron. The p_{T} spectrum of the true electrons for three signal mass points is also shown.

Muons

Muons [221,222] are reconstructed using information from all parts of the ATLAS detector. This includes tracks from the Inner Detector as described in Section 4.2.1 but with $p_{\mathrm{T}} > 2\,\mathrm{GeV}$, energy deposits in the calorimeters and tracks in the Muon Spectrometer. The latter are reconstructed from hits in the different Muon Spectrometer stations. Starting by creating short straight line track segments, these segments are then combined into preliminary tracks from other muon segments where the track candidates must loosely point to the interaction point and have a parabolic shape to account to the bending of muons in the magnetic field at first order. Using the measurements from RPCs (see Section 3.2) as second coordinate, three dimensional track candidates are created and checked in a global fit of the muon's trajectory through the magnetic field with taking into account interactions with the detector material and misalignments of the detector parts.

Taking into account the different detector parts, various ways to reconstruct a muon exist yielding five muon types: Combined muons, inside-out combined muons, muon spectrometer extrapolated muons, segment-tagged muons and calorimeter-based muons. In this analysis, mainly combined muons are used. These are reconstructed by matching a track in the Muon Spectrometer to a track in the Inner Detector and performing a combined track fit where the energy loss of the muon passing through the detector is considered.

After reconstruction, the muon identification quality (ID) is determined by whether it passes or fails a set of requirements. All muons are required to have at least one hit in the pixel detector, at least five hits in the strip detector and at most two holes in the complete Inner Detector. In the Muon Spectrometer, the number of high precision stations and high precision holes are checked. High precision stations contain at least three hits in the MDTs or CSCs, and precision hole stations contain less than three hits and include three holes. To ensure consistency between the measurements in the Inner Detector and Muon Spectrometer, the momentum of the muons is compared in both subdetectors. Based on cuts on these variables, muons are identified as either loose, medium or tight where all tight (medium) muons pass automatically the medium (loose) ID.

There are two additional working points for the extremes of high and low p_{T} muons. In the high p_{T} phase space, the muon trajectory approaches a straight line making a p_{T} measurement difficult. Thus, muons in an η–ϕ region where the alignment of the muon chambers is not known to sufficient precision are vetoed, yielding an optimal p_{T} measurement with small uncertainties, but coming at the cost of low efficiencies. In the low p_{T} phase space on the other hand, muons do not reach the most outer muon segments and the background of non-prompt muons increases such that dedicated selections are applied.

To further increase the separation between prompt and non-prompt muons, the isolation of the muon can be considered. Muon isolation is defined to be the sum of all transverse energy except the transverse energy of the muon itself contained in a ΔR cone around the muon divided by the muon p_{T}. Prompt muons generally tend to be

more isolated than non-prompt muons. The isolation can either be based on tracks from the Inner Detector [228] labelled $p_{\mathrm{T}}^{\mathrm{coneXX}}$, energy clusters from the calorimeters [224] labelled $E_{\mathrm{T}}^{\mathrm{coneXX}}$, or a combination of the two via particle flow objects [227] labelled $p_{\mathrm{T}}^{\mathrm{coneXX}} + \alpha E_{\mathrm{T,neflow}}^{\mathrm{coneXX}}$. As for electrons, the cone size can be either fixed (coneXX) with $\Delta R = XX/100$ or variable (varconeXX) depending on the muon p_{T} by

$$\Delta R = \min\left(\frac{10\,\mathrm{GeV}}{p_{\mathrm{T}}^{\mu}}, \frac{XX}{100}\right).$$

In a new approach, a multivariate discriminant, the prompt lepton BDT [229] with two working points is used.

Muons used in this analysis are required to pass $p_{\mathrm{T}} > 10\,\mathrm{GeV}$, $|\eta| < 2.5$ which corresponds to the coverage of the full Inner Detector. Furthermore, the muons need to satisfy $|d_0/\sigma_{d_0}| < 3.0$ and $|z_0 \sin\theta| < 0.5\,\mathrm{mm}$. The optimal ID and isolation working points have been determined in resonant HH production samples in the 1-lepton final state for $m_X = 1, 2, 3\,\mathrm{TeV}$. During the time of these studies no background or further signal samples were available. Thus, the prompt muon efficiency is determined from events in these samples where the true charged signal lepton is a muon, while the non-prompt muon efficiency is roughly estimated by only using events where the true charged lepton is an electron.

First, efficiencies the mentioned ID working points are evaluated except the low p_{T} working point due the selection removing low p_{T} muons. The muon ID efficiencies in the different samples are shown in Figure 4.11. While the kinematic preselection marginally reduces the muon efficiency, requiring an ID criterion has a larger detriment on the non-prompt muon efficiency than the prompt muon efficiency. In contrast to electrons, the muon ID is not sensitive to m_X. The efficiency difference between the loose, medium and tight ID working points is also small for both prompt and non-prompt muons. Only the high p_{T} working point reduces the efficiencies significantly due to the geometrical vetoes of insufficiently instrumented detector regions. However, a significant fraction of muons is expected to have a high p_{T} such that more detailed studies comparing the medium and the high p_{T} working points are necessary to determine which ID to use.

To estimate the effect of the worse resolution of high energetic muons on the sensitivity of the analysis, muons smeared in energy are compared to nominal muons passing the medium and high p_{T} ID working points. The comparisons are conducted once on the p_{T} distribution of the muons and once on the distribution of the final discriminant (see Section 5.9) which is defined as

$$m_{\mathrm{vis+met}} = \sqrt{\left(p^{H\to b\bar{b}} + p^{\ell} + p^{W_{\mathrm{had}}} + p^{\mathrm{met}}\right)^2} \tag{4.6}$$

with $p^{H\to b\bar{b}}$, p^{ℓ} and $p^{W_{\mathrm{had}}}$ being the four vectors of the $H \to b\bar{b}$ candidate, the charged signal lepton and the W_{had} candidate, respectively. The four vector of the missing transverse energy is defined as $p^{\mathrm{met}} = \left(E_{\mathrm{T}}^{\mathrm{miss}}, p_{\mathrm{x}}^{\mathrm{miss}}, p_{\mathrm{y}}^{\mathrm{miss}}, 0\right)$. The ratio of p_{T} and $m_{\mathrm{vis+met}}$ distributions obtained using smeared and nominal muons can be found in Figures 4.12 and 4.13. Resonant HH signal samples with $m_X = 4$ and $5\,\mathrm{TeV}$have been included to increase the number of events with high p_{T} muons.

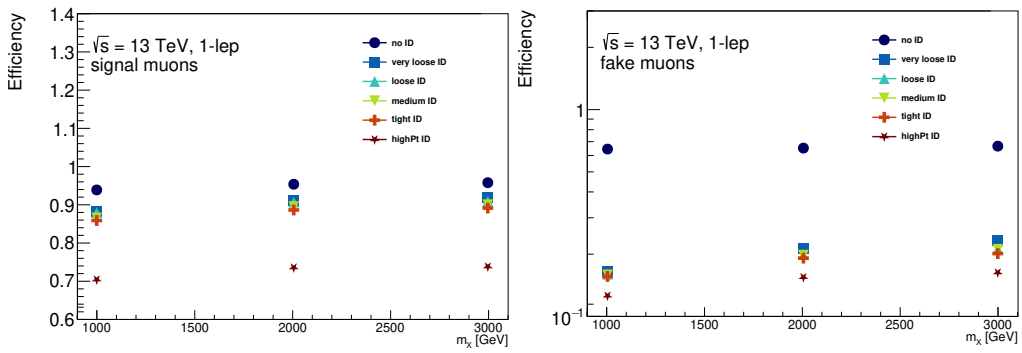

(a) true muon **(b)** true electron

Figure 4.11.: Efficiency of finding a reconstructed muon passing a certain ID in events split in the truth lepton flavour for three different m_X.

Figure 4.12 shows that, while the ratio of the p_{T} distributions of smeared and nominal muons is constant and close to unity for both ID working points for $p_{\mathrm{T}} < 300$ GeV, it spreads out for muons identified by the medium ID working point afterwards. Using the high p_{T} working point improves the ratio and, thus, reduces the impact of badly reconstructed high energetic muons. This effect however is completely washed out when looking at the ratio of $m_{\mathrm{vis+met}}$ distributions of smeared and nominal muons displayed in Figure 4.13, where the ratio mean is still close to unity, but many points are widely spread for both ID working points.

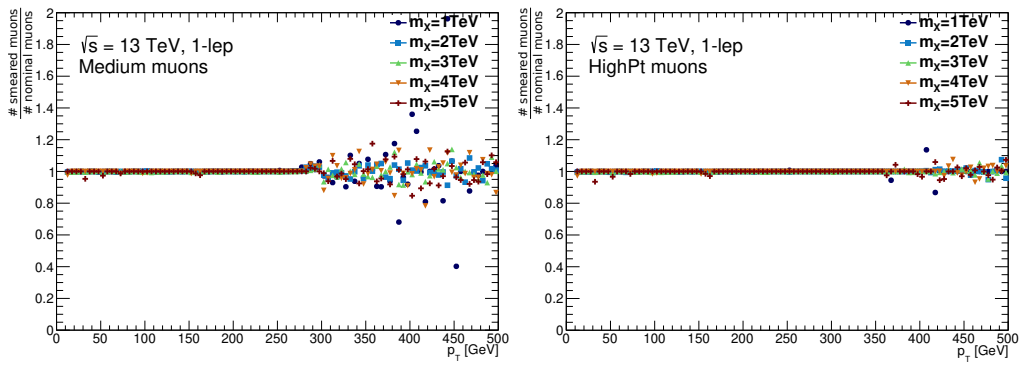

(a) medium ID **(b)** high p_{T} ID

Figure 4.12.: Ratio of the p_{T} distribution obtained using smeared or nominal muons passing the medium or high p_{T} ID for different m_X. The kinematic preselection is applied. Error bars are omitted to preserve the cleanness of the plot.

The gain in p_{T} resolution for high p_{T} muons when using the high p_{T} ID working point does not transfer to the resolution of $m_{\mathrm{vis+met}}$, where nearly no differences between the medium and high p_{T} ID working points are observed. Thus, the analysis will pursue using the medium ID working point to retain a high muon ID efficiency.

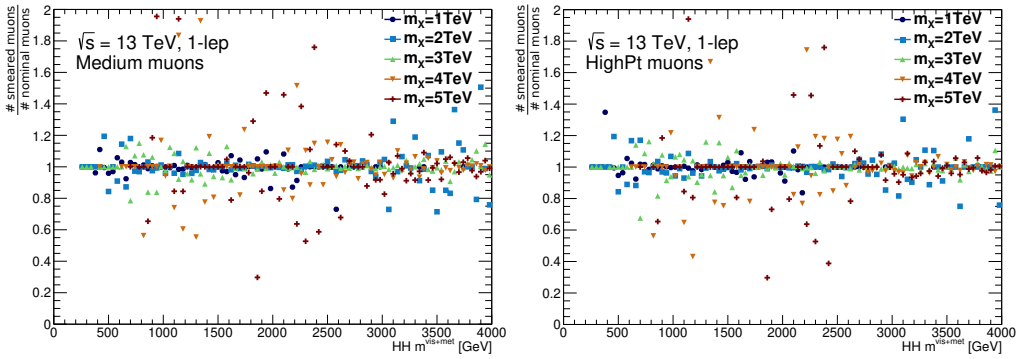

(a) medium ID **(b)** high p_{T} ID

Figure 4.13.: Ratio of the $m_{\mathrm{vis+met}}$ distributions obtained using smeared or nominal muons passing the medium or high p_{T} ID for different m_X. The kinematic preselection is applied. Error bars are omitted to preserve the cleanness of the plot.

Next, various isolation working points whose definitions are summarised in Table 4.3, are checked. The isolation efficiencies for the different signal samples can be found in Figure 4.14. The best performing working point is the TightTrackOnly isolation, yielding the highest prompt muon efficiency and with the non-prompt muon efficiency being comparable with the Loose or PFlowLoose Isolation working points. Especially for higher m_X, the prompt muon efficiency decreases significantly using any of the other isolation working points.

Working Point	Calorimeter	Track	Track $p_{\mathrm{T}}^{\mathrm{min}}$
Loose	$E_{\mathrm{T}}^{\mathrm{cone20}}/p_{\mathrm{T}}^{\mu} < 0.3$	$p_{\mathrm{T}}^{\mathrm{varcone30}}/p_{\mathrm{T}}^{\mu} < 0.15$	1.0 GeV
Tight	$E_{\mathrm{T}}^{\mathrm{cone20}}/p_{\mathrm{T}}^{\mu} < 0.15$	$p_{\mathrm{T}}^{\mathrm{varcone30}}/p_{\mathrm{T}}^{\mu} < 0.04$	1.0 GeV
PFlowLoose	$(p_{\mathrm{T}}^{\mathrm{varcone30}} + 0.4E_{\mathrm{T,neflow}}^{\mathrm{cone20}})/p_{\mathrm{T}}^{\mu} < 0.16$		0.5 GeV
PFlowTight	$(p_{\mathrm{T}}^{\mathrm{varcone30}} + 0.4E_{\mathrm{T,neflow}}^{\mathrm{cone20}})/p_{\mathrm{T}}^{\mu} < 0.045$		0.5 GeV
TightTrackOnly	-	$p_{\mathrm{T}}^{\mathrm{varcone30}}/p_{\mathrm{T}}^{\mu} < 0.06$	1.0 GeV
TightTrackOnlyFR	-	if $p_{\mathrm{T}}^{\mu} < 50$ GeV: $p_{\mathrm{T}}^{\mathrm{varcone30}}/p_{\mathrm{T}}^{\mu} < 0.06$ else $p_{\mathrm{T}}^{\mathrm{cone20}}/p_{\mathrm{T}}^{\mu} < 0.06$	1.0 GeV

Table 4.3.: Definitions of isolation working points available for muons [222].

The reason for the TightTrackOnly working point outperforming all other isolation working points can be seen in Figure 4.15 (a) which shows the fraction of kinematically preselected and medium identified muons passing a certain isolation working point depending on the muon p_{T}. For $p_{\mathrm{T}}^{\mu} \lesssim 50$ GeV, all isolation working points exhibits the same behaviour, but only the TightTrackOnly isolation continues to rise and approaches full efficiency for $p_{\mathrm{T}}^{\mu} \gtrsim 500$ GeV analogous to the electron isolation observations. The true muon p_{T} distribution in Figure 4.15 (b) shows that a large fraction of muons are actually expected to have $p_{\mathrm{T}} > 50$ GeV.

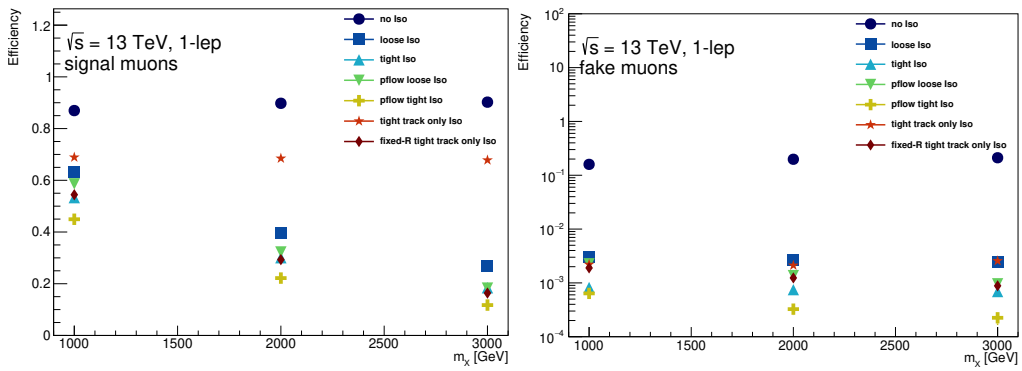

(a) true muon **(b)** true electron

Figure 4.14.: Efficiency of finding a reconstructed muon passing the medium ID and certain isolation criteria in events split by the truth lepton flavour for three different m_X.

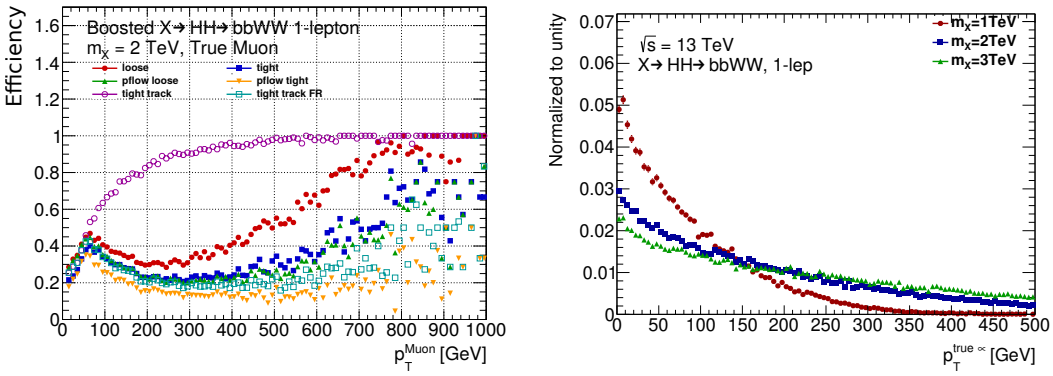

(a) muon isolation efficiency **(b)** true muon p_{T}

Figure 4.15.: Fraction of reconstructed muons passing the isolation depending on their p_{T} using $m_X = 2$ TeV signal events where the true lepton is a muon. The p_{T} spectrum of the true muons for three signal mass points is also shown.

4.2.3. Jets

When quarks and gluons hadronise, they leave collimated showers of hadrons as their detector signatures. These hadrons leave an energy deposit in the calorimeters and, if a hadron is charged, a track in the Inner Detector. All hadrons originating from the same parton can then be reconstructed as a single object called jet.

Jets can be reconstructed from various 4-vector objects called constituents [230]. Often, energy deposits in the form of topo-clusters [224] are used. These topo-clusters can either be calibrated to the electromagnetic energy scale as done in the electron reconstruction or to the hadronic energy scale using the local hadronic cell weighting procedure. It is also possible to use tracks from the Inner Detector [228] or a combination

of both tracks and clusters called particle flow (PFlow) objects [227] as the constituents. The latter are constructed by removing the energy deposits of charged particles only leaving the energy deposited by neutral particles while the energy as well as the position for charged particles are taken from tracks. If simulated events are investigated, it is also possible that the constituents are stable particles from the truth record.

For the reclustering, different jet algorithms have been developed [231–235]. The most common sequential algorithms use the formula

$$d_{ij} = \min\left(p^k_{\mathrm{T},i},\ p^k_{\mathrm{T},j}\right)\frac{\Delta R^2_{ij}}{R^2} \text{ with } k = \begin{cases} -2 & \text{anti-}k_t \\ 0 & \text{Cambridge–Aachen} \\ 2 & k_t \end{cases} \tag{4.7}$$

defining the algorithm type and R being the size parameter.

The transverse momenta of the constituents i and j are denoted as $p_{\mathrm{T},i/j}$ and the distance between i and j in detector coordinates is defined in terms of the rapidity instead of the pseudorapidity

$$\Delta R_{ij} = \sqrt{(y_i - y_j)^2 + (\phi_i - \phi_j)^2}.$$

Both d_{ij} and a cut-off value $d_{iB} = p^k_{T,i}$ are calculated for each pair of constituents. If $d_{ij} < d_{iB}$, the constituents are combined to a proto-jet which replaces i and j on the constituent list. Otherwise, the constituent i is labelled a jet and is removed from the list of constituents. This procedure is repeated until all constituents have been labelled as jets.

After the jets have been constructed, the jet energy scale (JES) needs to be corrected in several steps [236]. First, pileup corrections remove the excess energy from the jets resulting from additional proton-proton interactions in the same or previous bunch-crossings [237]. This correction consists of two components: one correction is based on the jet area and p_{T} density of the event, while the other is a residual correction obtained from simulation and parametrised in the average number of interactions per bunch-crossing and the number of vertices in the event. This is followed by an absolute JES calibration, which is derived from simulated events where the jet is corrected in a way that it agrees in direction and energy with truth jets. To account for differences between the jets based on their flavour, i.e. if the jet is initiated by a gluon, a light quark or a b-quark, the global sequential calibration is applied. Finally, an *in situ* jet calibration is applied, which addresses differences between data and simulation.

In order to reduce the number of jets that do not belong to the PV but are pileup jets, the Jet Vertex Tagger (JVT) [238] has been developed using a two dimensional likelihood function.

If the jet size is large enough or a boosted topology is present in the event, it is possible that the jet is not initiated by one parton but by multiple partons. The information on the number of initiating partons can be estimated by looking at the intrinsic energy distribution of the jet, called substructure. There are basically two sets of substructure variables. The first one is based on ratios of Energy Correlator Functions (ECFs) which

indicates the energy distribution inside a jet and are defined as

$$\mathrm{ECF}(N,\beta) = \sum_{i_1<i_2<\ldots<i_N\in J} \left(\prod_{a=1}^{N} p_{\mathrm{T},i_a}\right) \left(\prod_{b=1}^{N-1}\prod_{c=b+1}^{N} \Delta R_{i_b i_c}\Delta R_{jk}\Delta R_{ki}\right)^{\beta},$$

where the sum goes over all constituents i of a jet J and β is a positive tunable parameter [239]. The most prominent ratios are the C_N and D_N ratio series defined as

$$C_N(\beta) = \frac{ECF_{N+1}\times ECF_{N-1}}{ECF_N^2} \text{ and}$$
$$D_N(\beta) = \frac{ECF_{N+1}\times ECF_{N-1}\times ECF_1^N}{ECF_N^3},$$

where C_2 and D_2 with $\beta = 1$ have been found to well discriminate 2-prong jets (e.g of boosted hadronically decaying W bosons) from 1-prong jets (e.g. of quarks or gluons) [240]. In recent years, jet substructure variables based on more flexible, generalized forms of the standards ECFs have been developed, namely the M and N series [241] as well as the experimental L series [242].

Another option is to use a quantity called N-subjettiness τ_N. For this, the constituents of jet are reclustered using the k_t algorithm into exactly N subjets [243]. Using these subjets, τ_N is defined as

$$\tau_N(\alpha) = \frac{1}{d_0(\alpha)}\sum_{i\in J} p_{T,i}\cdot \min\left(\Delta R_{1i}^{\alpha}, \Delta R_{2i}^{\alpha}, \ldots, \Delta R_{Ni}^{\alpha}\right) \text{ with}$$
$$d_0(\alpha) = \sum_{i\in J} p_{T,i}\cdot \Delta R^{\alpha},$$

where the sum goes over the constituent particles of a given jet and ΔR_{ki} denotes the angular separation between the constituent i and the subjet candidate k. The parameter α is tunable but typically set to $\alpha = 1$. In this analysis, the subjet axis is defined by its hardest constituent called the "Winner Takes All" (WTA) axis [244]. Thus, N-subjettiness gives a measure of how well a given jet is described by being composed of at least N subjets. In practice, the ratio $\tau_{MN} = \tau_M/\tau_N$ with $M > N$ is used, since this ratio becomes small if a jet contains at least M subjets.

Table 4.4 summarises the different jet collections used in this thesis. More details will be provided in the following paragraphs.

Particle Flow Jets

In this thesis, particle flow (PFlow) jets [227] are reclustered from PFlow objects calibrated to the electromagnetic energy scale. The anti-k_t algorithm with a size parameter of $R = 0.4$ is used. Jets in this collection are required to fulfil $p_{\mathrm{T}} > 20\,\mathrm{GeV}$, $|\eta| < 4.5$ while passing the tight working point of the jet vertex tagger [245]. Although the size of these jets is not beneficial for the boosted signal topology since they are too large to

Collection	Inputs	Size R	min. p_{T} [GeV]	max. $\lvert\eta\rvert$	Use case
PFlow	EM PFlow objects	0.4	20	4.5	used in $E_{\mathrm{T}}^{\mathrm{miss}}$ calculation and overlap removal
small-R	LC topo-clusters	0.2	15	2.5	TAR jet inputs
VR track	selected tracks	$\frac{30\,\mathrm{GeV}}{p_{\mathrm{T}}}$	10	2.5	flavour tagging TAR jets
large-R	LC topo-clusters	1.0	200	2.0	trigger and cross checks
TAR	small-R jets and selected tracks	0.75	100	2.0	reconstruction of hadronically decaying analysis objects

Table 4.4.: Summary of all jet collections used in this thesis including their inputs and size parameter used in the anti-k_t algorithm. Furthermore, the basic kinematic selection and their use case in the thesis is briefly described.

resolve the hadronic decay products and too small to collect all hadronic decay products in a single jet, they are useful to ensure that energy is not double counted between leptons and hadronic objects. They are also used to calculate the missing transverse energy in the event.

Small-R Jets

Small-R jets are reclustered from topo-clusters calibrated to the hadronic scale. The anti-k_t algorithm with a size parameter of $R = 0.2$ is used. Only jets satisfying $p_{\mathrm{T}} > 15\,\mathrm{GeV}$ and $|\eta| < 2.5$ will be considered as inputs for the TAR jets.

VR Track Jets

Flavour tagging (see Section 4.2.5) in boosted topologies uses jet collections with a large size parameter, and often relies on flavour tagging variable-R (VR) track jets [246]. These jets are reclustered from selected tracks. The anti-k_t algorithm on selected tracks uses a variable size parameter depending on the jet p_{T}

$$R = \min\left(R_{\mathrm{max}}, \max\left(R_{\mathrm{min}}, \frac{\rho}{p_{\mathrm{T}}}\right)\right), \tag{4.8}$$

where ρ defines the energy scale of the size parameter and R_{min} and R_{max} the lower and upper size bounds. The $\rho = 30$ GeV, $R_{\mathrm{min}} = 0.02$ and $R_{\mathrm{max}} = 0.4$ have been found to be optimal for boosted $H \to b\bar{b}$ tagging [247].

The jets are required to satisfy $p_{\mathrm{T}} > 10$ GeV, $|\eta| < 2.5$ and to have at least two constituents.

Large-R Jets

Large-R jets [236], similar to small-R jets, are reclustered from topo-clusters calibrated to the hadronic scale. The anti-k_t algorithm with a size parameter of $R = 1.0$ is used. Additionally, trimming [248, 249] is applied to make the jet more robust against pileup. During trimming, the constituents of the jet are reclustered into subjets using the k_t algorithm and a size parameter of R_{sub}. For each of those subjets, the p_{T} is compared to the large-R jet p_{T} and if the ratio is smaller than a defined cut off, f_{cut}, the subjet is removed. The trimmed large-R jet obtains its quantities from the constituents of the surviving subjets. In ATLAS, $R_{\text{sub}} = 0.2$ and $f_{\text{cut}} = 0.05$ are used. To improve the jet energy, the large-R jets are corrected for non-prompt muon contributions that often occur in the context of heavy flavour quark decays.

Furthermore, the jets must satisfy $p_{\text{T}} > 200\,\text{GeV}$ and $|\eta| < 2.0$. In this analysis, the large-R jets are mainly used in the trigger and to perform cross checks on the modelling of TAR jets in the context of the analysis.

TAR Jets

A special jet collection is the Track-Assisted Reclustered (TAR) jet collection [250]. In contrast to the jet collections discussed so far, the calibrated small-R jets which are overlap removed against electrons (see Section 4.2.6) are used as inputs to the reclustering algorithm to form the TAR jet. Since the inputs are already calibrated, the k_t, anti-k_t or Cambridge–Aachen algorithm can be used with either a fixed or variable size parameter R, which can be chosen freely as well. Then trimming is applied on the small-R jets, removing small-R jets which do not carry at least 5% of the TAR jet momentum as shown in the left part of Figure 4.16, in order to reduce the pileup dependence of the jet.

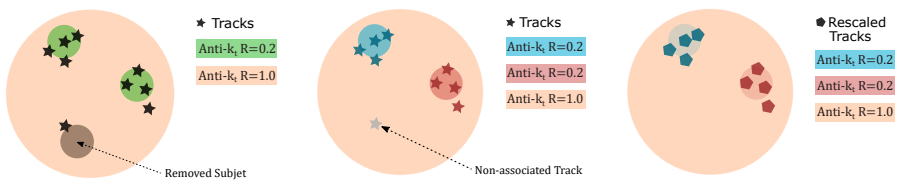

Figure 4.16.: Schematic representation of the TAR jet algorithm.

In the next steps, the tracks which have been overlap removed against leptons (see Section 4.2.6) are added to the algorithm by ghost associating [251] them to the surviving small-R jets. The tracks not associated to any small-R jet are removed from the collection as depicted in the middle diagram of Figure 4.16. The momentum of the surviving tracks is then rescaled according to

$$\left(p_{\text{T}}^{\text{track}}\right)' = p_{\text{T}}^{\text{track}} \times \frac{p_{\text{T}}^{j}}{\sum_{\text{track}\in j} p_{\text{T}}^{\text{track}}}, \tag{4.9}$$

with j being the small-R jet to which the track is associated. All quantities of the jet such as the mass or the substructure variables are then calculated from the rescaled tracks, combining the advantages of both input collections: the good energy resolution of small-R jets, the inclusion of energy contributions from neutral particles, and the excellent spatial resolution of tracks.

Dedicated studies have been conducted in the context of this analysis to find the optimal set of algorithm parameters for the analysis presented in this thesis. For this, the signal efficiency is compared to the $t\bar{t}$ background rejection, which is one of dominant backgrounds. The signal efficiencies and background rejections of different reconstruction parameters are presented in Figure 4.17. It is evident that the fixed size parameter outperforms the variable size parameter, while there is no difference in the performance between the anti-k_t and Cambridge–Aachen algorithms with regards to the signal efficiency and background rejection. While the background rejection increases significantly for very small radii, the signal efficiency decreases in the same manner. The best signal efficiency is achieved when using $R \approx 0.7$. Taking into account other mass points and the 0-lepton boosted channel, the anti-k_t reclustering algorithm with a size parameter of $R = 0.75$ is chosen. More details on the studies can be found in Ref. [26].

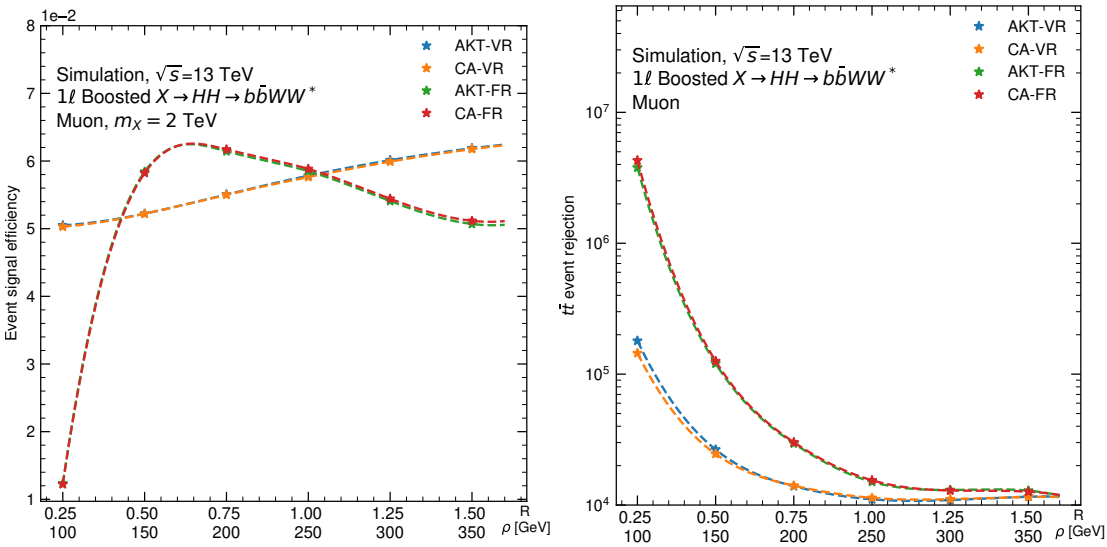

(a) $m_X = 2\,\text{TeV}$ signal **(b)** $t\bar{t}$ background

Figure 4.17.: Signal efficiency and background rejection (defined as the inverse of the efficiency) for different fixed size parameters R and size scales ρ using the anti-k_t or Cambridge–Aachen reclustering algorithms [26].

The TAR jets are required to satisfy $p_{\mathrm{T}} > 100$ GeV as a kinematic baseline and $|\eta| < 2.0$ to be in the range of the Inner Detector. Furthermore, only TAR jets containing at least two surviving tracks and two surviving small-R jets are included in the analysis. To allow flavour tagging, VR track jets are ghost-associated to the TAR jets, which provides a robust matching procedure that makes use of the catchment area of the

untrimmed TAR jet.

4.2.4. Missing Transverse Energy

As a hadron collider, the LHC does not collide elementary particles but protons composed of partons, each carrying only a fraction of the protons' momentum. Since the protons do not exhibit any significant transverse momentum, the transverse momentum of the partons is negligible compared to their longitudinal momentum. Therefore, it can be assumed that before the collision, the total transverse momentum of the event vanishes, and thus, the total transverse momentum of the event after the collision also vanishes. Since only weakly interacting particles such as neutrinos do not leave a signal in the detector, their energy is undetected resulting in an imbalance, namely missing transverse energy [252]:

$$\vec{p}_{\mathrm{T}}^{\mathrm{miss}} = -\sum_i \vec{p}_{\mathrm{T},i}^{\mathrm{vis}}, \tag{4.10}$$

where $\vec{p}_{\mathrm{T},i}^{\mathrm{vis}}$ refers to the calibrated momentum of all measured objects. These objects are typically electrons, muons, jets, photons and hadronically decaying τ-leptons that are used in the analysis selection. Additionally, tracks which are matched to the PV but have not been used in the reconstruction of an object are included as the track soft term. Generally, the missing transverse energy is split into its magnitude ($E_{\mathrm{T}}^{\mathrm{miss}}$) and its azimuthal angle (ϕ^{miss}).

Since the detector does not instrumentally cover every area and also has a finite resolution, it is also possible that particles are poorly reconstructed or undetected. Thus, the imbalance does not purely correspond to only weakly interacting particles [253].

In this analysis, loose electrons, loose muons and PFlow jets together with the track soft term are used to calculate the missing transverse energy.

4.2.5. b-Tagging

Being able to identify whether a jet originates from a hadron containing a b-quark (b-jets), a c-quark (c-jets) or a light quark or gluon (light jet) is very beneficial in identifying certain signal processes such as $H \to b\bar{b}$ decays. Therefore, many algorithms to distinguish b-jets from c-jets and light jets exist in ATLAS and are referred to as b-tagging [254].

The algorithms exploit the comparable long lifetime of hadrons containing a b-quark, allowing them to travel a noticeable distance in the detector before they decay. Given that the Inner Detector is very close to the interaction point and has a high spatial resolution, it is likely that the decay of such a hadron results in a secondary vertex which is displaced from the primary vertex. This signature is exploited by low-level algorithms by either analysing properties of individual tracks associated to a jet, or using tracks directly to construct a secondary displaced vertex. These algorithms are complemented and combined with high-level algorithms based on machine learning algorithms [255,256].

The tagger used in this analysis is the DL1r tagger, which is a feed-forward deep neural network with a multidimensional output corresponding to the probabilities of a jet being either a b-jet, a c-jet or a light jet. The decision is based on the kinematics of the jet and the outcome of the low-level algorithms. Furthermore, quantities relating to the secondary vertex found in the jet by the Secondary Vertex Finder (SV1) [256,257] and all displaced vertices in the jet by the JetFitter algorithm [258] are considered. Additional discriminating variables created by a recurrent neural network which exploits spatial and kinematic correlations between the tracks originating from the same hadron [259] are also taken into account in the decision making.

Since no b-tagger configuration has been derived for TAR jets, VR track jets which have been ghost-associated to the TAR jets are b-tagged instead. While the VR track jet can either pass or fail a certain b-tagging working point, TAR jets can be b-tagged multiple times based on the number of b-tagged VR track jets associated to the TAR jet.

Four working points are provided using a fixed cut on the b-tagger output score corresponding to approximately 60%, 70%, 77% and 85% b-tagging efficiency measured in $t\bar{t}$ events. To decide which working point to use, the number of b-tags of a TAR jet is investigated and displayed in Figure 4.18. A distinction between TAR jets matched to the true $H \to b\bar{b}$ system and matched to the true hadronically decaying W (W_{had}) is made. While a working point resulting in as many events as possible with two b-tags is preferable for the TAR jet truth matched to $H \to b\bar{b}$ system, the TAR jets that are truth matched to W_{had} should have no b-tags. The 77% working point is chosen as a compromise between these two ideals.

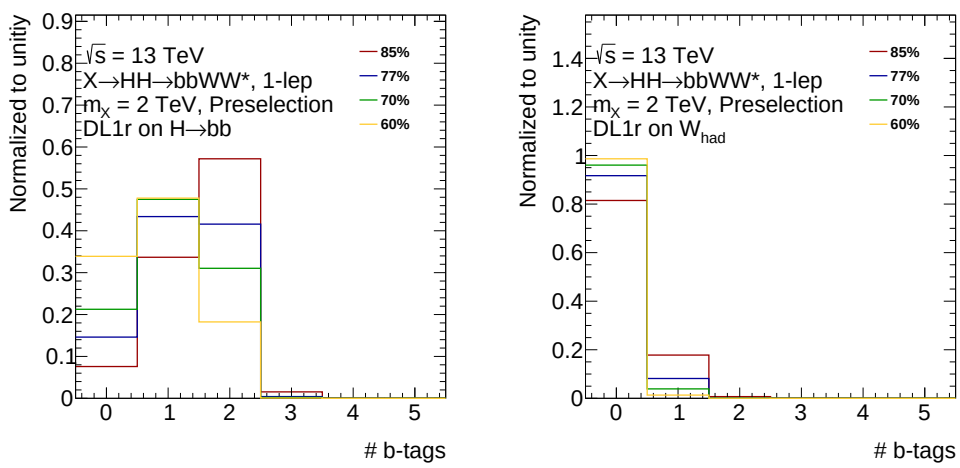

(a) $H \to b\bar{b}$ **(b)** W_{had}

Figure 4.18.: The number of b-tags of the TAR jet truth matched to either the $H \to b\bar{b}$ system or W_{had} using different b-tagging working points of the DL1r tagger in events of the $m_X = 2\,\text{TeV}$ signal mass point.

4.2.6. Overlap Removal

Since all reconstruction algorithms in ATLAS take into account all tracks and calorimeter clusters without checking if they have been used in the reconstruction of another object, energy is double counted by geometrically overlapping objects. To resolve the double counting of energy, a ΔR based overlap removal (OLR) is applied. As in the sequential jet reclustering algorithms, the ΔR in the OLR uses the rapidity instead of the pseudorapidity

$$\Delta R_{\mathrm{OLR}} = \sqrt{\Delta y^2 + \Delta\phi^2}. \tag{4.11}$$

The analysis presented in this thesis includes muons, electrons, PFlow jets, small-R jets and tracks in the overlap removal. Large-R jets, photons and τ-leptons are not used since they are not explicitly part of the analysis. TAR jets do not need to be included since the OLR is applied on their inputs, i.e. small-R jets and tracks. All objects included in the OLR pass the respective object selection discussed earlier in this section.

The following steps are applied in subsequent order:

1. A muon is rejected if it is a calorimeter-tagged muon and it shares the track in the Inner Detector with an electron. If a muon is not calorimeter-tagged and it shares the Inner Detector track with an electron, the electron is rejected.
2. Due to issues identified in the PFlow algorithm a special overlap removal for particle flow jets against muons is necessary. A particle flow jet is rejected if $\Delta R(\mu, \mathrm{jet}) < 0.4$ and
   - the muon is isolated, i.e $E_{\mathrm{T}}^{\mathrm{cone40}} < y_0$, or
   - the muon p_{T} exceeds a certain fraction of the summed track p_{T} of the jet, i.e.

     $$\frac{p_{\mathrm{T}}^{\mu}}{\sum\limits_{\mathrm{tracks}} p_{\mathrm{T}}^{\mathrm{tracks}}} > x_2,$$

     or
   - the following is satisfied

     $$E_{\mathrm{T}}^{\mathrm{cone40}} < y_0 + \frac{y_2 - y_1}{x_2 - x_1} \cdot \left(\frac{p_{\mathrm{T}}^{\mu}}{\sum\limits_{\mathrm{tracks}} p_{\mathrm{T}}^{\mathrm{tracks}}} - x_1 \right).$$

   Studies show that there are two sets of values depending on the number of tracks in the PFlow jet. If $n_{\text{tracks in jet}} < (\geq)\ 4$, then $x_1 = 0.7\ (0.6)$, $x_2 = 0.85\ (0.9)$, $y_0 = y_1 = 15\ (5)\,\mathrm{GeV}$ and $y_2 = 30\ (30)\,\mathrm{GeV}$ [260].
3. Furthermore, a PFlow jet is rejected against a muon if $n_{\text{tracks in jet}} < 3$ and either the muon is ghost-associated to the jet or $\Delta R(\mu, \mathrm{jet}) < 0.2$. A muon is rejected against a PFlow jet if

   $$\Delta R(\mu, \mathrm{jet}) < \min\left(0.4,\ 0.04 + \frac{10\,\mathrm{GeV}}{p_{\mathrm{T}}^{\mu}}\right).$$

4. A PFlow jet is rejected against an electron if $\Delta R(e, \text{jet}) < 0.2$. An electron is rejected against a PFlow jet if

$$\Delta R(e, \text{jet}) < \min\left(0.4,\ 0.04 + \frac{10\,\text{GeV}}{p_{\text{T}}^{e}}\right).$$

5. Finally, a track is rejected if it is either matched to an electron or a muon. A small-R jet is rejected against an electron if $\Delta R(e, j) < 0.2$. No OLR of small-R jets against muons is performed since the energy deposited in the calorimeter by muons is small compared to the hadronic energy.

4.3. Dataset and Luminosity

The instantaneous luminosity of an accelerator is a measure for how much data it provides at that moment and related directly to the event rate. Integrating the instantaneous luminosity over a certain period of time, $\int \mathcal{L} dt$, is proportional to the total number of events produced during this period.

In the ATLAS experiment, the luminosity is measured in many complementary approaches and detector subcomponents [261]. Primarily luminosity sensitive detectors such as LUCID-2 [262] or the Beam Condition Monitor detector provide an absolute calibration of the luminosity. This calibration is obtained in special LHC runs with specifically tailored conditions and a low instantaneous luminosity using van der Meer scans [263, 264]. These calibrations are then transferred to the LHC conditions used in runs for collecting analysis data. Throughout the runs, the measurements of the above mentioned detector components are compared to the results of other subdetectors such as the number of tracks in the InnerDetector or gap currents in the LAr colorimeters to estimate any possible change in the primary calibration.

During Run 2, the LHC delivered a total of $\int \mathcal{L} dt = 156$ fb^{-1} of which ATLAS collected $\int \mathcal{L} dt = 147$ fb^{-1}. However, only events passing the data quality requirements of ATLAS (GoodRunsLists) [265] are considered in the analysis. This corresponds to $\int \mathcal{L} dt = 139$ fb^{-1} of data using the GoodRunsLists listed in Appendix A.2.

Figure 4.19 (a) shows the time development of the integrated luminosity as measured by ATLAS. While the years 2017 and 2018 provided the largest amount of data, it came at the cost of more interactions happening simultaneously. This can be seen in Figure 4.19 (b) which shows the average number of interactions per bunch crossing.

4.4. MC Simulation of Signals and Backgrounds

To be able to separate signal from background events, it is crucial to identify the differences between these processes in reconstructed events. Therefore, they are simulated using the MC simulation approach as discussed in Section 3.3.

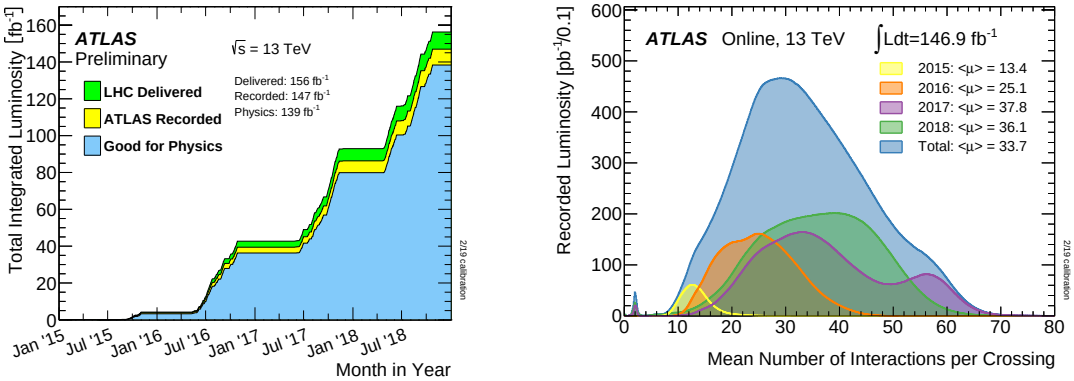

(a) integrated luminosity **(b)** average number of interactions

Figure 4.19.: Integrated luminosity that has been provided by the LHC, recorded by ATLAS and usable for analysis together with the average number of interactions per bunch crossing for the full Run 2 dataset [266].

4.4.1. Signal Samples

The $X \to HH$ samples are generated at leading order in α_S using MADGRAPH 2.6.1 [267] with the NNPDF2.3LO PDF set [268]. HERWIG 7v7.1.3 [269] is used for hadronisation and parton shower simulation with the heavy quark flavour decays being performed by EVTGEN 1.6.0 [270]. Samples are produced for m_X = 0.8, 0.9, 1.0, 1.2, 1.4, 1.6, 1.8, 2.0, 2.5, 3.0, 4.0, and 5.0 TeV. The AFII detector simulation is used for all mass points and the full ATLAS detector simulation is used to produce an extra set of $m_X = 2$ TeV samples to check the AFII modelling. The branching ratios of each H are set to 50% $b\bar{b}$ decays and to 50% WW^* or ZZ^* decays, respectively. A filter ensures one $H \to b\bar{b}$ decay and one $H \to VV^*$ decay in the event.

The $X \to SH$ samples are generated at leading order in α_S using PYTHIA 8.244 [271] in the A14 tune [272] using the NNPDF2.3LO PDF set. The hadronisation and parton shower are also simulated using PYTHIA 8.244 with EVTGEN 1.7.0 for heavy flavour decays. The grid of m_X–m_S mass points generated is shown in Table 4.5 and is chosen to allow both H and S to be produced on-shell. The AFII detector simulation is used for all of the mass points. The H is constrained to decay exclusively to $b\bar{b}$ and the S to WW.

All signal samples (HH and SH) are split by the number of charged leptons from the VV decay. For the fully hadronic samples (0-lepton), W and Z bosons are constrained to decay hadronically. For the 1-lepton samples, a filter is applied that requires exactly one lepton and one neutrino from W decays in the event. Each mass point has 50000 events, except the $m_X = 4$ and 5 TeV mass points of the HH production which are only generated with 20000 events.

A complete list of the signal MC samples is given in Appendix A.2.

m_S [GeV] \ m_X [GeV]	350	500	750	1000	1500	2000	2500	3000
170	1	1	0/1	0/1	0/1	0/1	0/1	0/1
240	-	1	0/1	0/1	0/1	0/1	0/1	0/1
400	-	-	0/1	0/1	0/1	0/1	0/1	0/1
550	-	-	0/1	0/1	0/1	0/1	0/1	0/1
750	-	-	-	0/1	0/1	0/1	0/1	0/1
1000	-	-	-	-	0/1	0/1	0/1	0/1
1500	-	-	-	-	-	0/1	0/1	0/1
2000	-	-	-	-	-	-	0/1	0/1
2500	-	-	-	-	-	-	-	0/1

Table 4.5.: Signal mass points generated for the $X \to SH$ samples in the 0-lepton and 1-lepton channels are indicated by a 0 or 1, respectively. Otherwise the mass point is not used.

4.4.2. Background Samples

For the backgrounds, the following processes have been considered: top quark pair production ($t\bar{t}$), massive vector boson production in association with jets (V+jets), single top quark production (single top), vector boson pair production (diBoson) and multiple jet production (dijet). Most of these samples are split by the number of prompt leptons they yield in the final state and sometimes samples with alternative generators are used for modelling comparisons. All background samples are produced with the full detector simulation.

$t\bar{t}$

The production of $t\bar{t}$ events is modelled using the Powheg Box v2 [273–276] generator at next-to-leading order in α_S using the NNPDF3.0nlo [277] PDF set and an h_{damp} parameter of $1.5\,m_{\text{top}}$ [278], which effectively regulates the high-p_{T} radiation against which the $t\bar{t}$ system recoils. The hadronisation and parton shower is modelled by Pythia 8.230 in the A14 tune using the NNPDF2.3lo set of PDFs with the heavy quark flavour decays being performed by EvtGen 1.6.0.

V+jets

The production of V+jets samples where the vector boson decays leptonically are simulated with the Sherpa 2.2.1 generator [279] at next-to-leading order in α_S for up to two partons, and leading order for up to four partons calculated with Comix [280] and OpenLoops [281–283]. They are matched with the Sherpa parton shower [284] using the MEPS@NLO prescription [285–288] with the NNPDF3.0nnlo PDF set. The samples were normalised to a next-to-next-to-leading order prediction [289]. The samples are split by the scalar sum of the hard scattered objects' p_{T}, H_{T}, and the presence of

heavy flavour quarks in the final state.

The production of V+jets samples where the vector boson decays hadronically are simulated with the Herwig ++2.7.1 which is also used for hadronisation and parton showering using the CTEQ6L1 PDF set [290]. The underlying event is simulated using the UEEE5 tune [291, 292].

single top

The associated production of top quarks with W bosons (tW) is modelled with the Powheg Box v2 generator at next-to-leading order in α_S and the NNPDF3.0nlo PDF set where the diagram removal scheme [293] removes interference and overlaps with $t\bar{t}$ events. The events were interfaced to Pythia 8.230 using the A14 tune and the NNPDF2.3lo PDF set.

Single-top t-channel production is modelled using the Powheg Box v2 generator at next-to-leading order in α_S using the four-flavour scheme [294] and the NNPDF3.0nlo PDF set. The events are interfaced with Pythia 8.230 using the A14 and the NNPDF2.3lo PDF set for hadronisation and parton showering.

Single-top s-channel production is modelled using the Powheg Box v2 generator at next-to-leading order in α_s using the NNPDF3.0nlo PDF set. The events are interfaced with Pythia 8.230 in the A14 tune using the NNPDF2.3lo PDF set for hadronisation and parton showering.

diboson

Samples of diboson final states (VV) are simulated with the Sherpa 2.2.1 or 2.2.2 generator depending on the process. The samples include off-shell effects and Higgs boson contributions. They are generated at next-to-leading order in α_s for up to one additional parton and at leading order for up to three additional parton emissions.

Samples for the loop-induced processes $gg \to VV$ are generated at leading order for up to one additional parton emission. The matrix element calculations are matched and merged with the Sherpa parton shower using Comix and MEPS@NLO and virtual QCD corrections are provided by OpenLoops with the NNPDF3.0nnlo PDF set.

The V+γ background is simulated using the MadGraph5_aMC@NLO 2.3.3 generator [267] interfaced with Pythia 8.212 in the A14 tune and EvtGen 1.6.0 for hadronisation and parton showering. It uses the NNPDF2.3lo PDF set.

dijet

Multijet production is generated using Pythia 8.230 in the A14 tune at leading-order in α_s which are matched to the parton shower using the NNPDF2.3lo PDF set. The renormalisation and factorisation scales are set to the geometric mean of the squared transverse masses of the two outgoing particles

$$p_{\mathrm{T}}^{\mathrm{hat}} = \sqrt{(p_{\mathrm{T},1}^2 + m_1^2)(p_{\mathrm{T},2}^2 + m_2^2)}. \tag{4.12}$$

The samples are created in slices filtered by the p_{T} of the leading truth jet.

A complete list of the background MC samples is given in Appendix A.2.

CHAPTER 5

The Boosted 1-Lepton Analysis

This thesis focusses on the boosted 1-lepton topology in the search for resonant HH and SH production in the $b\bar{b}WW^{(*)}$ decay channel as depicted in Figure 4.3. Due to the boost of the final state particles, four objects can be generally reconstructed in the event: the Higgs boson decaying to a $b\bar{b}$-pair ($H \to b\bar{b}$), the hadronically decaying W boson (W_{had}) and the charged lepton (ℓ) as well as the corresponding neutrino (ν) from the leptonically decaying W boson. With the event being characterised by the unique topology of a prompt lepton overlapping with the hadronic decay products of a W boson, the TAR jet collection is used for reconstructing $H \to b\bar{b}$ and W_{had} in order to cope with the dense environment expected. Since the properties of $H \to b\bar{b}$ and W_{had} differ significantly, but both are reconstructed as TAR jets, a classification algorithm is developed that labels one TAR jet as $H \to b\bar{b}$ candidate and another TAR jet as W_{had} candidate.

During the event selection, various aspects need to be taken into account such as triggers and orthogonality to other channels. In addition to signal regions which aim to maximise the signal sensitivity, validation regions to allow cross checks in a region similar to the signal regions, and control regions to constrain or to estimate the backgrounds, are defined. In contrast to prompt lepton processes, non-prompt lepton processes cannot be simulated accurately such that a data driven approach for their background estimate is pursued instead. Despite the better modelling of prompt lepton processes, the phase space investigated in this analysis is unusual and very challenging such that the normalisation of the dominant backgrounds needs to be corrected. This is done by fitting the backgrounds to data in the control regions to obtain a normalisation factor.

This chapter is structured as follows: In Section 5.1, the object reconstruction and classification within the context of this analysis is discussed. Sections 5.2–5.6 elaborate on the event selection including the trigger strategy, orthogonality to other channels, the preselection and the signal, validation and control region definitions. Section 5.7

describes the non-prompt lepton estimate while Section 5.8 discusses the constraints to the background normalisations. The variable used as the final discriminant is introduced in Section 5.9 before the chapter is concluded by the investigation of the modelling in the various regions in Section 5.10.

5.1. Objects within the Analysis

5.1.1. TAR Jet Classification

Different classification methods are evaluated on several signal mass points to see which method has the highest classification efficiency as well as truth matching efficiency. The classification efficiency corresponds to the fraction of events where a classification is possible. The truth matching efficiency refers to the fraction of events where the $H \to b\bar{b}$ and W_{had} candidates are correctly classified. Based on the event topology, the following three methods are studied in detail.

- **ΔR based:** in this method, the TAR jets are classified into $H \to b\bar{b}$ and W_{had} candidates based on the ΔR between the jet and the signal lepton. The jet closest to the lepton is labelled as the W_{had} candidate, and the jet furthest from the lepton the $H \to b\bar{b}$ candidate.

- **p_{T} based:** similar to the ΔR based classification, the jet closest to the lepton is classified as the W_{had} candidate. The $H \to b\bar{b}$ candidate is defined to be the p_{T} leading jet which is not classified as W_{had} candidate.

- **b-tag based:** in this method, the $H \to b\bar{b}$ candidate is classified before the W_{had} candidate. The jet with the highest number of b-tags over a configurable threshold is labelled the $H \to b\bar{b}$ candidate, the jet of the remaining jets which is closest to the lepton is classified as the W_{had} candidate.

In Figure 5.1, the classification and truth matching efficiencies for the three methods are shown. By construction, the classification of the ΔR and p_{T} based methods is fully efficient, because there are always two jets fulfilling the requirements when only selecting events with at least two TAR jets. The classification efficiency for the b-tag based method takes into account the b-tagging efficiency and is thus not fully efficient. To have a fairer comparison, the $H \to b\bar{b}$ candidate classified using the first two methods is required to be b-tagged as well. No requirement is applied to the W_{had} candidate. While the classification efficiency of the ΔR and p_{T} based methods drops below the b-tag based method, the truth matching efficiency is higher for these methods and above 90% for all signal mass points. Thus, the p_{T} based classification is chosen for this analysis.

Furthermore, the truth matching efficiency can be increased when only considering the three leading jets in the event if there are more than three jets passing the selection. This allows for the scenario that the W_{had} candidate is not one of the two leading leading TAR jets, while preventing a softer TAR jets from radiation that are close to the identified lepton to be classified as the W_{had} candidate.

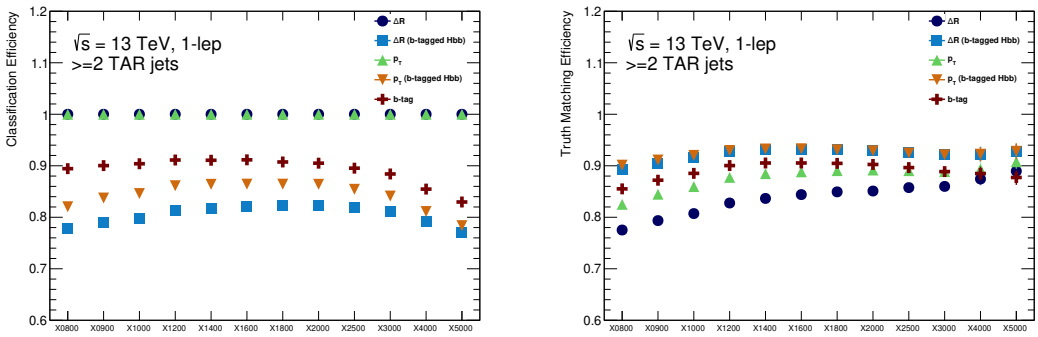

(a) Classification Efficiency **(b)** Truth matching efficiency

Figure 5.1.: Classification and truth matching efficiency of three classification methods for several HH signal mass points between $m_X = 0.8\,\text{TeV}$ and $m_X = 5\,\text{TeV}$. At least two TAR jets and one signal lepton are required. In all cases where b-tagging is used, the threshold is ≥ 1 b-tag using the 77% working point of the DL1r tagger.

5.1.2. Neutrino Reconstruction

The neutrino is most difficult object to reconstruct since it is not measured directly by the ATLAS detector. Assuming that the neutrino carries most of the unmeasured energy in the event, it is possible to use the $E_{\text{T}}^{\text{miss}}$ to estimate the transverse components of the neutrino momentum. However, since this variable is sensitive to all detector activity in the entire event, this approximation results in a large uncertainty.

However, at hadron colliders such as the LHC, there is no possibility to measure the p_{z} of the neutrino. Instead it can only be reconstructed using analytical or numerical calculations. Given that the neutrino is produced in the decay of a W boson, the W boson mass can be used to constrain the neutrino p_{z} by requiring

$$m_W^2 = (p^\ell + p^\nu)^2,$$

where p^ℓ and p^ν are the four vectors of the charged lepton and neutrino, respectively. In the case of $H \to WW^*$ decays, it is also possible that the neutrino results from an off-shell W boson, the W boson mass constraint is replaced by the Higgs boson mass constraint, that also takes into account the four vector of the hadronically decaying W boson:

$$m_H^2 = \big(\underbrace{p_{W_{\text{had}}} + p_\ell}_{=p_{\text{vis}}} + p_\nu\big)^2 \tag{5.1}$$

$$\Leftrightarrow \underbrace{\frac{m_H^2 - m_{\text{vis}}^2}{2} + -p_{\text{x}}^{\text{vis}} p_{\text{x}}^\nu - p_{\text{y}}^{\text{vis}} p_{\text{y}}^\nu}_{=A} + p_{\text{z}}^{\text{vis}} p_{\text{z}}^\nu = E^{\text{vis}} \sqrt{(p_T^\nu)^2 + (p_z^\nu)^2}. \tag{5.2}$$

This implies

$$
\begin{aligned}
(A + p_{\mathrm{z}}^{\mathrm{vis}} p_{\mathrm{z}}^{\nu})^2 &= (E^{\mathrm{vis}})^2((p_{\mathrm{T}}^{\nu})^2 + (p_{\mathrm{z}}^{\nu})^2) \\
\Leftrightarrow 0 &= \underbrace{\frac{(E^{\mathrm{vis}} p_{\mathrm{T}}^{\nu})^2 - A^2}{(E^{\mathrm{vis}})^2 - (p_{\mathrm{z}}^{\mathrm{vis}})^2}}_{=q} \underbrace{- \frac{2 A p_{\mathrm{z}}^{\mathrm{vis}}}{(E^{\mathrm{vis}})^2 - (p_{\mathrm{z}}^{\mathrm{vis}})^2} p_{\mathrm{z}}^{\nu}}_{=p} + (p_{\mathrm{z}}^{\nu})^2 \\
\Rightarrow p_{\mathrm{z}}^{\nu_{1,2}} &= -\frac{p}{2} \pm \sqrt{\left(\frac{p}{2}\right)^2 - q}
\end{aligned}
\tag{5.3}
$$

Squaring Eq. 5.2 results in the analytical approach can have none, one or two valid solutions which can still be complex. Figure 5.2 shows that approximately 20% of the events do not have a valid solution for p_{z}^{ν} regardless of the value of m_X. If the solution is complex, the imaginary part is set to zero. If there are two valid solutions, the neutrino p_{z} which yields the smaller distance between charged lepton and neutrino is chosen to account for the boosted topology.

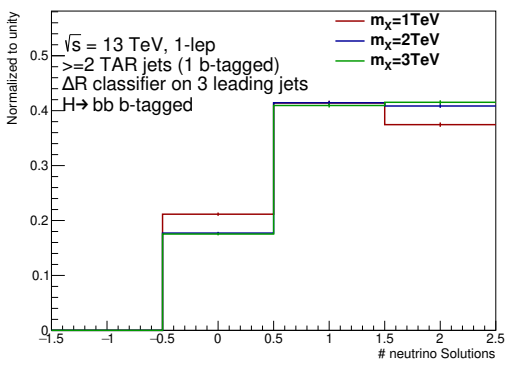

Figure 5.2.: Number of valid solutions for the neutrino p_{z} obtained using the analytical approach for three selected m_X.

The numerical approach can be realised through multivariate techniques such as a deep neural network trained to estimate p_{z}^{ν} [295]. Compared to the analytical approach, all events have a valid solution but the gain in resolution for this approach is small, such that the numerical approach has not been implemented in the analysis.

5.1.3. Classification and Reconstruction Performance

To estimate the performance of the reconstruction and classification of the different analysis objects, their quantities are compared to the quantities of the true objects. The comparison of the p_{T} of lepton, neutrino, $H \to b\bar{b}$ candidate and W_{had} candidate are shown in Figure 5.3 and the comparison of the neutrino p_{z} and the masses of the $H \to b\bar{b}$ and W_{had} candidates in Figure 5.4. Generally, only few differences between the events originating from different m_X are observed, indicating that the reconstruction is stable across a wide range of energy.

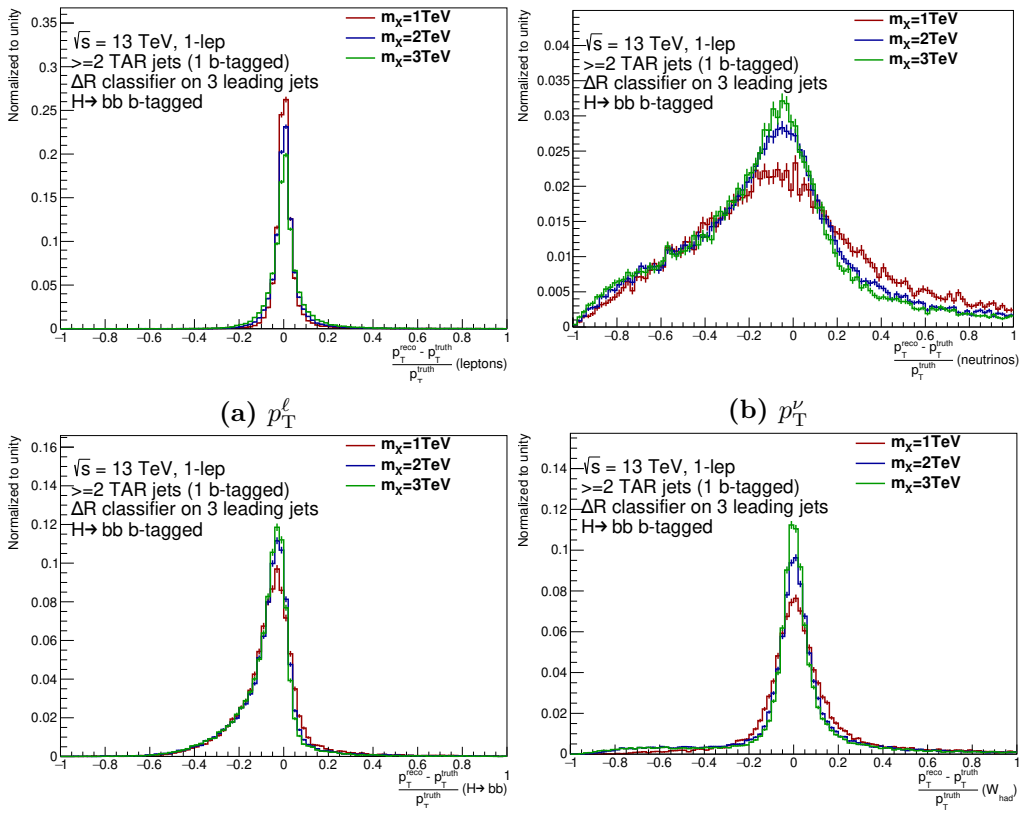

(a) p_{T}^{ℓ} (b) p_{T}^{ν}

(c) $p_{\mathrm{T}}^{H\to b\bar{b}}$ (d) $p_{\mathrm{T}}^{W_{\mathrm{had}}}$

Figure 5.3.: Comparison of the p_{T} of the reconstructed and classified objects in the analysis to the p_{T} of the true objects for three selected mass points. The neutrino p_{T} is compared to $E_{\mathrm{T}}^{\mathrm{miss}}$.

The reconstruction of p_{T} of the charged lepton, namely the electron or muon, yields the best resolution since the lepton energy is well calibrated due to the applied ID and isolation requirements. With a slightly broader p_{T} comparison distribution, the performance of the classified TAR jets is also very good since jets are known to be measured less accurately than leptons. It should also be noted that the mean of the p_{T} comparison distribution of the $H \to b\bar{b}$ candidate is shifted to lower values, indicating that the reconstruction most likely fails to fully account for leptonic B-hadron decays. The worst p_{T} reconstruction is observed for neutrinos. This is expected, given that $E_{\mathrm{T}}^{\mathrm{miss}}$ is an event variable that includes contributions from other non-prompt neutrinos and energy mismeasurements of all particles in the event.

Since the reconstruction of the neutrino p_{z} performs so poorly, the usage of the neutrino p_{z} and variables depending on it are avoided in the analysis. The mass reconstruction of the $H \to b\bar{b}$ candidate is sufficiently good enough to be considered in the selection. In the mass reconstruction of the W_{had} candidate, the muon channel performs very

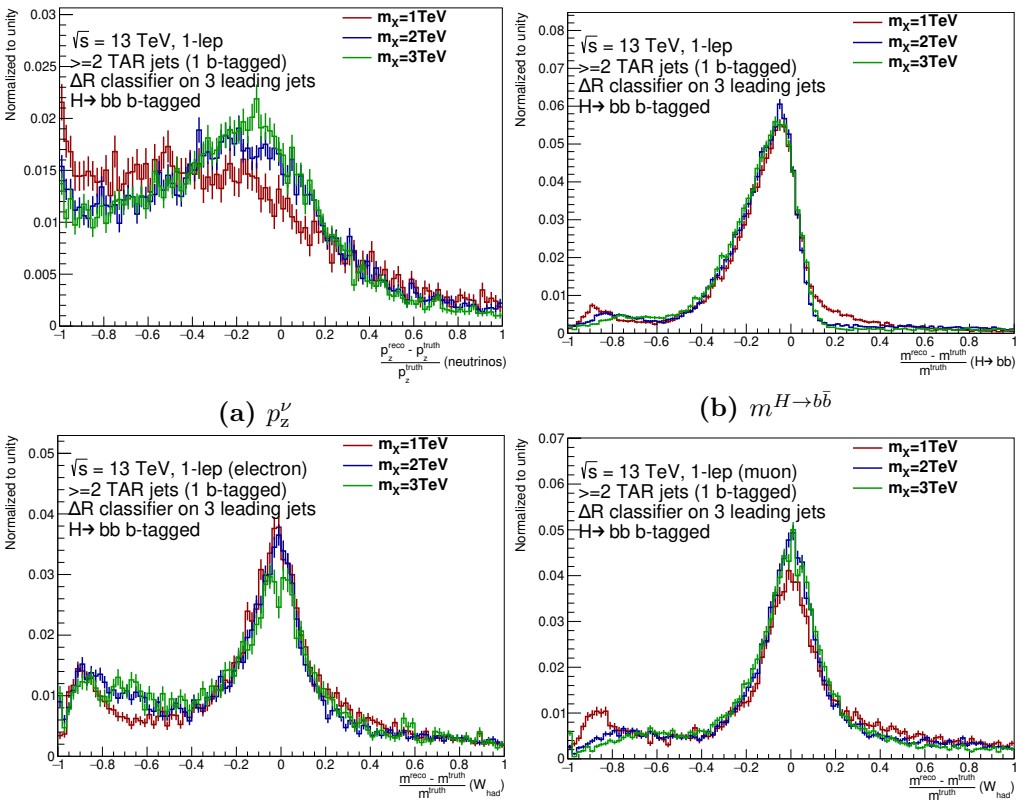

(a) p_z^{ν} (b) $m^{H\to b\bar{b}}$

(c) $m^{W_{\text{had}}}$ electron channel (d) $m^{W_{\text{had}}}$ muon channel

Figure 5.4.: Comparison of the p_z of the reconstructed neutrino in the analysis to the p_z of the true neutrino as well as the comparison of the masses of the $H \to b\bar{b}$ and W_{had} candidates to the true $H \to b\bar{b}$ and W_{had} masses for three selected mass points. The W_{had} mass comparison is split into electron and muon channels.

well, especially considering that approximately half of the reconstructed W bosons are expected to be off-shell. The W_{had} mass reconstruction in the electron channel on the other hand suffers from the reconstructed mass being too small indicating that the OLR between the small-R input jets and electrons is too strict.

5.2. Trigger Strategy

As described in Section 3.2, not every recorded collision at ATLAS can be stored permanently. To serve the needs of all different analyses conducted in the ATLAS experiment, various trigger categories [188,296] exist, exploiting the characteristics of all the different physics objects. To keep the data rate small, either a high p_{T} threshold is chosen or not every event that fires the trigger is stored.

Based on the physics objects available in this analysis, the best trigger candidates can

be found in the categories of single electron triggers [297], single muon triggers [298], single as well as multi large-R jet triggers [299] and b-jet triggers [300]. A complete list of investigated triggers is given in Appendix A.3. Within each category a logical disjunction of the individual triggers is applied to ensure a coverage of each time period as well as to exploit different combinations of object quality and the p_{T} threshold of the respective trigger.

Figure 5.5 shows the trigger efficiency of events corresponding to three selected signal mass points $m_X = 1$, 2 and 3 TeV chosen to represent the full range of the boosted 1-lepton signals. Here, single electron and single muon triggers are combined into single lepton triggers (singleLep) by logical disjunction yielding an efficiency between 45% for $m_X = 1$ TeV and 90% for $m_X = 3$ TeV. While the single large-R jet triggers (LRJ) are nearly fully efficient for $m_X \geq 2$ TeV, they are only around 60% efficient for lower resonance masses. The single large-R jet triggers are chosen as baseline triggers. The low efficiency at $m_X \leq 1$ TeV can be recovered by checking other sets of triggers on events that not triggered by the single large-R jet trigger such as single lepton triggers, multi-large-R jet triggers (multiLRJ) and b-jet triggers (Bjet). The best efficiency is achieved when combining the single large-R jet triggers with the single lepton triggers.

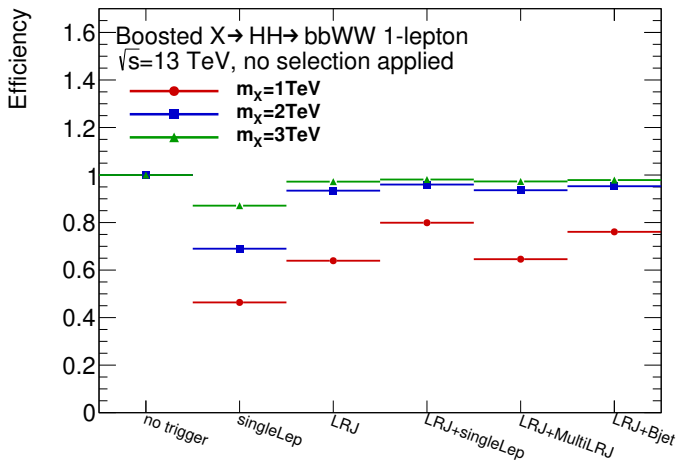

Figure 5.5.: Efficiency of several trigger collections consisting of a logical disjunction of specific object triggers for three selected m_X. The trigger collections are valid for all years of Run 2 (2015–2018) and no distinction between the electron and muon channel is made. No event or object selection is applied.

Since the single large-R jet triggers do not use TAR jets, but rather large-R jets, the difference in the jet definitions need to be evaluated. In Figure 5.6, the efficiency of the logical disjunction of single large-R jet triggers as a function of the leading jet p_{T} is shown for large-R jets and TAR jets. It can be clearly seen, that for leading jets with $p_{\mathrm{T}}^{J} \gtrsim 480$ GeV, the efficiency flattens to a plateau and the single large-R jet triggers are fully efficient. Furthermore, there is no appreciable difference regardless of whether the large-R jet or TAR jet algorithm was used. The difference in low large-R jet p_{T} between

electron and muon channels can be explained by the electron energy subtraction from the large-R jet energy in cases of geometrical overlaps to decouple these two objects. Thus for the electron channel, the p_{T} of the jet corresponding to the W_{had} candidate is reduced compared to the p_{T} of the large-R jet that triggered the event.

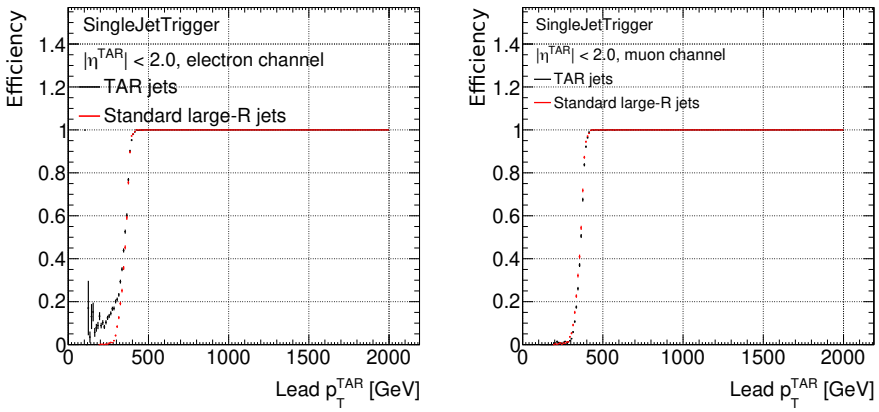

(a) electron channel **(b)** muon channel

Figure 5.6.: Comparison between the logical disjunct single large-R jet trigger efficiency for large-R jets and TAR jets depending on the leading jet p_{T} evaluated on all available HH signal mass points [26].

Given that the usage of single lepton triggers significantly complicates the non-prompt background estimate (see Section 5.7), the necessity of the inclusion of single lepton triggers was re-evaluated. Figure 5.7 shows the fraction of events triggered by either single large-R jet, single electron or single muon triggers. Cuts on the TAR jets and leptons ensure that only events in the trigger efficiency plateau are considered. For the single large-R jet triggers, $p_{\mathrm{T}}^{\text{lead TAR jet}} > 500\,\mathrm{GeV}$ is required, and for the single lepton triggers, the lepton must pass the ID required by the trigger, with the signal lepton matched to the triggered lepton. Additionally, for single electron triggers, $p_{\mathrm{T}}^{e} > p_{\mathrm{T}}^{e\,\text{threshold}} + 1\,\mathrm{GeV}$ is required and, for muon triggers, $p_{\mathrm{T}}^{\mu} > 1.05 \cdot p_{\mathrm{T}}^{\mu\,\text{threshold}}$.

As already seen in Figure 5.5, the single lepton triggers are only relevant for low $m_X \lesssim 1\,\mathrm{TeV}$. However, the most dominant prompt lepton backgrounds which are $t\bar{t}$ and W+jets production, are also dominated by events triggered by single lepton triggers. Thus, not using the single lepton triggers corresponds to the removal of less sensitive analysis regions and, therefore, only events triggered by single large-R jet triggers are used in the analysis selection.

5.3. Orthogonality to Other Search Channels

While an individual analysis channel is optimised for its own phase space including the physics objects used, a combination with other analysis channels can improve the overall

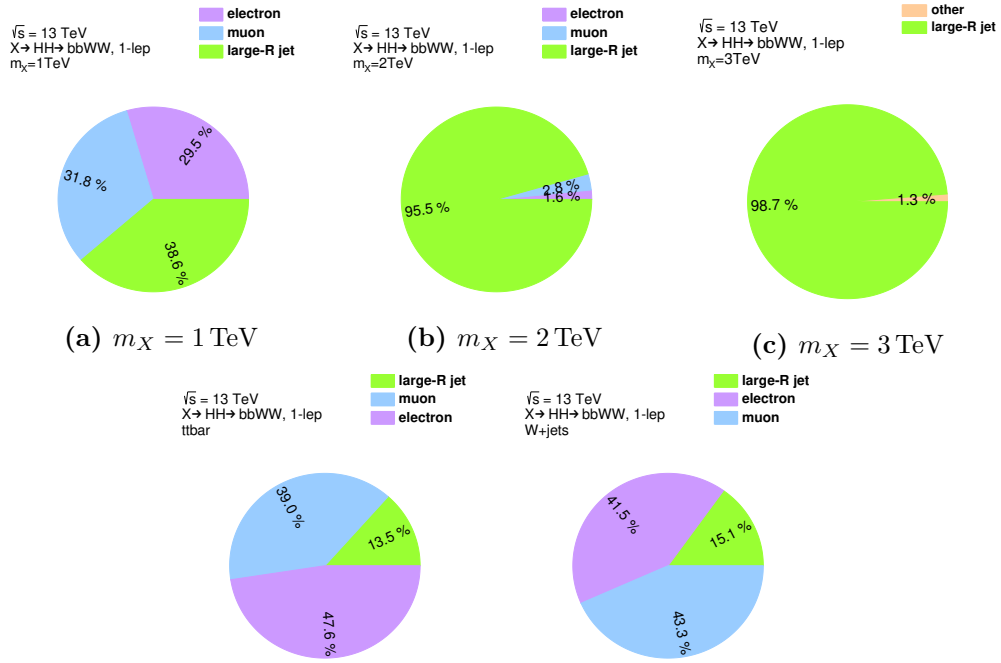

(a) $m_X = 1\,\text{TeV}$ **(b)** $m_X = 2\,\text{TeV}$ **(c)** $m_X = 3\,\text{TeV}$

(d) $t\bar{t}$ **(e)** W+jets

Figure 5.7.: Fraction of events triggered by either single large-R jet, single electron or single muon triggers in the energy range of the trigger efficiency plateau for three selected signal mass points (top) and the two most dominant prompt lepton backgrounds (bottom). Events are only required to have at least two TAR jets and one signal lepton at maximum.

sensitivity by adding additional phase spaces that are also sensitive to the same signal processes. However, to allow a simple combination, the different analyses are constructed to be orthogonal.

In the case of the boosted 1-lepton channel, orthogonality of the signal regions needs to be ensured to the other topologies within the $b\bar{b}WW$ decay channel for HH and SH production, respectively, and also to the other HH decay channels investigating the same m_X range as the boosted 1-lepton analysis such as $X \to HH \to b\bar{b}b\bar{b}$ [12] and $X \to HH \to b\bar{b}\tau^+\tau^-$ [14].

Since the $X \to HH \to b\bar{b}\tau^+\tau^-$ as well as the 0-lepton final state searches of the $b\bar{b}WW$ topologies implement a lepton veto, requiring a lepton in the boosted 1-lepton analysis ensures orthogonality to these channels. The orthogonality to $X \to HH \to b\bar{b}b\bar{b}$ can be imposed by using the number of b-tagged jets in the event. In the boosted $b\bar{b}b\bar{b}$ topology, events with at least two b-tagged large-R jets are selected such that requiring exactly one b-tagged TAR jet for the boosted $b\bar{b}WW$ searches makes the analyses orthogonal. Here, requiring one b-tagged TAR jet is considered to be equivalent to requiring one b-tagged large-R jet. The resolved $b\bar{b}b\bar{b}$ topology can be vetoed by rejecting events with

more than two b-tagged PFlow jets.

The orthogonality to the other 1-lepton topologies, namely the split-boosted and resolved topologies , is more complex, but at the same time only needed for SH production since resonant HH production is only investigated by the boosted 1-lepton topology. The main difference between the split-boosted and boosted 1-lepton topologies is the distance between the charged lepton and the hadronically decaying W boson. Since the W_{had} candidate does not need to be defined in the same way in the two topologies, using a cut on the distance between the lepton and the closest TAR jet ($\min \Delta R(\ell, J)$) is a well defined alternative orthogonality criterion and shown in Figure 5.8. While the $m_X - m_S$ combinations that can be associated with the boosted topology ($m_S \lesssim 0.3 \cdot m_X$) have the majority of events at $\min \Delta R(\ell, J) \lesssim 1.0$ (left to the vertical red lines in Figure 5.8), the majority of the split-boosted 1-lepton topology can be found in the $\min \Delta R(\ell, J) \gtrsim 1$ range of the plots. Thus, boosted 1-lepton events are required to fulfil $\min \Delta R(\ell, J) < 1.0$.

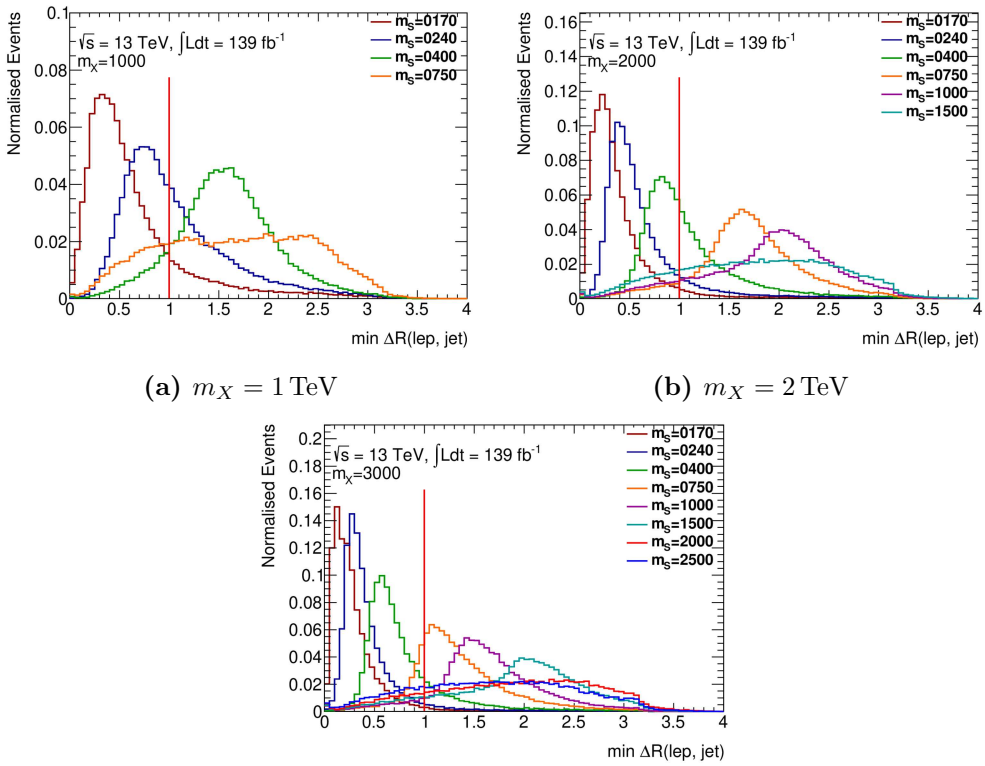

(a) $m_X = 1\,\text{TeV}$ **(b)** $m_X = 2\,\text{TeV}$

(c) $m_X = 3\,\text{TeV}$

Figure 5.8.: Distribution of the ΔR between the lepton and the closest TAR jet as variable discriminating the boosted and split-boosted 1-lepton analysis for various combinations of m_X and m_S. All values of m_S are given in GeV [26, 301].

The orthogonality to the resolved 1-lepton topology depends on the investigated mass points. If $m_X \leq 750\,\text{GeV}$ or $m_S < 0.3 \cdot m_X$, the resolved analysis ensures orthogonality

by vetoing events that have a b-tagged large-R jet in the event [207]. For the other mass point combinations, events with two b-tagged PFlow jets are rejected.

5.4. Preselection

Based on the analysis objects and the event topology, a preselection is defined to select events in the boosted 1-lepton phase space:

- **Single large-R trigger fired** by the event as discussed in Section 5.2. This requirement is accompanied by a cut on $p_{\mathrm{T}}^{\text{lead TAR jet}} > 500\,\mathrm{GeV}$ to be in the trigger efficiency plateau. This decision limits the sensitivity to low $m_X \lesssim 1\,\mathrm{TeV}$ significantly but benefits the simplicity and sensitivity of the analyses for higher m_X.

- **At least two TAR jets** passing the requirements listed in Section 4.2.3 to ensure that there is one TAR jet present for the reconstruction of the $H \to b\bar{b}$ and one for the reconstruction of the W_{had}. No upper cut on the number of TAR jets is implemented.

- **VR track jet overlap veto** to perform b-tagging only on well defined VR track jets. Thus, events are vetoed if $\Delta R(\mathrm{jet}_i, \mathrm{jet}_j) < \min(R_{\mathrm{jet}_i}, R_{\mathrm{jet}_j})$ where i runs over all jets passing the requirements and being considered b-tagging while j runs over all jets passing the requirements but with a loosened $p_{\mathrm{T}} > 5$ GeV. The case where $i = j$ is omitted.

- **Exactly one signal muon** as defined in Section 4.2.2. In simulated prompt lepton background as well as signal events, the muon is matched to the true prompt muon in the event such that all non-prompt lepton events are estimated in a data driven approach (see Section 5.7).

- $\boldsymbol{\Delta R(\ell, \text{closest TAR jet}) < 1.0}$ distinguishes between boosted and split-boosted regions in the 1-lepton channel as discussed in Section 5.3.

- $\boldsymbol{p_{\mathrm{T}}^{H\to b\bar{b}} > 500}$ **GeV** is found to increase the signal sensitivity for $m_X \gtrsim 1\,\mathrm{TeV}$. The signal contamination in this region is very small because the leading TAR jet, which must satisfy $p_{\mathrm{T}} > 500\,\mathrm{GeV}$ due to the trigger conditions, is classified in nearly all cases as $H \to b\bar{b}$ candidate in resonant HH production.

Furthermore, it is planned to implement a requirement that there be at most two b-tagged PFlow jets in the event using the 77% DL1r tagger working point to ensure orthogonality to the resolved $X \to HH \to b\bar{b}b\bar{b}$ analysis as discussed in Section 5.3. This has not been done at the time of thesis writing.

During the course of the analysis, the electron channel was removed from this analysis since the added complexity was not worth the small gain in sensitivity. More details are given in Appendix A.9.

5.5. Signal and Validation Regions

The signal regions (SR) and validation regions (VR) are defined simultaneously to ensure that the validation regions are similar to the signal regions to allow checks on the modelling of variables and the background estimate. But this is only a small signal contribution in the validation regions. While the definitions of signal and validation regions are based upon studies with $X \to HH$ MC events, additional selections optimised for SH and HH production, respectively, are applied to signal and validation regions afterwards.

Based on the boosted 1-lepton topology of the $X \to HH \to b\bar{b}WW^*$ process where the $H \to b\bar{b}$ is reconstructed as a single TAR jet, exactly one b-tagged TAR jet in the event is expected, and thus required for all signal and validation regions. Furthermore, this b-tagged TAR jet must classified as $H \to b\bar{b}$ candidate.

To increase the sensitivity of the analysis, it is distinguished whether the $H \to b\bar{b}$ candidate has one or two b-tags. While requiring the $H \to b\bar{b}$ candidate having two b-tags increases the signal purity, a non-negligible amount of signal events is discarded due to the efficiency of the used b-tagging working point. Thus, also considering event where the $H \to b\bar{b}$ candidate has only one b-tag can recover the signal efficiency at the cost of reduced signal purity. Keeping the regions separated allows to exploit both the purity of the two b-tag regions and signal efficiency added by the one b-tag region.

Another powerful variable to distinguish between signal and backgrounds is the mass of the $H \to b\bar{b}$ candidate which peaks near the Higgs boson mass. Due to leptonic B-hadron decays, this peak is shifted to slightly lower values. Nevertheless, it can be used to distinguish the signal TAR jets from the main backgrounds, as can be seen in Figure 5.9. It shows the TAR mass distribution of $H \to b\bar{b}$ candidates of events passing the preselection (see Section 5.4) with the exception of the $p_{\mathrm{T}}^{H\to b\bar{b}} > 500$ GeV cut, but instead containing exactly one b-tagged TAR jet. The shown signal is the weighted sum of all individual signal mass points is scaled to 25% of the sum of backgrounds.

While the sum of background distributions exhibits a falling spectrum with three peaks, the signal (red line) is mostly located between $100\,\mathrm{GeV} \leq m_{\mathrm{TAR}}^{H\to b\bar{b}} \leq 130\,\mathrm{GeV}$ with a much smaller second peak at low values. The largest background peak can be found below $m_{\mathrm{TAR}}^{H\to b\bar{b}} \lesssim 30\,\mathrm{GeV}$, consistent with single quark or gluon initiated TAR jets. The second background peak is at $m_{\mathrm{TAR}}^{H\to b\bar{b}} \approx 80$ GeV, consistent with fully contained hadronically decaying W bosons. This peak is mainly populated by single top and $t\bar{t}$ events. The last background peak can be found at $m_{\mathrm{TAR}}^{H\to b\bar{b}} \approx 175$ GeV, consistent with the top quark mass and is only populated by $t\bar{t}$ events where all decay products of a boosted hadronically decaying top quark are collected within a single TAR jet.

To take into account the different kinematics of the $H \to b\bar{b}$ candidates, a p_{T} dependent mass window is defined using the strategy described in Section A.4. To distinguish between signal and validation regions, it is checked whether the $H \to b\bar{b}$ candidate passes (p) or fails (f) a certain efficiency threshold of the $H \to b\bar{b}$ mass (m_H) window cut and is single or double b-tagged, yielding four combinations in total.

The m_H window efficiencies under consideration are displayed in Figure 5.10. Using

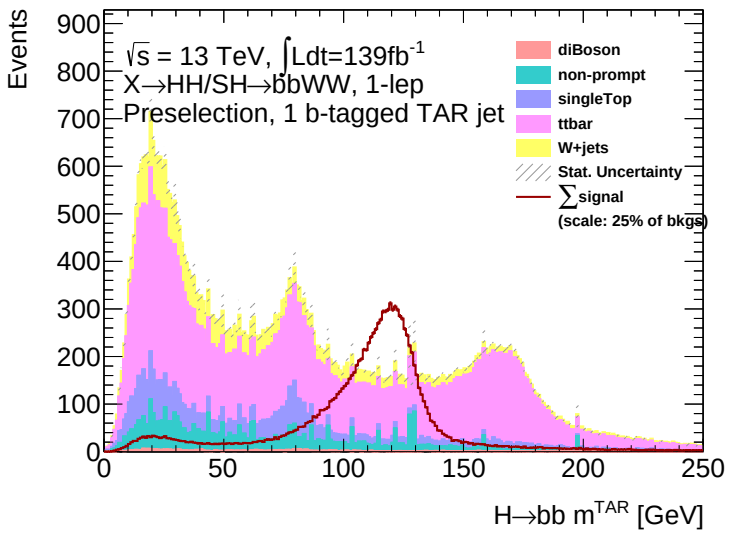

Figure 5.9.: Signal and background distribution of the TAR jet mass of the $H \to b\bar{b}$ candidate. The non-prompt lepton background has been estimated following the description provided in Section 5.7. The signal is the weighted sum of all individual signal samples which is scaled to 25% of the sum of background events. The preselection except the cut on the $p_{\mathrm{T}}^{H\to b\bar{b}} > 500$ GeV cut is applied. Furthermore, exactly one b-tagged jet in the event is required.

an efficiency of 70% ensures to keep a good amount of signal while at the same time removing a sufficient fraction of background events. It is therefore chosen as baseline m_H window efficiency. The 80% efficient m_H window extends the options for the definition of the validation region.

To have a measure which region should be considered as a signal region and which region as a validation region, the signal purity and signal efficiency are investigated in Figure 5.11. As signal purity, the simplified significance expression $s/\sqrt{b}$ is used, where s corresponds to the number of signal events and $\sqrt{b}$ is the statistical Poisson uncertainty on the number of background events. The background in this case consists of the corrected prompt-lepton backgrounds (see Section 5.8) and the estimated non-prompt lepton background (see Section 5.7).

The overall highest signal purity and efficiency is obtained for the $H \to b\bar{b}$ candidate to pass the m_H window and to have two b-tags, followed by the region where the $H \to b\bar{b}$ candidate passes the m_H window and has one b-tag. This is especially relevant for for high $m_X \geq 3\,\mathrm{TeV}$ where the $H \to b\bar{b}$ system becomes so boosted, such that the b-jets within the TAR jet start to overlap. These two regions are therefore considered as signal regions.

The region with the lowest purity, where the $H \to b\bar{b}$ candidate fails the m_H window and has one b-tag, is considered as validation region and further lowered in signal purity by requiring the $H \to b\bar{b}$ candidate to fail the 80% efficient m_H window instead of the

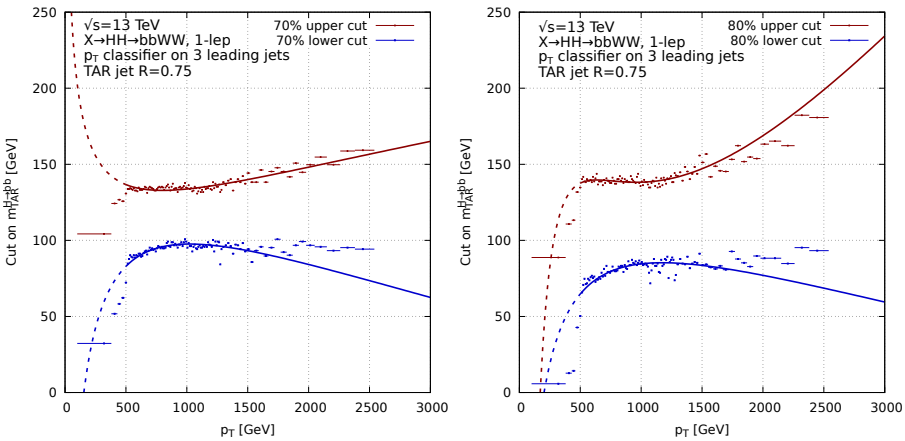

(a) 70% WP **(b)** 80% WP

Figure 5.10.: $H \to b\bar{b}$ mass (m_H) windows depending on $p_{\mathrm{T}}^{H\to b\bar{b}}$ evaluated to contain a certain percentage of $X \to HH \to b\bar{b}WW^*$ events and corresponding fits. The dashed part of the fit will not be used in the analysis due to the applied cut on $p_{\mathrm{T}}^{H\to b\bar{b}} > 500$ GeV in the preselection.

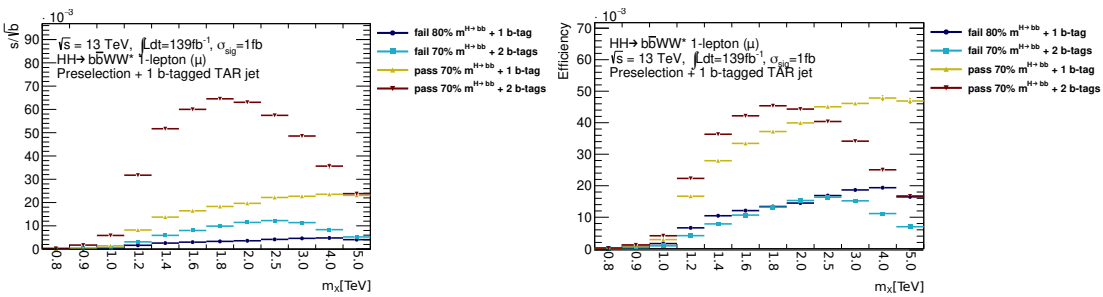

(a) signal purity **(b)** signal efficiency

Figure 5.11.: Purity and efficiency of the four region definition options for the full range of HH production mass points. The region definition with the lowest purity (dark blue) is constructed as potential validation region reducing its purity on purpose. The expected signal cross section is set to 1 fb for all mass points.

70% efficient window. Since, at the time of writing this thesis, having one validation region appears sufficient, the remaining region, where $H \to b\bar{b}$ candidate fails the m_H window and has two b-tags is also labelled a signal region but is expected to overall contribute only minimally to the analysis sensitivity.

A summary of the signal and validation region definitions can be found in Table 5.1. To increase the signal sensitivity, the signal regions are further optimised. These optimised selections are also included in Table 5.1. The background composition in the signal and validation regions are shown in Figure 5.12 for the HH selection and in Figure 5.13 for the SH selection applied, respectively. In all regions, the $t\bar{t}$ and W+jets are the

most dominant backgrounds, where the relative $t\bar{t}$ contribution is larger when the HH selection is applied than when the SH selection is applied. Since SRp2 is the most sensitive signal region, all further optimisations are based on this region.

region	name	mass window	number of b-tags
signal	SRp2	pass 70%	2
signal	SRp1	pass 70%	1
signal	SRf2	fail 70%	2
validation	VRf1	fail 80%	1
SH selection	$H \to b\bar{b}$ candidate passes 80% C_2 window derived from SH samples		
HH selection	$H \to b\bar{b}$ candidate passes 80% C_2 window derived from SH samples and event passes the 80% $\Delta R(W_{\text{had}}, \ell)$ window		

Table 5.1.: Summary of the final signal and validation regions of the muon channel based on the mass window cut and the number of b-tags of the $H \to b\bar{b}$ candidate. The optimised SH and HH selections are also listed. Each region furthermore requires exactly one b-tagged TAR jet in the event.

5.5.1. The HH Selection

Various substructure and kinematic variables have been checked for selecting $X \to HH \to b\bar{b}WW^*$ events and the most promising variables are

- $\boldsymbol{\Delta R(\ell, W_{\text{had}})}$ the distance between the lepton (muon) and the W_{had} candidate
- $\boldsymbol{H \to b\bar{b}\ C_2}$ substructure variable to check if the $H \to b\bar{b}$ candidate is more 2-prong-like than 1-prong-like (see Section 4.2.3).

Figure 5.14 shows the distributions of C_2 of the $H \to b\bar{b}$ candidate and ΔR between the W_{had} candidate and the lepton in SRp2. It can be seen that generally the separation power is higher for ΔR than for C_2, but this depends on how boosted the signal is. For the HH signal, a high m_X and thus, a high p_T of the considered objects, corresponds to a smaller ΔR. However, the separation power is present for all shown values of m_X.

To make the cut on $\Delta R(\ell, W_{\text{had}})$ less dependent on m_X, the same procedure as for the m_H window cut is used with adjusted settings explained in detail in Appendix A.4. Due to the small number of events, especially in the most sensitive signal region, only the windows yielding a signal efficiency of 80% displayed in Figure 5.15 are considered.

Comparing the purity of the two window definitions in Figure 5.16 (a), the window cut on $\Delta R(W_{\text{had}}, \ell)$ performs best for nearly all m_X. Only for $m_X < 1\,\text{TeV}$, no difference is visible, but the sensitivity to this phase space is very limited due to the boosted selection applied. The window on $H \to b\bar{b}$ C_2 is derived twice: once using the HH production

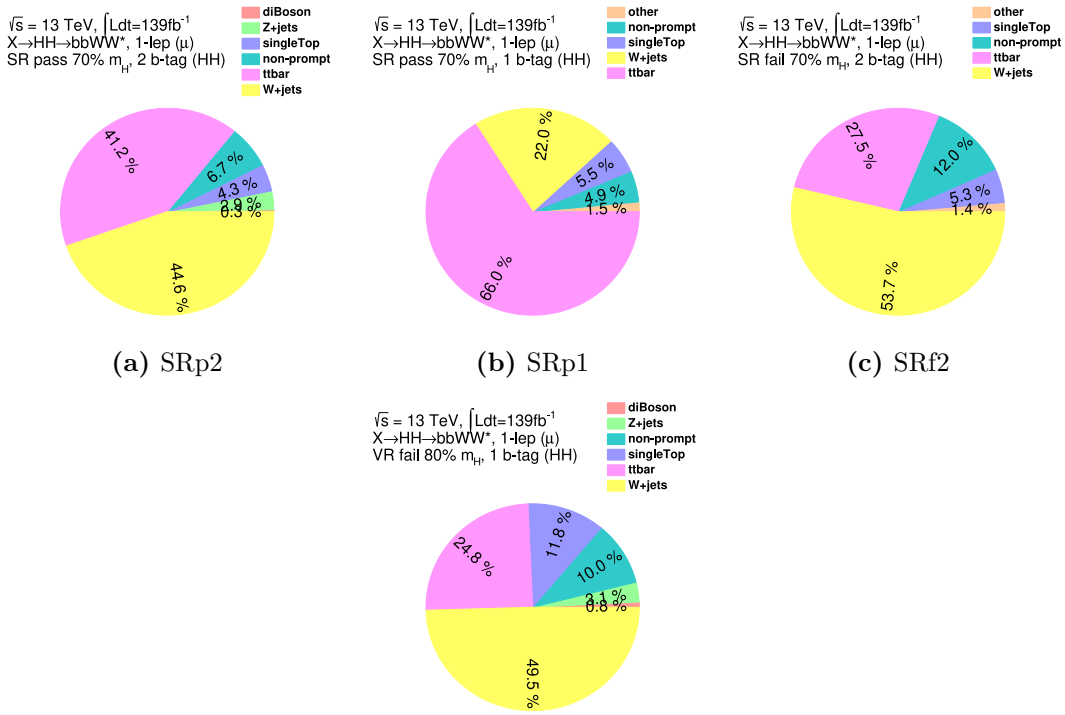

(a) SRp2 **(b)** SRp1 **(c)** SRf2

(d) VRf1

Figure 5.12.: Background composition in the three signal regions (top) and the validation region (bottom) when the HH selection is applied. The non-prompt lepton background is estimated as described in Section 5.7 and the background normalisation is corrected according to Section 5.8.

mass points and once the SH production mass points. However, the window derived from the SH production mass points actually performs better or equally well than the one derived from the HH production mass points. The corresponding signal efficiencies in Figure 5.16 (b) are very similar for all window definitions by design. The cut on a window dependent on $\Delta R(W_{\text{had}}, \ell)$ results in the lowest signal efficiency. Considering the increase in purity, this loss in signal efficiency in the most sensitive signal region is acceptable.

To move the HH selection closer to the SH selection discussed in the next section, events are also required to pass the 80% $H \to b\bar{b}$ C_2 window derived from SH signals.

5.5.2. SH Optimization

While the boost of the objects only depends on m_X in the case of HH production, the kinematics are more complex for SH production. Varying m_X while leaving m_S constant, the behaviour will be the same as described for the HH signal, but when increasing m_S while keeping m_X constant, the boost of the WW system decreases. For

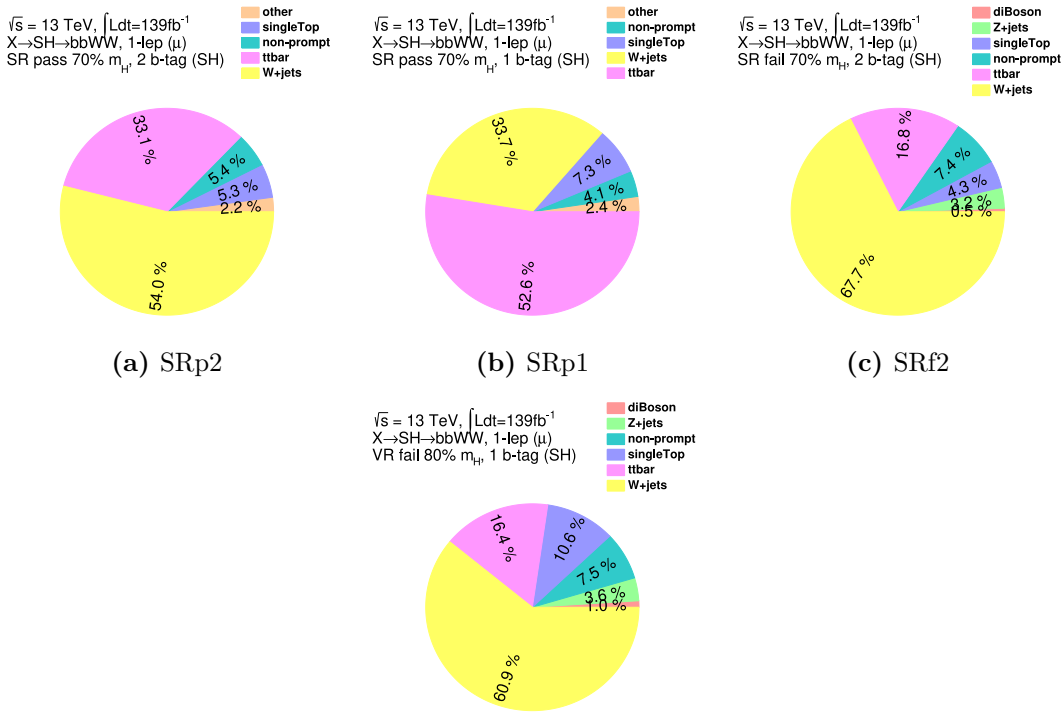

(a) SRp2 **(b)** SRp1 **(c)** SRf2

(d) VRf1

Figure 5.13.: Background composition in the three signal regions (top) and the validation region (bottom) when the SH selection is applied. The non-prompt lepton background is estimated as described in Section 5.7 and the background normalisation is corrected according to Section 5.8.

example, in this case, the ΔR between the lepton and the W_{had} increases, without being necessarily reflected in the p_{T} distribution of either of the two objects. This can also be seen in Figure 5.17, where $\Delta R(\ell, W_{\text{had}})$ distribution of the backgrounds and three SH signals. While the background distribution is unchanged compared to Figure 5.14 (b), the HH signal is replaced by three selected SH mass points. While the blue and red lines (same m_S, different m_X) exhibit the same shape but the blue line (higher m_X) is shifted to lower values, the shape between the blue and green lines (same m_X, different m_S) differs and becomes flatter for the green line (higher m_S) making $\Delta R(W_{\text{had}}, \ell)$ unusable in distinguishing signal from background.

Instead the highest separation power is expected from the $H \to b\bar{b}$ C_2 and the W_{had} mass. The distributions of both variables in SRp2 are shown in Figure 5.18. While there are only small differences between the $H \to b\bar{b}$ C_2 distribution between the HH and SH signals, the W_{had} mass distribution features only a single peak at m_W if $m_S \ll m_X$ since both W bosons from the scalar boson decay are real and on-shell. This, however, breaks down if m_S approaches m_X and the W_{had} candidate is not classified correctly [301].

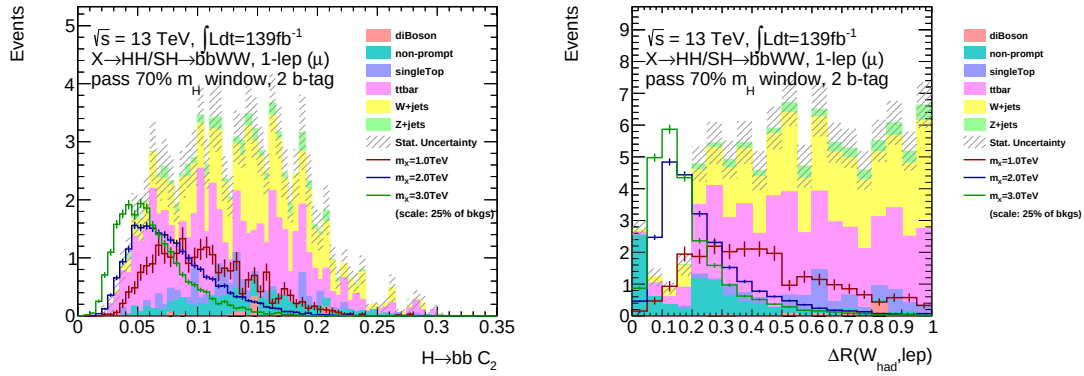

(a) $H \to b\bar{b}\ C_2$ (b) $\Delta R(W_{\text{had}}, \ell)$

Figure 5.14.: Distributions of the candidate variables for optimising the selection of HH production in SRp2. The signal yield is scaled to match 25% of the sum of backgrounds.

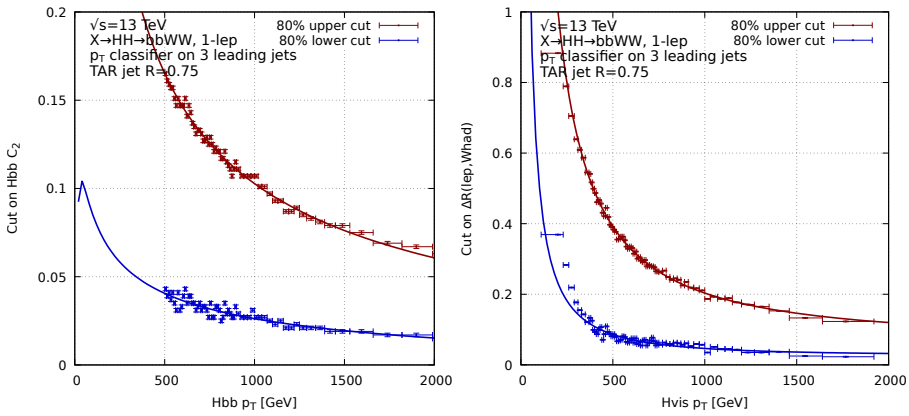

(a) $H \to b\bar{b}\ C_2$ (b) $\Delta R(W_{\text{had}}, \ell)$

Figure 5.15.: Selection windows on $H \to b\bar{b}\ C_2$ depending on $p_{\text{T}}^{H\to b\bar{b}}$ and on $\Delta R(W_{\text{had}}, \ell)$ depending on $p_{\text{T}}^{W_{\text{had}}+\ell}$ yielding 80% signal efficiency in all three signal regions combined.

While the details on the C_2 and W_{had} mass window constructions can be found in Appendix A.4, the considered windows corresponding to 80% signal efficiency are displayed in Figure 5.19. Given that the shape of the W_{had} mass window results from misclassified W_{had} candidates, requiring $m_{\text{TAR}}^{W_{\text{had}}} > 50\,\text{GeV}$ is investigated as alternative to the W_{had} mass window accepting the potential loss in sensitivity in the transition region between boosted and split boosted signals.

The resulting signal purity and signal efficiency are shown in Figure 5.20. In contrast to HH production, the efficiency as well as the purity depends on m_X and m_S limiting the sensitive phase space. While at first glance, the fixed cut on the W_{had} mass seems to

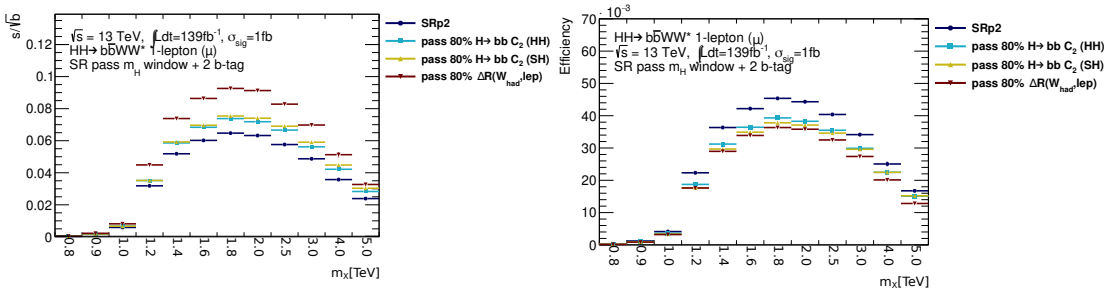

(a) signal purity **(b)** signal efficiency

Figure 5.16.: Purity and efficiency of the considered optimisation options for the full range of HH production mass points. The expected signal cross section is set to 1 fb for all mass points.

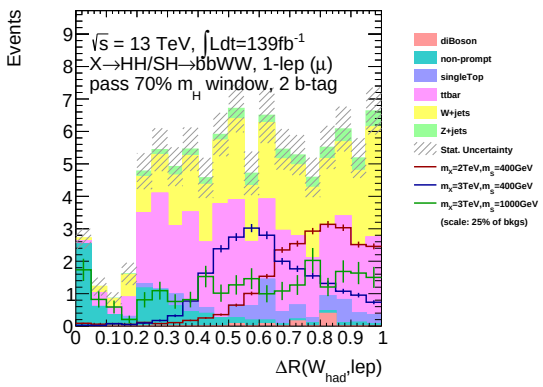

Figure 5.17.: Distribution of $dR(W_{\text{had}}, \ell)$ in SRp2. The signal yield is scaled to match 25% of the sum of backgrounds.

be the best criteria, it further decreases the small sensitivity to signals which are in the transition region to the split-boosted topology. Using cuts on a W_{had} mass window does not improve the signal purity, and with a reduced signal efficiency, the signal sensitivity is also reduced. Therefore, a cut on the $H \to b\bar{b}$ C_2 window is applied. While it does not improve the purity as much as a fixed cut on the W_{had} mass in the boosted topology, it also does not decrease the signal purity in more split-boosted topologies such that an overall improvement of the signal sensitivity is achieved.

5.6. Control Regions

Although MC simulations of various physics processes work quite well, processes with non-prompt leptons cannot be modelled well due to higher order effects resulting in such non-prompt leptons. Therefore, most analyses estimate the non-prompt lepton background in a data driven approach. The data in at least one control region (CR)

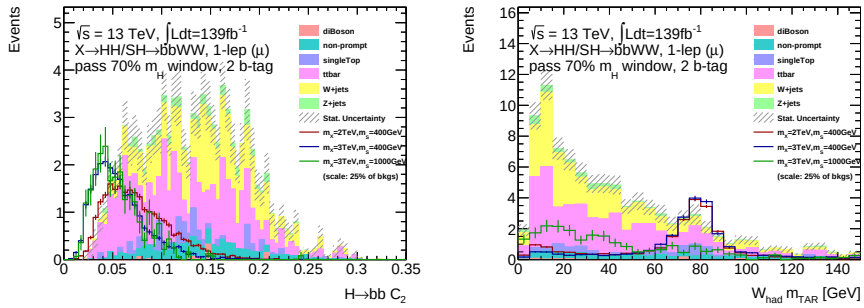

(a) $H \to b\bar{b}$ C_2 **(b)** W_{had} mass

Figure 5.18.: Distributions of the candidate variables for optimising the selection of SH production in SRp2. The signal yield is scaled to match 25% of the sum of backgrounds.

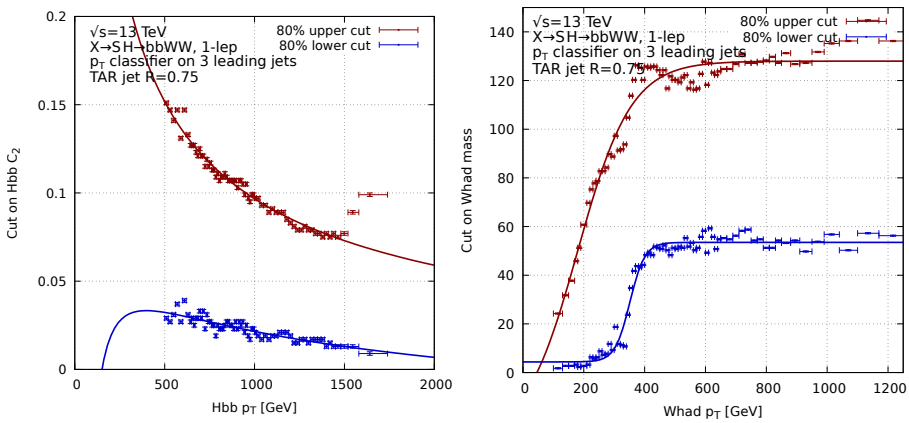

(a) $H \to b\bar{b}$ C_2 **(b)** W_{had} mass

Figure 5.19.: Selection windows on $H \to b\bar{b}$ C_2 depending on $p_{\text{T}}^{H\to b\bar{b}}$ and on W_{had} mass depending on $p_{\text{T}}^{W_{\text{had}}}$ yielding 80% signal efficiency in all three signal regions combined.

enriched in non-prompt lepton events is used to draw conclusions on the non-prompt lepton contribution in the signal and validation regions. Several methods have been developed in ATLAS, and the one used in this analysis is described and evaluated in Section 5.7.

Despite prompt lepton MC simulation being relatively well modelled, the unique phase space that is investigated in this analysis requires an independent estimate of the normalisation and the composition of backgrounds. The shape of distributions using simulated events is assumed to be well modelled. This independent estimate can be determined by fitting the simulated background events to data in dedicated control regions where the number of events of the background process of interest is enhanced. In this analysis,

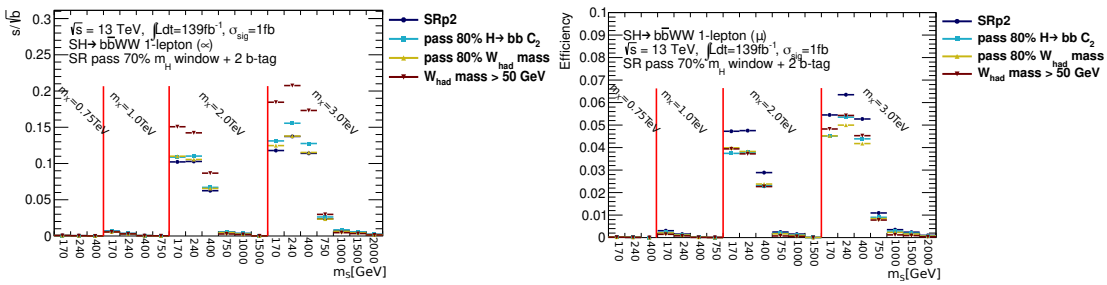

(a) signal purity **(b)** signal efficiency

Figure 5.20.: Purity and efficiency of the considered optimisation options for the full range of SH production mass points. The expected signal cross section is set to 1 fb for all mass points.

only prompt lepton $t\bar{t}$ and prompt lepton W+jets normalisations are determined in this manner since they contribute $> 85\%$ of the backgrounds in the signal regions.

Since non-prompt lepton events at hadron colliders are generally dominated by multijet production from strong interactions (QCD), a control region to estimate the non-prompt lepton background is constructed to maximise the contribution of multijet events.

In total, three control regions, namely $t\bar{t}$ CR, W+jets CR and QCD CR, are constructed. It is important to note that each control region is orthogonal to the signal region and also to the other control regions. In addition, the signal contribution in these control regions should be small to avoid the inclusion of potentially interesting data.

Based on the topological differences between the three considered backgrounds whose topologies are sketched in Figure 5.21, and the signal, the following quantities have been investigated, with the corresponding distributions displayed in Figure 5.22.

- **number of b-tagged TAR jets in the event:** for $t\bar{t}$ events, two b-tagged TAR jets are expected, while for multijet and W+jets events, no b-tagged TAR jets should occur in the event. The signal in contrast only has one b-tagged TAR jet in the event.

- **$m_{\mathrm{TAR}}^{H\to b\bar{b}}$ and $m_{\mathrm{TAR}}^{W_{\mathrm{had}}}$:** these variables can be used to reduce the signal contribution in the control regions. The $H \to b\bar{b}$ candidates for multijet and W+jets events are mostly single quark jets which correspond to very low masses outside the derived m_H window. Depending on the boost, the $H \to b\bar{b}$ candidate in case of $t\bar{t}$ events generally contains all or most decay products of the hadronically decaying top quark, resulting in a broad mass range which also includes the derived m_H window. Therefore, in the $t\bar{t}$ CR, the mass of the W_{had} candidate is considered instead. Since the W_{had} candidate is defined to be the TAR jet closest to the lepton, this is the jet initiated by the b quark for a top quark that decays leptonically ($t \to b\ell\nu$) and consequently corresponds to a small mass. The signal process features a broad spectrum with the tendency to higher masses due to the on-shell and off-shell nature of the W boson.

- $\boldsymbol{m_{\mathrm{T}}^{W_{\mathrm{lep}}}}$**:** to differentiate between QCD and W+jets backgrounds, the transverse mass of the lepton combined with the missing transverse energy of the event is used. For the W+jets background, this refers to the leptonically decaying W boson in contrast to QCD processes where this is a simply falling distribution.

The optimised cuts to define the $t\bar{t}$ CR, W+jets CR and QCD CR are summarised in Table 5.2.

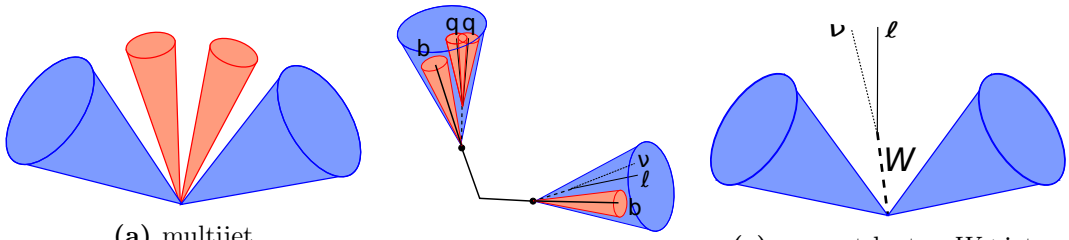

(a) multijet **(b)** prompt lepton $t\bar{t}$ **(c)** prompt lepton W+jets

Figure 5.21.: Sketch of the backgrounds for which a control region is to be defined. Multijet is picked as an example for non-prompt lepton background. Red cones denote jets with a small size parameter $R \leq 0.4$ and blue cones jets with a large size parameter $R \geq 0.75$.

control region	Cuts
$t\bar{t}$	2 b-tagged TAR jets in the event, $m_{\mathrm{TAR}}^{W_{\mathrm{had}}} < 20\,\mathrm{GeV}$
W+jets	0 b-tagged TAR jets in the event, $H \to b\bar{b}$ candidate fails 70% m_H window, 60 GeV $< m_T^{W_{\mathrm{lep}}} <$ 120 GeV
QCD	0 b-tagged TAR jets in the event, $H \to b\bar{b}$ candidate fails 70% m_H window, $m_T^{W_{\mathrm{lep}}} <$ 60 GeV or $m_T^{W_{\mathrm{lep}}} >$ 120 GeV

Table 5.2.: Chosen cuts for control region definitions. All regions pass the preselection.

Figure 5.23 shows which backgrounds contribute to the individual control regions in the muon channel. While the $t\bar{t}$ CR and W+jets CR are dominated by the respective desired background, the QCD CR is dominated by prompt lepton W+jets (60% compared to 14% of the total estimated non-prompt lepton background using the method described in Section 5.7) which is caused by the considered phase space, where a well identified and isolated muon very close or even inside a TAR jet is required. Additional cuts have been tried but have not been implemented to preserve enough events in this control region.

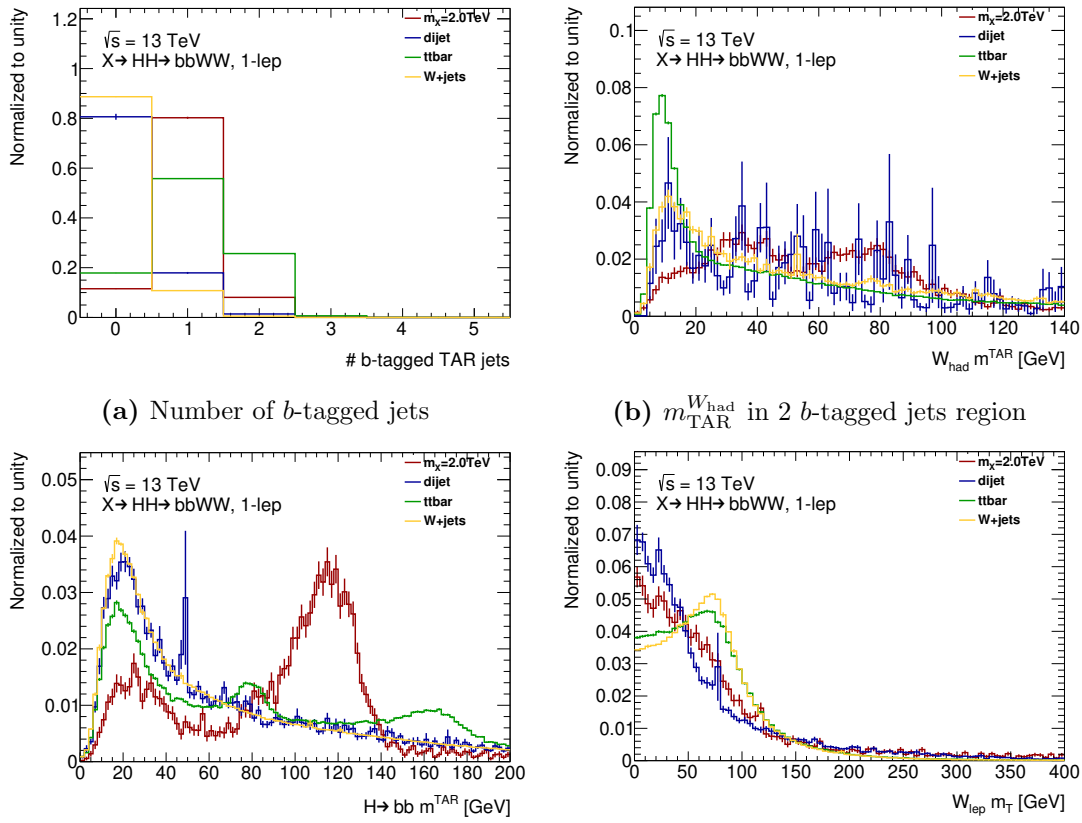

(a) Number of b-tagged jets

(b) $m_{\mathrm{TAR}}^{W_{\mathrm{had}}}$ in 2 b-tagged jets region

(c) $m_{\mathrm{TAR}}^{H\to b\bar{b}}$ in 0 b-tagged jets region

(d) $m_{\mathrm{T}}^{W_{\mathrm{lep}}}$ in 0 b-tagged jets region

Figure 5.22.: Distributions of variables considered in for the control region definition. The preselection is applied. The non-prompt lepton contribution is approximated by simulated dijet events without applying the lepton truth matching criterion. It should not be taken as an exact non-prompt lepton estimate but as a guideline.

5.7. Non-Prompt Lepton Background Estimate

While backgrounds with prompt leptons can be simulated well with Monte Carlo generators, it is difficult to accurately simulate the non-prompt lepton background which includes multijet events as well as all-hadronic final states, for example in $t\bar{t}$ or W+jets events. Therefore, a data driven approach called matrix method [302] is used to estimate the non-prompt lepton background. The basic idea is to use loose and tight lepton definitions. The number of such tight leptons (N_T) and loose not tight leptons (N_{LnT}) can be described by

$$\begin{pmatrix} N_T \\ N_{LnT} \end{pmatrix} = \begin{pmatrix} \epsilon & f \\ 1-\epsilon & 1-f \end{pmatrix} \begin{pmatrix} N_{\text{prompt}} \\ N_{\text{non-prompt}} \end{pmatrix}. \tag{5.4}$$

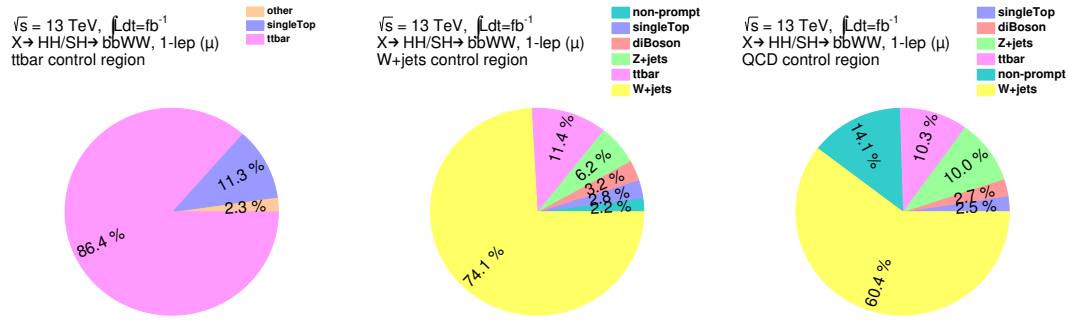

(a) $t\bar{t}$ CR **(b)** W+jets CR **(c)** QCD CR

Figure 5.23.: Composition of the expected backgrounds in the individual control regions after correcting the normalisation (see Section 5.8). The non-prompt background is estimated with the method described in Section 5.7. If these backgrounds contribute less than 2%, they are collected in the "other" category.

Here, N_{prompt} is the number of prompt leptons and $N_{\text{non-prompt}}$ is the number of non-prompt leptons. Loose prompt leptons have an efficiency ϵ to also pass the tight requirement while loose non-prompt leptons have a fake efficiency f to pass the tight lepton selection. The definition of loose and tight selections of muons in the analysis based on ID and isolation requirements can be found in Table 5.3. Therefore, any selection of events that favours leptons with an ID or isolation stricter than the loose lepton selection such as single lepton triggers biases the estimate.

Selection	ID	isolation
Loose	loose	-
Tight	medium	TightTrackOnly

Table 5.3.: Requirements on loose and tight muons used in the non-prompt lepton estimate by the matrix method.

Inverting the matrix in Eq. 5.4 gives rise to the number of tight non-prompt leptons via

$$\begin{aligned} N_{T,\text{non-prompt}} &= f \cdot N_{\text{non-prompt}} \\ &= f\frac{\epsilon - 1}{\epsilon + f} N_T + f\frac{\epsilon}{\epsilon + f} N_{LnT}. \end{aligned} \tag{5.5}$$

This yields fake weights w_i for each lepton i

$$w_i = \begin{cases} f\frac{\epsilon-1}{\epsilon+f} & \text{if lepton is tight} \\ f\frac{\epsilon}{\epsilon+f} & \text{if lepton is loose and not tight} \end{cases}. \tag{5.6}$$

When these weights are applied to all loose leptons in data, it results in an estimate on the non-prompt lepton background events. The corresponding statistical uncertainty on $N_{T,\text{non-prompt}}$ can be expressed as

$$\sigma_{N_{T,\text{non-prompt}}} = \sqrt{\sum_i w_i^2}. \tag{5.7}$$

These weights can then be stored and used to create distributions of any variable in the non-prompt lepton background. In the case of multi-lepton events, the weight is calculated for each lepton in the event and then stored in conjunction with the lepton.

To obtain an accurate description of the non-prompt lepton background distributions in all variables, it is necessary that f and ϵ are binned in variables that sufficiently describe the kinematics of the lepton.

The efficiencies for prompt leptons are estimated from simulated prompt lepton background processes in the combined signal regions. This explicitly excludes the signal from this background estimate. To ensure that the prompt lepton events do not contain any contribution from non-prompt lepton events, the lepton under consideration is required to be matched to the true prompt lepton in the event. The fake efficiency of non-prompt leptons is determined from data in the QCD CR, from which the corrected prompt lepton background contribution is subtracted (see Section 5.8). In certain bins, the efficiency can be negative since the number of expected prompt lepton MC events can be larger than the observed data events due to statistical fluctuations or potential mismodelling in the simulation. In such cases the efficiency is manually set to zero to avoid unphysical effects.

For the non-prompt muon background, dependencies on the muon p_{T} and the ΔR of the muon to the closest TAR jet have been observed. There are also small dependencies on the η and isolation of the muon, but due to the small number of events in the considered phase space, a binning of the efficiencies in two variables is considered to be sufficient. This takes into account the fact that the non-prompt lepton background is relatively small compared to W+jets and $t\bar{t}$ backgrounds. To reduce the dependence on statistical fluctuations, a binning is chosen such that the relative statistical uncertainty is below 15% in each bin.

The final efficiencies as a function of the muon p_{T} and ΔR between the muon and the closest jet are depicted in Figure 5.24. As can be seen, the prompt efficiencies are consistently very close to $\epsilon = 1$ except for a few bins, where the ΔR and the p_{T} are small. The fake efficiencies are significantly lower ($f \leq 0.1$), supporting the assumption, that the investigated phase space is really dominated by prompt lepton backgrounds when applying the tight lepton selection. Loosening the muon ID, and more importantly the isolation, results in a steep increase in the number of non-prompt leptons. Since the non-prompt lepton background is comparably small with respect to $t\bar{t}$ or W+jets backgrounds, it was decided to assign very conservative uncertainties with regards to the assumptions made in this background estimate (see Section 6.3).

The modelling of the obtained non-prompt background estimate is checked in Section 5.10 in the validation as well as in Appendix A.6 in the different control regions for

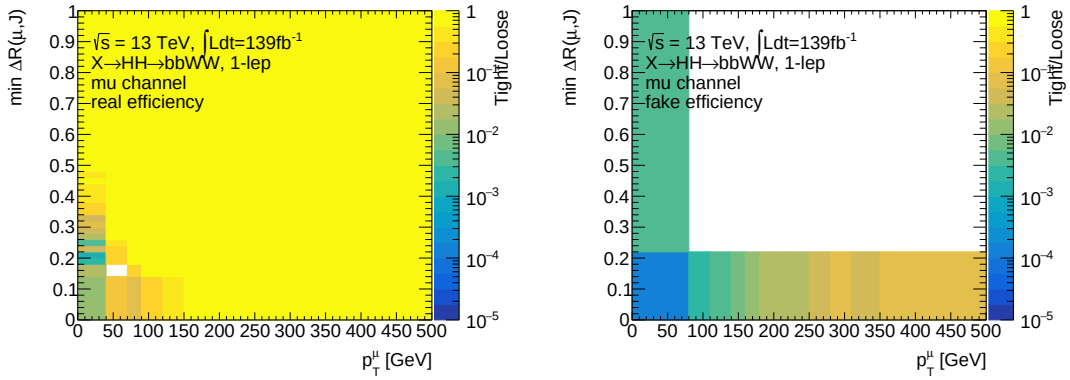

(a) ϵ **(b)** f

Figure 5.24.: Efficiency ϵ and fake efficiency f for the muon channel binned in p_{T} of the muon and the ΔR between the muon and the closest TAR jet where the relative statistical uncertainty in each bin must be smaller than 15%. The white space corresponds to efficiencies equal to zero.

selected variables.

5.8. Normalisation factors

Figures 5.25 (a)–(c) show the number of expected and observed events in the three control regions. It is evident that the sum of expected prompt lepton backgrounds overestimates the data in all three control regions.

Since the non-prompt lepton background is estimated in a data driven way in the QCD CR (see Section 5.7), prompt lepton background events are subtracted from data. This often results in negative event yields for the non-prompt lepton background which are unphysical. Therefore, it is necessary to correct the normalisation of the prompt lepton backgrounds. Given that $t\bar{t}$ and W+jets are the most dominant backgrounds, these two background yields are corrected by normalisation factors (NFs). On the other hand, the correct NFs can only be obtained with a valid non-prompt lepton background estimate. In order to resolve the dependencies, the NFs are obtained in an iterative procedure.

In the first step, only NFs for the $t\bar{t}$ ($\mathrm{NF}_{t\bar{t}}$) and W+jets ($\mathrm{NF}_{W+\mathrm{jets}}$) background contributions are calculated. Instead of the valid data driven non-prompt lepton estimate, simulated dijet events are used as an approximation for the non-prompt lepton background contribution. Since the dijet simulation is known to not be accurate, its normalisation is kept as a free floating parameter as well but will not be used in the analysis later on.

Then, the non-prompt lepton background contribution is estimated as described in Section 5.7, where the prompt lepton $t\bar{t}$ and W+jets background contributions are corrected by the obtained NFs.

In the second iteration, the NFs for the $t\bar{t}$ and W+jets background contributions

are recalculated using the valid non-prompt lepton background estimate whose normalisation is also kept as a free parameter ($\mathrm{NF}_{\text{non-prompt}}$). This allows corrections on the approximation of the non-prompt lepton background by simulated dijet events in the previous iteration.

In both cases, the NFs are obtained by simultaneously fitting the sum of expected background events to the data yield using a single bin containing all events in each of the three control regions: $t\bar{t}$ CR, W+jets CR and QCD CR, respectively. Applying this correction, the agreement between observed and expected background events is established in all three control regions as shown in Figures 5.25 (d)–(f).

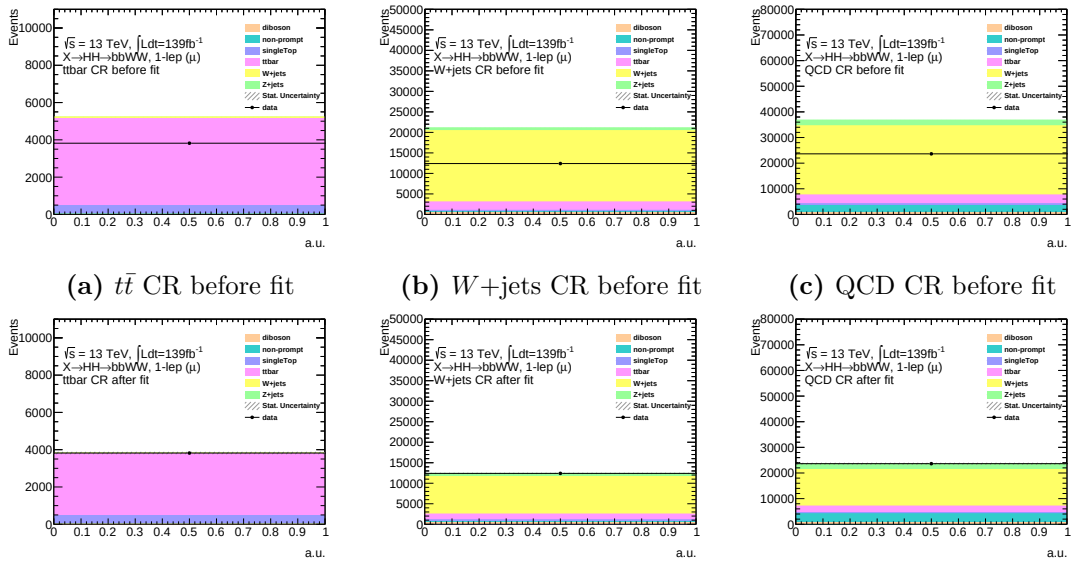

(a) $t\bar{t}$ CR before fit **(b)** W+jets CR before fit **(c)** QCD CR before fit

(d) $t\bar{t}$ CR after fit **(e)** W+jets CR after fit **(f)** QCD CR after fit

Figure 5.25.: Number of background events split into the different backgrounds in the $t\bar{t}$ CR, W+jets CR and QCD CR before and after performing the background normalisation fits. These plots correspond to the second iteration where the data driven non-prompt lepton estimate is included in the backgrounds [26].

The resulting NFs for both iterations are summarised in Table 5.4. While $\mathrm{NF}_{t\bar{t}}$ stays constant within the uncertainty between the two iterations, the $\mathrm{NF}_{W+\text{jets}}$ rises slightly from 0.48 in the first iteration to 0.53 in the second iteration. The second iteration includes the non-prompt lepton estimate where the NF was determined to be $\mathrm{NF}_{\text{non-prompt}} = 1.18$. This is the only NF to have a value larger than unity. The reason for the change in $\mathrm{NF}_{W+\text{jets}}$ can be understood from the anti-correlation between the NFs of the W+jets and dijet or non-prompt lepton backgrounds, respectively. This is visible in the correlation matrix displayed in Figure 5.26. The $t\bar{t}$ CR is nearly only populated by $t\bar{t}$ events. This reduces the correlations to the other background normalisations. The large contribution of W+jets in the QCD CR, however, anti-correlates $\mathrm{NF}_{W+\text{jets}}$ strongly to $\mathrm{NF}_{\text{non-prompt}}$.

Iteration	$\mathrm{NF}_{t\bar{t}}$	$\mathrm{NF}_{W+\mathrm{jets}}$	$\mathrm{NF}_{\mathrm{dijet/non\text{-}prompt}}$
with dijet MC	0.72 ± 0.01	0.48 ± 0.01	0.67 ± 0.04
with non-prompt lepton estimate	0.71 ± 0.01	0.53 ± 0.01	1.18 ± 0.09

Table 5.4.: Normalisation factors of the $t\bar{t}$, W+jets and dijet or non-prompt backgrounds, respectively, obtained after the first and second iteration of the background normalisation fit [26, 301]. The NF for the dijet sample in the first iteration is only listed for completion and will not be used in the analysis.

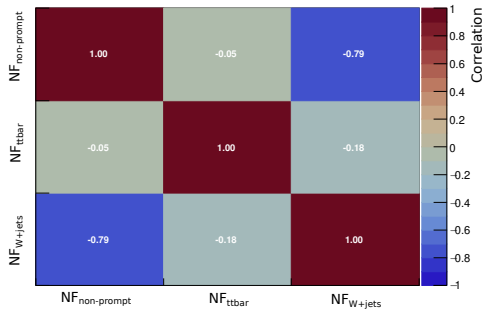

Figure 5.26.: Correlation matrix between all three NFs obtained from the background normalisation fit including the non-prompt lepton background [26, 301].

Additionally, number of observed data events and the event yields of all the background processes in the three control regions before (pre-fit) and after (post-fit) the background normalisation fit are given in Table 5.5. Since systematic uncertainties, or uncertainties on MC statistics are not included in the background normalisation fits at this stage, only the $t\bar{t}$, W+jets and non-prompt lepton backgrounds are allowed to vary and are assigned a finite uncertainty. The listed values confirm the designed closure between the observed data and the corrected number of expected background events.

5.9. Final Discriminant

Traditionally, analyses searching for resonant production of heavy particles use the invariant mass of all decay products as final discriminant since it allows a direct interpretation of the mass of the heavy particle.

In the boosted 1-lepton topology, the invariant mass is defined as

$$m^{HH/SH} = \sqrt{(p^{H\to b\bar{b}})^2 + (p^{W_{\mathrm{had}}})^2 + (p^{\ell})^2 + (p^{\nu})^2} \tag{5.8}$$

where p^i denotes the four vector of the respective object. Considering that the neutrino four vector and especially, the neutrino p_{z} cannot be reconstructed simply and results

Region	$t\bar{t}$ CR	W+jets CR	QCD CR
Observed events	3820	12404	23633
$\sum$ Pre-fit events	5224.6 ± 0.5	21134.7 ± 1.8	36817.7 ± 2.7
Pre-fit $t\bar{t}$ events	4673.8 ± 0.5	2003.01 ± 0.20	3434.83 ± 0.34
Pre-fit W+jets events	74.911 ± 0.007	17383.9 ± 1.7	26965.7 ± 2.7
Pre-fit diboson events	2.99 ± 0.00	396.11 ± 0.00	629.69 ± 0.00
Pre-fit single top events	434.11 ± 0.00	352.34 ± 0.00	587.06 ± 0.00
Pre-fit Z+jets events	11.26 ± 0.00	775.96 ± 0.00	2364.07 ± 0.00
Pre-fit non-prompt lepton events	27.5825 ± 0.0028	223.403 ± 0.022	2836.34 ± 0.28
$\sum$ Post-fit events	3820 ± 60	12400 ± 110	23630 ± 150
Post-fit $t\bar{t}$ events	3300 ± 60	1414 ± 26	2425 ± 46
Post-fit W+jets events	39.6 ± 0.6	9200 ± 130	14270 ± 200
Post-fit diboson events	2.99 ± 0.00	396.11 ± 0.00	629.69 ± 0.00
Post-fit single top events	434.11 ± 0.00	352.33 ± 0.00	587.06 ± 0.00
Post-fit Z+jets events	11.26 ± 0.00	775.96 ± 0.00	2364.07 ± 0.00
Post-fit non-prompt lepton events	32.7 ± 2.6	265 ± 21	3360 ± 260

Table 5.5.: The number of observed data events and event yields for the various background processes before and after the background normalisation fit in all three control regions. Since systematic uncertainties, or uncertainties on MC statistics are not included in the background normalisation fits at this stage, only the $t\bar{t}$, W+jets and non-prompt lepton backgrounds are assigned a finite uncertainty. [26, 301].

in a loss of 20% of signal events due to the invalidity of solutions, alternatives to the invariant mass are investigated.

The first alternative only uses the measured objects to calculate the invariant mass and does not consider the neutrino four vector at all:

$$m_{\text{vis}}^{HH/SH} = \sqrt{(p^{H\to b\bar{b}})^2 + (p^{W_{\text{had}}})^2 + (p^{\ell})^2} \tag{5.9}$$

and is therefore called visible mass. The second alternative is a compromise between the visible and the invariant mass by replacing the neutrino four vector by the $E_{\text{T}}^{\text{miss}}$ four vector $p^{\text{met}} = (E_{\text{T}}^{\text{miss}}, p_{\text{x}}^{\text{miss}}, p_{\text{y}}^{\text{miss}}, 0)$:

$$m_{\text{vis+met}}^{HH/SH} = \sqrt{(p^{H\to b\bar{b}})^2 + (p^{W_{\text{had}}})^2 + (p^{\ell})^2 + (p^{\text{met}})^2}. \tag{5.10}$$

This is consequently called visible+met mass. The last alternative is to use the transverse mass defined as

$$(m_{\text{T}}^{HH/SH}) = \sqrt{\left(\sum_i E_T^i\right)^2 - \left(\sum_i \vec{p}_T^{\,i}\right)^2}, \tag{5.11}$$

where i stands for all analysis objects of relevance, namely $H \to b\bar{b}$ candidate, W_{had} candidate, charged lepton and the neutrino where the transverse part of the neutrino corresponds to $E_{\text{T}}^{\text{miss}}$ and $\vec{p}_{\text{T}}^{\,\text{miss}}$.

The distributions of different mass definitions can be seen in Figure 5.27 for three HH mass points and the two dominant prompt lepton backgrounds in the SRp2 signal region. The standard definition of the invariant mass does indeed show the sharpest peaks for all three resonance masses. However, the visible+met mass yields a very good alternative where all mass peaks are shifted to slightly lower values than the m_X corresponding to the signal. Furthermore, the larger m_X is, the less signal is sharply peaked. Since the backgrounds peak at $m_{\text{vis+met}}^{HH/SH} \approx 1.3\,\text{TeV}$, and exhibit a falling spectrum for higher values of $m_{\text{vis+met}}^{(HH/SH)}$, the signal broadening for high m_X does not harm the signal sensitivity. Looking at the other two alternatives, m_{vis} and m_{T}, the distributions become significantly broader and are shifted to lower values due to their definition considering less energy of the event. Therefore, $m_{\text{vis+met}}$ is chosen as the final discriminant in the analysis.

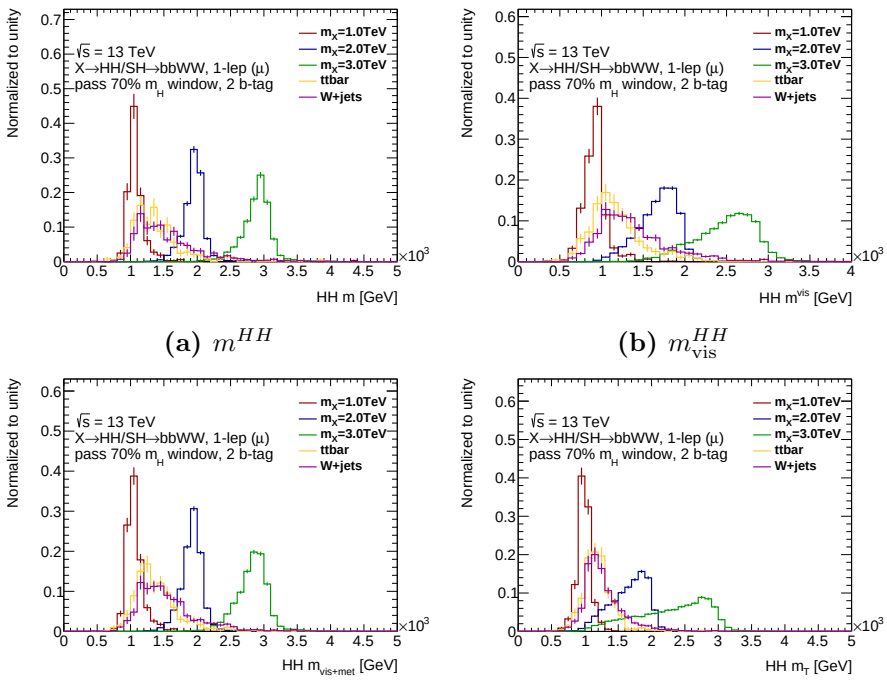

(a) m^{HH} (b) m_{vis}^{HH}

(c) $m_{\text{vis+met}}^{HH}$ (d) m_{T}^{HH}

Figure 5.27.: Options considered for the final discriminant in the boosted 1-lepton analysis in the SRp2 signal region.

Figure 5.28 shows the distribution of $m_{\text{vis+met}}$ in the all three signal regions for the prompt and non-prompt lepton backgrounds and selected signals. On the left-hand side, signals corresponding to the HH production are displayed and, thus, the HH selection is applied. In all three signal regions, three signal mass peaks are clearly visible corresponding to $m_X = 1$, 2 and 3 TeV, where the peaks in SRf1 (Figure 5.28 (a)), are broader compared to the other signal regions. Furthermore, the background composition

is different in this region, such that the shape of the background differs and features a longer tail to high $m_{\text{vis+met}}$ values.

On the right-hand side, signal distributions corresponding to SH production are displayed and consequently the SH selection is applied to the three signal regions. The background behaviour basically remains the same with respect to the HH selection except for the number of background events approximately doubling. For the signal mass points shown, only two clean mass peaks corresponding to $m_X = 2$ and 3 TeVwith $m_S = 400$ GeV can be seen in all three signal regions. The last signal peak corresponding to $m_X = 3$ TeV with $m_S = 1$ TeV is also present but smeared out. This is due to the misclassification of the W_{had} candidate coming from the transition to the split-boosted topology, resulting in incorrectly reconstructed SH systems. Nevertheless, the variable's separation power is still present, allowing it to play the role of the final discriminant.

5.10. Background Modelling

In this section, the modelling of distributions of selected variables characterising the boosted 1-lepton analysis validation region are discussed. The discussion with regards to the modelling in the control regions can be found in Appendix A.6.

The variables of interest are:

- $\boldsymbol{p_{\mathrm{T}}}$ of the lepton,
- $\boldsymbol{E_{\mathrm{T}}^{\mathrm{miss}}}$ (an approximate measure of the neutrino p_{T}),
- $\boldsymbol{m_{\mathrm{TAR}}}$ of the $H \to b\bar{b}$ candidate,
- $\boldsymbol{\Delta R(W_{\mathrm{had}}, \ell)}$ defining the boosted phase space,
- $\boldsymbol{m_{\mathrm{vis+met}}}$ of the reconstructed HH or SH system, respectively. As final discriminant, it is probably the most important variable in this analysis.

A more extensive list of variables can be found in Section A.7.

The backgrounds consist of simulated prompt lepton events as well as the estimated non-prompt lepton contribution. The normalisations of the dominant prompt lepton backgrounds, $t\bar{t}$ and W+jets, as well as of the non-prompt lepton background are corrected. Since this correction is done by fitting the expected background yields to the observed data in all three control regions simultaneously, this does not correct any shape mismodelling.

The aforementioned variables are displayed in VRf1 with the SH selection (a) and the HH selection (b) applied in each of Figures 5.29–5.33. Due to the selection definitions, the validation region with the HH selection applied contains fewer events, and thus exhibits larger statistical uncertainties. Despite the backgrounds being corrected in their normalisation, the expected number of events is underestimated by around 5% on average when the SH selection is applied to the validation region. This discrepancy is reduced if the HH selection is applied. Given the currently estimated size of the

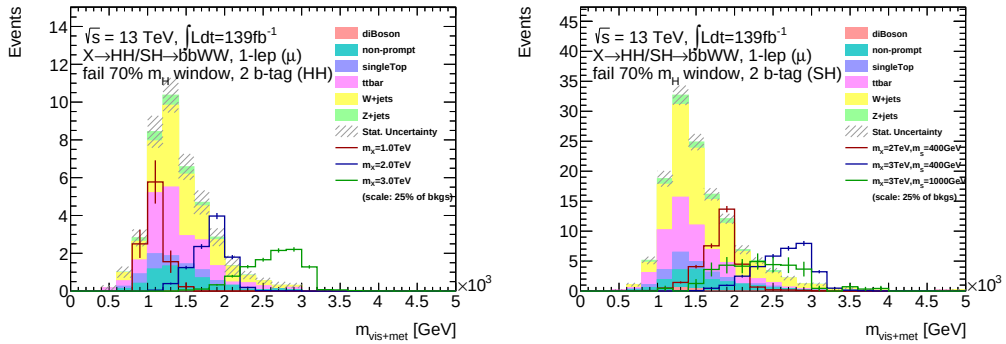

(a) SRf2, HH selection

(b) SRf2, SH selection

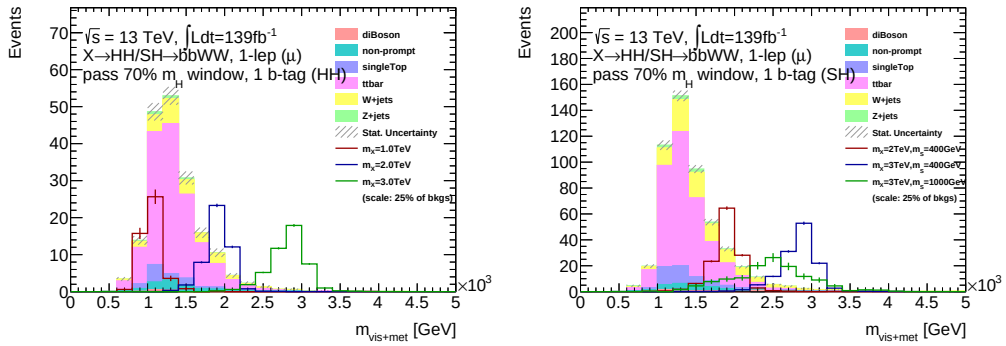

(c) SRp1, HH selection

(d) SRp1, SH selection

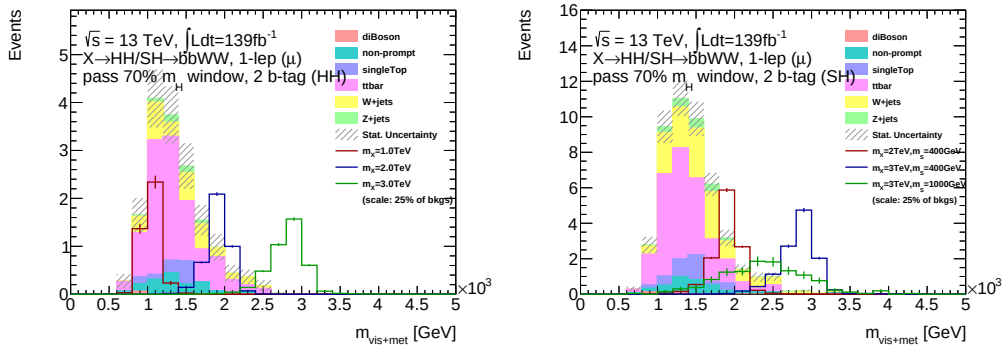

(e) SRp2, HH selection

(f) SRp2, SH selection

Figure 5.28.: Distribution of the final discriminant $m_{\text{vis+met}}$ in the three signal regions with HH selection (top) and SH selection (bottom) applied. The non-prompt background shown is estimated by the method described in Section 5.7. The signal is scaled to match 25% of the sum of backgrounds.

systematic uncertainties, which does not take correlations into account, this inaccuracy in the normalisation is covered by these (see Chapter 6).

The distributions of the lepton p_{T} in Figure 5.29 (a) and of the $E_{\text{T}}^{\text{miss}}$ in Figure 5.30 (a)

exhibit that for low values, there is an excess of data over the expected background events. For higher values, the data match the expected backgrounds well within statistical uncertainties not taking the normalisation offset into account. The effect is larger in the $E_{\mathrm{T}}^{\mathrm{miss}}$ distribution. However, applying the HH selection (Figures 5.29 (b) and 5.30), not only the normalisation offset vanishes, but also shape discrepancies are significantly reduced compared to the SH selection.

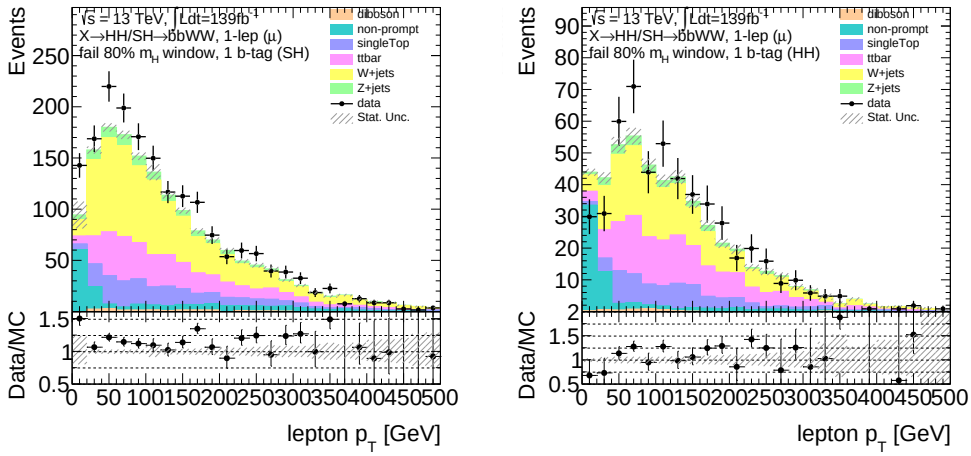

(a) SH selection **(b)** HH selection

Figure 5.29.: Distribution of p_{T}^{ℓ} in VRf1 with applying the SH or HH selection. The normalisation of the backgrounds is corrected.

Despite the offset, the distribution of the mass of the $H \to b\bar{b}$ candidate (Figure 5.31) does not show any differences between the estimate and the data that is not already covered by the statistical uncertainty.

Since $\Delta R(W_{\mathrm{had}}, \ell)$ is used in the definition of the HH selection, the shape of the $\Delta R(W_{\mathrm{had}}, \ell)$ distributions shown in Figure 5.32 differs significantly between the SH and HH selections. This difference also explains why the normalisation offset and mismodelling nearly vanishes in the HH selection. A significant part of the non-prompt lepton background contributes to the lowest bin of the distribution. This is cut away in the HH selection, reducing the mismodelling caused by this background. Furthermore, in the validation regions with the SH selection applied, the underestimation of the backgrounds is caused by the region $\Delta R(W_{\mathrm{had}}, \ell) > 0.35$. This is also cut away to a large part in the HH selection, and thus removes the normalisation offset. In the region $0.45 < \Delta R(W_{\mathrm{had}}, \ell) < 0.7$, the estimated background yield is smaller than the observed data. Since the background estimate features a smooth distribution, it is possible that this simply corresponds to an upward fluctuation in data.

In the final discriminant displayed in Figure 5.33, there is a clear mismodelling present in the validation region with the SH selection applied. For $m_{\mathrm{vis+met}} \lesssim 1.5\,\mathrm{GeV}$, the background underestimates the data, while in the tail of the distribution the background

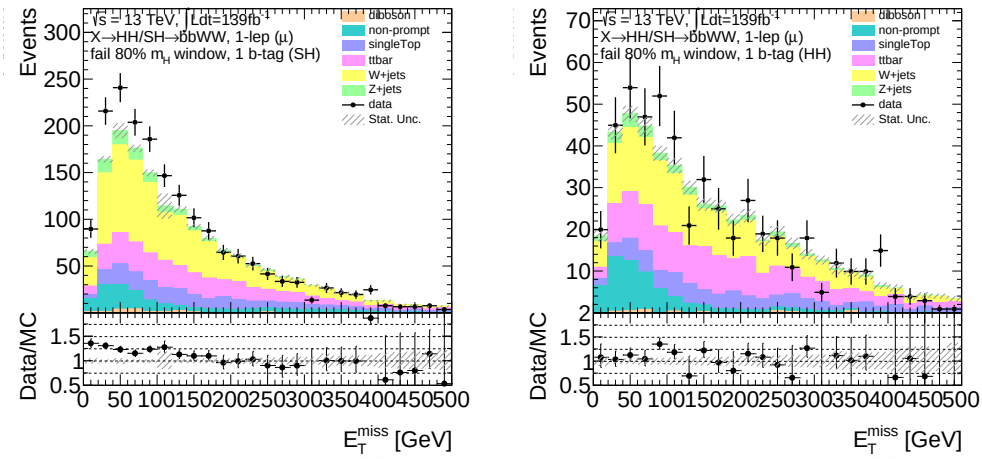

(a) SH selection **(b)** HH selection

Figure 5.30.: Distribution of $E_{\mathrm{T}}^{\mathrm{miss}}$ in VRf1 with applying the SH or HH selection. The normalisation of the backgrounds is corrected.

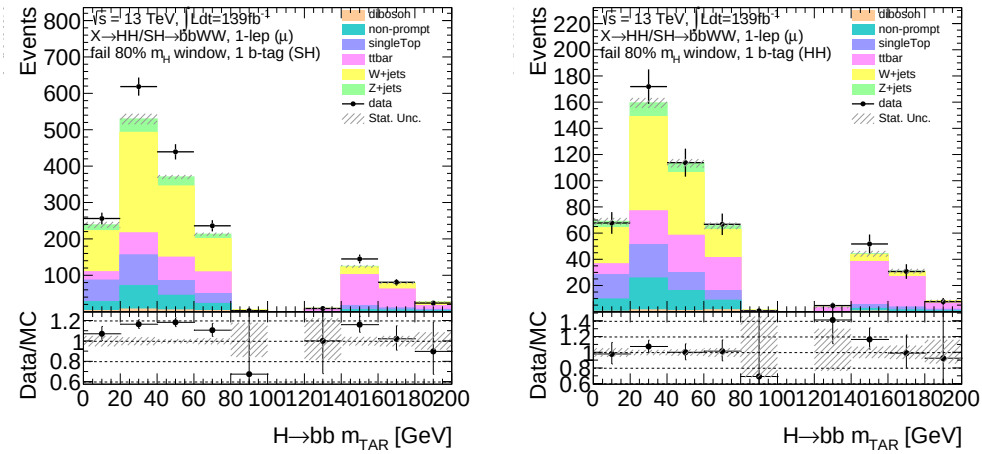

(a) SH selection **(b)** HH selection

Figure 5.31.: Distribution of $m_{\mathrm{TAR}}^{H\to b\bar{b}}$ in VRf1 with applying the SH or HH selection. The normalisation of the backgrounds is corrected.

overestimates the observed data. This is related to the W+jets background where the modelling of events in which the lepton is produced collinear to a jet is known to be inaccurate.

For the HH selection, the mismodelling in the tail of the $m_{\mathrm{vis+met}}$ distribution nearly vanishes due the the reduced W+jets contribution and is now consistent with the background prediction within statistical uncertainties. Only one bin at $m_{\mathrm{vis+met}} = 900\,\mathrm{GeV}$

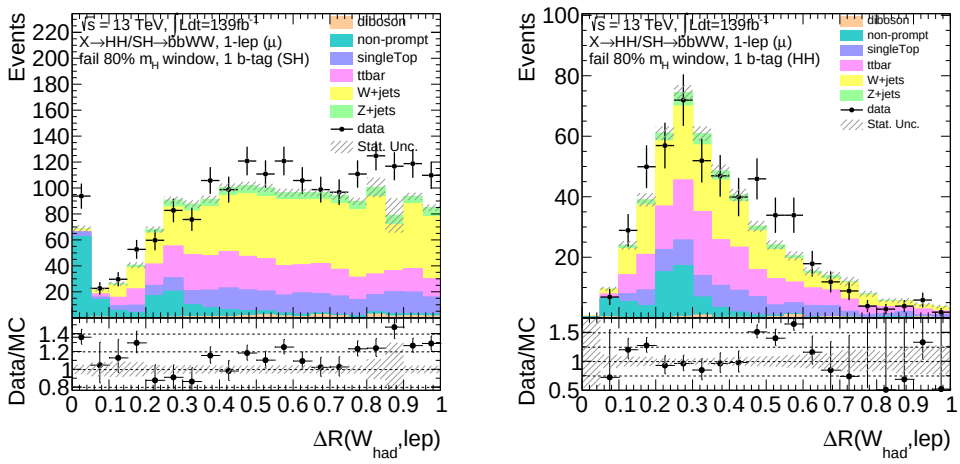

(a) *SH* selection **(b)** *HH* selection

Figure 5.32.: Distribution of $\Delta R(W_{\text{had}}, \ell)$ in VRf1 with applying the *SH* or *HH* selection. The normalisation of the backgrounds is corrected.

features an underestimation of background. This might correspond to the three underestimated bins in the $\Delta R(W_{\text{had}}, \ell)$ distribution. Based on the estimated approximate impact of the systematic uncertainties in Chapter 6, the remaining discrepancies will be well covered.

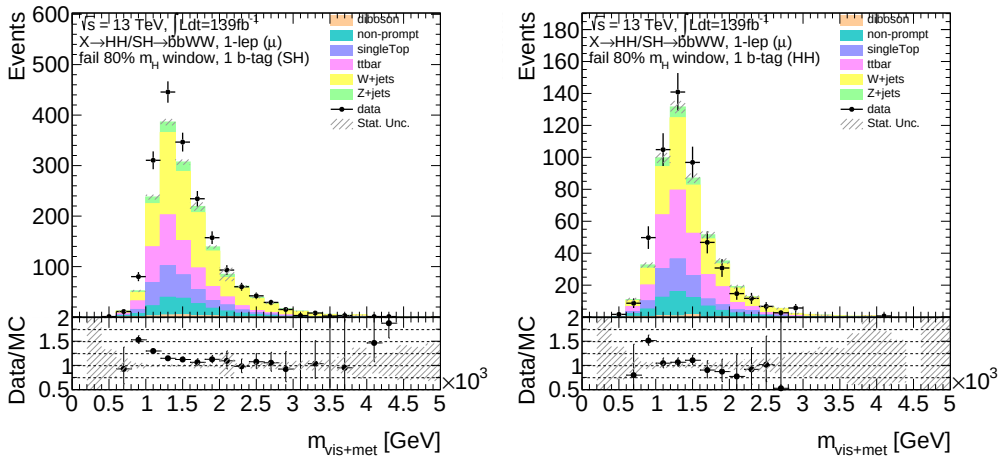

(a) *SH* selection **(b)** *HH* selection

Figure 5.33.: Distribution of $m_{\text{vis+met}}$ in VRf1 with applying the *SH* or *HH* selection. The normalisation of the backgrounds is corrected.

All in all, the modelling especially when applying the *HH* selection is sufficient con-

sidering that only statistical uncertainties are shown in this section. The mismodelling observed when applying the SH selection originates from the W+jets modelling which is known to be inaccurate. All other prompt lepton backgrounds and in particular the $t\bar{t}$ background are modelled well as can be also seen in the comparison between expected and observed events in the control regions in Appendix A.6. The non-prompt background estimate is also sufficiently well described considering its strong dependence on the W+jets background. The remaining differences between data and expected backgrounds will be covered by closure uncertainties on the W+jets background but also on the non-prompt lepton background estimate (see Sections 6.2 and 6.3).

CHAPTER 6

Systematic Uncertainties

In addition to the statistical uncertainties on the individual simulated signal and background processes, systematic uncertainties also need to be taken into account when interpreting the obtained results. These uncertainties are represented by nuisance parameters which account for systematic variations of different origins. These nuisance parameters are then fed through the statistical analysis as discussed in Chapter 7 to be taken into account in the final limit setting. The comparisons between the nominal and varied samples are done in the context of the final discriminant $m_{\text{vis+met}}$.

In this analysis, three categories of systematic uncertainties are discussed.

- The first category is presented in Section 6.1 and summarises uncertainties caused by imperfections of the experiment in simulation. It includes uncertainties on the reconstruction of the various objects but also on the luminosity measurement, for example.
- In the second category, theoretical uncertainties on the simulation, also known as modelling uncertainties, are discussed (see Section 6.2). These account for the assumptions and approximations made in the matrix element calculation and parton shower algorithm such as the used parton distribution function and the amount of initial and final state radiation.
- The third and final category considered in this analysis describes the uncertainties of the non-prompt lepton background estimate in Section 6.3. Due to the data driven approach, this background is treated in a special manner and includes uncertainties regarding possible selection biases and the validity of the used method.

Due to technical difficulties, it has not been possible to evaluate the size of all systematic uncertainties for every single signal and background process at the time of writing this thesis. However, a detailed investigation on their effect has been carried out on a

selected number of HH signal mass points and the dominant prompt lepton backgrounds of $t\bar{t}$ and W+jets processes. For the experimental uncertainties, only the $t\bar{t}$ background with reduced statistics corresponding to 0.7% of the full statistics has been available.

6.1. Experimental Uncertainties

Experimental uncertainties refer to all uncertainties based upon detector measurements. This includes the luminosity measurements but also energy and position measurements which are then used in track, cluster, and object reconstruction. Uncertainties on algorithms such as b-tagging are also classified under experimental uncertainties. All these uncertainties are associated to nuisance parameters that are used in the calculation of the likelihood (see Section 7.1). Generally, the nuisance parameters vary the nominal value by one standard deviation up (up variation) and by one standard deviation down (down variation).

Except for the luminosity variation which is a normalisation uncertainty, all other variations are considered as combined normalisation and shape uncertainty on the $m_{\text{vis+met}}$ distribution as final discriminant. Without performing the whole chain of statistical tests as described in Chapter 7, the impact of the nuisance parameter is quantified by comparing the nominal to the systematically varied $m_{\text{vis+met}}$ distribution and building the average absolute relative difference

$$\delta^{\text{avg}} = \frac{1}{n_{\text{bins}}} \sum_{i=1}^{n_{\text{bins}}} \left| \frac{n_{\text{var}}^{(i)} - n_{\text{nom}}^{(i)}}{n_{\text{nom}}^{(i)}} \right|, \tag{6.1}$$

where n_{bins} refers to the number of bins in the $m_{\text{vis+met}}$ distribution and $n_{\text{var}}^{(i)}$ and $n_{\text{nom}}^{(i)}$ refer to the yields of the varied and nominal distribution in bin i, respectively. Another measure is the maximum absolute relative difference defined as

$$\delta^{\text{max}} = \max_{i \in \text{bins}} \left(\left| \frac{n_{\text{var}}^{(i)} - n_{\text{nom}}^{(i)}}{n_{\text{nom}}^{(i)}} \right| \right). \tag{6.2}$$

The difference between δ^{avg} and δ^{max} indicates whether the deviations between the nominal and varied distribution is at a constant level (small difference) or fluctuating (large difference) across bins.

A summary of the ten most dominant uncertainties is given in Table 6.1 for two selected HH signal mass points in SRp2 and the $t\bar{t}$ background in the $t\bar{t}$ CR. The full list of nuisance parameters and their impact on the $m_{\text{vis+met}}$ distribution for signals and backgrounds in the different regions can be found in Appendix A.8.

In general, the dominant nuisance parameters correspond to the jet energy resolution (JER) and the jet energy scale (JES) explained in more detail in Section 6.1.5. For the signal process, the uncertainties on the muon resolution in the Inner Detector and Muon Spectrometer are also non-negligible. It is noteworthy that the impact in terms of δ^{avg} on the $m_X = 2\,\text{TeV}$ signal is smaller by a factor of three compared to the $m_X = 4\,\text{TeV}$

signal overall. Therefore, only the $m_X = 4\,\text{TeV}$ mass point is considered in the rest of this section since it gives an idea on the maximum systematic uncertainty of the signal. Furthermore, $\delta^{\text{max}} \gg \delta^{\text{avg}}$ in all cases, indicating that statistical fluctuations are present.

ranking	nuisance parameter	δ^{avg}	δ^{max}
1	JER (effective 2)	3.14%	256%
2	JER (effective 3)	2.92%	220%
3	JER (effective 1)	2.86%	169%
4	JER (effective 4)	2.63%	96%
5	μ resolution (Muon Spectrometer)	2.17%	34%
6	μ resolution (Inner Detector)	1.69%	29%
7	JER (effective 5)	1.34%	104%
8	JER (effective 6)	1.31%	77%
9	JES (AFII)	1.02%	31%
10	JES (flavour response)	0.75%	65%

(a) $m_X = 2.0\,\text{TeV}$

ranking	nuisance parameter	δ^{avg}	δ^{max}
1	JER (effective 3)	10.66%	245%
2	JER (effective 2)	10.66%	218%
3	μ resolution (Muon Spectrometer)	10.36%	78%
4	JER (effective 1)	10.27%	186%
5	JER (effective 5)	8.72%	213%
6	JER (effective 6)	8.57%	117%
7	μ resolution (Inner Detector)	7.99%	57%
8	JER (effective 4)	6.42%	227%
9	μ residual bias	5.95%	91%
10	JES (mixed 1)	4.66%	112%

(b) $m_X = 4.0\,\text{TeV}$

ranking	nuisance parameter	δ^{avg}	δ^{max}
1	JER (effective 2)	5.81%	4411%
2	JER (effective 3)	5.33%	3218%
3	JER (effective 6)	4.78%	3958%
4	JER (effective 1)	4.77%	3884%
5	JER (effective 4)	4.52%	3219%
6	JER (effective 5)	4.29%	2063%
7	JES (mixed 1)	0.85%	1039%
8	JES (flavour composition)	0.69%	680%
9	JES (flavour response)	0.66%	1136%
10	JES (pileup ρ)	0.60%	628%

(c) $t\bar{t}$

Table 6.1.: Summary of the ten leading nuisance parameters based their δ^{avg} impact on $m_{\text{vis+met}}$ of two HH signal mass points evaluated in SRp2 with the HH selection applied and the $t\bar{t}$ background evaluated in the $t\bar{t}$ CR.

6.1.1. Luminosity

The luminosity measurement as discussed in Section 4.3 yields an uncertainty of 1.7% [261, 262], affecting only the normalisation of the samples in a fully correlated way.

The pileup profile of the simulated events as discussed in Section 3.3 is reweighted to match the profile observed in data, introducing additional uncertainties [303]. These are combined into a single nuisance parameter which is propagated to the final results. This nuisance parameter does not show any deviation compared to the nominal distribution in any of the considered regions.

6.1.2. Tracks

The reconstruction of tracks [209, 211, 215–218] is sensitive to the position of the interaction point as well as residual misalignments. Thus, nuisance parameters are assigned to the resolution of the impact parameters d_0 and z_0 of the interaction point. Potential misalignment biases are accounted for by nuisance parameters on the d_0, z_0 and p_{T} of the track. These uncertainties are measured in minimum bias as well as $Z \to \mu^+\mu^-$ events.

Furthermore, the estimated track reconstruction efficiency contains uncertainties from the measurements and algorithms used. In the same manner, uncertainties on track fake rates, i.e. the fraction of reconstructed tracks that do not correspond to real particles passing through the detector, are assigned in minimum bias events. For tracks in dense environments such as jets, extra uncertainties account for the differences in track efficiencies and fake rates compared to those of isolated tracks measured in dijet events.

While the impact on the track uncertainties is expected to be small since they only occur in the TAR jet reconstruction, none of the nuisance parameters seem to have an impact on the analysis.

6.1.3. Muons

In the reconstruction of muons, several sources of systematic uncertainties need to be considered [221, 222]. To account for differences in simulated and recorded data events, scale factors on the efficiencies of reconstruction, identification, the track to vertex association (TTVA) and isolation are derived in $J/\psi \to \mu^+\mu^-$ and $Z \to \mu^+\mu^-$ events. The uncertainties on the measurement of these scale factors are propagated through the analysis by two nuisance parameters each: one corresponding to the statistical component and one to the systematic component.

Another set of uncertainties arise from the muon momentum calibration. A distinction is made between charge-dependent and charge-independent momentum corrections. While the resolution of the Inner Detector as well as of the Muon Spectrometer and the energy scale are considered charge-independent, the residual bias and the closure between data and simulation determinations on the momentum scale depend on the muon charge.

As shown in Table 6.1, the nuisance parameters corresponding to the muon resolution in the Muon Spectrometer and the Inner Detector are included in the highest ranked uncertainties for both considered signal mass points. These nuisance parameters are however not relevant for the $t\bar{t}$ background. Figure 6.1 shows the comparison between the nominal and systematically varied $m_{\text{vis+met}}$ distribution with respect to the Muon Spectrometer and Inner Detector resolutions for the $m_X = 4\,\text{TeV}$ signal mass point. All variations in the individual bins are small compared to the statistical error.

Since the muons from background processes generally have a lower p_{T}, they are less sensitive to uncertainties in the resolutions of the the Muon Spectrometer and Inner Detector. If it turns out that these nuisance parameters become dominant uncertainties in determination of exclusion limits, the usage of the high p_{T} working point of the muon ID must be considered again to reduce the impact of this nuisance parameter at the cost of decreased signal efficiency (see Section 4.2.2).

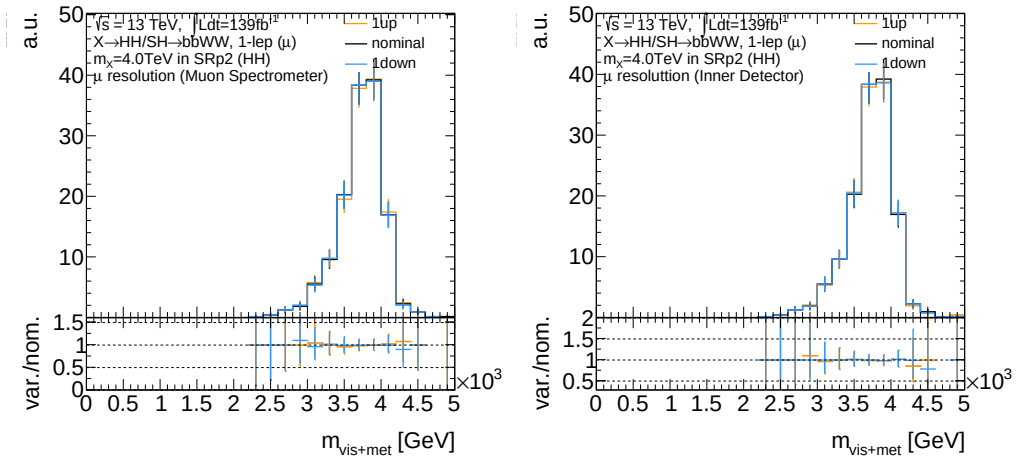

(a) Muon Spectrometer resolution **(b)** Inner Detector resolution

Figure 6.1.: Comparison between the nominal and systematically varied $m_{\text{vis+met}}$ distributions of the $m_X = 4.0\,\text{TeV}$ signal mass point for the Muon Spectrometer and Inner Detector resultions of muons in SRp2 with the HH selection applied.

6.1.4. Electrons

Similar to the muon uncertainties, the electron nuisance parameters are distinguished between efficiency related and energy measurement related uncertainties [219, 220]. These uncertainties are measured in $J/\psi \to e^+e^-$ and $Z \to e^+e^-$ events.

Since this analysis considers only muons as signal leptons, it is expected to be insensitive to uncertainties assigned to electrons. Therefore, all efficiency related nuisance parameters are combined into three nuisance parameters which correspond to the electron efficiency scale factor measurements with regards to reconstruction, identification and isolation. For the same reason, also the uncertainties on the energy measurements

are implemented as three nuisance parameters. One corresponds to the uncertainty on the electromagnetic energy scale, one to the electromagnetic resolution and the last one accounts for differences between full and fast detector simulation and is therefore only relevant for the signal process.

As expected, the nuisance parameters associated to electrons do not or only marginally impact the $m_{\text{vis+met}}$ distribution. The corresponding values of δ^{avg} are at least three orders of magnitude smaller than the largest δ^{avg} in all samples.

6.1.5. Jets

Due to their hadronic nature, most jet collections are reconstructed mainly in the outer components of the calorimeter. The granularity in this part of the calorimeter is not very fine and the interplay of neutral and charged particles is more complex than for electromagnetic showers. This results in the jet energy scale (JES) and jet energy resolution (JER) being the dominant uncertainties.

For PFlow jets, the uncertainties on the JES originate from the *in situ* measurements of the Z+jet, the γ+jet and the multijet p_{T} balances as well as measurements of single particles and testbeams addressing various energy ranges [227, 237]. Since these are mostly evaluated in the central part of the detector, the calibration needs to be transferred to the forward region called intercalibration. Furthermore, the effect of pileup and differences in the jet flavour, i.e. whether the jet originates from a b, c or light hadron or a gluon, must be taken into account. There are also cases where the jet is not contained within the hadronic calorimeter but punches through to the Muon Spectrometer resulting in additional uncertainties due to the energy of the jet not being fully collected within the calorimeter. Finally, a closure test between simulation and data is performed. These uncertainties result in over one hundred different nuisance parameters that would need to be evaluated in the context of the analysis. Therefore, a reduction of nuisance parameters is performed by exploiting correlations between eigenvectors associated to the various nuisance parameters to construct effective nuisance parameters. The category reduction used in this analysis reduces the number of nuisance parameters to approximately 30 while the origin of the uncertainties is still preserved to a certain degree.

The JER of PFlow jets has fewer nuisance parameters which correspond to the two used measurement methods, random cones and dijet balance [237]. An additional uncertainty addresses the closure between simulated and recorded data events. If the simulation yields a smaller resolution than the data which occurs in most phase space regions, the simulated events are smeared to match the data resolution. If the opposite is the case, the data is smeared. Since the JER also depends on the JES, its uncertainties are also propagated to the JER measurement. This results in approximately 30 nuisance parameters in total which are reduced to eight nuisance parameters in the simple JER reduction scheme. In this scheme, only simulated events are smeared.

Studies to derive uncertainties on JES and JER for small-R jets are discussed in Appendix C. To obtain an impression on how the JER and JES uncertainties on small-R jets impact the TAR jets, the nuisance parameters derived for PFlow jets are applied

to the small-R jets as well. The nuisance parameters are fully correlated between both jet collections.

Since VR track jets are solely used for b-tagging TAR jets, their uncertainties are covered by the nuisance parameters obtained for flavour tagging in Section 6.1.7.

Table 6.1 shows that many of the jet nuisance parameters are highly ranked. In particular, the uncertainties corresponding to the JER greatly influence the distribution of $m_{\text{vis+met}}$. Due to the correlation between the jet collections, it is difficult to determine whether the small-R jets via the TAR jets or the PFlow jets via $E_{\text{T}}^{\text{miss}}$ are responsible for the variations of the $m_{\text{vis+met}}$. Therefore, the impact of one of the JER nuiscance parameters is checked on other variables as well and is summarised in Table 6.2 for the $m_X = 4\,\text{TeV}$ signal mass point and the $t\bar{t}$ background.

Variable	δ^{avg}	δ^{max}
$E_{\text{T}}^{\text{miss}}$	38.27%	240.96%
$m_{\text{vis+met}}$	10.66%	218.18%
lepton p_{T}	0.01%	0.17%
W_{had} p_{T}	0.01%	0.15%
$H \to b\bar{b}$ p_{T}	0.01%	0.15%
W_{had} m_{TAR}	0.01%	0.20%
$\Delta R(W_{\text{had}}, \ell)$	0.01%	0.31%
$H \to b\bar{b}$ m_{TAR}	0.00%	0.23%

(a) $m_X = 4.0\,\text{TeV}$ in SRp2 (HH)

Variable	δ^{avg}	δ^{max}
$E_{\text{T}}^{\text{miss}}$	39.60%	6653.04%
$m_{\text{vis+met}}$	5.81%	4411.23%
lepton p_{T}	0.12%	17.57%
$H \to b\bar{b}$ p_{T}	0.05%	26.16%
$H \to b\bar{b}$ m_{TAR}	0.04%	16.64%
$\Delta R(W_{\text{had}}, \ell)$	0.02%	13.79%
W_{had} p_{T}	0.02%	15.89%
W_{had} m_{TAR}	0.00%	24.50%

(b) $t\bar{t}$ in ttbar CR

Table 6.2.: Summary of the impact of the second effective JER nuisance parameter on a selected set of variables on signal and background. The entries are sorted in descending order in δ^{avg}.

The $E_{\text{T}}^{\text{miss}}$ is the variable most affected by the JER nuisance parameter. Therefore, it can be assumed that the JER impact on PFlow jets and its transferred impact on $E_{\text{T}}^{\text{miss}}$ distribution is more relevant than the influence of small-R jets on the TAR jets. The distributions of the mass and p_{T} of the $H \to b\bar{b}$ and W_{had} candidates barely show any variation. Again, δ^{max} is much larger than δ^{avg} which becomes also visible in the distributions of $E_{\text{T}}^{\text{miss}}$ and $m_{\text{vis+met}}$ displayed in Figure 6.2 for the $m_X = 4\,\text{TeV}$ mass point and the $t\bar{t}$ background. There are significantly more variations in the $E_{\text{T}}^{\text{miss}}$ distribution than in the $m_{\text{vis+met}}$ distribution, where the deviation in each bin is smaller than the statistical uncertainty.

6.1.6. Missing Transverse Energy

Since the $E_{\text{T}}^{\text{miss}}$ is reconstructed from all other objects in the event and additional soft tracks, the uncertainties from the reconstruction of other objects are propagated to the $E_{\text{T}}^{\text{miss}}$ and only the soft track terms are assigned dedicated nuisance parameters [252,253]. Two variations, one longitudinal and one transverse to the direction of the hard scattered

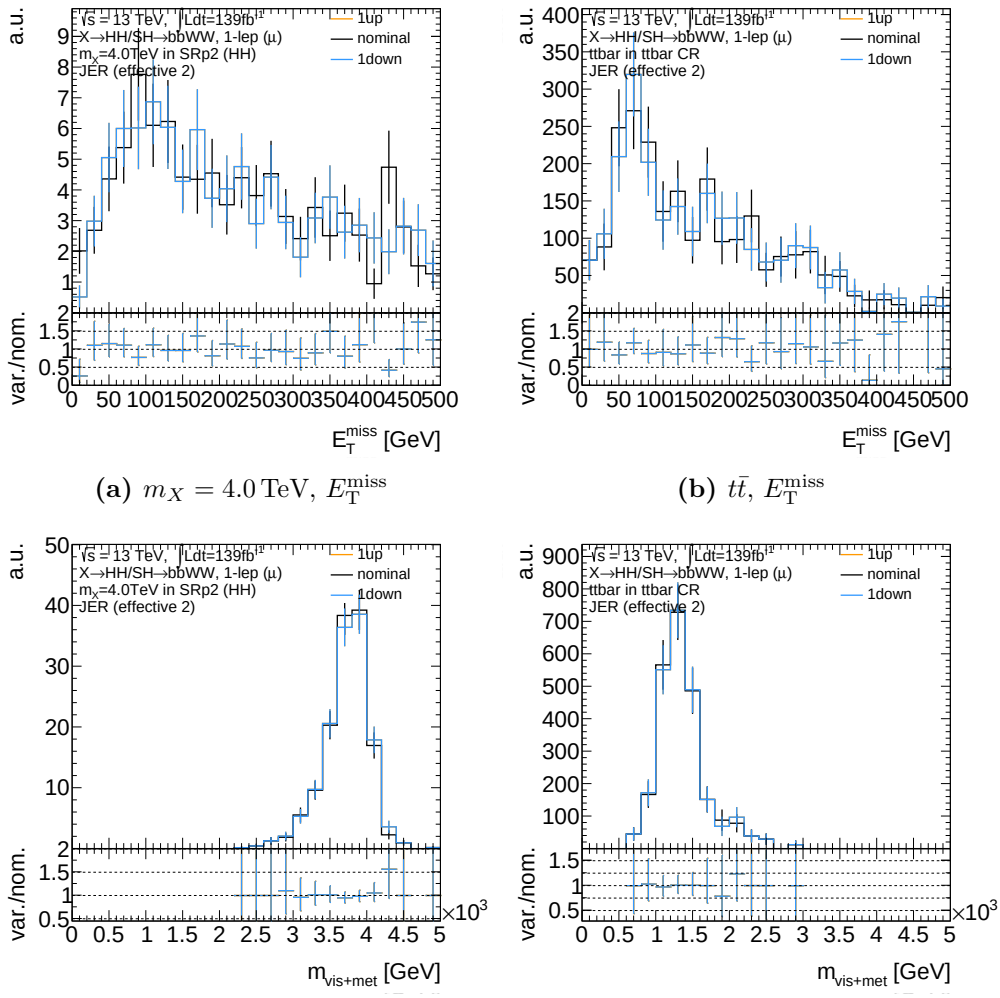

(a) $m_X = 4.0\,\text{TeV}$, E_T^miss **(b)** $t\bar{t}$, E_T^miss

(c) $m_X = 4.0\,\text{TeV}$, $m_\text{vis+met}$ **(d)** $t\bar{t}$, $m_\text{vis+met}$

Figure 6.2.: Comparison between the nominal and systematically varied E_T^miss (top) and $m_\text{vis+met}$ (bottom) distributions of the $m_X = 4.0\,\text{TeV}$ signal mass point (left) and the $t\bar{t}$ background (right) evaluating the second effective JER nuisance parameter.

transverse momentum, are determined by smearing the soft term magnitude.

Table 6.3 shows the ten nuisance parameters which affect the E_T^miss distribution the most. For all considered samples, the JER uncertainties are the highest ranked nuisance parameters. The shown values of δ^avg are all in the same order of magnitude, implying that the E_T^miss distribution is sensitive to many variations. Furthermore, these variations are directly propagated to the $m_\text{vis+met}$ distribution making the E_T^miss the quantity most susceptible to systematic uncertainties.

While for the $t\bar{t}$ background only JES uncertainties follow, the E_T^miss distribution

corresponding to the $m_X = 4\,\text{TeV}$ signal is also influenced by the muon resolution in the Muon Spectrometer.

ranking	nuisance parameter	δ^{avg}	δ^{max}
1	JER (effective 4)	50.74%	229.41%
2	JER (effective 1)	47.04%	207.65%
3	JER (effective 6)	46.20%	191.42%
4	JER (effective 5)	43.49%	185.94%
5	JER (effective 3)	39.30%	207.82%
6	JER (effective 2)	38.27%	240.96%
7	JES (mixed 1)	31.15%	161.62%
8	μ Muon Spectrometer resolution	25.82%	138.03%
9	JES (flavour response)	24.25%	122.15%
10	JES (AFII)	23.16%	132.60%

(a) $m_X = 4.0\,\text{TeV}$ in SRp2 (HH)

ranking	nuisance parameter	δ^{avg}	δ^{max}
1	JER (effective 2)	39.60%	6653.04%
2	JER (effective 6)	36.81%	5312.09%
3	JER (effective 3)	35.77%	4007.83%
4	JER (effective 4)	34.73%	5053.49%
5	JER (effective 1)	34.32%	5926.19%
6	JER (effective 5)	31.26%	4946.11%
7	JES (mixed 1)	22.26%	2596.90%
8	JES (flavour composition)	20.75%	4117.64%
9	JES (flavour response)	19.44%	4237.28%
10	JES (pileup N_{PV})	12.70%	1590.52%

(b) $t\bar{t}$ in $t\bar{t}$ CR

Table 6.3.: Summary of the ten leading nuisance parameters including their impact on th $E_{\text{T}}^{\text{miss}}$ distribution for signal and background processes.

6.1.7. *b*-Tagging

The uncertainties arising from the b-tagging algorithm are derived for each jet collection separately [254, 255]. Currently, only b-tagging uncertainties on VR track jets are taken into account. The uncertainties will be extended to PFlow jets, once the orthogonality cuts to the resolved $HH \to b\bar{b}b\bar{b}$ and, in the case of split-boosted SH mass points, to the resolved 1-lepton $SH \to b\bar{b}WW$ analyses are included in the event selection.

As for the JES and JER, the b-tagging variations are evaluated by constructing eigenvector variations for each of the jet flavours: b-, c- and light jets. Exploiting correlations between the eigenvectors, it is possible to reduce the number of eigenvectors using the

loose eigenvector reduction scheme [255]. Twelve nuisance parameters remain, of which five are associated to light jets, four to c-jets and three to b-jets.

Furthermore, efficiency extrapolations from b-jets and c-jets need to be taken into account, since the b-tagging algorithms are trained on samples containing certain flavour fractions which do not necessarily agree with the composition of jet flavours in data. This adds two more nuisance parameters.

In contrast to the previous analysis [13], the nuisance parameters assigned to b-tagging uncertainties do not appear within the ten dominating uncertainties. The first nuisance parameter associated to b-tagging can be found at rank 26 for the $m_X = 4\,\text{TeV}$ signal, while for $t\bar{t}$, it is ranked in twelfth position.

6.2. Modelling Uncertainties on Simulated Events

Further systematic uncertainties arise from theoretical assumptions and approximations made during the event simulation of physics processes. The cross section of a process $pp \to X$ in the n-th order of perturbation can be expressed as

$$\sigma^{(n)} = f^{\text{part}}(x_1, \mu_F) \otimes f^{\text{part}}(x_2, \mu_F) \otimes \hat{\sigma}^{(n)}(x_1, x_2, \mu_R) \tag{6.3}$$

where f^{part} denotes the parton distribution function depending on the parton momentum fraction x and

$$\hat{\sigma}^{(n)} = \alpha_s \hat{\sigma}^{(1)} + \alpha_s^2 \hat{\sigma}^{(2)} + \cdots + \alpha_s^n \hat{\sigma}^{(n)} + \mathcal{O}\left(\alpha_s^{n+1}\right) \tag{6.4}$$

denotes the partonic cross section of the process such as $gg \to X$. The factorisation and renormalization scales μ_F and μ_R, respectively, define the energy scale at which value of the strong coupling constant α_s is assumed.

This reveals three sources of systematic uncertainties on the theoretical prediction of cross sections:

- missing higher orders in α_s in the partonic cross section and the parton distribution functions,
- the functional form or the dataset used to obtain the parton distribution function,
- the determination of α_s to a fixed order.

These uncertainties can affect both the normalisation and the shape of the final discriminant.

Furthermore, uncertainties on cross sections and branching ratios used in the normalisation of the simulated processes are considered since their calculation can be performed at different orders in α_s than the cross section used in the event generation. This is a pure normalisation uncertainty.

While the modelling uncertainties on the signal processes as well as the dominant $t\bar{t}$, W+jets and single top prompt lepton backgrounds are evaluated in detail, the remaining

backgrounds are assigned a conservative normalisation uncertainty of 30% on the cross section since they contribute less than 5% to all signal regions. To estimate the dependence of the results on the choice of the uncertainty size, a normalisation uncertainty of 50% is evaluated as well.

Table 6.4 summarises the average impact on the final discriminant in SRp2 with the HH selection applied. Only the W+jets parton shower uncertainty is evaluated in the W+jets CR to reduce the influence of statistical uncertainties. The largest uncertainty by far is observed in the W+jets scale variations. This is mostly due to large differences in the normalisation which will be reduced with the application of corresponding NFs (see Section 5.8).

Systematic uncertainty	HH signal	$t\bar{t}$	$W(\rightarrow \ell\nu)$+jets
cross section	-	5.59%	4.98%
branching ratio	5.17%	3.34%	-
parton distribution function	n.e.	17.8%	3.8%
renormalisation & factorisation scale	n.e.	19.62%	74.63%
matrix element & parton shower	n.e.	n.e.	16.6% (in W+jets CR)

Table 6.4.: Summary of all categories of modelling uncertainties considered. The shown values correspond to the uncertainties on the normalisation of the samples in the most sensitive signal region SRp2 with the HH selection applied. Only the parton shower variation on the W+jets background is evaluated on the shape of $m_{\text{vis+met}}$ in the W+jets CR. The scale variations are obtained by adding the individual scale uncertainties in quadrature. For the $t\bar{t}$ background, the refined approach of varying FSR $m_F = 0.625$ is pursued in this summary. The value "n.e." denotes that the uncertainty is not yet evaluated and "-" denotes that an evaluation is not necessary [26].

6.2.1. Parton Distribution Function

To evaluate uncertainties on the parton density functions, various parton distribution functions are combined in the PDF4LHC set [304] allowing to test systematic variations represented by eigenvectors. These are statistically independent and can therefore be combined in a single nuisance parameter. This uncertainty is currently evaluated for the $t\bar{t}$ and W+jets backgrounds. The outcome of varying the nominal parton distribution function is depicted in Figure 6.3 as a function of $m_{\text{vis+met}}$ in SRp2.

Both the up and down variations are comparably flat across the whole range of the $m_{\text{vis+met}}$ distribution such that the shape component is removed for the benefit of reduced statistical fluctuations. Therefore, these nuisance parameters only affect the normalisation of the samples.

For the $t\bar{t}$ and W+jets background processes the uncertainty amounts to 15.0% and

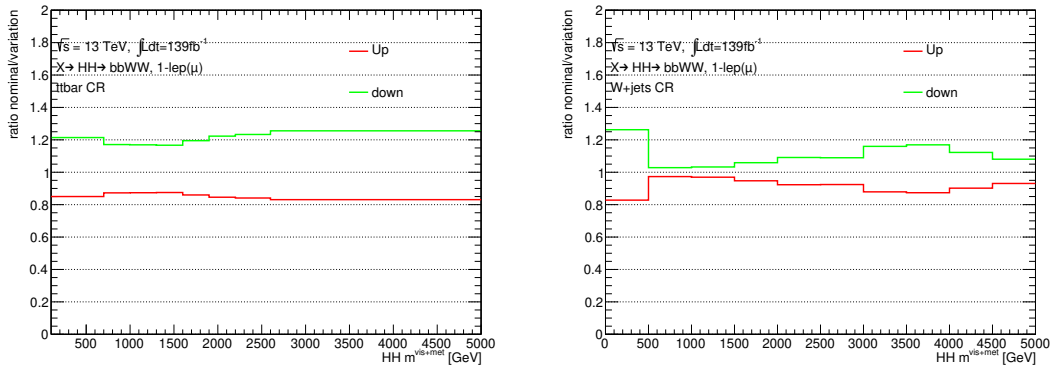

(a) $t\bar{t}$ **(b)** W+jets

Figure 6.3.: Up and down variation associated to the parton distribution function on the $t\bar{t}$ and W+jets backgrounds in the respective control region [26].

4.6% in the respective control regions which are dominated by these backgrounds and thus, have the smallest statistical uncertainties. The variation is however comparable to the ones obtained in the signal regions with 17.8% (SRP2), 15.4% (SRp1) and 17.7% (SRf2) for the $t\bar{t}$ background and 3.6% (SRp2), 4.4% (SRp1) and 3.2% (SRf2) for the W+jets background [26].

6.2.2. Renormalisation and Factorisation Scales

To account for the exclusion of higher order terms in α_s in the calculation, the factorisation and renormalisation scales are varied. This also affects the amount of initial and final state radiation. The general recipe to evaluate this uncertainty for all samples is to reweight the events by internal weight variations corresponding to varying one of scales to either $\mu_{F/R} = 0.5$ or $\mu_{F/R} = 2.0$ while keeping the other scale constant $\mu_{R/F} = 1.0$. For the W+jets background, μ_R and μ_F are also varied simultaneously in the same direction. In contrast, for the $t\bar{t}$ background, additional weights exists that explicitly vary the amount of initial and final state radiation up and down (ISR and FSR). The various variations are shown in Figure 6.4 in the respective control regions. For the same reason, bins with a relative statistical uncertainty of more than 20% are merged with neighbouring bins until the statistical uncertainty is below this threshold. Due to the large differences between up and down variations, they are kept separate and are not symmetrised.

For the $t\bar{t}$ background, most uncertainties are in the range of 20%. However, the down variation of FSR yield very large uncertainties of $> 35\%$ in each bin begging the question if this uncertainty is actually overestimated.

To protect the uncertainty from very high weights in the tails of the variation, weight

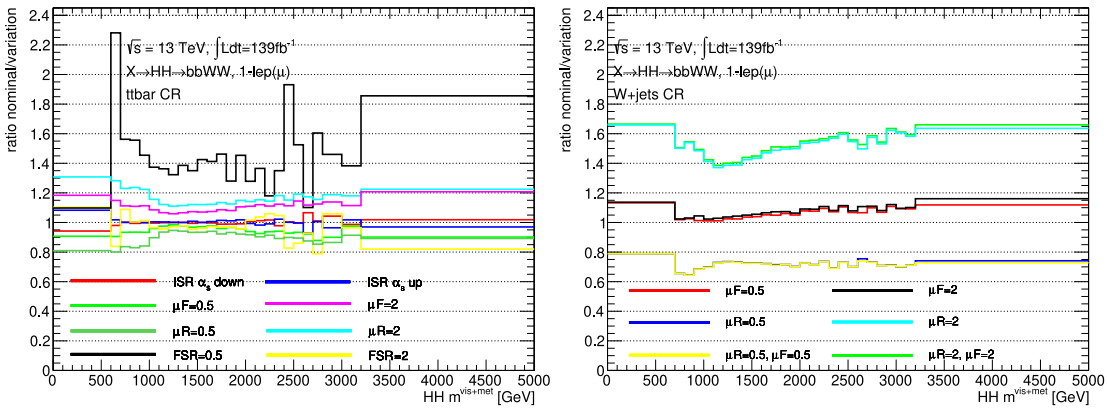

(a) $t\bar{t}$ **(b)** W+jets

Figure 6.4.: Up and down variation associated to the various scale variations on the $t\bar{t}$ and W+jets backgrounds in the respective control regions [26]. The binning is chosen in a way that the relative statistical uncertainty per bin is at most 20%.

variations must either satisfy

$$\frac{\text{varied weight}}{\text{nominal weight}} < \alpha^{\text{thresh}}, \tag{6.5}$$

of if not, the nominal weight will be used. Nominally, the weight threshold is set to $\alpha^{\text{thresh}} = 10$, which cuts away a significant part of the FSR scale down variation. To correct this large uncertainty, either a higher weight threshold of $\alpha^{\text{thresh}} = 50$ could be considered. Another option is to use 0.625 as down variation for FSR [305]. The modified uncertainty values in the $t\bar{t}$ CR are displayed in Figure 6.5. The FSR scale uncertainty decreases to less than 20% in both approaches. In contrast to modifying α^{thresh}, using FSR = 0.625 is more stable across the bins and also leaves the other scale variations untouched. Therefore, this approach is pursued from now on.

For the W+jets background, the picture is similar. The largest impact with $> 40\%$ is determined by varying μ_F in both directions. As for the PDF variation, the shape dependence on the uncertainties is comparably small such that the variations are only applied to the normalisation of the respective sample. Table 6.5 summarises the scale variations for the $t\bar{t}$ background as well as for the W+jets background.

6.2.3. Matrix Element and Parton Shower

Uncertainties on the matrix element calculation and the parton showering that have not been covered by the uncertainties in Sections 6.2.1 and 6.2.2 are estimated by using alternative generators in the both simulation steps.

For the HH signal, no variation on the matrix element calculation is conducted but the parton shower generator Herwig 7 will be replaced by the Pythia 8 generator in alternative samples that are then compared. The difference will be taken as an uncer-

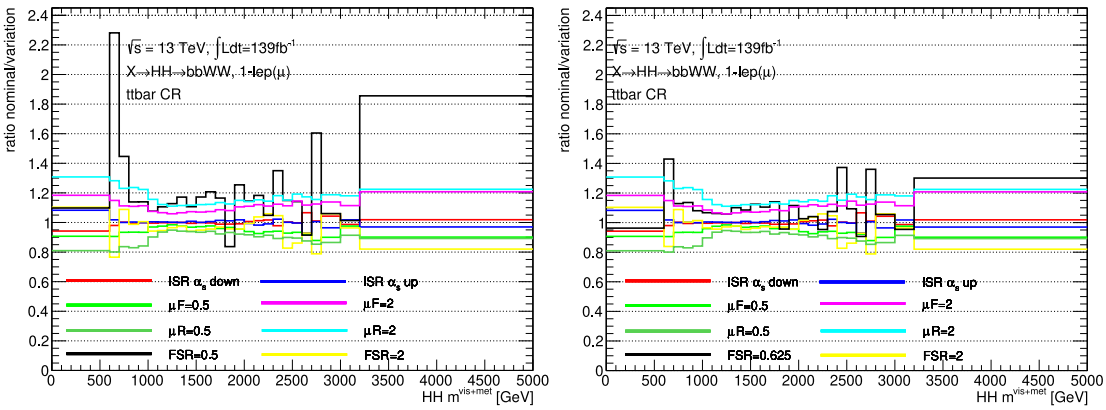

(a) $\alpha^{\text{thresh}} < 50$ **(b)** FSR $= 0.625$

Figure 6.5.: Up and down variations associated to the various scale variations on the $t\bar{t}$ background in the $t\bar{t}$ CR with adjusted weight threshold or FSR scale variation [26]. The binning is chosen in a way that the relative statistical uncertainty per bin is at most 20%.

variation	uncertainty
μ_F up	7.68%
μ_F down	3.33%
μ_R up	13.39%
μ_R down	7.84%
ISR up	0.32%
ISR down	0.23%
FSR up	2.95%
FSR down	8.08%

(a) $t\bar{t}$

μ_F	μ_R	uncertainty
0.5	1.0	3.7%
2.0	1.0	5.3%
1.0	0.5	27.8%
1.0	2.0	43.8%
0.5	0.5	28.0%
2.0	2.0	45.3%

(b) W+jets

Table 6.5.: Up and down variation associated to the various scale variations on the $t\bar{t}$ and W+jets backgrounds in the respective control regions [26]. For the $t\bar{t}$ background, the approach of using FSR $\mu_R = 0.625$ is pursued.

tainty. Since this analysis uses TAR jets, the effect of a different hadronisation model will be in particular interesting to test the effect on these objects.

The strategy for the SH signal is yet to be determined. One option is to extrapolate the obtained parton shower uncertainties on the HH signals to the SH signals given that both signals exploit the same topology. The other option would be to produce alternative samples.

Regarding the $t\bar{t}$ and single top backgrounds, two generator variations are made. In the first variation, the nominal matrix element generator Powheg is replaced by aMC@NLO. The second variation involves the nominal parton shower generator Pythia 8

being replaced by HERWIG 7. In both cases, the observed differences will be propagated as uncertainties.

Nominally, the W+jets background uses SHERPA 2.2.1 for the matrix element calculation and parton shower. Alternative samples generated with MADGRAPH for the matrix element calculation and PYTHIA 8 for the parton shower are compared. Here, only shape differences are considered since the normalisation of W+jets background is constrained by a control region fit. The $m_{\text{vis+met}}$ distributions of W+jets simulated with the nominal and alternative generators in SRp2 with either the HH or SH selection applied as well as in the W+jets CR are displayed in Figure 6.6. While the comparison between nominal and alternative generator is dominated by statistical uncertainties in the signal regions, the ratio between nominal and alternative generators in W+jets CR exhibits a slope. Therefore, this uncertainty will be included as shape uncertainty.

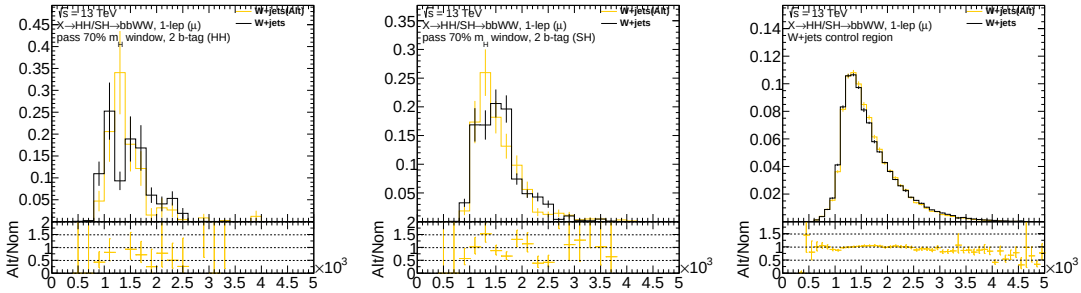

(a) SRp2 (HH selection) **(b)** SRp2 (SH selection) **(c)** W+jets CR

Figure 6.6.: Difference between the normalised nominal and alternative W+jets backgrounds depending on the final discriminant $m_{\text{vis+met}}$ in the most sensitive signal region SRp2 with either the HH or SH selection applied or in the W+jets CR.

6.2.4. Cross Sections and Branching Ratios

Uncertainties on the cross sections have been mostly covered in the previous sections, but some effects are still uncovered, such as the connection between the different order calculations in the generators. Therefore, a normalisation uncertainty on the cross section of the dominant backgrounds predicted by the SM is included. For the $t\bar{t}$ background, this uncertainty amounts to 5.59%, for the W+jets background to 4.98% and to 4.38% to the single top background. The uncertainty on the W+jets background also includes the uncertainty on the leptonic branching ratio. Since in the model independent signal approach pursued in this analysis no cross section prediction exists, no uncertainty is assigned to the assumed signal cross section.

Additionally, uncertainties on the branching ratios on the desired 1-lepton final state must be taken into account for all SM decays. These amount to 3.34% for the $t\bar{t}$ and single top backgrounds and to 5.17% on the HH signal.

The values of SM cross sections and branching ratios as well as their uncertainties follow the descriptions in Refs. [3, 105, 306–308].

6.3. Non-Prompt Lepton Estimate Uncertainties

The data driven approach used to estimate the non-prompt lepton background (see Section 5.7) requires the evaluation of dedicated uncertainties [302]. Those uncertainties address biases from the selection, choices made in the efficiency parametrisation and the validity of the method itself. Furthermore, statistical and systematic uncertainties on the simulated prompt lepton backgrounds need to be propagated.

6.3.1. Propagation of Prompt Lepton Background Uncertainties

Simulated prompt lepton backgrounds are considered in the determination of the real efficiencies and are subtracted from data when calculating the fake efficiencies. Therefore, their statistical and systematic uncertainties need to be propagated through the efficiencies to the final background estimate.

Nominally, the statistical uncertainties on the real and fake efficiencies are derived in each bin yielding a large set of nuisance parameters. Since the binning of the efficiencies is chosen to keep the statistical uncertainty comparably small, correlations between the bins are exploited to combine the nuisance parameters into a single uncertainty.

The systematic uncertainties on the prompt lepton backgrounds need to be propagated through to the non-prompt lepton background estimate via the efficiencies. Since the non-prompt lepton background only contributes at most by 12% to the backgrounds in the signal regions, a simplified approach is pursued: each prompt lepton background is assigned a conservative 50% normalisation uncertainty covering all other systematic effects. These variations are treated as fully uncorrelated making the associated uncertainty even more conservative.

New real and fake efficiencies are calculated for each varied background individually and the differences to the nominal efficiencies are taken as uncertainties on the prompt lepton subtraction. To end up with one uncertainty per prompt-lepton background, the maximum of the absolute of the up and down variations in each bin is used. The resulting variations on the real and fake efficiencies can be seen in Figures 6.7 and 6.8, respectively, as a function of the muon p_{T} and the ΔR between the muon and the closest TAR jet.

For the real efficiency ϵ, the relative uncertainty of the individual bins is $\lesssim 10\%$ on average with very bins exposing a larger uncertainty of at most 50%. For the fake efficiency f, the relative uncertainty of the individual bins is larger with $\lesssim 40\%$ on average where especially, the low p_{T} and high ΔR bin features a large uncertainty of 200% when varying the W+jets background normalisation by 50%. This is due to the fact that this region is dominated by the W+jets background. Therefore, the effect on the background estimate is expected to be small.

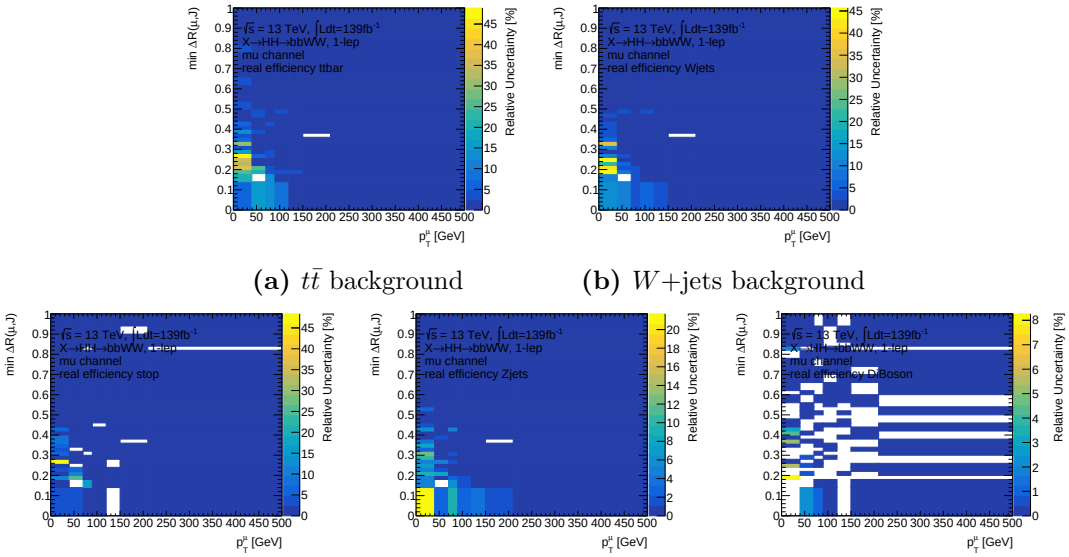

(a) $t\bar{t}$ background **(b)** W+jets background

(c) single top background **(d)** Z+jets background **(e)** diboson background

Figure 6.7.: Propagated systematic uncertainties from the prompt lepton backgrounds to the real efficiency. Shown is the maximum absolute value of the relative up and down variation in each bin. The white colour corresponds to a vanishing uncertainty.

6.3.2. Selection Biases

The lepton and event selection applied also influence the real and fake efficiencies. The first bias is generally introduced by the choice of triggers. In this analysis, only single large-R jet triggers are used which do not bias the presence of prompt or non-prompt leptons in the event.

A correlation exists between the non-prompt leptons and the $E_{\mathrm{T}}^{\mathrm{miss}}$ of the event. This is caused by the nature of non-prompt leptons often being accompanied by an underlying jet which influences the lepton p_{T}, the $E_{\mathrm{T}}^{\mathrm{miss}}$, and the fake efficiencies. Therefore, applying a cut on the $E_{\mathrm{T}}^{\mathrm{miss}}$ biases the fake efficiencies. Although no explicit cut on the $E_{\mathrm{T}}^{\mathrm{miss}}$ is included in the event selection in this analysis, cuts on any other objects influence the $E_{\mathrm{T}}^{\mathrm{miss}}$ calculation. An uncertainty is evaluated by splitting the $E_{\mathrm{T}}^{\mathrm{miss}}$ in a low and high $E_{\mathrm{T}}^{\mathrm{miss}}$ region where the boundary is set at 80 GeV and calculating both the real and fake efficiencies in these two regions independently. Figure 6.9 shows the maximum absolute differences to the efficiencies obtained in the inclusive $E_{\mathrm{T}}^{\mathrm{miss}}$ region in each bin which are then propagated as uncertainties.

The effect on the real efficiency ($\lesssim$ 250%) appears to be larger than on the fake efficiency ($\lesssim$ 100%). However, this large uncertainty on the real efficiency is driven by the low p_{T}, low ΔR area and is significantly smaller ($\lesssim$ 20%)a large part of p_{T}-ΔR plane shows small relative uncertainties on the real efficiency ($\lesssim$ 20%) in the remaining region. Therefore, the uncertainty on the real efficiency will also be propagated to the non-prompt lepton estimate. This ensures that any potential bias of the real efficiencies

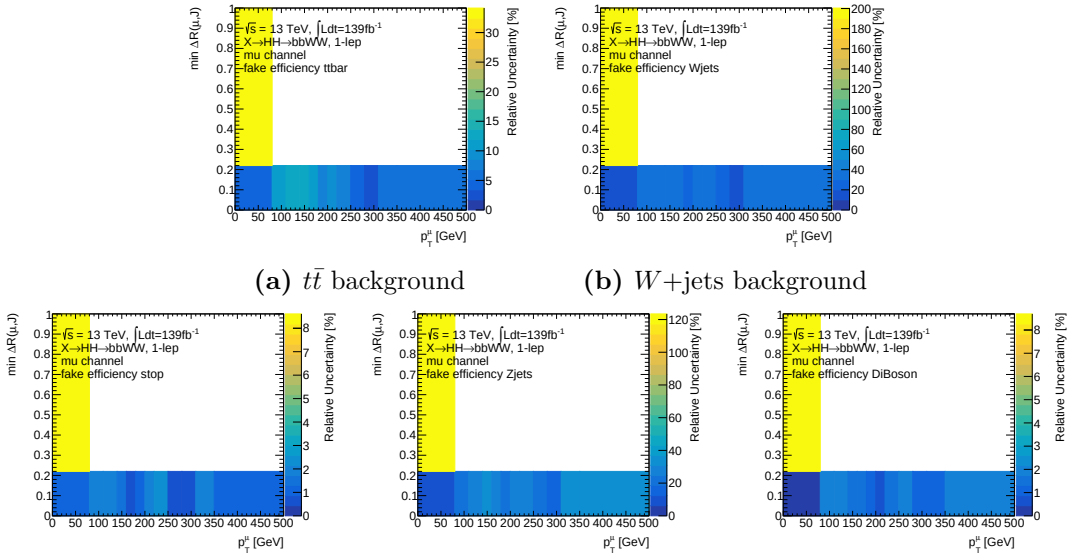

(a) $t\bar{t}$ background **(b)** W+jets background

(c) single top background **(d)** Z+jets background **(e)** diboson background

Figure 6.8.: Propagated systematic uncertainties from the prompt lepton backgrounds to the fake efficiency. Shown is the maximum absolute value of the relative up and down variation in each bin. The white colour corresponds to a vanishing uncertainty.

is accounted for.

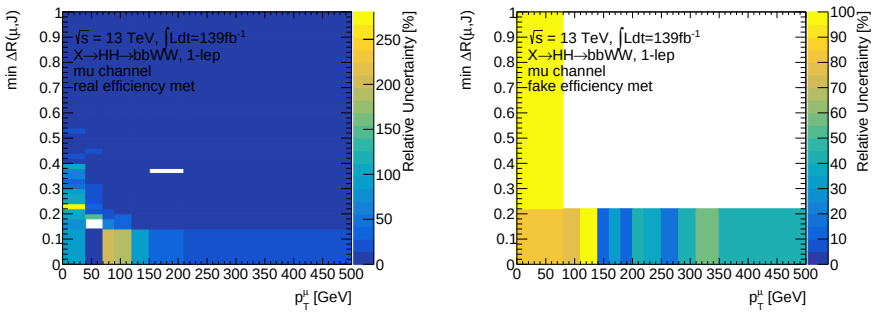

(a) real efficiency **(b)** fake efficieny

Figure 6.9.: Uncertainty on the efficiencies due a possible bias cased by the $E_{\mathrm{T}}^{\mathrm{miss}}$. Shown is the maximum absolute deviation of the low/high $E_{\mathrm{T}}^{\mathrm{miss}}$ region from the inclusive $E_{\mathrm{T}}^{\mathrm{miss}}$ region. The white colour corresponds to a vanishing uncertainty.

Another bias is introduced by the transverse impact parameter d_0, which is designed to distinguish prompt from non-prompt leptons. The stricter the cut, the more likely the lepton is a prompt lepton and, thus, influencing the efficiencies. Thus, a cut on the d_0 significance ($|d_0/\sigma_{d_0}| < 3.0$) is applied in the muon selection. To account for the bias, an even stricter cut of $|d_0/\sigma_{d_0}| < 2.0$ is applied to all muons which are used in the

efficiency calculation. The difference to the efficiencies obtained from nominal leptons is then assigned as uncertainty. The relative effects on the real and fake efficiencies are shown in Figure 6.10. As in the case of the $E_{\mathrm{T}}^{\mathrm{miss}}$ bias uncertainty, the effect on the real efficiency appears to be larger than on the fake efficiency, but is significantly smaller with $\lesssim 15\%$ for the real efficiency and $\lesssim 10\%$ for the fake efficiency.

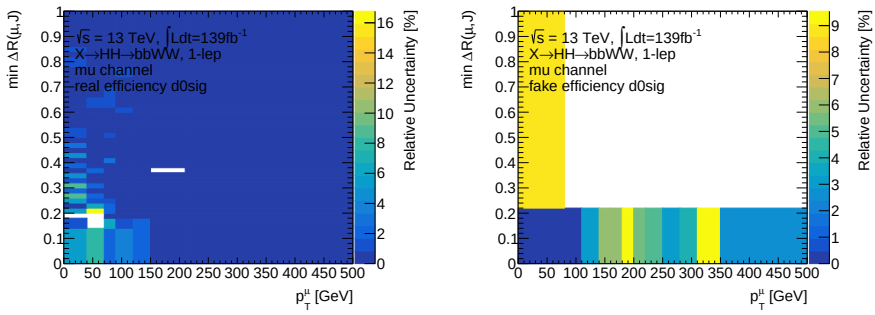

(a) real efficiency **(b)** fake efficiency

Figure 6.10.: Uncertainty on the efficiencies due to a possible bias introduced by cutting on the $|d_0/\sigma_{d_0}|$ in the muon preselection. Shown is the relative effect on the efficiencies when tightening the cut. The white colour corresponds to a vanishing uncertainty.

The last bias considered is due to the background composition differences between control and signal regions. This is only relevant for the fake efficiency. A non-prompt lepton is more likely to pass the tight selection depending on its origin. To derive an uncertainty on this bias, all prompt lepton backgrounds as well as all-hadronic $t\bar{t}$ and dijet samples with the lepton truth matching requirement being inverted are compared in the control and signal regions. The differences in the yields in each bin is taken as an uncertainty and the relative effect on the fake efficiency is shown in Figure 6.11. With a size of up to 500% and on average $\lesssim 200\%$, it is the largest uncertainty on the efficiency.

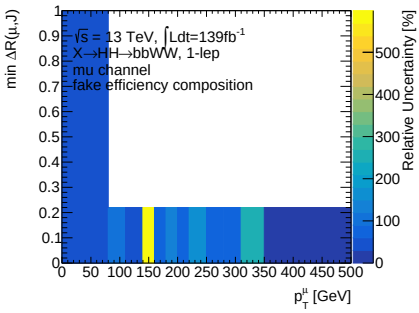

Figure 6.11.: Uncertainty on the fake efficiency related to the background composition in the control and signal regions. The white colour corresponds to a vanishing uncertainty.

6.3.3. Parametrisation of Efficiencies

In contrast to what has been discussed so far, the parametrisation uncertainty is determined after the non-prompt lepton background has been estimated and accounts for the information used to bin the efficiencies. The general idea of the matrix method implies that all distributions of all objects in the event are modelled well if the efficiencies are binned in sufficient variables that represent all quantities of the lepton in which the efficiencies are not flat. Since the available statistics restricts the choice of variables as well as the binning of these variables, an uncertainty is assigned to account for missed relevant characteristics of the lepton. In this analysis, the nominal parametrisation the efficiencies is performed in two dimensions exploiting the muon p_{T} and the ΔR between the muon and the closest TAR jet. The uncertainty is determined alternatively by one dimensional parametrisations. The following variables are considered:

- p_{T}^{ℓ} (transverse momentum of the lepton without extra information of $\min \Delta R(\ell, J)$)
- $\min \Delta R(\ell, J)$ (geometric distance between the lepton and the closest TAR jet without extra information of p_{T}^{ℓ})
- η^{ℓ} (pseudorapidity of the lepton)
- $p_{\mathrm{T}}^{\mathrm{varcone20}}$ (track isolation of the lepton)
- $E_{\mathrm{T}}^{\mathrm{cone20,topo}}$ (calorimeter isolation of the lepton)
- $p_{\mathrm{T}}^{\min J}$ (transverse momentum of the closest jet to the lepton)
- $p_{\mathrm{T}}^{J_0}$ (transverse momentum of the leading jet, which is not the closest jet and, thus, indirectly defined based on the lepton)

The efficiencies displayed in Figure 6.12 are all rebinned such that the relative statistical uncertainty in each bin is less than 15% and are used to estimate the non-prompt lepton background. The resulting estimates are then compared in all three signal regions combined for both SH and HH selection applied, respectively. The differences in the $m_{\mathrm{vis+met}}$ distribution are quoted as uncertainty for each bin. To further reduce statistical fluctuations, bins of the $m_{\mathrm{vis+met}}$ distribution which show a relative statistical error larger than 10% are merged with neighbouring bins.

Since the normalisation of the non-prompt lepton background is inaccurate, it is corrected by a background-only fit in the control regions. Due to strong anti-correlations to the W+jets background estimate, which represents a much larger background, small differences in the W+jets normalisation can lead to large effects on the non-prompt lepton normalisation. Therefore, the normalisation of W+jets and also $t\bar{t}$ backgrounds is fixed resulting in the non-prompt lepton background being scaled to a fixed yield. Taking the relative uncertainty

$$\frac{N_{\mathrm{varied}} - N_{\mathrm{nominal}}}{N_{\mathrm{nominal}}},$$

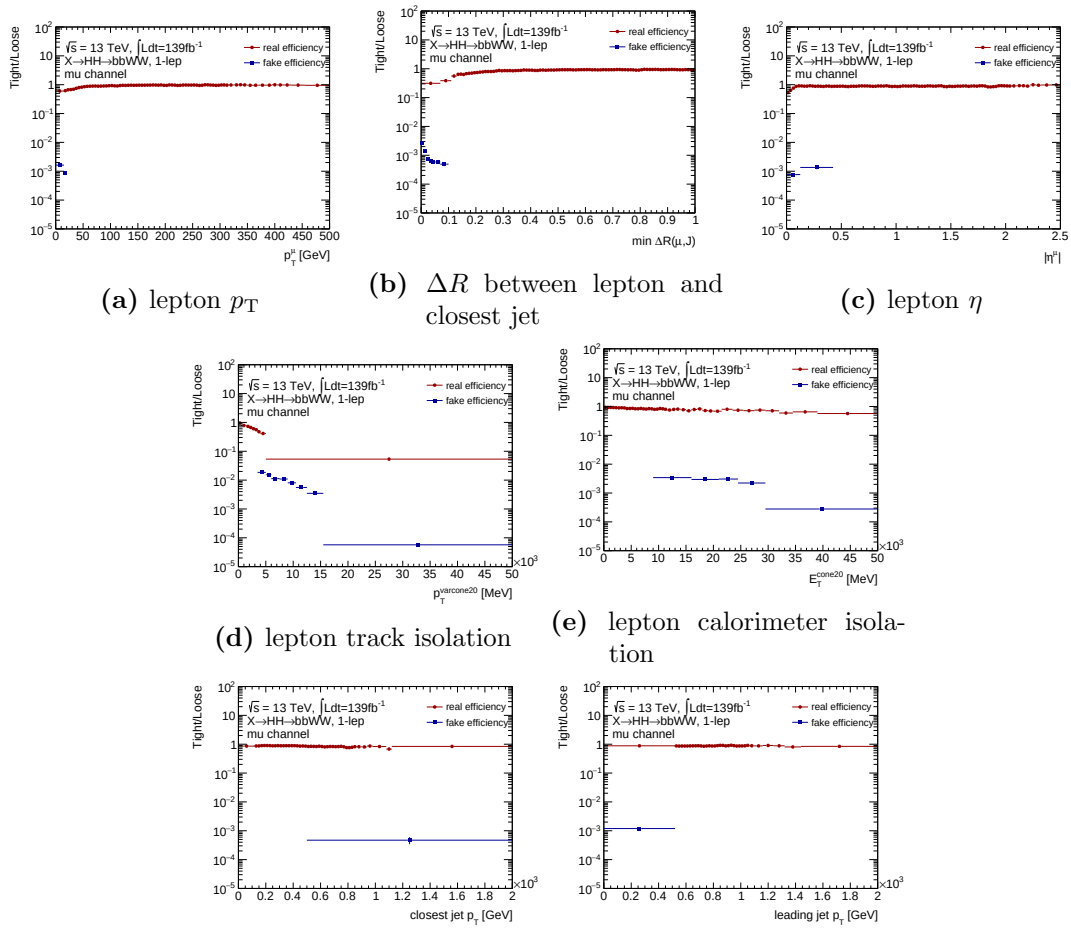

(a) lepton p_{T} **(b)** ΔR between lepton and closest jet **(c)** lepton η

(d) lepton track isolation **(e)** lepton calorimeter isolation

(f) closest jet p_{T} **(g)** leading jet p_{T}

Figure 6.12.: Real and fake efficiencies binned in alternative variables. Each efficiency has been rebinned such that the relative statistical error is $\leq 15\%$. Empty bins have an efficiency smaller than 10^{-5}.

cancels the exact value of the yield such that the estimates are all normalized to unity resulting in this uncertainty being mainly a shape uncertainty. The differences in the shape of the $m_{\mathrm{vis+met}}$ distribution are displayed in Figure 6.13. Since there is no reason to assume that one variable yields a better background estimate than any other variable, it was decided to use the value that covers at least 80% of the absolute of all relative differences obtained. This still results in very conservative uncertainties close to 100% in some bins, but does not include extreme deviations. In this setting, the 80% coverage corresponds to the second largest absolute value of the relative differences.

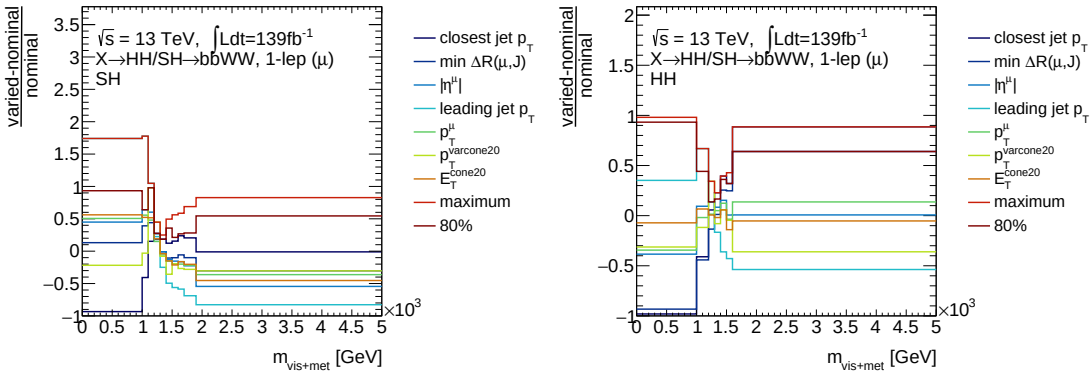

(a) SH selection (b) HH selection

Figure 6.13.: Relative uncertainty on the non-prompt lepton background estimate in the three signal regions combined with the SH and HH selection applied. The dark red line corresponds to the maximum and the red line covers 80% the values of the absolute of relative differences in each bin.

6.3.4. Validity of the Method

To estimate the validity of the method itself, a closure test is performed and a non-closure uncertainty is derived. As for the parametrisation uncertainty, this uncertainty is derived from the non-prompt lepton estimate. The closure is tested in the validation region VRf1 with either the SH or HH selection applied. The estimated non-prompt lepton background is compared to the expected non-prompt lepton background which corresponds to data with all prompt lepton backgrounds subtracted. The comparison can be found in Figure 6.16 and shows the largest deviation of all variations considered by far. This closure test also includes the mismodelling of the W+jets background (discussed in Section 6.2) which is propagated to the expected non-prompt lepton background estimate. Since the W+jets background yield is significantly higher than the one of the non-prompt lepton background, an even small mismodelling translates to a large non-closure uncertainty of up to 1000% relative to the non-prompt lepton background. The average uncertainties are around 250%, if the SH selection is applied, and around 140%, if the HH selection is applied. Due to the small contribution of the non-prompt lepton background to the total backgrounds, the effect on the final limits is expected to be small.

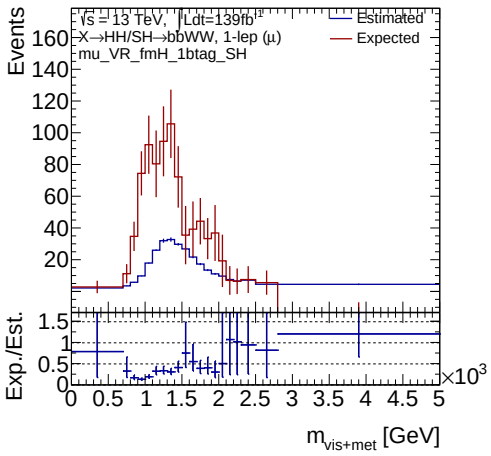

Figure 6.14.: SH selection

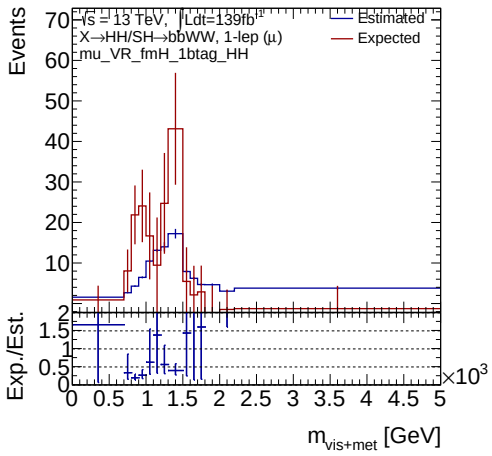

Figure 6.15.: HH selection

Figure 6.16.: Expectation and estimate of the non-prompt lepton background in the validation region with the SH or HH selection applied. The relative difference (expected-estimate)/estimate will be used as non-closure uncertainty.

CHAPTER 7

Statistical Analysis of the $X \to HH/SH \to b\bar{b}WW^{(*)}$ analysis

To interpret the number of events in the signal and control regions, statistical tests are performed. Depending on whether an excess of data over the number of expected events is observed, signal significances or exclusion limits on the production cross section of $pp \to X \to HH$ or $pp \to X \to SH \to b\bar{b}WW$ are extracted. Since the data in the signal regions has not been unblinded, yet, the results from searches for resonant Higgs boson pair production in other decay channels [12,309] are considered as references. So far, no excess in data has been observed in the considered phase space. Therefore, it is assumed that this analysis also will not reveal an excess and upper limits on the cross section of resonant HH production and on the cross section and branching ratio of resonant $SH \to b\bar{b}WW$ production are set.

7.1. Limit Setting Procedure

To extract information from data, probability density functions (PDFs) are frequently utilised in particle physics. These PDFs are characterised by free parameters which are adjusted in likelihood fits to observed data. In the limit setting procedure, the signal strength μ defined as ratio between observed and assumed signal cross section is the free parameter of interest. The signal strength is obtained by maximising a likelihood function as described in Section 7.1.1.

Since setting upper limits amounts to statistically excluding the background-only hypothesis for certain parameter values of μ, a test statistic needs to be constructed. Here, the profile likelihood ratio is chosen where the exact definition is discussed in Section 7.1.2.

The actual limits are then set on the cross section which yields the largest value of μ that rejects the background-only hypothesis in a defined confidence interval. Given the low statistics in the signal regions, a more conservative approach called $\mathrm{CL_s}$ method [310]

is employed which also takes into account the signal plus background hypothesis. More details are provided in Section 7.1.3.

7.1.1. Likelihood Model

The parametric model employed in particle physics describes the nominal predictions of various signal and background processes. In addition, it also includes information on systematic uncertainties parametrized by nuisance parameters $\boldsymbol{\theta}$. By construction, each nuisance parameter θ_i is expressed in units standard deviations and ranges between $-1 \leq \theta_i \leq +1$. The nominal prediction is retrieved if $\theta_i = 0$. It may be that a single systematic uncertainty is described by more than one nuisance parameter as discussed in Section 6.

The PDFs representing the signal and background processes are parametrised by free parameters corresponding to the signal strength μ or normalisation factors of the backgrounds. The normalisation factors can be constrained from data comparisons in control regions. Since the number of signal and background events are distributed according to a Poisson PDF, the PDF for the number of observed events can be expressed as

$$P\left(n \middle| \lambda\left(\mu, \alpha_{\mathrm{NF}}, \boldsymbol{\theta}\right)\right) = \frac{\lambda^n}{n!} e^{-\lambda} \tag{7.1}$$

with n denoting the number of observed events and λ being the Poisson expectation of signal and background events. The Poisson expectation depends on the signal strength μ, the normalisation factors of certain backgrounds α_{NF} and the nuisance parameters $\boldsymbol{\theta}$

$$\lambda(\mu, \alpha_{\mathrm{NF}}, \boldsymbol{\theta}) = \mu s(\boldsymbol{\theta}) + \sum_{\beta \in \mathrm{bkgs}} \alpha_{\mathrm{NF},\beta} b_\beta(\boldsymbol{\theta}) \tag{7.2}$$

where s and b denote the number of expected signal and background events, respectively. The signal strength, defined as the ratio of observed and assumed cross section, can take on values between zero and any positive number. A scenario where $\mu = 0$ corresponds to no signal, and $\mu = 1$ denotes that the observed signal matches the prediction of the model. Negative values of μ are excluded as unphysical. A PDF is constructed for the events in each signal and control region.

Given that the signal and control regions are defined in orthogonal phase spaces, the likelihood function is then constructed as a product of all defined PDFs [311]

$$L\left(n, \boldsymbol{\theta}^0 \middle| \mu, \alpha_{\mathrm{NF}}, \boldsymbol{\theta}\right) = \prod_{s \in \mathrm{SR}} P\left(n_s \middle| \lambda_s\left(\mu, \alpha_{\mathrm{NF}}, \boldsymbol{\theta}\right)\right) \times \prod_{c \in \mathrm{CR}} P\left(n_c \middle| \lambda_c\left(\mu, \alpha_{\mathrm{NF}}, \boldsymbol{\theta}\right)\right) \times C\left(\boldsymbol{\theta}^0, \boldsymbol{\theta}\right) \tag{7.3}$$

where $C(\boldsymbol{\theta}^0, \boldsymbol{\theta})$ accounts for systematic variations via the corresponding nuisance parameters $\boldsymbol{\theta}$. In the case of uncorrelated nuisance parameters, $C(\boldsymbol{\theta}^0, \boldsymbol{\theta})$ can be written as a product of PDFs for each nuisance parameter θ_i, which are typically Gaussian distributed

$$C\left(\boldsymbol{\theta}^0, \boldsymbol{\theta}\right) = \prod_i \frac{1}{\sqrt{2\pi}} e^{-\frac{1}{2}\left(\theta_i^0 - \theta_i\right)^2}. \tag{7.4}$$

The parameter θ_i^0 modifies the central value of the nuisance parameter θ_i such that the systematic variation is no longer symmetric around the nominal measurement. For most nuisance parameters, $\theta_i^0 = 0$ is assumed and only varied to create pseudoexperiments (see Section 7.1.2).

The analysis presented in this thesis is not a simple counting experiment, but utilizes the shape of the final discriminant to obtain the exclusion limits. However, a variable split in x bins can be regarded as x counting experiments. Since all events are Poisson distributed, also the events in a single bin are Poisson distributed. Thus, the Poisson distribution from Eq. 7.1 can be modified to

$$P\left(n \middle| \lambda\left(\mu, \alpha_{\mathrm{NF}}, \boldsymbol{\theta}\right)\right) = \prod_{b \in \mathrm{bins}} \frac{\lambda_b^{n_b}}{n_b!} e^{-\lambda_b} \tag{7.5}$$

with n_b and λ_b being the number of observed and expected events in bin b, respectively. While shape and statistical uncertainties are applied separately per bin, the normalisation uncertainties affect all bins in the same way.

7.1.2. Test Statistic

According to the Neyman-Pearson lemma [312] the optimal test statistic to reject the null hypothesis H_0 against an alternative hypothesis H_1 is given by its likelihood ratio. For the analysis presented in this thesis, the profile likelihood ratio is used as test statistic for a given value of μ,

$$q_\mu = -2 \ln \left(\frac{L\left(\mu, \hat{\hat{\boldsymbol{\theta}}}\right)}{L\left(\hat{\mu}, \hat{\boldsymbol{\theta}}\right)} \right) \tag{7.6}$$

where the parameters of the likelihood function correspond to maximum likelihood (ML) estimators [313].

ML estimators are the values of the free parameters, for example μ, which maximise the likelihood and are denoted as $\hat{\mu}$ in this example. To find the ML estimators, the likelihood function $L(\mu)$ must be differentiable. In the asymptotic limit of large statistics, the ML estimators are consistent, unbiased and efficient meaning that there exists no better estimator for the true value of the parameters [314].

In Eq. 7.6, two kinds of ML estimators are used. In the denominator, all parameters are chosen to maximise the likelihood. Therefore, they are called unconditional ML estimators $\hat{\mu}$ and $\hat{\boldsymbol{\theta}}$. In the numerator, a conditional ML estimator $\hat{\hat{\boldsymbol{\theta}}}$ is introduced which maximises the likelihood for a given value of μ. Since the unconditional ML estimate will always be larger or of the same size than the conditional ML estimate the ratio of the likelihoods can only take on values between zero and one.

7.1.3. $\mathrm{CL_s}$ Limits

For the statistical analysis presented, two hypotheses are defined:

The null hypothesis (H_0) corresponds to the background-only hypothesis which is characterised by $\mu = 0$.

The alternative hypothesis (H_1) takes into account background and signal with an assumed signal strength $\mu > 0$.

Exclusion limits are obtained for the alternative hypothesis at a certain confidence level (CL).

To define the confidence level, the frequentist probability value (p-value) defined as

$$p_\mu = \int_{q_\mu^{\text{obs}}}^{\infty} f(q_\mu|\mu, \boldsymbol{\theta}) dq_\mu \tag{7.7}$$

is considered. The p-value indicates with which probability data can be measured that is at least as incompatible with the predictions of the tested hypothesis as the observed test statistic q_μ^{obs}. In general, the distribution of the test statistic $f(q_\mu|\mu, \boldsymbol{\theta})$ must be determined by conducting toy experiments with randomised numbers of events and systematic central values $\boldsymbol{\theta}^0$. However, according to Wilks' theorem [315], $f(q_\mu|\mu, \boldsymbol{\theta})$ approaches a χ^2 distribution depending only on a single parameter μ if the data sample possesses sufficient statistics. This approximation of the asymptotic regime yields reasonable results with samples sizes of ten or more events, and will also be used for obtaining the exclusion limits in this thesis.

The 95% CL exclusion limit corresponds to the maximum value of μ for which the $p_\mu = 0.05$. However, this can result in spurious signal exclusions in regions poorly populated by backgrounds and is thus susceptible to statistical downward fluctuations in the data.

The CL_s method [310] has been developed to mitigate these spurious exclusions by not only testing the alternative hypothesis but also the null hypothesis simultaneously

$$1 - \text{CL}_\text{s} = \frac{p_\mu}{p_0} = \frac{\int_{q_\mu^{\text{obs}}}^{\infty} f(q_\mu|\mu, \boldsymbol{\theta}) dq_\mu}{\int_{q_\mu^{\text{obs}}}^{\infty} f(q_\mu|0, \boldsymbol{\theta}) dq_\mu}. \tag{7.8}$$

Compared to 95% CL, the 95% CL_s is more conservative, especially in the low statistics region due to normalising p_μ by p_0 of the null hypothesis. Thus, both sources of statistical uncertainties, the detection of a non-existent signal and the non-detection of an existing signal, are covered by the numerator and denominator of the CL_s exclusion limit, respectively.

7.2. Expected Upper Limits in the Boosted 1-Lepton Topology

In this analysis, upper limits on the cross section times branching ratio are quoted by maximising the likelihood using the shape of $m_{\text{vis+met}}$ as final discriminant between signal and background. Due to technical difficulties in the evaluation of the systematic uncertainties, the exclusion limits presented in the following only include statistical uncertainties on the data as well as the estimated backgrounds.

All MC predicted signal and background events are normalised to the full Run 2 integrated luminosity of $\int \mathcal{L} dt = 139$ fb^{-1}. The cross sections and branching ratios of the simulated background processes follow the SM predictions, while no theoretical cross section or branching ratio for the processes $pp \to X \to HH$ or $pp \to X \to SH \to b\bar{b}WW$ exist. Therefore,

$$\sigma(pp \to X \to HH) = 1\,\text{pb and} \tag{7.9}$$

$$\sigma(pp \to X \to SH) \times \mathcal{BR}(SH \to b\bar{b}WW) = 1\,\text{pb} \tag{7.10}$$

is at first arbitrarily assumed and are accounted for in the exclusion limit setting. The branching ratios follow the SM predictions with $\mathcal{BR}(HH \to b\bar{b}WW^*) = 0.248$ and $\mathcal{BR}(WW^{(*)} \to qq\ell\nu) = 0.438$.

To increase the sensitivity to all potential signals, all three signal regions, namely SRp2, SRp1 and SRf2, are considered in a combined limit setting. Furthermore, the normalisation of $t\bar{t}$, W+jets and non-prompt lepton backgrounds is constrained by fits in the CRs as discussed in Section 5.8.

Since the number of expected background events is very low for $m_{\text{vis+met}} \gtrsim 3\,\text{TeV}$ as shown in Figure 5.28 in Section 5.9, variable bin widths are introduced. Starting with 100 GeV bins in the range $0\,\text{GeV} \leq m_{\text{vis+met}} < 5400\,\text{GeV}$, bins that contain less than ten unweighted expected background events are iteratively merged with the neighbouring bin. Thus, all bins contain at least ten unweighted expected background events. This ensures that the fine binning in the region with high statistics is can be exploited, while the low statistics region will still allow a stable likelihood fit. The $m_{\text{vis+met}}$ distribution with this variable binning is shown in Figure 7.1 for the three signal regions and the HH or SH selection applied. Generally, the first bins and last bins are merged. Furthermore, more bins are merged when applying the stricter HH selection compared to applying the SH selection. SRp1 is the signal region with the largest number of background events and, thus, maintains a comparable fine binning up to high m_X values.

At the time of writing this thesis, the data in the signal regions has not been unblinded. Thus, an artificial dataset is constructed from the sum of expected background yields called Asimov dataset [313]. The Asimov dataset is used to obtain expected upper limits. The final observed limits can differ depending on statistical upward or downward fluctuations of the recorded data, which would result in smaller or larger upper limits on the signal cross section, respectively. The possibility that a signal is present in data also exists, although it is expected to not be measurable currently.

7.2.1. Resonant HH Production

The corresponding 95% CL$_\text{s}$ upper limits on $\sigma(pp \to X \to HH)$ combining all three signal regions are displayed in Figure 7.2 (a) with the values also being summarised in Table 7.1.

The sensitivity of the analysis continuously improves with increasing m_X, resulting in the lowest upper limit being $\sigma(pp \to X \to HH) = 2.8\,\text{fb}$ at $m_X = 5\,\text{TeV}$ considering only statistical uncertainties. The reason is due to the signal efficiency, which is very

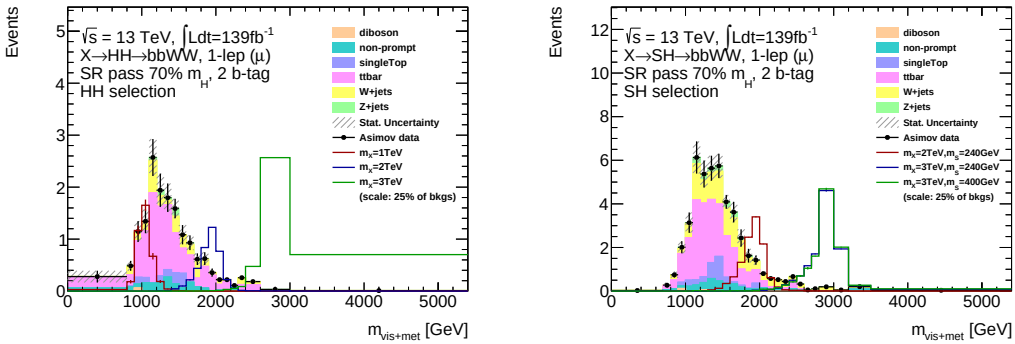

(a) SRp2 (HH selection)

(b) SRp2 (SH selection)

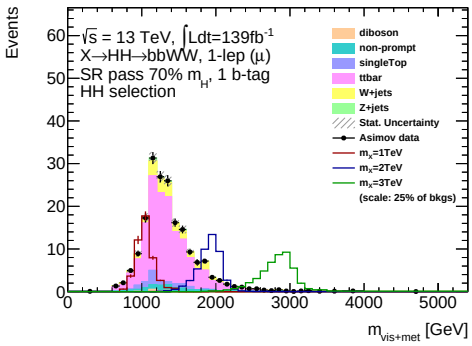

(c) SRp1 (HH selection)

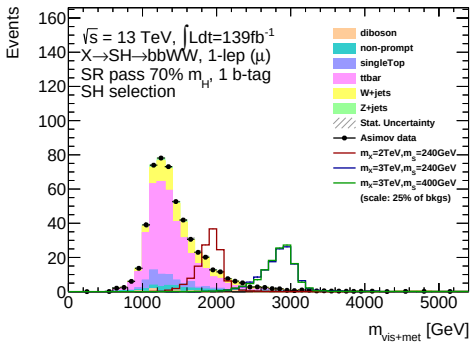

(d) SRp1 (SH selection)

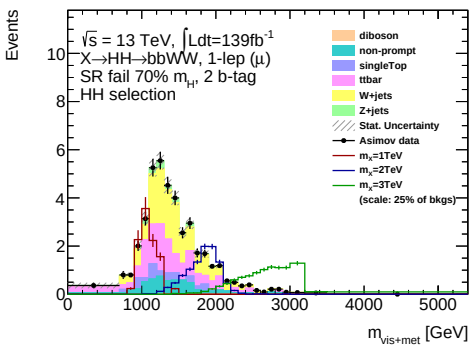

(e) SRf2 (HH selection)

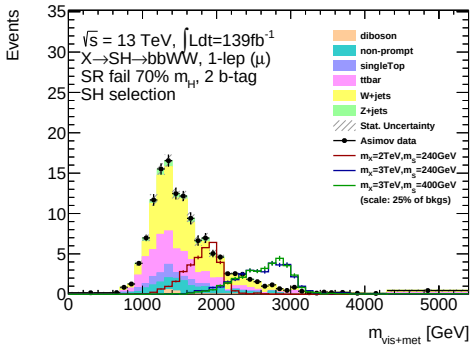

(f) SRf2 (SH selection)

Figure 7.1.: Diestribution of the final discriminant $m_{\text{vis+met}}$ in the three signal regions SRp2 (top), SRp1 (middle), SRf2 (bottom) with the HH selection (left) and SH selection (right) applied. The binning is adjusted to variable bin widths such that each bin contains at least ten unweighted background events. The signal is scaled to 25% of the signal and the data points labelled Asimov data correspond to the sum of backgrounds [26, 301].

low for $m_X \leq 1\,\text{TeV}$ because of the $p_{\text{T}}^{H\to b\bar{b}} > 500\,\text{GeV}$ cut, and the HH selection which favours events belonging to high m_X values. Additionally, in the $m_{\text{vis+met}} \geq 3\,\text{TeV}$ region where high $m_X \geq 3\,\text{TeV}$ signal events can be observed, nearly no background events are expected.

Furthermore, Figure 7.2 shows the exclusion limits obtained in the individual signal regions all applying the HH selection. While for $m_X \leq 2\,\text{TeV}$, the exclusion limits obtained in SRp2 purely drive the sensitivity of the combined limits, SRp1 becomes more relevant afterwards and drives the sensitivity for $m_X \geq 4\,\text{TeV}$. The reason is, that the decay products of Higgs boson decaying to a $b\bar{b}$-pair cannot be reconstructed as resolved VR track jets resulting in only one b-tag due to the high boost. SRf2 only contributes marginally to the combined exclusion limits.

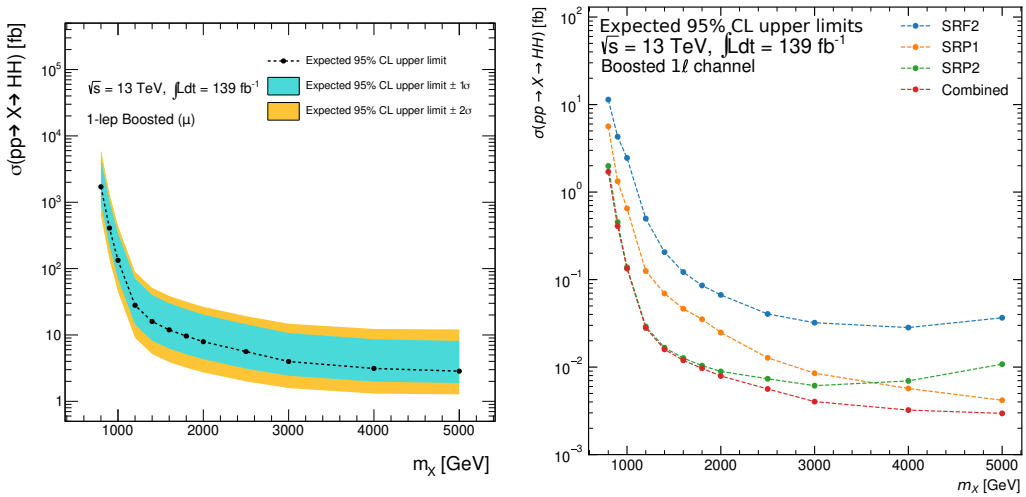

(a) with uncertainty bands

(b) split in signal regions

Figure 7.2.: Expected 95% CL_s upper limits on $\sigma(pp \to X \to HH)$ as a function of m_X. The HH selection is applied to all three signal regions. Only statistical uncertainties on the number of data and background events are considered [26,301].

7.2.2. Resonant SH Production

The picture is more complex for resonant SH production since here two mass values m_X and m_S need to be considered. Therefore, the expected 95% CL_s upper limits on $\sigma(pp \to X \to SH) \times \mathcal{BR}(SH \to b\bar{b}WW)$ are shown in dependence of m_X and m_S in Figure 7.3. The exclusion limits in the regions between the investigated mass point combinations are estimated using triangular interpolation resulting in the triangular shade patterns observed. The values of the upper limits corresponding to the investigated mass point combinations together with their 1σ and 2σ error intervals are also summarised in Table 7.2.

As in the search for resonant HH production, the sensitivity of the analysis generally

m_X [TeV]	0.8	0.9	1.0	1.2	1.4	1.6	1.8	2.0	2.5	3.0	4.0	5.0
-2σ [fb]	700	190	60	14	8	6	4.5	3.6	2.5	1.6	1.1	0.7
-1σ [fb]	1100	270	90	19	11	8	6.4	5.2	3.6	2.4	1.8	1.5
median [fb]	1700	410	130	28	16	12	9.6	7.9	5.6	4.0	3.1	2.8
$+1\sigma$ [fb]	2800	640	200	42	24	18	14.8	12.3	8.9	6.7	5.5	5.2
$+2\sigma$ [fb]	4400	960	300	62	35	27	22.1	18.6	13.6	10.8	9.2	9.2

Table 7.1.: Expected 95% $\mathrm{CL_s}$ upper limits on $\sigma(pp \to X \to HH)$ for several values of m_X using all three signal regions. The median as well as the $\pm 1\sigma$ and $\pm 2\sigma$ bounds are given. The HH selection is applied to all three signal regions. Only statistical uncertainties on the number of data and background events are considered [26].

increases for higher values of m_X for the same reasons. At the same time, the sensitivity decreases for increasing m_S since the signal topology becomes consistent with the split-boosted topology, which is explicitly vetoed by the preselection (see Section 5.4).

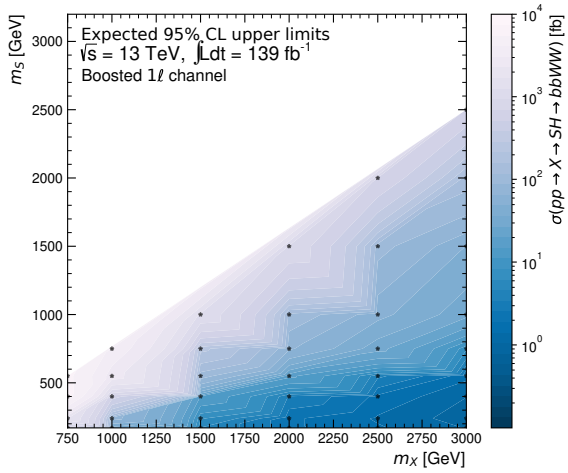

Figure 7.3.: Expected 95% $\mathrm{CL_s}$ upper limits on $\sigma(pp \to X \to SH) \times \mathcal{BR}(SH \to b\bar{b}WW)$ as a function of m_X and m_S. A triangulation interpolation is used between the available mass points. The SH selection is applied to all three SRs. Only statistical uncertainties on the number of data and background events are considered [26].

To be allow a more detailed study of the exclusion limits, for each considered m_X only the dependence on the m_S is shown in Figure 7.4. The decoupling of m_X and m_S actually reveals that, for $m_X \geq 2\,\mathrm{TeV}$, the sensitivity increases for $m_S = 240\,\mathrm{GeV}$ compared to lowest m_S value investigated which is 70 GeV smaller. This can be explained by the lepton identification and isolation which, in very boosted topologies, becomes worse and can be recovered by reducing the boost of the scalar particle decay products marginally. Therefore, the best limit is obtained for $m_X = 3\,\mathrm{TeV}$ and $m_S = 240\,\mathrm{GeV}$

m_S \ m_X	0.75 TeV	1.0 TeV	1.5 TeV	2.0 TeV	2.5 TeV	3.0 TeV
170 GeV	610^{+330}_{-200}	31^{+15}_{-10}	$3.7^{+1.7}_{-1.1}$	$2.0^{+1.0}_{-0.7}$	$1.5^{+0.8}_{-0.5}$	$1.0^{+0.6}_{-0.4}$
240 GeV	1800^{+800}_{-500}	74^{+36}_{-23}	$4.3^{+2.0}_{-1.3}$	$2.0^{+1.0}_{-0.7}$	$1.3^{+0.7}_{-0.4}$	$0.87^{+0.53}_{-0.32}$
400 GeV	6000^{+2600}_{-1800}	590^{+270}_{-180}	15^{+7}_{-5}	$3.3^{+1.7}_{-1.1}$	$1.8^{+0.9}_{-0.6}$	$1.1^{+0.6}_{-0.4}$
550 GeV	6000^{+2400}_{-1700}	2600^{+1200}_{-800}	100^{+44}_{-30}	16^{+8}_{-5}	$3.7^{+1.9}_{-1.2}$	$1.5^{+0.9}_{-0.6}$
750 GeV	-	3800^{+1500}_{-1100}	230^{+100}_{-70}	68^{+32}_{-21}	30^{+15}_{-10}	$6.5^{+3.8}_{-2.4}$
1000 GeV	-	-	1190^{+470}_{-340}	108^{+50}_{-33}	53^{+27}_{-17}	29^{+16}_{-10}
1500 GeV	-	-	-	900^{+350}_{-250}	98^{+50}_{-32}	49^{+26}_{-16}
2000 GeV	-	-	-	-	690^{+280}_{-200}	140^{+70}_{-40}
2500 GeV	-	-	-	-	-	650^{+280}_{-190}

Table 7.2.: Expected 95% $\mathrm{CL_s}$ upper limits on $\sigma(pp \to X \to SH) \times \mathcal{BR}(SH \to b\bar{b}WW)$ for several values of m_S and m_X using all three signal regions. The median as well as the $\pm 1\sigma$ bounds are given in fb. The SH selection is applied to all three signal regions. Only statistical uncertainties on the number of data and background events are considered [26].

with $\sigma(pp \to X \to SH) \times \mathcal{BR}(SH \to b\bar{b}WW) = 0.87\,\mathrm{fb}$ considering only statistical uncertainties.

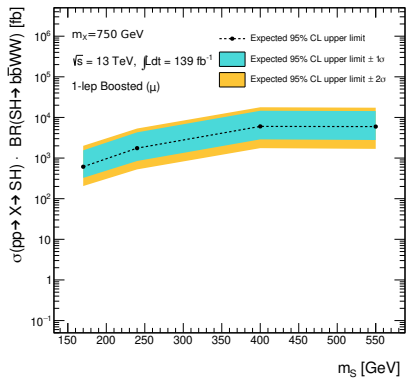

(a) $m_X = 0.75\,\text{TeV}$

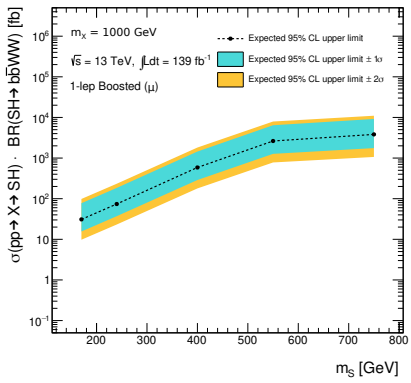

(b) $m_X = 1.0\,\text{TeV}$

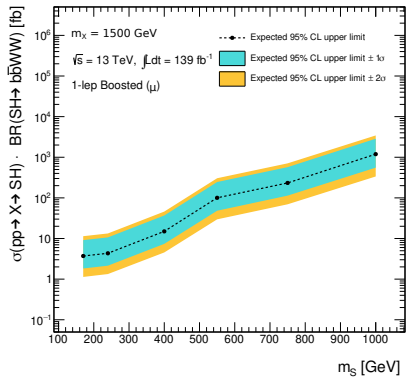

(c) $m_X = 1.5\,\text{TeV}$

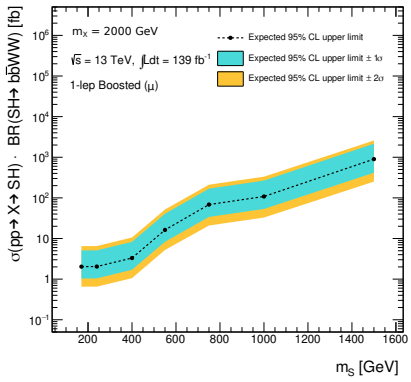

(d) $m_X = 2.0\,\text{TeV}$

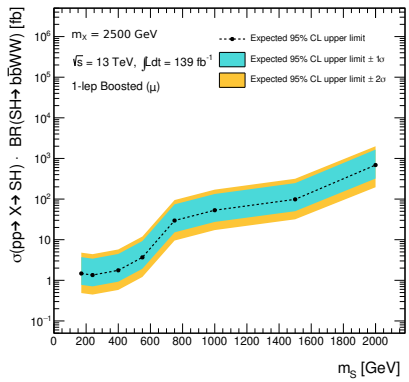

(e) $m_X = 2.5\,\text{TeV}$

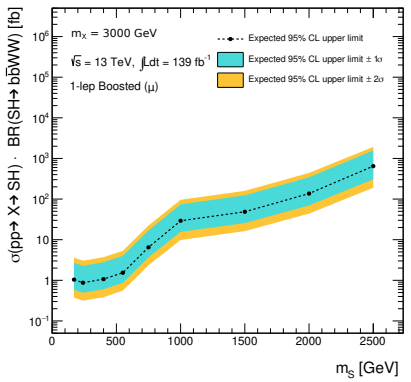

(f) $m_X = 3.0\,\text{TeV}$

Figure 7.4.: Expected 95% CL_s upper limits on $\sigma(pp \to X \to SH) \times \mathcal{BR}(SH \to b\bar{b}WW)$ as a function of m_S for several values of m_X separately. The SH selection is applied to all three SRs. Only statistical uncertainties on the number of data and background events are considered [26, 301].

CHAPTER 8

Conclusions and Outlook

This thesis presents the search for resonant Higgs boson pair production (HH) as well as resonant production of a new scalar particle in conjunction with a Higgs boson (SH) using the full Run 2 dataset recorded by ATLAS and corresponding to $\int \mathcal{L} dt = 139$ fb^{-1}. The obtained results can be interpreted and constrain the investigated phase space in the context of various models. With the Higgs boson coupling strength increasing with the mass of particles to which it couples, exploring the extended Higgs sector is a promising approach to search for BSM particles which do not interact with other SM particles.

The analysis is performed in the $b\bar{b}WW^*$ decay channel with a muon in the final state. Due to the interplay between the mass scales m_X and m_S, various interesting topologies arise of which the boosted topology is studied in detail in this thesis. The mass of the scalar resonance considered ranges between $m_X = 800\,\text{GeV}$ and $m_X = 5\,\text{TeV}$ for HH production and between $m_X = 750\,\text{GeV}$ to $m_X = 3\,\text{TeV}$ for SH production. The latter introduces a second mass scale m_S which covers the range between $m_S = 170\,\text{GeV}$ and $m_S = 2.5\,\text{TeV}$ where $m_S < m_X - m_H$ is required.

The boosted topology is characterised by one charged lepton, two large-R jets and missing transverse energy in the event, where one large-R jet reconstructs the $H \to b\bar{b}$ candidate and one the W_{had} candidate. The expected overlap between the charged lepton and the W_{had} candidate results in a unique signature not present in many backgrounds. However, this topology also comes with challenges in the reconstruction of the lepton and the overlap between leptonic and hadronic energies. Therefore, a novel approach in the large-R jet reconstruction is pursued with the track assisted reclustered (TAR) jets which provide good resolution in dense environments, as well as a disentanglement from the lepton, such that lepton and TAR jet can be treated as separate objects despite their geometrical overlap.

The backgrounds in this search are classified into prompt and non-prompt lepton backgrounds. The prompt lepton backgrounds are estimated by simulation with a correction

for their normalisation by a fit to data in dedicated control regions. In contrast, the non-prompt lepton background is estimated using a data driven approach called the matrix method. The dominant backgrounds in the analysis signal regions are the prompt lepton $t\bar{t}$ and W+jets backgrounds, which contribute over 80% of the background events.

To obtain the highest possible sensitivity to the different signals, three signal regions are defined. These are based on the $H \to b\bar{b}$ candidate passing or failing a predetermined mass window and its number of b-tags. Furthermore, dedicated selections for HH and SH signals, respectively, are applied. Since no excess over the expected number of background events is anticipated, expected 95% $\mathrm{CL_s}$ upper limits are evaluated on the cross section of $X \to HH$ as well as on the cross section and branching ratio of $X \to SH \to b\bar{b}WW$. These exclusion limits only consider statistical uncertainties on the number of data and background events.

The best upper limits are set on $m_X = 5\,\mathrm{TeV}$ with $\sigma(pp \to X \to HH) = 2.8\,\mathrm{fb}$ and on $m_X = 3\,\mathrm{TeV}$ and $m_S = 240\,\mathrm{GeV}$ with $\sigma(pp \to X \to SH) \times \mathcal{BR}(SH \to b\bar{b}WW) = 0.87\,\mathrm{fb}$. While the best upper limit on the HH production is comparable with the best exclusion limit obtained by the boosted 0-lepton topology in the $b\bar{b}WW^*$ decay channel [26] and by the boosted $X \to HH \to b\bar{b}b\bar{b}$ analysis [12], it is the first time that limits on SH production are set in this phase space.

A full treatment of systematic uncertainties in this analysis is still pending. Nuisance parameters associated to experimental, modelling and non-prompt lepton background estimate uncertainties are identified and a first estimate of their impact is made where the modelling uncertainties of the $t\bar{t}$ and W+jets backgrounds have the largest impacts. Since the analysis as a search is expected to be dominated by statistical uncertainties, a worsening of the currently evaluated expected upper limits by more than an order of magnitude is not anticipated.

With the LHC starting its Run 3 in summer 2022, a future search using the Run 3 dataset will profit from much more data statistics in the coming years, addressing the limiting factor of the current search. Furthermore, reconstruction algorithms and analysis strategies will be improved and updated.

For the future search, it is planned to also include the electron channel in the analysis. To exploit the resulting increase of the branching ratio by a factor of two, studies are currently conducted to improve the reconstruction of electrons in dense environments by a dedicated ID working point [316]. There are also plans to design a tagger for the identification of jets containing overlapping with an electron using deep learning methods [317].

Further improvements can result from using more advanced as techniques such as multivariate algorithms. These have already been studied in the context of the neutrino reconstruction in the boosted 1-lepton topology and, moreover, are pursued in the resolved 1-lepton topology [207] and many other HH analysis [14, 18]. All these use cases show improvements with respect to a simple cut based analysis.

The discovery of resonant HH or SH production would start a new chapter of particle physics and offer a completely new field of research. Depending on the observed properties, it could either be the window to the dark part of the universe or help under-

standing the some of the open questions of the light universe such as matter–anti-matter asymmetry. If the properties of the new resonance(s) are consistent with 2HDM models for example, an additional source of CP violation could be present.

On the other hand, setting more and more stringent exclusion limits helps to constrain the phase space where new phenomena could manifest. This allows to focus and optimise searches on these interesting phase space regions and thus, increase the discovery probability. By comparing these upper limits to theoretical predictions, benchmarks of models can be excluded. This makes room for novel models and theories which could provide the breakthroughs in explaining the universe.

The last chapter of the search for resonant HH and SH production is not yet written. We know that something is out there – we just have to find the correct path to catch it.

Thank you

Zwei Dinge sind unendlich, das Universum und die menschliche Dummheit, aber bei dem Universum bin ich mir noch nicht ganz sicher.

– Albert Einstein

If somebody – like me – tries to explain the universe in all its endlessness and open questions by particles so small that one will never be able to see them, that somebody must be either very brave or foolish. Luckily, I was not alone.

I like to thank everybody who accompanied me on my way to finally finishing this thesis – just ensuring that everybody who think they deserved a *Thank you* actually got one. But if you read my thesis to this point, you might correctly guess that that my acknowledgements are not done by a one-liner.

Mien hööchste Dank geiht an mien Doktervader **Stan Lai**. Dat weer, is un schall mi jümmens en Ehr wesen, dat ik dat eerste Liddmaat – sogoor al vör di sülms – in dien Warkgrupp wesen dröff. Döör dien unfastboret Weten, dien politisch Korrektheit un diene harte Aart, hest du mi in de Deelkenphysik quasi groottrucken. Dorbi weet ik besünners to schätzen, dat diene Döör jümmens open stunn un du man blot denn de „Boss“ büst, wenn sik dat nich verhinnern lett. Opletzt will ik di torügg besinnen, dat du toseggt hest, mi bestahn to loten, wenn de Dokterarbeit op Plattdüütsch upsett ward – un de Danksaag is döörut en deel von en Dokterarbeit.

I also like to thank **Ariane Frey** for agreeing to be the co-referee of this thesis. Seven and a half years ago, I started with your *Einführung in die Kern- und Teilchenphysik* lecture and the circle now closes with you also grading my last particle physics “exam”.

Furthermore, I also want to thank my (former) colleagues and students – most of you apparently managed to leave the institute before me.

Michel Janus for your support during my Bachelor’s degree and beyond and for always being my role model in student supervision.

Jason Veatch for his support during my Master’s and PhD degree despite you being busy with *HH*ighly important convenor duties in the last year.

Timo Dreyer for being my favourite neighbour, for keeping up with my ideas on mas-

terclasses and for not sharing Serhat's and Lino's humour.

Petar Bokan for our physics and people – mostly people discussions that have been always very fruitful, especially if topped with ice cream or hot chocolate.

Serhat Ördek and Lino Gerlach for trying really hard to convince me of your humour despite the constant lack of success.

Ishan Pokharel for connecting everybody even across working groups by inviting them to poker nights at Timo's place and for being the best source of instute gossip.

Joshua Beirer for surviving being the first student I (inofficially) supervised and even coming back to the group and my supervision. This definitely makes you my favourite sla... I mean student.

Nils Gillwald for the legendary `#WorksOutOfTheBox`. Despite all the difficulties and frustration, it was always fun to work together.

Naman K. Bhalla for dealing with the unthankful fitting framework and your great personality and thoughts – but you should rethink your office hours.

Yannik Buch and Janne van den Hout for being very productive during your Bachelor's thesis and allowed a progress of the analysis.

Due to two years Corona pandemic, it was very hard to get to know the "new" colleagues but I still like to thank **Andrès Melo**, **Julian Utehs** and **Joana Niermann** for preserving the atmosphere of AG Lai after all the "old" people left.

I would also like to thank the $\boldsymbol{b\bar{b}VV^{(*)}}$ **analysis team** for their support, discussions and friendly as well as personal working environment. Every analysis encounters technical issues but the infamous second event crash is definitely unique to us! However, the results that we have seen so far seem definitely worth all the frustration.

Abschließend möchte ich mich bei allen bedanken, die mein Leben außerhalb der Teilchenphysik bereichern.

Vera und Michi, dafür, dass ihr schon in der Schulzeit dafür gesorgt habt, dass ich nicht nur fließend Physik spreche, sondern wir alle auch einen Titel im Ausdenken blödsinniger Geschichten gewisser *Alter Egos* verdient hätten.

Lars, dafür uns das Schicksal damals in der O-Phase und(!) als Nachbarn zusammen geführt hat. Die zahlreichen Abende, an denen ich zu dir hoch-„geschlappt„bin, sind mit die schönsten Erinnerungen meiner Studienzeit.

Mama und Papa, ich kann euch gar nicht genug dafür danken, dass ihr mich zu dem Menschen geformt habt, der ich heute bin. Ich bewundere euren unbrechbaren Willen mir alles zu ermöglichen, was in eurer Macht steht – auch wenn das bedeutet, sich durch eine Bachelorarbeit voller halber Sätze zu quälen. Für mich seid ihr die besten Eltern der Welt.

Simon, für einfach alles. Du bist zu mir gezogen, obwohl man den Bayern bekanntlich nicht aus seinem Wald bekommt. Du bleibst da, obwohl ich echt... anstrengend bin, wenn es nicht nach meinem Kopf geht. Mit deiner Familie hast du mir eine wundervolle weitere Heimat geschenkt. Du machst mich glücklicher, als jede Schokolade es je könnte – übrigens, danke, dass du meinen Schokoladenkonsum während der Schreibphase der Doktorarbeit unkommentiert gelassen hast. Ich liebe dich.

Bibliography

[1] ATLAS Collaboration, *Observation of a new particle in the search for the Standard Model Higgs boson with the ATLAS detector at the LHC*, Phys. Lett. B **716** (2012) 1.

[2] CMS Collaboration, *Observation of a new boson at a mass of 125 GeV with the CMS experiment at the LHC*, Phys. Lett. B **716** (2012) 30.

[3] Particle Data Group Collaboration, P. A. Zyla et al., *Review of Particle Physics*, PTEP **2020** (2020) 083C01.

[4] S. Dawson, S. Dittmaier, and M. Spira, *Neutral Higgs-boson pair production at hadron colliders: QCD corrections*, Phys. Rev. **D58** (1998) 115012.

[5] D. de Florian and J. Mazzitelli, *Higgs boson pair production at next-to-next-to-leading order in QCD*, Phys. Rev. Lett. **111** (2013) 201801.

[6] D. Y. Shao, et al., *Threshold resummation effects in Higgs boson pair production at the LHC*, JHEP **07** (2013) 169.

[7] D. de Florian and J. Mazzitelli, *Higgs pair production at next-to-next-to-leading logarithmic accuracy at the LHC*, JHEP **09** (2015) 053.

[8] S. Borowka, et al., *Higgs Boson Pair Production in Gluon Fusion at Next-to-Leading Order with Full Top-Quark Mass Dependence*, Phys. Rev. Lett. **117** (2016) 012001.

[9] J. Baglio, et al., *Gluon fusion into Higgs pairs at NLO QCD and the top mass scheme*, Eur. Phys. J. C **79** (2019) 459.

[10] M. Grazzini, et al., *Higgs boson pair production at NNLO with top quark mass effects*, JHEP **05** (2018) 059.

[11] J. Baglio, et al., *$gg \to HH$: Combined uncertainties*, Phys. Rev. D **103** (2021) 056002.

[12] ATLAS Collaboration, *Search for pair production of Higgs bosons in the $b\bar{b}b\bar{b}$ final state using proton–proton collisions at $\sqrt{s} = 13$ TeV with the ATLAS detector*, Phys. Rev. D **94** (2016) 052002.

[13] ATLAS Collaboration, *Search for Higgs boson pair production in the $b\bar{b}WW^*$ decay mode at $\sqrt{s} = 13$ TeV with the ATLAS detector*, JHEP **04** (2019) 092.

[14] ATLAS Collaboration, *A search for resonant and non-resonant Higgs boson pair production in the $b\bar{b}\tau^+\tau^-$ decay channel in pp collisions at $\sqrt{s} = 13$ TeV with the ATLAS detector*, Phys. Rev. Lett. **121** (2018) 191801.

[15] ATLAS Collaboration, *Search for Higgs boson pair production in the $\gamma\gamma b\bar{b}$ final state with 13 TeV pp collision data collected by the ATLAS experiment*, JHEP **11** (2018) 040.

[16] ATLAS Collaboration, *Search for Higgs boson pair production in the $WW^{(*)}WW^{(*)}$ decay channel using ATLAS data recorded at $\sqrt{s} = 13$ TeV*, JHEP **05** (2019) 124.

[17] ATLAS Collaboration, *Search for Higgs boson pair production in the $\gamma\gamma WW^*$ channel using pp collision data recorded at $\sqrt{s} = 13$ TeV with the ATLAS detector*, Eur. Phys. J. C **78** (2018) 1007.

[18] ATLAS Collaboration, *Search for non-resonant Higgs boson pair production in the $bb\ell\nu\ell\nu$ final state with the ATLAS detector in pp collisions at $\sqrt{s} = 13$ TeV*, Phys. Lett. B **801** (2020) 135145.

[19] CMS Collaboration, *Search for nonresonant Higgs boson pair production in the $b\bar{b}b\bar{b}$ final state at $\sqrt{s} = 13$ TeV*, JHEP **04** (2019) 112.

[20] CMS Collaboration, *Search for production of Higgs boson pairs in the four b quark final state using large-area jets in proton–proton collisions at $\sqrt{s} = 13$ TeV*, JHEP **01** (2019) 040.

[21] CMS Collaboration, *Search for resonant and nonresonant Higgs boson pair production in the $b\bar{b}\ell\nu\ell\nu$ final state in proton–proton collisions at $\sqrt{s} = 13$ TeV*, JHEP **01** (2018) 054.

[22] CMS Collaboration, *Search for Higgs boson pair production in events with two bottom quarks and two tau leptons in proton–proton collisions at $\sqrt{s} = 13$ TeV*, Phys. Lett. B **778** (2018) 101.

[23] CMS Collaboration, *Search for Higgs boson pair production in the $\gamma\gamma b\bar{b}$ final state in pp collisions at $\sqrt{s} = 13$ TeV*, Phys. Lett. B **788** (2019) 7.

[24] ATLAS Collaboration, *Combination of searches for Higgs boson pairs in pp collisions at $\sqrt{s} = 13$ TeV with the ATLAS detector*, Phys. Lett. B **800** (2020) 135103.

[25] CMS Collaboration, *Combination of Searches for Higgs Boson Pair Production in Proton–Proton Collisions at $\sqrt{s} = 13$ TeV*, Phys. Rev. Lett. **122** (2019) 121803.

[26] ATLAS Collaboration, *Search for resonant boosted HH and SH production in the $b\bar{b}VV$ decay channel with 0 or 1 leptons in the final state using the full Run 2 ATLAS data*, 2021.

[27] LHC Higgs Cross Section Working Group Collaboration, D. de Florian et al., *Handbook of LHC Higgs Cross Sections: 4. Deciphering the Nature of the Higgs Sector*, `arXiv:1610.07922 [hep-ph]`.

[28] F. Halzen and A. D. Martin, *Quarks and Leptons: An Introductory Course in Modern Particle Physics*. Wiley, 1984.

[29] M. E. Peskin and D. V. Schroeder, *An Introduction to quantum field theory*. Addison-Wesley, 1995.

[30] M. Thomson, *Modern particle physics*. Cambridge University Press, 2013.

[31] J. Lagrange, *Mécanique analytique*. No. Bd. 1 in Mécanique analytique. Courcier, 1811.

[32] J. Lagrange, *Mécanique analytique*. No. Bd. 2 in Mécanique analytique. Courcier, 1815.

[33] R. P. Feynman, *The Theory of positrons*, Phys. Rev. **76** (1949) 749–759.

[34] R. P. Feynman, *Space - time approach to quantum electrodynamics*, Phys. Rev. **76** (1949) 769–789.

[35] E. Noether, *Invariant Variation Problems*, Gott. Nachr. **1918** (1918) 235–257.

[36] J. J. Thomson, *Cathode rays*, Phil. Mag. Ser. 5 **44** (1897) 293–316.

[37] S. H. Neddermeyer and C. D. Anderson, *Note on the Nature of Cosmic Ray Particles*, Phys. Rev. **51** (1937) 884–886.

[38] M. L. Perl et al., *Evidence for Anomalous Lepton Production in e+ - e- Annihilation*, Phys. Rev. Lett. **35** (1975) 1489–1492.

[39] C. L. Cowan, et al., *Detection of the free neutrino: A Confirmation*, Science **124** (1956) 103–104.

[40] G. Danby, et al., *Observation of High-Energy Neutrino Reactions and the Existence of Two Kinds of Neutrinos*, Phys. Rev. Lett. **9** (1962) 36–44.

[41] DONUT Collaboration, K. Kodama et al., *Observation of tau neutrino interactions*, Phys. Lett. B **504** (2001) 218–224.

[42] E. D. Bloom et al., *High-Energy Inelastic e p Scattering at 6-Degrees and 10-Degrees*, Phys. Rev. Lett. **23** (1969) 930–934.

[43] M. Breidenbach, et al., *Observed behavior of highly inelastic electron-proton scattering*, Phys. Rev. Lett. **23** (1969) 935–939.

[44] J. D. Bjorken and E. A. Paschos, *Inelastic Electron Proton and gamma Proton Scattering, and the Structure of the Nucleon*, Phys. Rev. **185** (1969) 1975–1982.

[45] SLAC-SP-017 Collaboration, J. E. Augustin et al., *Discovery of a Narrow Resonance in e^+e^- Annihilation*, Phys. Rev. Lett. **33** (1974) 1406–1408.

[46] E598 Collaboration, J. J. Aubert et al., *Experimental Observation of a Heavy Particle J*, Phys. Rev. Lett. **33** (1974) 1404–1406.

[47] S. W. Herb et al., *Observation of a Dimuon Resonance at 9.5-GeV in 400-GeV Proton-Nucleus Collisions*, Phys. Rev. Lett. **39** (1977) 252–255.

[48] CDF Collaboration, F. Abe et al., *Observation of top quark production in $\bar{p}p$ collisions*, Phys. Rev. Lett. **74** (1995) 2626–2631.

[49] D0 Collaboration, S. Abachi et al., *Observation of the top quark*, Phys. Rev. Lett. **74** (1995) 2632–2637.

[50] A. Einstein, *Über einem die Erzeugung und Verwandlung des Lichtes betreffenden heuristischen Gesichtspunkt*, Annalen der physik **4** (1905).

[51] PLUTO Collaboration, C. Berger et al., *Evidence for Gluon Bremsstrahlung in e+ e- Annihilations at High-Energies*, Phys. Lett. B **86** (1979) 418–425.

[52] TASSO Collaboration, R. Brandelik et al., *Evidence for Planar Events in e+ e- Annihilation at High-Energies*, Phys. Lett. B **86** (1979) 243–249.

[53] MARK-J Collaboration, D. P. Barber et al., *Discovery of Three Jet Events and a Test of Quantum Chromodynamics at PETRA Energies*, Phys. Rev. Lett. **43** (1979) 830.

[54] UA1 Collaboration, G. Arnison et al., *Experimental Observation of Isolated Large Transverse Energy Electrons with Associated Missing Energy at $\sqrt{s} = 540$ GeV*, Phys. Lett. B **122** (1983) 103–116.

[55] UA2 Collaboration, M. Banner et al., *Observation of Single Isolated Electrons of High Transverse Momentum in Events with Missing Transverse Energy at the CERN anti-p p Collider*, Phys. Lett. B **122** (1983) 476–485.

[56] UA1 Collaboration, G. Arnison et al., *Experimental Observation of Lepton Pairs of Invariant Mass Around 95-GeV/c**2 at the CERN SPS Collider*, Phys. Lett. B **126** (1983) 398–410.

[57] UA2 Collaboration, P. Bagnaia et al., *Evidence for $Z^0 \to e^+e^-$ at the CERN $\bar{p}p$ Collider*, Phys. Lett. B **129** (1983) 130–140.

[58] C. D. Anderson, *The Positive Electron*, Phys. Rev. **43** (1933) 491–494.

[59] C.-N. Yang and R. L. Mills, *Conservation of Isotopic Spin and Isotopic Gauge Invariance*, Phys. Rev. **96** (1954) 191–195.

[60] G. 't Hooft and M. J. G. Veltman, *Regularization and Renormalization of Gauge Fields*, Nucl. Phys. **B44** (1972) 189–213.

[61] P. A. M. Dirac, *Quantum theory of emission and absorption of radiation*, Proc. Roy. Soc. Lond. A **114** (1927) 243.

[62] E. Fermi, *Quantum Theory of Radiation*, Rev. Mod. Phys. **4** (1932) 87–132.

[63] S. Tomonaga, *On a relativistically invariant formulation of the quantum theory of wave fields*, Prog. Theor. Phys. **1** (1946) 27–42.

[64] J. S. Schwinger, *On Quantum electrodynamics and the magnetic moment of the electron*, Phys. Rev. **73** (1948) 416–417.

[65] J. S. Schwinger, *Quantum electrodynamics. I A covariant formulation*, Phys. Rev. **74** (1948) 1439.

[66] R. P. Feynman, *Space-time approach to nonrelativistic quantum mechanics*, Rev. Mod. Phys. **20** (1948) 367–387.

[67] R. P. Feynman, *Mathematical formulation of the quantum theory of electromagnetic interaction*, Phys. Rev. **80** (1950) 440–457.

[68] F. J. Dyson, *The Radiation theories of Tomonaga, Schwinger, and Feynman*, Phys. Rev. **75** (1949) 486–502.

[69] F. J. Dyson, *The S matrix in quantum electrodynamics*, Phys. Rev. **75** (1949) 1736–1755.

[70] W. Pauli, *Dear radioactive ladies and gentlemen*, Phys. Today **31N9** (1978) 27.

[71] E. Fermi, *An attempt of a theory of beta radiation. 1.*, Z. Phys. **88** (1934) 161–177.

[72] C. S. Wu, et al., *Experimental Test of Parity Conservation in β Decay*, Phys. Rev. **105** (1957) 1413–1414.

[73] M. Goldhaber, L. Grodzins, and A. W. Sunyar, *Helicity of Neutrinos*, Phys. Rev. **109** (1958) 1015–1017.

[74] S. L. Glashow, J. Iliopoulos, and L. Maiani, *Weak Interactions with Lepton-Hadron Symmetry*, Phys. Rev. D **2** (1970) 1285–1292.

[75] M. Kobayashi and T. Maskawa, *CP Violation in the Renormalizable Theory of Weak Interaction*, Prog. Theor. Phys. **49** (1973) 652–657.

[76] R. P. Feynman and M. Gell-Mann, *Theory of Fermi interaction*, Phys. Rev. **109** (1958) 193–198.

[77] E. C. G. Sudarshan and R. e. Marshak, *Chirality invariance and the universal Fermi interaction*, Phys. Rev. **109** (1958) 1860–1860.

[78] S. L. Glashow, *Partial Symmetries of Weak Interactions*, Nucl. Phys. **22** (1961) 579–588.

[79] S. Weinberg, *A Model of Leptons*, Phys. Rev. Lett. **19** (1967) 1264–1266.

[80] A. Salam, *Weak and Electromagnetic Interactions*, Proceedings of the 8th Nobel symposium, Ed. N. Svartholm, Almqvist & Wiskell, 1968, **Conf. Proc. C680519** (1968) 367–377.

[81] M. Gell-Mann, *The Eightfold Way: A Theory of strong interaction symmetry*,.

[82] Y. Nambu and G. Jona-Lasinio, *Dynamical Model of Elementary Particles Based on an Analogy with Superconductivity. I*, Phys. Rev. **122** (1961) 345–358.

[83] Y. Nambu and G. Jona-Lasinio, *Dynamical Model of Elementary Particles Based on an Analogy with Superconductivity. II*, Phys. Rev. **124** (1961) 246–254.

[84] M. Gell-Mann, *A Schematic Model of Baryons and Mesons*, Phys. Lett. **8** (1964) 214–215.

[85] G. Zweig, *Developments in the Quark Theory of Hadrons. Vol. 1. 1964 - 1978: An SU(3) model for strong interaction symmetry and its breaking. Version 2.* No. CERN-TH-412, NP-14146, PRINT-64-170. 2, 1964.

[86] D. J. Gross and F. Wilczek, *Ultraviolet Behavior of Nonabelian Gauge Theories*, Phys. Rev. Lett. **30** (1973) 1343–1346.

[87] H. D. Politzer, *Reliable Perturbative Results for Strong Interactions?*, Phys. Rev. Lett. **30** (1973) 1346–1349.

[88] H. Fritzsch, M. Gell-Mann, and H. Leutwyler, *Advantages of the Color Octet Gluon Picture*, Phys. Lett. B **47** (1973) 365–368.

[89] P. W. Higgs, *Broken symmetries, massless particles and gauge fields*, Phys. Lett. **12** (1964) 132–133.

[90] F. Englert and R. Brout, *Broken symmetry and the mass of gauge vector mesons*, Phys. Rev. Lett. **13** (1964) 321–323.

[91] P. W. Higgs, *Broken symmetries and the masses of gauge bosons*, Phys. Rev. Lett. **13** (1964) 508–509.

[92] G. Guralnik, C. Hagen, and T. Kibble, *Global conservation laws and massless particles*, Phys. Rev. Lett. **13** (1964) 585–587.

[93] P. W. Higgs, *Spontaneous symmetry breakdown without massless bosons*, Phys. Rev. **145** (1966) 1156–1163.

[94] T. Kibble, *Symmetry breaking in non-Abelian gauge theories*, Phys. Rev. **155** (1967) 1554–1561.

[95] J. Goldstone, *Field Theories with Superconductor Solutions*, Nuovo Cim. **19** (1961) 154–164.

[96] J. Goldstone, A. Salam, and S. Weinberg, *Broken Symmetries*, Phys. Rev. **127** (1962) 965–970.

[97] MuLan Collaboration, D. M. Webber et al., *Measurement of the Positive Muon Lifetime and Determination of the Fermi Constant to Part-per-Million Precision*, Phys. Rev. Lett. **106** (2011) 041803.

[98] ATLAS and CMS Collaborations, *Combined Measurement of the Higgs Boson Mass in pp Collisions at* $\sqrt{s} = 7$ *and* $8\,TeV$ *with the ATLAS and CMS Experiments*, Phys. Rev. Lett. **114** (2015) 191803.

[99] ATLAS Collaboration, *Study of the spin and parity of the Higgs boson in diboson decays with the ATLAS detector*, Eur. Phys. J. C **75** (2015) 476.

[100] ATLAS Collaboration, *Measurements of the Higgs boson production and decay rates and coupling strengths using pp collision data at* $\sqrt{s} = 7$ *and* $8\,TeV$ *in the ATLAS experiment*, Eur. Phys. J. C **76** (2016) 6.

[101] ATLAS Collaboration, *Combined measurements of Higgs boson production and decay using up to* $80\,fb^{-1}$ *of proton–proton collision data at* $\sqrt{s} = 13\,TeV$ *collected with the ATLAS experiment*, Phys. Rev. D **101** (2020) 012002.

[102] CMS Collaboration, *Constraints on the spin-parity and anomalous HVV couplings of the Higgs boson in proton collisions at* 7 *and* $8\,TeV$, Phys. Rev. D **92** (2015) 012004.

[103] CMS Collaboration, *Precise determination of the mass of the Higgs boson and tests of compatibility of its couplings with the standard model predictions using proton collisions at* 7 *and* $8\,TeV$, Eur. Phys. J. C **75** (2015) 212.

[104] CMS Collaboration, *Combined measurements of Higgs boson couplings in proton–proton collisions at* $\sqrt{s} = 13$ *TeV*, Eur. Phys. J. C **79** (2019) 421.

[105] LHC Higgs Cross Section Working Group, *Handbook of LHC Higgs Cross Sections: 4. Deciphering the Nature of the Higgs Sector*, `arXiv:1610.07922 [hep-ph]`.

[106] C. Anastasiou, et al., *Higgs Boson Gluon-Fusion Production in QCD at Three Loops*, Phys. Rev. Lett. **114** (2015) 212001.

[107] C. Anastasiou, et al., *High precision determination of the gluon fusion Higgs boson cross-section at the LHC*, JHEP **05** (2016) 058.

[108] Y. Li, et al., *Soft-virtual corrections to Higgs production at* N^3LO, Phys. Rev. **D91** (2015) 036008.

[109] U. Aglietti, et al., *Two-loop light fermion contribution to Higgs production and decays*, Phys. Lett. B **595** (2004) 432–441.

[110] S. Actis, et al., *NLO electroweak corrections to Higgs boson production at hadron colliders*, Phys. Lett. B **670** (2008) 12–17.

[111] R. V. Harlander and W. B. Kilgore, *Next-to-next-to-leading order Higgs production at hadron colliders*, Phys. Rev. Lett. **88** (2002) 201801.

[112] C. Anastasiou and K. Melnikov, *Higgs boson production at hadron colliders in NNLO QCD*, Nucl. Phys. **B646** (2002) 220–256.

[113] V. Ravindran, J. Smith, and W. L. van Neerven, *NNLO corrections to the total cross-section for Higgs boson production in hadron hadron collisions*, Nucl. Phys. **B665** (2003) 325–366.

[114] J. Baglio and A. Djouadi, *Higgs production at the lHC*, JHEP **03** (2011) 055.

[115] A. Djouadi, M. Spira, and P. Zerwas, *Production of Higgs bosons in proton colliders: QCD corrections*, Phys. Lett. **B264** (1991) 440–446.

[116] S. Dawson, *Radiative corrections to Higgs boson production*, Nucl. Phys. **B359** (1991) 283–300.

[117] M. Spira, et al., *Higgs boson production at the LHC*, Nucl. Phys. **B453** (1995) 17–82.

[118] ATLAS Collaboration, *A search for the dimuon decay of the Standard Model Higgs boson with the ATLAS detector*, Phys. Lett. B **812** (2021) 135980.

[119] A. Einstein, *The Foundation of the General Theory of Relativity*, Annalen Phys. **49** (1916) 769–822.

[120] M. B. Green, J. H. Schwarz, and E. Witten, *Superstring Theory. Vol. 1: Introduction.* Cambridge Monographs on Mathematical Physics. 7, 1988.

[121] M. B. Green, J. H. Schwarz, and E. Witten, *Superstring Theory. Vol. 2: Loop Amplitudes, Anomalies and Phenomenology.* 7, 1988.

[122] A. O. Sushkov, et al., *New Experimental Limits on Non-Newtonian Forces in the Micrometer Range*, Phys. Rev. Lett. **107** (2011) 171101.

[123] J. F. Donoghue, *The effective field theory treatment of quantum gravity*, AIP Conference Proceedings **1483** (2012) 73–94.

[124] M. Persic, P. Salucci, and F. Stel, *The Universal rotation curve of spiral galaxies: 1. The Dark matter connection*, Mon. Not. Roy. Astron. Soc. **281** (1996) 27.

[125] L. Hernquist, et al., *The Lyman alpha forest in the cold dark matter model*, Astrophys. J. Lett. **457** (1996) L51.

[126] G. Bertone, D. Hooper, and J. Silk, *Particle dark matter: Evidence, candidates and constraints*, Phys. Rept. **405** (2005) 279–390.

[127] P. J. E. Peebles and B. Ratra, *The Cosmological Constant and Dark Energy*, Rev. Mod. Phys. **75** (2003) 559–606.

[128] E. J. Copeland, M. Sami, and S. Tsujikawa, *Dynamics of dark energy*, Int. J. Mod. Phys. D **15** (2006) 1753–1936.

[129] Planck Collaboration, *Planck 2018 results - I. Overview and the cosmological legacy of Planck*, A&A **641** (2020) A1.

[130] A. D. Sakharov, *Violation of CP Invariance, C asymmetry, and baryon asymmetry of the universe*, Pisma Zh. Eksp. Teor. Fiz. **5** (1967) 32–35.

[131] J. H. Christenson, et al., *Evidence for the 2π Decay of the K_2^0 Meson*, Phys. Rev. Lett. **13** (1964) 138–140.

[132] Belle Collaboration, K. Abe et al., *Observation of large CP violation in the neutral B meson system*, Phys. Rev. Lett. **87** (2001) 091802.

[133] BaBar Collaboration, B. Aubert et al., *Observation of CP violation in the B^0 meson system*, Phys. Rev. Lett. **87** (2001) 091801.

[134] BELLE Collaboration, M. Staric et al., *Evidence for D^0 - $\bar{D}^0$ Mixing*, Phys. Rev. Lett. **98** (2007) 211803.

[135] BaBar Collaboration, B. Aubert et al., *Evidence for $D^0 - \overline{D}^0$ Mixing*, Phys. Rev. Lett. **98** (2007) 211802.

[136] Super-Kamiokande Collaboration, Y. Fukuda et al., *Evidence for oscillation of atmospheric neutrinos*, Phys. Rev. Lett. **81** (1998) 1562–1567.

[137] LSND Collaboration, A. Aguilar-Arevalo et al., *Evidence for neutrino oscillations from the observation of $\bar{\nu}_e$ appearance in a $\bar{\nu}_\mu$ beam*, Phys. Rev. D **64** (2001) 112007.

[138] SNO Collaboration, Q. R. Ahmad et al., *Measurement of day and night neutrino energy spectra at SNO and constraints on neutrino mixing parameters*, Phys. Rev. Lett. **89** (2002) 011302.

[139] KamLAND Collaboration, K. Eguchi et al., *First results from KamLAND: Evidence for reactor anti-neutrino disappearance*, Phys. Rev. Lett. **90** (2003) 021802.

[140] Super-Kamiokande Collaboration, Y. Ashie et al., *A Measurement of atmospheric neutrino oscillation parameters by SUPER-KAMIOKANDE I*, Phys. Rev. D **71** (2005) 112005.

[141] T2K Collaboration, K. Abe et al., *Indication of Electron Neutrino Appearance from an Accelerator-produced Off-axis Muon Neutrino Beam*, Phys. Rev. Lett. **107** (2011) 041801.

[142] Double Chooz Collaboration, Y. Abe et al., *Indication of Reactor $\bar{\nu}_e$ Disappearance in the Double Chooz Experiment*, Phys. Rev. Lett. **108** (2012) 131801.

[143] RENO Collaboration, J. K. Ahn et al., *Observation of Reactor Electron Antineutrino Disappearance in the RENO Experiment*, Phys. Rev. Lett. **108** (2012) 191802.

[144] Z. Maki, M. Nakagawa, and S. Sakata, *Remarks on the unified model of elementary particles*, Prog. Theor. Phys. **28** (1962) 870–880.

[145] B. Pontecorvo, *Neutrino Experiments and the Problem of Conservation of Leptonic Charge*, Zh. Eksp. Teor. Fiz. **53** (1967) 1717–1725.

[146] Muon g-2 Collaboration, B. Abi et al., *Measurement of the Positive Muon Anomalous Magnetic Moment to 0.46 ppm*, Phys. Rev. Lett. **126** (2021) 141801.

[147] LHCb Collaboration, *Test of lepton universality in beauty-quark decays*, `arXiv:2103.11769 [hep-ex]`.

[148] BaBar Collaboration, J. P. Lees et al., *Measurement of an Excess of $\bar{B} \to D^{(*)}\tau^-\bar{\nu}_\tau$ Decays and Implications for Charged Higgs Bosons*, Phys. Rev. D **88** (2013) 072012.

[149] Belle Collaboration, M. Huschle et al., *Measurement of the branching ratio of $\bar{B} \to D^{(*)}\tau^-\bar{\nu}_\tau$ relative to $\bar{B} \to D^{(*)}\ell^-\bar{\nu}_\ell$ decays with hadronic tagging at Belle*, Phys. Rev. D **92** (2015) 072014.

[150] C. Abel et al., *Measurement of the Permanent Electric Dipole Moment of the Neutron*, Phys. Rev. Lett. **124** (2020) 081803.

[151] A. Djouadi, *The Anatomy of electro-weak symmetry breaking. II. The Higgs bosons in the minimal supersymmetric model*, Phys. Rept. **459** (2008) 1–241.

[152] J. Baglio, et al., *The measurement of the Higgs self-coupling at the LHC: theoretical status*, JHEP **04** (2013) 151.

[153] A. Djouadi et al., *The Minimal supersymmetric standard model: Group summary report*, 1998, `arXiv:hep-ph/9901246`.

[154] S. P. Martin, *A Supersymmetry primer*, Adv. Ser. Direct. High Energy Phys. **18** (1998) 1–98.

[155] P. Fayet and S. Ferrara, *Supersymmetry*, Phys. Rept. **32** (1977) 249–334.

[156] H. P. Nilles, *Supersymmetry, Supergravity and Particle Physics*, Phys. Rept. **110** (1984) 1–162.

[157] H. E. Haber and G. L. Kane, *The Search for Supersymmetry: Probing Physics Beyond the Standard Model*, Phys. Rept. **117** (1985) 75–263.

[158] M. Drees and S. P. Martin, pp. , 146–215. 3, 1995. `arXiv:hep-ph/9504324`.

[159] D. J. H. Chung, et al., *The Soft supersymmetry breaking Lagrangian: Theory and applications*, Phys. Rept. **407** (2005) 1–203.

[160] T. D. Lee, *A Theory of Spontaneous T Violation*, Phys. Rev. D **8** (1973) 1226–1239.

[161] A. Efrati and Y. Nir, *What if $\lambda_{hhh} \neq 3m_h^2/v$*, `arXiv:1401.0935 [hep-ph]`.

[162] J. Alison et al., *Higgs boson potential at colliders: Status and perspectives*, Rev. Phys. **5** (2020) 100045.

[163] H. Davoudiasl, et al., *The New minimal standard model*, Phys. Lett. B **609** (2005) 117–123.

[164] R. M. Schabinger and J. D. Wells, *A Minimal spontaneously broken hidden sector and its impact on Higgs boson physics at the large hadron collider*, Phys. Rev. D **72** (2005) 093007.

[165] B. Patt and F. Wilczek, *Higgs-field portal into hidden sectors*, `arXiv:hep-ph/0605188`.

[166] V. Barger, et al., *LHC Phenomenology of an Extended Standard Model with a Real Scalar Singlet*, Phys. Rev. D **77** (2008) 035005.

[167] M. Bowen, Y. Cui, and J. D. Wells, *Narrow trans-TeV Higgs bosons and H —> hh decays: Two LHC search paths for a hidden sector Higgs boson*, JHEP **03** (2007) 036.

[168] M. J. Dolan, C. Englert, and M. Spannowsky, *New Physics in LHC Higgs boson pair production*, Phys. Rev. D **87** (2013) 055002.

[169] G. M. Pruna and T. Robens, *Higgs singlet extension parameter space in the light of the LHC discovery*, Phys. Rev. D **88** (2013) 115012.

[170] J. M. No and M. Ramsey-Musolf, *Probing the Higgs Portal at the LHC Through Resonant di-Higgs Production*, Phys. Rev. D **89** (2014) 095031.

[171] C.-Y. Chen, S. Dawson, and I. M. Lewis, *Exploring resonant di-Higgs boson production in the Higgs singlet model*, Phys. Rev. D **91** (2015) 035015.

[172] S. I. Godunov, et al., *Extending the Higgs sector: an extra singlet*, Eur. Phys. J. C **76** (2016) 1.

[173] T. Robens and T. Stefaniak, *LHC Benchmark Scenarios for the Real Higgs Singlet Extension of the Standard Model*, Eur. Phys. J. C **76** (2016) 268.

[174] M. Carena, Z. Liu, and M. Riembau, *Probing the electroweak phase transition via enhanced di-Higgs boson production*, Phys. Rev. D **97** (2018) 095032.

[175] J. E. Kim, *Light Pseudoscalars, Particle Physics and Cosmology*, Phys. Rept. **150** (1987) 1–177.

[176] M. Trodden, *Electroweak baryogenesis: A Brief review*, pp. , 471–480. 1998. `arXiv:hep-ph/9805252`.

[177] G. C. Branco, et al., *Theory and phenomenology of two-Higgs-doublet models*, Phys. Rept. **516** (2012) 1–102.

[178] T. Robens, T. Stefaniak, and J. Wittbrodt, *Two-real-scalar-singlet extension of the SM: LHC phenomenology and benchmark scenarios*, Eur. Phys. J. C **80** (2020) 151.

[179] M. Muhlleitner, et al., *The N2HDM under Theoretical and Experimental Scrutiny*, JHEP **03** (2017) 094.

[180] L. Evans and P. Bryant, *LHC Machine*, JINST **3** (2008) S08001.

[181] *LEP Design Report: Vol.2. The LEP Main Ring*,.

[182] ATLAS Collaboration, *The ATLAS Experiment at the CERN Large Hadron Collider*, JINST **3** (2008) S08003.

[183] CMS Collaboration, *The CMS experiment at the CERN LHC*, JINST **3** (2008) S08004.

[184] LHCb Collaboration, *The LHCb Detector at the LHC*, JINST **3** (2008) S08005.

[185] ALICE Collaboration, *The ALICE experiment at the CERN LHC*, JINST **3** (2008) S08002.

[186] *LHC-long-term*, https://lhc-commissioning.web.cern.ch/schedule/LHC-long-term.htm. Accessed: 2021-11-22.

[187] B. Abbott et al., *Production and integration of the ATLAS Insertable B-Layer*, JINST **13** (2018) T05008.

[188] ATLAS Collaboration, *Performance of the ATLAS trigger system in 2015*, Eur. Phys. J. C **77** (2017) 317.

[189] ATLAS Collaboration, *ATLAS New Small Wheel: Technical Design Report*, 2013. https://cds.cern.ch/record/1552862.

[190] ATLAS Collaboration, *ATLAS Liquid Argon Calorimeter Phase-I Upgrade: Technical Design Report*, 2013. https://cds.cern.ch/record/1602230.

[191] ATLAS Collaboration, *ATLAS TDAQ System Phase-I Upgrade: Technical Design Report*, 2013. https://cds.cern.ch/record/1602235.

[192] ATLAS Collaboration, *ATLAS Inner Tracker Strip Detector: Technical Design Report*, 2017. https://cds.cern.ch/record/2257755.

[193] ATLAS Collaboration, *ATLAS Inner Tracker Pixel Detector: Technical Design Report*, 2017. https://cds.cern.ch/record/2285585.

[194] ATLAS Collaboration, *A High-Granularity Timing Detector for the ATLAS Phase-II Upgrade: Technical Design Report*, 2020. https://cds.cern.ch/record/2719855.

[195] ATLAS Collaboration, *ATLAS LAr Calorimeter Phase-II Upgrade: Technical Design Report*, 2017. https://cds.cern.ch/record/2285582.

[196] ATLAS Collaboration, *ATLAS Tile Calorimeter Phase-II Upgrade: Technical Design Report*, 2017. https://cds.cern.ch/record/2285583.

[197] ATLAS Collaboration, *ATLAS Muon Spectrometer Phase-II Upgrade: Technical Design Report*, 2017. https://cds.cern.ch/record/2285580.

[198] ATLAS Collaboration, *ATLAS TDAQ Phase-II Upgrade: Technical Design Report*, 2017. https://cds.cern.ch/record/2285584.

[199] ATLAS Collaboration, *The ATLAS Simulation Infrastructure*, Eur. Phys. J. C **70** (2010) 823.

[200] A. Buckley et al., *General-purpose event generators for LHC physics*, Phys. Rept. **504** (2011) 145–233.

[201] S. Höche, *Introduction to parton-shower event generators*, pp. , 235–295. 2015. arXiv:1411.4085 [hep-ph].

[202] M. Dobbs and J. B. Hansen, *The HepMC C++ Monte Carlo event record for High Energy Physics*, Comput. Phys. Commun. **134** (2001) 41–46.

[203] GEANT4 Collaboration, S. Agostinelli, et al., GEANT4 – *a simulation toolkit*, Nucl. Instrum. Meth. A **506** (2003) 250.

[204] J. Allison, *Geant4 developments and applications*, IEEE Trans. Nucl. Sci. **53** (2006) 270.

[205] A. Ribon et al., *Status of Geant4 hadronic physics for the simulation of LHC experiments at the start of the LHC physics program*, https://lcgapp.cern.ch/project/docs/noteStatusHadronic2010.pdf.

[206] ATLAS Collaboration, *Performance of the Fast ATLAS Tracking Simulation (FATRAS) and the ATLAS Fast Calorimeter Simulation (FastCaloSim) with single particles*, ATL-SOFT-PUB-2014-001, 2014, https://cds.cern.ch/record/1669341.

[207] ATLAS Collaboration, *Search for Higgs boson pair production in the $b\bar{b}WW$ single lepton resolved final state with 139* fb^{-1} *of pp collision data with the ATLAS detector*, Feb, 2021.

[208] B. C. Forland, *Inaugural ATLAS Searches for Resonant Di-Higgs and SH signals in the Boosted, Fully-hadronic bbVV Final State at ATLAS using $\sqrt{s}$ = 13 TeV data and Novel Machine Learning Techniques.*, Dec, 2021. https://cds.cern.ch/record/2799055. CERN-THESIS-2021-248.

[209] T. Cornelissen, et al., *The new ATLAS track reconstruction (NEWT)*, J. Phys. Conf. Ser. **119** (2008) 032014.

[210] D. Wicke, *A New algorithm for solving tracking ambiguities*,.

[211] ATLAS Collaboration, *Performance of the ATLAS track reconstruction algorithms in dense environments in LHC Run 2*, Eur. Phys. J. C **77** (2017) 673.

[212] A. Rosenfeld and J. L. Pfaltz, *Sequential Operations in Digital Picture Processing*, J. ACM **13** (1966) 471–494.

[213] R. Fruhwirth, *Application of Kalman filtering to track and vertex fitting*, Nucl. Instrum. Meth. A **262** (1987) 444–450.

[214] ATLAS Collaboration, *ATLAS tracking event data model*,.

[215] ATLAS Collaboration, *A neural network clustering algorithm for the ATLAS silicon pixel detector*, JINST **9** (2014) P09009.

[216] ATLAS Collaboration, *Training and validation of the ATLAS pixel clustering neural networks*, ATL-PHYS-PUB-2018-002, 2018, https://cds.cern.ch/record/2309474.

[217] ATLAS Collaboration, *Reconstruction of primary vertices at the ATLAS experiment in Run 1 proton–proton collisions at the LHC*, Eur. Phys. J. C **77** (2017) 332.

[218] ATLAS Collaboration, *Vertex Reconstruction Performance of the ATLAS Detector at* $\sqrt{s} = 13$ *TeV*, ATL-PHYS-PUB-2015-026, 2015, https://cds.cern.ch/record/2037717.

[219] ATLAS Collaboration, *Measurement of the photon identification efficiencies with the ATLAS detector using LHC Run 2 data collected in 2015 and 2016*, Eur. Phys. J. C **79** (2019) 205.

[220] ATLAS Collaboration, *Electron and photon performance measurements with the ATLAS detector using the 2015–2017 LHC proton–proton collision data*, JINST **14** (2019) P12006.

[221] ATLAS Collaboration, *Muon reconstruction performance of the ATLAS detector in proton–proton collision data at* $\sqrt{s} = 13$ *TeV*, Eur. Phys. J. C **76** (2016) 292.

[222] ATLAS Collaboration, *Muon reconstruction and identification efficiency in ATLAS using the full Run 2 pp collision data set at* $\sqrt{s} = 13$ *TeV*, Eur. Phys. J. C **81** (2020) 578.

[223] ATLAS Collaboration, *Improved electron reconstruction in ATLAS using the Gaussian Sum Filter-based model for bremsstrahlung*, ATLAS-CONF-2012-047, 2012, https://cds.cern.ch/record/1449796.

[224] ATLAS Collaboration, *Topological cell clustering in the ATLAS calorimeters and its performance in LHC Run 1*, Eur. Phys. J. C **77** (2017) 490.

[225] ATLAS Collaboration, *Electron and photon energy calibration with the ATLAS detector using 2015–2016 LHC proton–proton collision data*, JINST **14** (2019) P03017.

[226] M. Cacciari and G. P. Salam, *Pileup subtraction using jet areas*, Phys. Lett. B **659** (2008) 119–126.

[227] ATLAS Collaboration, *Jet reconstruction and performance using particle flow with the ATLAS Detector*, Eur. Phys. J. C **77** (2017) 466.

[228] ATLAS Collaboration, *Track Reconstruction Performance of the ATLAS Inner Detector at* $\sqrt{s} = 13$ *TeV*, ATL-PHYS-PUB-2015-018, 2015, https://cds.cern.ch/record/2037683.

[229] ATLAS Collaboration, *Evidence for the associated production of the Higgs boson and a top quark pair with the ATLAS detector*, Phys. Rev. D **97** (2018) 072003.

[230] ATLAS Collaboration, *Properties of jets and inputs to jet reconstruction and calibration with the ATLAS detector using proton–proton collisions at* $\sqrt{s} = 13$ *TeV*, ATL-PHYS-PUB-2015-036, 2015, https://cds.cern.ch/record/2044564.

[231] M. Cacciari, G. P. Salam, and G. Soyez, *FastJet user manual*, Eur. Phys. J. C **72** (2012) 1896.

[232] G. C. Blazey et al., *Run II jet physics*, pp. , 47–77. 5, 2000. arXiv:hep-ex/0005012.

[233] M. Cacciari, G. P. Salam, and G. Soyez, *The anti-*k_t *jet clustering algorithm*, JHEP **04** (2008) 063.

[234] S. Catani, et al., *Longitudinally invariant* K_t *clustering algorithms for hadron hadron collisions*, Nucl. Phys. B **406** (1993) 187–224.

[235] Y. L. Dokshitzer, et al., *Better jet clustering algorithms*, JHEP **08** (1997) 001.

[236] ATLAS Collaboration, *In situ calibration of large-radius jet energy and mass in* 13 *TeV proton–proton collisions with the ATLAS detector*, Eur. Phys. J. C **79** (2019) 135.

[237] ATLAS Collaboration, *Jet energy scale measurements and their systematic uncertainties in proton–proton collisions at* $\sqrt{s} = 13$ *TeV with the ATLAS detector*, Phys. Rev. D **96** (2017) 072002.

[238] ATLAS Collaboration, *Performance of pile-up mitigation techniques for jets in pp collisions at* $\sqrt{s} = 8$ *TeV using the ATLAS detector*, Eur. Phys. J. C **76** (2016) 581.

[239] A. J. Larkoski, G. P. Salam, and J. Thaler, *Energy Correlation Functions for Jet Substructure*, JHEP **06** (2013) 108.

[240] ATLAS Collaboration, *Identification of boosted, hadronically decaying* W *bosons and comparisons with ATLAS data taken at* $\sqrt{s} = 8$ *TeV*, Eur. Phys. J. C **76** (2016) 154.

[241] I. Moult, L. Necib, and J. Thaler, *New Angles on Energy Correlation Functions*, JHEP **12** (2016) 153.

[242] M. LeBlanc, *2-prong vs 3-prong jet discrimination using generalised ECFs*, Hadronic Calibration Workshop, 2018, https://indico.cern.ch/event/711895/contributions/3128617/.

[243] J. Thaler and K. Van Tilburg, *Identifying Boosted Objects with N-subjettiness*, JHEP **03** (2011) 015.

[244] A. J. Larkoski, D. Neill, and J. Thaler, *Jet Shapes with the Broadening Axis*, JHEP **04** (2014) 017.

[245] ATLAS Collaboration, *Tagging and suppression of pileup jets with the ATLAS detector*, ATLAS-CONF-2014-018, 2014, https://cds.cern.ch/record/1700870.

[246] D. Krohn, J. Thaler, and L.-T. Wang, *Jets with Variable R*, JHEP **06** (2009) 059.

[247] ATLAS Collaboration, *Variable Radius, Exclusive-k_T, and Center-of-Mass Subjet Reconstruction for Higgs($\to b\bar{b}$) Tagging in ATLAS*, ATL-PHYS-PUB-2017-010, 2017, https://cds.cern.ch/record/2268678.

[248] D. Krohn, J. Thaler, and L.-T. Wang, *Jet Trimming*, JHEP **02** (2010) 084.

[249] ATLAS Collaboration, *Performance of jet substructure techniques for large-R jets in proton–proton collisions at $\sqrt{s} = 7$ TeV using the ATLAS detector*, JHEP **09** (2013) 076.

[250] ATLAS Collaboration, *Track assisted techniques for jet substructure*, ATL-PHYS-PUB-2018-012, 2018, https://cds.cern.ch/record/2630864.

[251] M. Cacciari, G. P. Salam, and G. Soyez, *The Catchment Area of Jets*, JHEP **04** (2008) 005.

[252] ATLAS Collaboration, *E_T^{miss} performance in the ATLAS detector using 2015–2016 LHC pp collisions*, ATLAS-CONF-2018-023, 2018, https://cds.cern.ch/record/2625233.

[253] ATLAS Collaboration, *Object-based missing transverse momentum significance in the ATLAS Detector*, ATLAS-CONF-2018-038, 2018, https://cds.cern.ch/record/2630948.

[254] ATLAS Collaboration, *Performance of b-jet identification in the ATLAS experiment*, JINST **11** (2016) P04008.

[255] ATLAS Collaboration, *ATLAS b-jet identification performance and efficiency measurement with $t\bar{t}$ events in pp collisions at $\sqrt{s} = 13$ TeV*, Eur. Phys. J. C **79** (2019) 970.

[256] ATLAS Collaboration, *Optimisation and performance studies of the ATLAS b-tagging algorithms for the 2017-18 LHC run*, ATL-PHYS-PUB-2017-013, 2017, https://cds.cern.ch/record/2273281.

[257] ATLAS Collaboration, *Commissioning of the ATLAS high performance b-tagging algorithms in the 7 TeV collision data*, ATLAS-CONF-2011-102, 2011, https://cds.cern.ch/record/1369219.

[258] ATLAS Collaboration, *Topological b-hadron decay reconstruction and identification of b-jets with the JetFitter package in the ATLAS experiment at the LHC*, ATL-PHYS-PUB-2018-025, 2018, https://cds.cern.ch/record/2645405.

[259] ATLAS Collaboration, *Identification of Jets Containing b-Hadrons with Recurrent Neural Networks at the ATLAS Experiment*, ATL-PHYS-PUB-2017-003, 2017, https://cds.cern.ch/record/2255226.

[260] ATLAS Collaboration, C. Young, *JetEtmiss: PFlow Overlap and μ Bug*, https://indico.cern.ch/event/814156/contributions/3396841/attachments/1830226/2997072/Presentation.pdf. Accessed: 2022-01-08.

[261] ATLAS Collaboration, *Luminosity determination in pp collisions at $\sqrt{s} = 13$ TeV using the ATLAS detector at the LHC*, ATLAS-CONF-2019-021, 2019, https://cds.cern.ch/record/2677054.

[262] G. Avoni et al., *The new LUCID-2 detector for luminosity measurement and monitoring in ATLAS*, JINST **13** (2018) P07017.

[263] S. van der Meer, *Calibration of the effective beam height in the ISR*, https://cds.cern.ch/record/296752.

[264] P. Grafström and W. Kozanecki, *Luminosity determination at proton colliders*, Prog. Part. Nucl. Phys. **81** (2015) 97–148.

[265] ATLAS Collaboration, *ATLAS data quality operations and performance for 2015–2018 data-taking*, JINST **15** (2020) P04003.

[266] ATLAS Collaboration, *Luminosity Public Plots Run 2*, https://twiki.cern.ch/twiki/bin/view/AtlasPublic/LuminosityPublicResultsRun2. Accessed: 2022-01-10.

[267] J. Alwall, et al., *The automated computation of tree-level and next-to-leading order differential cross sections, and their matching to parton shower simulations*, JHEP **07** (2014) 079.

[268] R. D. Ball et al., *Parton distributions with LHC data*, Nucl. Phys. B **867** (2013) 244.

[269] J. Bellm et al., *Herwig 7.0/Herwig++ 3.0 release note*, Eur. Phys. J. C **76** (2016) 196.

[270] D. J. Lange, *The EvtGen particle decay simulation package*, Nucl. Instrum. Meth. A **462** (2001) 152.

[271] T. Sjöstrand, et al., *An introduction to PYTHIA 8.2*, Comput. Phys. Commun. **191** (2015) 159.

[272] ATLAS Collaboration, *ATLAS Pythia 8 tunes to* 7 *TeV data*, ATL-PHYS-PUB-2014-021, 2014, https://cds.cern.ch/record/1966419.

[273] S. Frixione, P. Nason, and G. Ridolfi, *A positive-weight next-to-leading-order Monte Carlo for heavy flavour hadroproduction*, JHEP **09** (2007) 126.

[274] P. Nason, *A new method for combining NLO QCD with shower Monte Carlo algorithms*, JHEP **11** (2004) 040.

[275] S. Frixione, P. Nason, and C. Oleari, *Matching NLO QCD computations with parton shower simulations: the POWHEG method*, JHEP **11** (2007) 070.

[276] S. Alioli, et al., *A general framework for implementing NLO calculations in shower Monte Carlo programs: the POWHEG BOX*, JHEP **06** (2010) 043.

[277] NNPDF Collaboration, R. D. Ball et al., *Parton distributions for the LHC run II*, JHEP **04** (2015) 040.

[278] ATLAS Collaboration, *Studies on top-quark Monte Carlo modelling for Top2016*, ATL-PHYS-PUB-2016-020, 2016, https://cds.cern.ch/record/2216168.

[279] E. Bothmann et al., *Event generation with Sherpa 2.2*, SciPost Phys. **7** (2019) 034.

[280] T. Gleisberg and S. Höche, *Comix, a new matrix element generator*, JHEP **12** (2008) 039.

[281] F. Buccioni, et al., *OpenLoops 2*, Eur. Phys. J. C **79** (2019) 866.

[282] F. Cascioli, P. Maierhöfer, and S. Pozzorini, *Scattering Amplitudes with Open Loops*, Phys. Rev. Lett. **108** (2012) 111601.

[283] A. Denner, S. Dittmaier, and L. Hofer, Collier*: A fortran-based complex one-loop library in extended regularizations*, Comput. Phys. Commun. **212** (2017) 220–238.

[284] S. Schumann and F. Krauss, *A parton shower algorithm based on Catani–Seymour dipole factorisation*, JHEP **03** (2008) 038.

[285] S. Höche, et al., *A critical appraisal of NLO+PS matching methods*, JHEP **09** (2012) 049.

[286] S. Höche, et al., *QCD matrix elements + parton showers. The NLO case*, JHEP **04** (2013) 027.

[287] S. Catani, et al., *QCD Matrix Elements + Parton Showers*, JHEP **11** (2001) 063.

[288] S. Höche, et al., *QCD matrix elements and truncated showers*, JHEP **05** (2009) 053.

[289] C. Anastasiou, et al., *High precision QCD at hadron colliders: Electroweak gauge boson rapidity distributions at next-to-next-to leading order*, Phys. Rev. D **69** (2004) 094008.

[290] J. Pumplin et al., *New Generation of Parton Distributions with Uncertainties from Global QCD Analysis*, JHEP **07** (2002) 012.

[291] S. Gieseke, C. Rohr, and A. Siodmok, *Colour reconnections in Herwig++*, Eur. Phys. J. C **72** (2012) 2225.

[292] S. Gieseke, C. Rohr, and A. Siodmok, *The Underlying Event in Herwig++*, pp. , 785–788. 2012. `arXiv:1206.2205 [hep-ph]`.

[293] S. Frixione, et al., *Single-top hadroproduction in association with a W boson*, JHEP **07** (2008) 029.

[294] R. Frederix, E. Re, and P. Torrielli, *Single-top t-channel hadroproduction in the four-flavour scheme with POWHEG and aMC@NLO*, JHEP **09** (2012) 130.

[295] Y. Buch, *Neutrino reconstruction using machine learning techniques for the boosted resonant $HH \to b\bar{b}WW^*$ search at ATLAS*, Aug, 2020. `https://www.uni-goettingen.de/de/document/download/d9a2391d69cfb79e1698bbb641560c6a.pdf/BSc_Buch_Yannik.pdf`. II.Physik-UniGö-BSc-2020/07.

[296] ATLAS Collaboration, *Operation of the ATLAS trigger system in Run 2*, JINST **15** (2020) P10004.

[297] ATLAS Collaboration, *Performance of electron and photon triggers in ATLAS during LHC Run 2*, Eur. Phys. J. C **80** (2020) 47.

[298] ATLAS Collaboration, *Performance of the ATLAS muon triggers in Run 2*, JINST **15** (2020) P09015.

[299] ATLAS Collaboration, *The performance of the jet trigger for the ATLAS detector during 2011 data taking*, Eur. Phys. J. C **76** (2016) 526.

[300] ATLAS Collaboration, *Configuration and performance of the ATLAS b-jet triggers in Run 2*, `arXiv:2106.03584 [hep-ex]`.

[301] N. K. Bhalla, *Searches for resonant Higgs boson pair production in the $b\bar{b}WW^*$ decay channel for the boosted single-lepton final state at ATLAS*,.

[302] ATLAS Collaboration, *Tools for estimating fake/non-prompt lepton backgrounds in ATLAS*, tech. rep., CERN, Geneva, Sep, 2019. https://cds.cern.ch/record/2686919.

[303] ATLAS Collaboration, *Measurement of the Inelastic Proton–Proton Cross Section at $\sqrt{s} = 13$ TeV with the ATLAS Detector at the LHC*, Phys. Rev. Lett. **117** (2016) 182002.

[304] J. Butterworth et al., *PDF4LHC recommendations for LHC Run II*, J. Phys. G **43** (2016) 023001.

[305] ATLAS Collaboration, *Search for heavy resonances in four-top-quark final states in pp collisions at $\sqrt{s} = 13$ TeV with the ATLAS detector*, ATLAS-CONF-2021-048, 2021, https://cds.cern.ch/record/2781173.

[306] LHCTopWG, *NLO single-top channel cross sections*, 2017. https://twiki.cern.ch/twiki/bin/view/LHCPhysics/SingleTopRefXsec.

[307] LHCTopWG, *NNLO+NNLL top-quark-pair cross sections*, 2015. https://twiki.cern.ch/twiki/bin/view/LHCPhysics/TtbarNNLO.

[308] ATLAS Collaboration, *ATLAS simulation of boson plus jets processes in Run 2*, ATL-PHYS-PUB-2017-006, 2017, https://cds.cern.ch/record/2261937.

[309] ATLAS Collaboration, *Reconstruction and identification of boosted di-τ systems in a search for Higgs boson pairs using 13 TeV proton–proton collision data in ATLAS*, JHEP **11** (2020) 163.

[310] A. L. Read, *Presentation of search results: the CL_S technique*, J. Phys. G **28** (2002) 2693.

[311] ROOT Collaboration, K. Cranmer, et al., *HistFactory: A tool for creating statistical models for use with RooFit and RooStats*, CERN-OPEN-2012-016 (2012).

[312] J. Neyman and E. S. Pearson, *On the Problem of the Most Efficient Tests of Statistical Hypotheses*, Phil. Trans. Roy. Soc. Lond. A **231** (1933) 289–337.

[313] G. Cowan, et al., *Asymptotic formulae for likelihood-based tests of new physics*, Eur. Phys. J. C **71** (2011) 1554, Erratum: Eur. Phys. J. C **73** (2013) 2501.

[314] R. Rossi, *Mathematical Statistics: An Introduction to Likelihood Based Inference*. Wiley, 2018.

[315] S. S. Wilks, *The Large-Sample Distribution of the Likelihood Ratio for Testing Composite Hypotheses*, Annals Math. Statist. **9** (1938) 60–62.

[316] ATLAS Collaboration Collaboration, L. Christopher and D. Kar, *Electrons in Dense Environments at ATLAS at HEPP2020*, https://indico.cern.ch/event/850451/contributions/3683355/, 2020. Accessed: 2022-02-21.

[317] ATLAS Collaboration Collaboration, D. Zhong, *Deep Learning based Tagger for Boosted $WW^{(*)}$ semi-leptonic ($\ell\nu qq$) Decays at ATLAS at ATLAS Hadronic Calibration Workshop 2021 (HCW2021)*, https://indico.cern.ch/event/1070531/contributions/4565664/.

[318] ATLAS Collaboration, *Athena*, Apr, 2019. https://doi.org/10.5281/zenodo.3932810.

[319] M. Baak et al., *HistFitter software framework for statistical data analysis*, Eur. Phys. J. C **75** (2015) 153.

[320] L. Moneta et al., *The RooStats Project*, PoS **ACAT2010** (2010) 057.

[321] W. Verkerke and D. Kirkby, *The RooFit toolkit for data modeling*, 2003, arXiv:physics/0306116 [physics.data-an].

[322] R. Brun and F. Rademakers, *ROOT – An object oriented data analysis framework*, Nucl. Instrum. Meth. A **389** (1997) 81 – 86.

[323] I. Antcheva et al., *ROOT: A C++ framework for petabyte data storage, statistical analysis and visualization*, Comput. Phys. Commun. **182** (2011) 1384–1385.

[324] F. James, *MINUIT Function Minimization and Error Analysis: Reference Manual Version 94.1*, CERN-D-506 (1994).

[325] F. James and M. Roos, *Minuit: A System for Function Minimization and Analysis of the Parameter Errors and Correlations*, Comput. Phys. Commun. **10** (1975) 343–367.

[326] J. van den Hout, *Investigation of systematic uncertainties in the search for resonant di-Higgs production in the bbWW* decay channel*, Jul, 2021. https://uni-goettingen.de/de/document/download/6b59c362654c7a31141468ed623c74c5.pdf/BSc_van_den_Hout_Janne.pdf. II.Physik-UniGö-BSc-2021/02.

[327] ATLAS Collaboration, *Expected Tracking Performance of the ATLAS Inner Tracker at the HL-LHC*, ATL-PHYS-PUB-2019-014, 2019, https://cds.cern.ch/record/2669540.

[328] ATLAS Collaboration, *Expected tracking and related performance with the updated ATLAS Inner Tracker layout at the High-Luminosity LHC*, ATL-PHYS-PUB-2021-024, 2021, https://cds.cern.ch/record/2776651.

[329] *ATLAS Detector Description Database*, https://atlas-geometry-db.web.cern.ch/atlas-geometry-db/. Accessed: 2022-02-03.

[330] A. Ferrari, et al., *FLUKA: A multi-particle transport code (program version 2005)*. CERN Yellow Reports: Monographs. CERN, 2005. https://cds.cern.ch/record/898301.

[331] ATLAS Collaboration, *In situ calibrations for R-scan jets*, Apr, 2018.

[332] ATLAS Collaboration, *Jet energy scale and resolution measured in proton–proton collisions at* $\sqrt{s} = 13$ *TeV with the ATLAS detector*, Eur. Phys. J. C **81** (2020) 689.

[333] B. Efron, *Bootstrap Methods: Another Look at the Jackknife*, Annals Statist. **7** (1979) 1–26.

Appendices

APPENDIX A

Auxiliary Material of the Analysis

This chapter contains auxiliary material of the analysis presented in this thesis such as a detailed lists of samples or triggers, an overview of the technical setup as well as extra plots, tables and side studies which exceed the scope of the main matter of this thesis.

A.1. Technical Setup

The technical workflow of the analysis described in this thesis is the following: The samples consisting of simulated or recorded data events exist in the xAOD format. This is the most general format that contains all information from the detector, namely tracks and energy clusters, which have already been reconstructed into physics objects such as electrons, muons, taus, photons and some basic jet collections. Due to their generality, these samples are quite large and most information is not needed by the analysis.

Therefore, a derived xAOD file (DxAOD) is created using the following four methods:

Skimming: Events that are not interesting for the analysis because they do not fire the desired trigger or do not contain the desired objects are removed from the sample.

Slimming: Whole object collections or not needed properties of the objects are removed. For example, photons are not stored in the DxAOD or the variable describing the shower width of electrons in the calorimeter is removed.

Thinning: Individual objects not passing a certain selection are removed. For example, there is a p_{T} threshold implemented for various objects due to recommendations or analysis requirements.

Augmentation: In contrast to the other three methods, information or object collections are added by this method. This is for example useful if instead of the standard

PFlow jet collection, the trimmed large-R jet and the small-R jet collections are used both of which are not reconstructed on xAOD level.

This analysis uses the EXOT8 derivation.

The DxAODs are then processed through an analysis framework of choice. Various commonly used frameworks exist in ATLAS. This analysis uses the CxAOD framework which was used in the previous iteration of the analysis and other Higgs boson pair production searches as well. More details are given in Section A.1.1.

The CxAOD framework can output a set of histograms or data trees. The histograms are used to create most plots shown in this thesis, while the trees are stored in ntuples which are the input for the statistical analysis which is conducted by the HISTFITTER framework in this thesis (see Section A.1.2 for more details) that produces the exclusion limits.

A.1.1. CxAOD Framework

The CxAOD framework is a two step analysis framework, that runs within ATHENA 21.2 [318] and is written purely in C++. The first step is the CxAODMaker which transforms the DxAODs into calibrated xAODs (CxAODs). As the name says, this first step is mainly about the calibration of objects and the inclusion of systematic uncertainties on these calibrations which are provided centrally by specialised ATLAS groups. In addition, a preselection is applied to reduce the number of events passed on to the second step. Here, the CxAODReader translates the CxAODs into histograms which can be plotted directly, or into ntuples which can be used in further analysis steps. The CxAODReader is the place where the event selection is applied and most studies are conducted, due to the shorter runtime compared to the CxAODMaker.

Both the CxAODMaker and CxAODReader depend on tools and additional information stored in the CxAODTools and CxAODOperations, respectively. It is also possible to include external tools to the analysis such as the 4-prong tagger. A sketch of the CxAOD framework can be found in Figure A.1.

A.1.2. HistFitter Framework

For the statistical analysis the HISTFITTER framework [319] is used which is written in C++ for CPU intensive calculations and in python for the user interface. It performs the complete statistical analyses by employing various tools into a coherent and programmable framework. It makes use of the HISTFACTORY [311] and ROOSTAT [320] packages which themselves are based on ROOFIT [321] and ROOT [322, 323]. In all fits, the minimisation of the goodness-of-fit quantity is performed by MINUIT [324, 325]. A schematic illustration of the workflow of HISTFITTER framework is shown in Figure A.2.

The usual workflow starts with the user providing the raw input data files which consist of ntuples of the estimated backgrounds, the observed data and if a model dependent analysis is performed, also the expected signal. The HISTFITTER framework prepares histograms to model the physics processes of interest in defined regions. A special feature

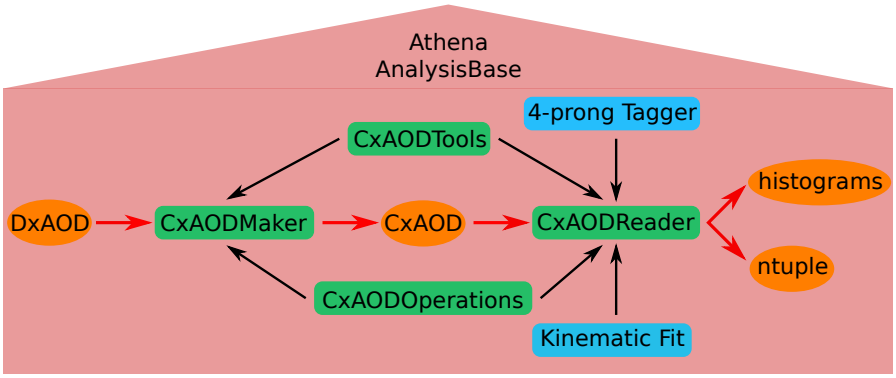

Figure A.1.: Schematic illustration of the CxAOD framework used for the analysis. The orange ellipsoids correspond to the data formats at the different stages. The green boxes denote packages within the CxAODFramework and the blue boxes external packages that are included. The red arrows show the path of the data files and the black arrows the package dependencies.

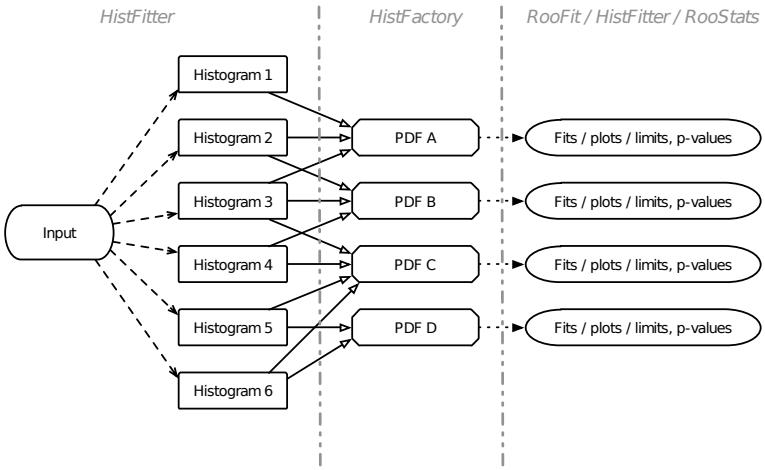

Figure A.2.: Schematic illustration of the workflow in the HistFitter framework [319].

is the incorporation of the concept of control, validation and signal regions to constrain, extrapolate and validate the backgrounds before using them in the signal enhanced phase space of the analysis.

In the second step, the histograms are combined to form probability density functions (PDFs) to extract information from data called workspaces. Since the regions are defined to be orthogonal, separate PDFs are created for each region but with shared free parameters. This allows to correlate systematic uncertainties across all regions.

These PDFs are fitted to data using a likelihood function in the third step. If at least one control region has been defined, a fit of the PDFs in the CR can be used to coherently constrain the normalisation of selected backgrounds in the SR due to the

shared free parameters. For the same reason, the background modelling verification in the validation region after the fit is statistically rigorous although the validation region has not been used in the fit. Another advantage is the usage of transfer factors (TF) to cancel systematic uncertainties

$$N_{\mathrm{est}}^{\mathrm{SR}} = N_{\mathrm{obs}}^{\mathrm{CR}} \underbrace{\left[\frac{N_{\mathrm{MC}}^{\mathrm{SR}}}{N_{\mathrm{MC}}^{\mathrm{CR}}}\right]}_{\mathrm{TF}} = \mathrm{NF} \cdot N_{\mathrm{MC}}^{\mathrm{SR}}, \tag{A.1}$$

where $N_{\mathrm{est}}^{\mathrm{SR}}$ is the number of estimated background events in the signal region, $N_{\mathrm{obs}}^{\mathrm{CR}}$ the number of observed events in the control region, N_{MC} the number of raw simulated events in the signal and control regions, respectively and NF the normalisation factor obtained from the background normalisation fit. Therefore, only statistical and extrapolation uncertainties on the backgrounds remain.

The final PDFs are then used as inputs for hypothesis tests. The HistFitter framework supports four kinds of hypothesis tests which all use the frequentist approach and likelihood ratios as test statistics:

Signal hypothesis test is used if no excess is observed in data. Exclusion limits are calculated which are then interpreted to exclude parameter ranges of predefined models, for example masses of unknown particles or mixing angles.

Signal strength upper limits place exclusion limits on the cross section of a process. This can be either done in the context of a certain model, or model independently by comparing the expected background to data.

Background-only hypothesis tests is part of the exclusion limit calculations above where the signal strength is explicitly set to 0.

Significance determination is done in a model independent way on potentially observed event excesses.

The exclusion limits are all calculated using the $\mathrm{CL_s}$ method.

A.2. Samples

This section gives the names the good runs lists required to be passed by recorded data events and the names of all simulated signal and background samples used during the analysis described in this thesis. All samples have been produced in three campaigns related to the different years of data taking as summarised in Table A.1. Thus, each sample exists with three different r-tags indicated by the generalised rXXXX notation in the sample name since all other parts of the name remain the same. The r-tag corresponding to each MC campaign can be found in Table A.1 as well.

MC campaign	Year	r-tag
mc16a	2015/16	r9364
mc16d	2017	r10201
mc16e	2018	r10724

Table A.1.: MC campaigns relevant for the analysis presented in this thesis with their corresponding years and r-tags.

A.2.1. Good Runs Lists

2015:

data15_13TeV.periodAllYear_DetStatus-v89-pro21-02_Unknown_PHYS_StandardGRL_All_Good_25ns.xml

2016:

data16_13TeV.periodAllYear_DetStatus-v89-pro21-01_DQDefects-00-02-04_PHYS_StandardGRL_All_Good_25ns.xml

2017:

data17_13TeV.periodAllYear_DetStatus-v99-pro22-01_Unknown_PHYS_StandardGRL_All_Good_25ns_Triggerno17e33prim.xml

2018:

data18_13TeV.periodAllYear_DetStatus-v102-pro22-04_Unknown_PHYS_StandardGRL_All_Good_25ns_Triggerno17e33prim.xml

A.2.2. Signal samples

$X \to HH \to bbWW^*$ 1-lepton:

mc16_13TeV.450220.MadGraphHerwig7EvtGen_PDF23LO_X800tohh_WWbb_1lep.deriv.DAOD_EXOT8.e7592_a875_rXXXX_p4128

mc16_13TeV.450221.MadGraphHerwig7EvtGen_PDF23LO_X900tohh_WWbb_1lep.deriv.DAOD_EXOT8.e7592_a875_rXXXX_p4128

mc16_13TeV.450219.MadGraphHerwig7EvtGen_PDF23LO_X1000tohh_WWbb_1lep.deriv.DAOD_EXOT8.e7329_a875_rXXXX_p4128

mc16_13TeV.450222.MadGraphHerwig7EvtGen_PDF23LO_X1200tohh_WWbb_1lep.deriv.DAOD_EXOT8.e7592_a875_rXXXX_p4128

mc16_13TeV.450223.MadGraphHerwig7EvtGen_PDF23LO_X1400tohh_WWbb_1lep.deriv.DAOD_EXOT8.e7592_a875_rXXXX_p4128

mc16_13TeV.450224.MadGraphHerwig7EvtGen_PDF23LO_X1600tohh_WWbb_1lep.deriv.DAOD_EXOT8.e7592_a875_rXXXX_p4128

mc16_13TeV.450225.MadGraphHerwig7EvtGen_PDF23LO_X1800tohh_WWbb_1lep.deriv.DAOD_EXOT8.e7592_a875_rXXXX_p4128

mc16_13TeV.450229.MadGraphHerwig7EvtGen_PDF23LO_X2000tohh_WWbb_1lep.deriv.DAOD_EXOT8.e7329_a875_rXXXX_p4128

mc16_13TeV.450226.MadGraphHerwig7EvtGen_PDF23LO_X2500tohh_WWbb_1lep.deriv.DAOD_EXOT8.e7592_a875_rXXXX_p4128

mc16_13TeV.450239.MadGraphHerwig7EvtGen_PDF23LO_X3000tohh_WWbb_1lep.deriv.DAOD_EXOT8.e7329_a875_rXXXX_p4128

mc16_13TeV.450227.MadGraphHerwig7EvtGen_PDF23LO_X4000tohh_WWbb_1lep.deriv.DAOD_EXOT8.e7592_a875_rXXXX_p4128

mc16_13TeV.450228.MadGraphHerwig7EvtGen_PDF23LO_X5000tohh_WWbb_1lep.deriv.DAOD_EXOT8.e7592_a875_rXXXX_p4128

$X \to SH \to bbWW$ 1-lepton:

mc16_13TeV.800751.Py8EG_A14NNPDF23LO_XHS_X350_S170_bbWW_1lep.deriv.DAOD_EXOT8.e8312_a875_rXXXX_p4128

mc16_13TeV.800752.Py8EG_A14NNPDF23LO_XHS_X500_S170_bbWW_1lep.deriv.DAOD_EXOT8.e8312_a875_rXXXX_p4128

mc16_13TeV.800753.Py8EG_A14NNPDF23LO_XHS_X500_S240_bbWW_1lep.deriv.DAOD_EXOT8.e8312_a875_rXXXX_p4128

mc16_13TeV.800754.Py8EG_A14NNPDF23LO_XHS_X750_S170_bbWW_1lep.deriv.DAOD_EXOT8.e8312_a875_rXXXX_p4128

mc16_13TeV.800755.Py8EG_A14NNPDF23LO_XHS_X750_S240_bbWW_1lep.deriv.DAOD_EXOT8.e8312_a875_rXXXX_p4128

mc16_13TeV.800756.Py8EG_A14NNPDF23LO_XHS_X750_S400_bbWW_1lep.deriv.DAOD_EXOT8.e8312_a875_rXXXX_p4128

mc16_13TeV.800757.Py8EG_A14NNPDF23LO_XHS_X750_S550_bbWW_1lep.deriv.DAOD_EXOT8.e8312_a875_rXXXX_p4128

mc16_13TeV.800758.Py8EG_A14NNPDF23LO_XHS_X1000_S170_bbWW_1lep.deriv.DAOD_EXOT8.e8312_a875_rXXXX_p4128

mc16_13TeV.800759.Py8EG_A14NNPDF23LO_XHS_X1000_S240_bbWW_1lep.deriv.DAOD_EXOT8.e8312_a875_rXXXX_p4128
mc16_13TeV.800760.Py8EG_A14NNPDF23LO_XHS_X1000_S400_bbWW_1lep.deriv.DAOD_EXOT8.e8312_a875_rXXXX_p4128
mc16_13TeV.800761.Py8EG_A14NNPDF23LO_XHS_X1000_S550_bbWW_1lep.deriv.DAOD_EXOT8.e8312_a875_rXXXX_p4128
mc16_13TeV.800762.Py8EG_A14NNPDF23LO_XHS_X1000_S750_bbWW_1lep.deriv.DAOD_EXOT8.e8312_a875_rXXXX_p4128
mc16_13TeV.800763.Py8EG_A14NNPDF23LO_XHS_X1500_S170_bbWW_1lep.deriv.DAOD_EXOT8.e8312_a875_rXXXX_p4128
mc16_13TeV.800764.Py8EG_A14NNPDF23LO_XHS_X1500_S240_bbWW_1lep.deriv.DAOD_EXOT8.e8312_a875_rXXXX_p4128
mc16_13TeV.800765.Py8EG_A14NNPDF23LO_XHS_X1500_S400_bbWW_1lep.deriv.DAOD_EXOT8.e8312_a875_rXXXX_p4128
mc16_13TeV.800766.Py8EG_A14NNPDF23LO_XHS_X1500_S550_bbWW_1lep.deriv.DAOD_EXOT8.e8312_a875_rXXXX_p4128
mc16_13TeV.800767.Py8EG_A14NNPDF23LO_XHS_X1500_S750_bbWW_1lep.deriv.DAOD_EXOT8.e8312_a875_rXXXX_p4128
mc16_13TeV.800768.Py8EG_A14NNPDF23LO_XHS_X1500_S1000_bbWW_1lep.deriv.DAOD_EXOT8.e8312_a875_rXXXX_p4128
mc16_13TeV.800769.Py8EG_A14NNPDF23LO_XHS_X2000_S170_bbWW_1lep.deriv.DAOD_EXOT8.e8312_a875_rXXXX_p4128
mc16_13TeV.800770.Py8EG_A14NNPDF23LO_XHS_X2000_S240_bbWW_1lep.deriv.DAOD_EXOT8.e8312_a875_rXXXX_p4128
mc16_13TeV.800771.Py8EG_A14NNPDF23LO_XHS_X2000_S400_bbWW_1lep.deriv.DAOD_EXOT8.e8312_a875_rXXXX_p4128
mc16_13TeV.800772.Py8EG_A14NNPDF23LO_XHS_X2000_S550_bbWW_1lep.deriv.DAOD_EXOT8.e8312_a875_rXXXX_p4128
mc16_13TeV.800773.Py8EG_A14NNPDF23LO_XHS_X2000_S750_bbWW_1lep.deriv.DAOD_EXOT8.e8312_a875_rXXXX_p4128
mc16_13TeV.800774.Py8EG_A14NNPDF23LO_XHS_X2000_S1000_bbWW_1lep.deriv.DAOD_EXOT8.e8312_a875_rXXXX_p4128
mc16_13TeV.800775.Py8EG_A14NNPDF23LO_XHS_X2000_S1500_bbWW_1lep.deriv.DAOD_EXOT8.e8312_a875_rXXXX_p4128
mc16_13TeV.800776.Py8EG_A14NNPDF23LO_XHS_X2500_S170_bbWW_1lep.deriv.DAOD_EXOT8.e8312_a875_rXXXX_p4128
mc16_13TeV.800777.Py8EG_A14NNPDF23LO_XHS_X2500_S240_bbWW_1lep.deriv.DAOD_EXOT8.e8312_a875_rXXXX_p4128
mc16_13TeV.800778.Py8EG_A14NNPDF23LO_XHS_X2500_S400_bbWW_1lep.deriv.DAOD_EXOT8.e8312_a875_rXXXX_p4128
mc16_13TeV.800779.Py8EG_A14NNPDF23LO_XHS_X2500_S550_bbWW_1lep.deriv.DAOD_EXOT8.e8312_a875_rXXXX_p4128
mc16_13TeV.800780.Py8EG_A14NNPDF23LO_XHS_X2500_S750_bbWW_1lep.deriv.DAOD_EXOT8.e8312_a875_rXXXX_p4128
mc16_13TeV.800781.Py8EG_A14NNPDF23LO_XHS_X2500_S1000_bbWW_1lep.deriv.DAOD_EXOT8.e8312_a875_rXXXX_p4128
mc16_13TeV.800782.Py8EG_A14NNPDF23LO_XHS_X2500_S1500_bbWW_1lep.deriv.DAOD_EXOT8.e8312_a875_rXXXX_p4128
mc16_13TeV.800783.Py8EG_A14NNPDF23LO_XHS_X2500_S2000_bbWW_1lep.deriv.DAOD_EXOT8.e8312_a875_rXXXX_p4128
mc16_13TeV.800784.Py8EG_A14NNPDF23LO_XHS_X3000_S170_bbWW_1lep.deriv.DAOD_EXOT8.e8312_a875_rXXXX_p4128
mc16_13TeV.800785.Py8EG_A14NNPDF23LO_XHS_X3000_S240_bbWW_1lep.deriv.DAOD_EXOT8.e8312_a875_rXXXX_p4128
mc16_13TeV.800786.Py8EG_A14NNPDF23LO_XHS_X3000_S400_bbWW_1lep.deriv.DAOD_EXOT8.e8312_a875_rXXXX_p4128
mc16_13TeV.800787.Py8EG_A14NNPDF23LO_XHS_X3000_S550_bbWW_1lep.deriv.DAOD_EXOT8.e8312_a875_rXXXX_p4128
mc16_13TeV.800788.Py8EG_A14NNPDF23LO_XHS_X3000_S750_bbWW_1lep.deriv.DAOD_EXOT8.e8312_a875_rXXXX_p4128
mc16_13TeV.800789.Py8EG_A14NNPDF23LO_XHS_X3000_S1000_bbWW_1lep.deriv.DAOD_EXOT8.e8312_a875_rXXXX_p4128
mc16_13TeV.800790.Py8EG_A14NNPDF23LO_XHS_X3000_S1500_bbWW_1lep.deriv.DAOD_EXOT8.e8312_a875_rXXXX_p4128
mc16_13TeV.800791.Py8EG_A14NNPDF23LO_XHS_X3000_S2000_bbWW_1lep.deriv.DAOD_EXOT8.e8312_a875_rXXXX_p4128
mc16_13TeV.800792.Py8EG_A14NNPDF23LO_XHS_X3000_S2500_bbWW_1lep.deriv.DAOD_EXOT8.e8312_a875_rXXXX_p4128

A.2.3. Background samples

$t\bar{t}$:

mc16_13TeV.410470.PhPy8EG_A14_ttbar_hdamp258p75_nonallhad.deriv.DAOD_EXOT8.e6337_s3126_rXXXX_p4004
mc16_13TeV.410471.PhPy8EG_A14_ttbar_hdamp258p75_allhad.deriv.DAOD_EXOT8.e6337_s3126_rXXXX_p4004

Single top:

mc16_13TeV.410644.PowhegPythia8EvtGen_A14_singletop_schan_lept_top.deriv.DAOD_EXOT8.e6527_s3126_rXXXX_p4004
mc16_13TeV.410645.PowhegPythia8EvtGen_A14_singletop_schan_lept_antitop.deriv.DAOD_EXOT8.e6527_s3126_rXXXX_p4004
mc16_13TeV.410646.PowhegPythia8EvtGen_A14_Wt_DR_inclusive_top.deriv.DAOD_EXOT8.e6552_s3126_rXXXX_p4004

mc16_13TeV.410647.PowhegPythia8EvtGen_A14_Wt_DR_inclusive_antitop.deriv.DAOD_EXOT8.e6552_s3126_rXXXX_p4004

mc16_13TeV.410654.PowhegPythia8EvtGen_A14_Wt_DS_inclusive_top.deriv.DAOD_EXOT8.e6552_s3126_rXXXX_p4004

mc16_13TeV.410655.PowhegPythia8EvtGen_A14_Wt_DS_inclusive_antitop.deriv.DAOD_EXOT8.e6552_s3126_rXXXX_p4004

mc16_13TeV.410658.PhPy8EG_A14_tchan_BW50_lept_top.deriv.DAOD_EXOT8.e6671_s3126_rXXXX_p4004

mc16_13TeV.410659.PhPy8EG_A14_tchan_BW50_lept_antitop.deriv.DAOD_EXOT8.e6671_s3126_rXXXX_p4004

$W \to e\nu$+jets:

mc16_13TeV.364170.Sherpa_221_NNPDF30NNLO_Wenu_MAXHTPTV0_70_CVetoBVeto.deriv.DAOD_EXOT8.e5340_s3126_rXXXX_p4004

mc16_13TeV.364171.Sherpa_221_NNPDF30NNLO_Wenu_MAXHTPTV0_70_CFilterBVeto.deriv.DAOD_EXOT8.e5340_s3126_rXXXX_p4004

mc16_13TeV.364172.Sherpa_221_NNPDF30NNLO_Wenu_MAXHTPTV0_70_BFilter.deriv.DAOD_EXOT8.e5340_s3126_rXXXX_p4004

mc16_13TeV.364173.Sherpa_221_NNPDF30NNLO_Wenu_MAXHTPTV70_140_CVetoBVeto.deriv.DAOD_EXOT8.e5340_s3126_rXXXX_p4004

mc16_13TeV.364174.Sherpa_221_NNPDF30NNLO_Wenu_MAXHTPTV70_140_CFilterBVeto.deriv.DAOD_EXOT8.e5340_s3126_rXXXX_p4004

mc16_13TeV.364175.Sherpa_221_NNPDF30NNLO_Wenu_MAXHTPTV70_140_BFilter.deriv.DAOD_EXOT8.e5340_s3126_rXXXX_p4004

mc16_13TeV.364176.Sherpa_221_NNPDF30NNLO_Wenu_MAXHTPTV140_280_CVetoBVeto.deriv.DAOD_EXOT8.e5340_s3126_rXXXX_p4004

mc16_13TeV.364177.Sherpa_221_NNPDF30NNLO_Wenu_MAXHTPTV140_280_CFilterBVeto.deriv.DAOD_EXOT8.e5340_s3126_rXXXX_p4004

mc16_13TeV.364178.Sherpa_221_NNPDF30NNLO_Wenu_MAXHTPTV140_280_BFilter.deriv.DAOD_EXOT8.e5340_s3126_rXXXX_p4004

mc16_13TeV.364179.Sherpa_221_NNPDF30NNLO_Wenu_MAXHTPTV280_500_CVetoBVeto.deriv.DAOD_EXOT8.e5340_s3126_rXXXX_p4004

mc16_13TeV.364180.Sherpa_221_NNPDF30NNLO_Wenu_MAXHTPTV280_500_CFilterBVeto.deriv.DAOD_EXOT8.e5340_s3126_rXXXX_p4004

mc16_13TeV.364181.Sherpa_221_NNPDF30NNLO_Wenu_MAXHTPTV280_500_BFilter.deriv.DAOD_EXOT8.e5340_s3126_rXXXX_p4004

mc16_13TeV.364182.Sherpa_221_NNPDF30NNLO_Wenu_MAXHTPTV500_1000.deriv.DAOD_EXOT8.e5340_s3126_rXXXX_p4004

mc16_13TeV.364183.Sherpa_221_NNPDF30NNLO_Wenu_MAXHTPTV1000_E_CMS.deriv.DAOD_EXOT8.e5340_s3126_rXXXX_p4004

$W \to \mu\nu$+jets:

mc16_13TeV.364156.Sherpa_221_NNPDF30NNLO_Wmunu_MAXHTPTV0_70_CVetoBVeto.deriv.DAOD_EXOT8.e5340_s3126_rXXXX_p4004

mc16_13TeV.364157.Sherpa_221_NNPDF30NNLO_Wmunu_MAXHTPTV0_70_CFilterBVeto.deriv.DAOD_EXOT8.e5340_s3126_rXXXX_p4004

mc16_13TeV.364158.Sherpa_221_NNPDF30NNLO_Wmunu_MAXHTPTV0_70_BFilter.deriv.DAOD_EXOT8.e5340_s3126_rXXXX_p4004

mc16_13TeV.364159.Sherpa_221_NNPDF30NNLO_Wmunu_MAXHTPTV70_140_CVetoBVeto.deriv.DAOD_EXOT8.e5340_s3126_rXXXX_p4004

mc16_13TeV.364160.Sherpa_221_NNPDF30NNLO_Wmunu_MAXHTPTV70_140_CFilterBVeto.deriv.DAOD_EXOT8.e5340_s3126_rXXXX_p4004

mc16_13TeV.364161.Sherpa_221_NNPDF30NNLO_Wmunu_MAXHTPTV70_140_BFilter.deriv.DAOD_EXOT8.e5340_s3126_rXXXX_p4004

mc16_13TeV.364162.Sherpa_221_NNPDF30NNLO_Wmunu_MAXHTPTV140_280_CVetoBVeto.deriv.DAOD_EXOT8.e5340_s3126_rXXXX_p4004

mc16_13TeV.364163.Sherpa_221_NNPDF30NNLO_Wmunu_MAXHTPTV140_280_CFilterBVeto.deriv.DAOD_EXOT8.e5340_s3126_rXXXX_p4004

mc16_13TeV.364164.Sherpa_221_NNPDF30NNLO_Wmunu_MAXHTPTV140_280_BFilter.deriv.DAOD_EXOT8.e5340_s3126_rXXXX_p4004

mc16_13TeV.364165.Sherpa_221_NNPDF30NNLO_Wmunu_MAXHTPTV280_500_CVetoBVeto.deriv.DAOD_EXOT8.e5340_s3126_rXXXX_p4004

mc16_13TeV.364166.Sherpa_221_NNPDF30NNLO_Wmunu_MAXHTPTV280_500_CFilterBVeto.deriv.DAOD_EXOT8.e5340_s3126_rXXXX_p4004

mc16_13TeV.364167.Sherpa_221_NNPDF30NNLO_Wmunu_MAXHTPTV280_500_BFilter.deriv.DAOD_EXOT8.e5340_s3126_rXXXX_p4004

mc16_13TeV.364168.Sherpa_221_NNPDF30NNLO_Wmunu_MAXHTPTV500_1000.deriv.DAOD_EXOT8.e5340_s3126_rXXXX_p4004

mc16_13TeV.364169.Sherpa_221_NNPDF30NNLO_Wmunu_MAXHTPTV1000_E_CMS.deriv.DAOD_EXOT8.e5340_s3126_rXXXX_p4004

$W \to \tau\nu$+jets:

mc16_13TeV.364184.Sherpa_221_NNPDF30NNLO_Wtaunu_MAXHTPTV0_70_CVetoBVeto.deriv.DAOD_EXOT8.e5340_s3126_rXXXX_p4004

mc16_13TeV.364185.Sherpa_221_NNPDF30NNLO_Wtaunu_MAXHTPTV0_70_CFilterBVeto.deriv.DAOD_EXOT8.e5340_s3126_rXXXX_p4004

mc16_13TeV.364186.Sherpa_221_NNPDF30NNLO_Wtaunu_MAXHTPTV0_70_BFilter.deriv.DAOD_EXOT8.e5340_s3126_rXXXX_p4004

mc16_13TeV.364187.Sherpa_221_NNPDF30NNLO_Wtaunu_MAXHTPTV70_140_CVetoBVeto.deriv.DAOD_EXOT8.e5340_s3126_rXXXX_p4004

mc16_13TeV.364188.Sherpa_221_NNPDF30NNLO_Wtaunu_MAXHTPTV70_140_CFilterBVeto.deriv.DAOD_EXOT8.e5340_s3126_rXXXX_p4004

mc16_13TeV.364189.Sherpa_221_NNPDF30NNLO_Wtaunu_MAXHTPTV70_140_BFilter.deriv.DAOD_EXOT8.e5340_s3126_rXXXX_p4004

mc16_13TeV.364190.Sherpa_221_NNPDF30NNLO_Wtaunu_MAXHTPTV140_280_CVetoBVeto.deriv.DAOD_EXOT8.e5340_s3126_rXXXX_p4004

mc16_13TeV.364191.Sherpa_221_NNPDF30NNLO_Wtaunu_MAXHTPTV140_280_CFilterBVeto.deriv.DAOD_EXOT8.e5340_s3126_rXXXX_p4004

mc16_13TeV.364192.Sherpa_221_NNPDF30NNLO_Wtaunu_MAXHTPTV140_280_BFilter.deriv.DAOD_EXOT8.e5340_s3126_rXXXX_p4004

mc16_13TeV.364193.Sherpa_221_NNPDF30NNLO_Wtaunu_MAXHTPTV280_500_CVetoBVeto.deriv.DAOD_EXOT8.e5340_s3126_rXXXX_p4004

mc16_13TeV.364194.Sherpa_221_NNPDF30NNLO_Wtaunu_MAXHTPTV280_500_CFilterBVeto.deriv.DAOD_EXOT8.e5340_s3126_rXXXX_p4004

mc16_13TeV.364195.Sherpa_221_NNPDF30NNLO_Wtaunu_MAXHTPTV280_500_BFilter.deriv.DAOD_EXOT8.e5340_s3126_rXXXX_p4004

mc16_13TeV.364196.Sherpa_221_NNPDF30NNLO_Wtaunu_MAXHTPTV500_1000.deriv.DAOD_EXOT8.e5340_s3126_rXXXX_p4004

mc16_13TeV.364197.Sherpa_221_NNPDF30NNLO_Wtaunu_MAXHTPTV1000_E_CMS.deriv.DAOD_EXOT8.e5340_s3126_rXXXX_p4004

$W \to \ell\nu$+jets t-channel:

mc16_13TeV.308096.Sherpa_221_NNPDF30NNLO_Wenu2jets_Min_N_TChannel.deriv.DAOD_EXOT8.e5789_s3126_rXXXX_p4004

mc16_13TeV.308097.Sherpa_221_NNPDF30NNLO_Wmunu2jets_Min_N_TChannel.deriv.DAOD_EXOT8.e5767_s3126_rXXXX_p4004

mc16_13TeV.308098.Sherpa_221_NNPDF30NNLO_Wtaunu2jets_Min_N_TChannel.deriv.DAOD_EXOT8.e5767_s3126_rXXXX_p4004

$W \to e\nu$+jets (alternative):

mc16_13TeV.363600.MGPy8EG_N30NLO_Wenu_Ht0_70_CVetoBVeto.deriv.DAOD_EXOT8.e4944_s3126_rXXXX_p4128

mc16_13TeV.363601.MGPy8EG_N30NLO_Wenu_Ht0_70_CFilterBVeto.deriv.DAOD_EXOT8.e4944_s3126_rXXXX_p4128

mc16_13TeV.363602.MGPy8EG_N30NLO_Wenu_Ht0_70_BFilter.deriv.DAOD_EXOT8.e4944_s3126_rXXXX_p4128

mc16_13TeV.363603.MGPy8EG_N30NLO_Wenu_Ht70_140_CVetoBVeto.deriv.DAOD_EXOT8.e4944_s3126_rXXXX_p4128

mc16_13TeV.363604.MGPy8EG_N30NLO_Wenu_Ht70_140_CFilterBVeto.deriv.DAOD_EXOT8.e4944_s3126_rXXXX_p4128

mc16_13TeV.363605.MGPy8EG_N30NLO_Wenu_Ht70_140_BFilter.deriv.DAOD_EXOT8.e4944_s3126_rXXXX_p4128

mc16_13TeV.363606.MGPy8EG_N30NLO_Wenu_Ht140_280_CVetoBVeto.deriv.DAOD_EXOT8.e4944_s3126_rXXXX_p4128

mc16_13TeV.363607.MGPy8EG_N30NLO_Wenu_Ht140_280_CFilterBVeto.deriv.DAOD_EXOT8.e4944_s3126_rXXXX_p4128

mc16_13TeV.363608.MGPy8EG_N30NLO_Wenu_Ht140_280_BFilter.deriv.DAOD_EXOT8.e4944_s3126_rXXXX_p4128

mc16_13TeV.363609.MGPy8EG_N30NLO_Wenu_Ht280_500_CVetoBVeto.deriv.DAOD_EXOT8.e4944_s3126_rXXXX_p4128

mc16_13TeV.363610.MGPy8EG_N30NLO_Wenu_Ht280_500_CFilterBVeto.deriv.DAOD_EXOT8.e4944_s3126_rXXXX_p4128

mc16_13TeV.363611.MGPy8EG_N30NLO_Wenu_Ht280_500_BFilter.deriv.DAOD_EXOT8.e4944_s3126_rXXXX_p4128

mc16_13TeV.363612.MGPy8EG_N30NLO_Wenu_Ht500_700_CVetoBVeto.deriv.DAOD_EXOT8.e4944_s3126_rXXXX_p4128

mc16_13TeV.363613.MGPy8EG_N30NLO_Wenu_Ht500_700_CFilterBVeto.deriv.DAOD_EXOT8.e4944_s3126_rXXXX_p4128

mc16_13TeV.363614.MGPy8EG_N30NLO_Wenu_Ht500_700_BFilter.deriv.DAOD_EXOT8.e4944_s3126_rXXXX_p4128

mc16_13TeV.363615.MGPy8EG_N30NLO_Wenu_Ht700_1000_CVetoBVeto.deriv.DAOD_EXOT8.e4944_s3126_rXXXX_p4128

mc16_13TeV.363616.MGPy8EG_N30NLO_Wenu_Ht700_1000_CFilterBVeto.deriv.DAOD_EXOT8.e4944_s3126_rXXXX_p4128

mc16_13TeV.363617.MGPy8EG_N30NLO_Wenu_Ht700_1000_BFilter.deriv.DAOD_EXOT8.e4944_s3126_rXXXX_p4128

mc16_13TeV.363618.MGPy8EG_N30NLO_Wenu_Ht1000_2000_CVetoBVeto.deriv.DAOD_EXOT8.e4944_s3126_rXXXX_p4128

mc16_13TeV.363619.MGPy8EG_N30NLO_Wenu_Ht1000_2000_CFilterBVeto.deriv.DAOD_EXOT8.e4944_s3126_rXXXX_p4128

mc16_13TeV.363620.MGPy8EG_N30NLO_Wenu_Ht1000_2000_BFilter.deriv.DAOD_EXOT8.e4944_s3126_rXXXX_p4128

mc16_13TeV.363621.MGPy8EG_N30NLO_Wenu_Ht2000_E_CMS_CVetoBVeto.deriv.DAOD_EXOT8.e4944_s3126_rXXXX_p4128

mc16_13TeV.363622.MGPy8EG_N30NLO_Wenu_Ht2000_E_CMS_CFilterBVeto.deriv.DAOD_EXOT8.e4944_s3126_rXXXX_p4128

mc16_13TeV.363623.MGPy8EG_N30NLO_Wenu_Ht2000_E_CMS_BFilter.deriv.DAOD_EXOT8.e4944_s3126_rXXXX_p4128

$W \to \mu\nu$+jets (alternative):

mc16_13TeV.363624.MGPy8EG_N30NLO_Wmunu_Ht0_70_CVetoBVeto.deriv.DAOD_EXOT8.e4944_s3126_rXXXX_p4128

mc16_13TeV.363625.MGPy8EG_N30NLO_Wmunu_Ht0_70_CFilterBVeto.deriv.DAOD_EXOT8.e4944_s3126_rXXXX_p4128

mc16_13TeV.363626.MGPy8EG_N30NLO_Wmunu_Ht0_70_BFilter.deriv.DAOD_EXOT8.e4944_s3126_rXXXX_p4128

mc16_13TeV.363627.MGPy8EG_N30NLO_Wmunu_Ht70_140_CVetoBVeto.deriv.DAOD_EXOT8.e4944_s3126_rXXXX_p4128

mc16_13TeV.363628.MGPy8EG_N30NLO_Wmunu_Ht70_140_CFilterBVeto.deriv.DAOD_EXOT8.e4944_s3126_rXXXX_p4128

mc16_13TeV.363629.MGPy8EG_N30NLO_Wmunu_Ht70_140_BFilter.deriv.DAOD_EXOT8.e4944_s3126_rXXXX_p4128
mc16_13TeV.363630.MGPy8EG_N30NLO_Wmunu_Ht140_280_CVetoBVeto.deriv.DAOD_EXOT8.e4944_s3126_rXXXX_p4128
mc16_13TeV.363631.MGPy8EG_N30NLO_Wmunu_Ht140_280_CFilterBVeto.deriv.DAOD_EXOT8.e4944_s3126_rXXXX_p4128
mc16_13TeV.363632.MGPy8EG_N30NLO_Wmunu_Ht140_280_BFilter.deriv.DAOD_EXOT8.e4944_s3126_rXXXX_p4128
mc16_13TeV.363633.MGPy8EG_N30NLO_Wmunu_Ht280_500_CVetoBVeto.deriv.DAOD_EXOT8.e4944_s3126_rXXXX_p4128
mc16_13TeV.363634.MGPy8EG_N30NLO_Wmunu_Ht280_500_CFilterBVeto.deriv.DAOD_EXOT8.e4944_s3126_rXXXX_p4128
mc16_13TeV.363635.MGPy8EG_N30NLO_Wmunu_Ht280_500_BFilter.deriv.DAOD_EXOT8.e4944_s3126_rXXXX_p4128
mc16_13TeV.363636.MGPy8EG_N30NLO_Wmunu_Ht500_700_CVetoBVeto.deriv.DAOD_EXOT8.e4944_s3126_rXXXX_p4128
mc16_13TeV.363637.MGPy8EG_N30NLO_Wmunu_Ht500_700_CFilterBVeto.deriv.DAOD_EXOT8.e4944_s3126_rXXXX_p4128
mc16_13TeV.363638.MGPy8EG_N30NLO_Wmunu_Ht500_700_BFilter.deriv.DAOD_EXOT8.e4944_s3126_rXXXX_p4128
mc16_13TeV.363639.MGPy8EG_N30NLO_Wmunu_Ht700_1000_CVetoBVeto.deriv.DAOD_EXOT8.e4944_s3126_rXXXX_p4128
mc16_13TeV.363640.MGPy8EG_N30NLO_Wmunu_Ht700_1000_CFilterBVeto.deriv.DAOD_EXOT8.e4944_s3126_rXXXX_p4128
mc16_13TeV.363641.MGPy8EG_N30NLO_Wmunu_Ht700_1000_BFilter.deriv.DAOD_EXOT8.e4944_s3126_rXXXX_p4128
mc16_13TeV.363642.MGPy8EG_N30NLO_Wmunu_Ht1000_2000_CVetoBVeto.deriv.DAOD_EXOT8.e4944_s3126_rXXXX_p4128
mc16_13TeV.363643.MGPy8EG_N30NLO_Wmunu_Ht1000_2000_CFilterBVeto.deriv.DAOD_EXOT8.e4944_s3126_rXXXX_p4128
mc16_13TeV.363644.MGPy8EG_N30NLO_Wmunu_Ht1000_2000_BFilter.deriv.DAOD_EXOT8.e4944_s3126_rXXXX_p4128
mc16_13TeV.363645.MGPy8EG_N30NLO_Wmunu_Ht2000_E_CMS_CVetoBVeto.deriv.DAOD_EXOT8.e4944_s3126_rXXXX_p4128
mc16_13TeV.363646.MGPy8EG_N30NLO_Wmunu_Ht2000_E_CMS_CFilterBVeto.deriv.DAOD_EXOT8.e4944_s3126_rXXXX_p4128
mc16_13TeV.363647.MGPy8EG_N30NLO_Wmunu_Ht2000_E_CMS_BFilter.deriv.DAOD_EXOT8.e4944_s3126_rXXXX_p4128

$W \to \tau\nu$+jets (alternative):

mc16_13TeV.363648.MGPy8EG_N30NLO_Wtaunu_Ht0_70_CVetoBVeto.deriv.DAOD_EXOT8.e4944_s3126_rXXXX_p4128
mc16_13TeV.363649.MGPy8EG_N30NLO_Wtaunu_Ht0_70_CFilterBVeto.deriv.DAOD_EXOT8.e4944_s3126_rXXXX_p4128
mc16_13TeV.363650.MGPy8EG_N30NLO_Wtaunu_Ht0_70_BFilter.deriv.DAOD_EXOT8.e4944_s3126_rXXXX_p4128
mc16_13TeV.363651.MGPy8EG_N30NLO_Wtaunu_Ht70_140_CVetoBVeto.deriv.DAOD_EXOT8.e4944_s3126_rXXXX_p4128
mc16_13TeV.363652.MGPy8EG_N30NLO_Wtaunu_Ht70_140_CFilterBVeto.deriv.DAOD_EXOT8.e4944_s3126_rXXXX_p4128
mc16_13TeV.363653.MGPy8EG_N30NLO_Wtaunu_Ht70_140_BFilter.deriv.DAOD_EXOT8.e4944_s3126_rXXXX_p4128
mc16_13TeV.363654.MGPy8EG_N30NLO_Wtaunu_Ht140_280_CVetoBVeto.deriv.DAOD_EXOT8.e4944_s3126_rXXXX_p4128
mc16_13TeV.363655.MGPy8EG_N30NLO_Wtaunu_Ht140_280_CFilterBVeto.deriv.DAOD_EXOT8.e4944_s3126_rXXXX_p4128
mc16_13TeV.363656.MGPy8EG_N30NLO_Wtaunu_Ht140_280_BFilter.deriv.DAOD_EXOT8.e4944_s3126_rXXXX_p4128
mc16_13TeV.363657.MGPy8EG_N30NLO_Wtaunu_Ht280_500_CVetoBVeto.deriv.DAOD_EXOT8.e4944_s3126_rXXXX_p4128
mc16_13TeV.363658.MGPy8EG_N30NLO_Wtaunu_Ht280_500_CFilterBVeto.deriv.DAOD_EXOT8.e4944_s3126_rXXXX_p4128
mc16_13TeV.363659.MGPy8EG_N30NLO_Wtaunu_Ht280_500_BFilter.deriv.DAOD_EXOT8.e4944_s3126_rXXXX_p4128
mc16_13TeV.363660.MGPy8EG_N30NLO_Wtaunu_Ht500_700_CVetoBVeto.deriv.DAOD_EXOT8.e4944_s3126_rXXXX_p4128
mc16_13TeV.363661.MGPy8EG_N30NLO_Wtaunu_Ht500_700_CFilterBVeto.deriv.DAOD_EXOT8.e4944_s3126_rXXXX_p4128
mc16_13TeV.363662.MGPy8EG_N30NLO_Wtaunu_Ht500_700_BFilter.deriv.DAOD_EXOT8.e4944_s3126_rXXXX_p4128
mc16_13TeV.363663.MGPy8EG_N30NLO_Wtaunu_Ht700_1000_CVetoBVeto.deriv.DAOD_EXOT8.e4944_s3126_rXXXX_p4128
mc16_13TeV.363664.MGPy8EG_N30NLO_Wtaunu_Ht700_1000_CFilterBVeto.deriv.DAOD_EXOT8.e4944_s3126_rXXXX_p4128
mc16_13TeV.363665.MGPy8EG_N30NLO_Wtaunu_Ht700_1000_BFilter.deriv.DAOD_EXOT8.e4944_s3126_rXXXX_p4128
mc16_13TeV.363666.MGPy8EG_N30NLO_Wtaunu_Ht1000_2000_CVetoBVeto.deriv.DAOD_EXOT8.e4944_s3126_rXXXX_p4128
mc16_13TeV.363667.MGPy8EG_N30NLO_Wtaunu_Ht1000_2000_CFilterBVeto.deriv.DAOD_EXOT8.e4944_s3126_rXXXX_p4128
mc16_13TeV.363668.MGPy8EG_N30NLO_Wtaunu_Ht1000_2000_BFilter.deriv.DAOD_EXOT8.e4944_s3126_rXXXX_p4128
mc16_13TeV.363669.MGPy8EG_N30NLO_Wtaunu_Ht2000_E_CMS_CVetoBVeto.deriv.DAOD_EXOT8.e4944_s3126_rXXXX_p4128

mc16_13TeV.363670.MGPy8EG_N30NLO_Wtaunu_Ht2000_E_CMS_CFilterBVeto.deriv.DAOD_EXOT8.e4944_s3126_rXXXX_p4128

mc16_13TeV.363671.MGPy8EG_N30NLO_Wtaunu_Ht2000_E_CMS_BFilter.deriv.DAOD_EXOT8.e4944_s3126_rXXXX_p4128

$W \to qq$+jets:

mc16_13TeV.304673.Herwigpp_UEEE5CTEQ6L1_Wjhadronic_280_500.deriv.DAOD_EXOT8.e4571_s3126_rXXXX_p4004

mc16_13TeV.304674.Herwigpp_UEEE5CTEQ6L1_Wjhadronic_500_700.deriv.DAOD_EXOT8.e4571_s3126_rXXXX_p4004

mc16_13TeV.304675.Herwigpp_UEEE5CTEQ6L1_Wjhadronic_700_1000.deriv.DAOD_EXOT8.e4571_s3126_rXXXX_p4004

mc16_13TeV.304676.Herwigpp_UEEE5CTEQ6L1_Wjhadronic_1000_1400.deriv.DAOD_EXOT8.e4571_s3126_rXXXX_p4004

mc16_13TeV.304677.Herwigpp_UEEE5CTEQ6L1_Wjhadronic_1400.deriv.DAOD_EXOT8.e4571_s3126_rXXXX_p4004

$Z \to ee$+jets:

mc16_13TeV.364114.Sherpa_221_NNPDF30NNLO_Zee_MAXHTPTV0_70_CVetoBVeto.deriv.DAOD_EXOT8.e5299_s3126_rXXXX_p4004

mc16_13TeV.364115.Sherpa_221_NNPDF30NNLO_Zee_MAXHTPTV0_70_CFilterBVeto.deriv.DAOD_EXOT8.e5299_s3126_rXXXX_p4004

mc16_13TeV.364116.Sherpa_221_NNPDF30NNLO_Zee_MAXHTPTV0_70_BFilter.deriv.DAOD_EXOT8.e5299_s3126_rXXXX_p4004

mc16_13TeV.364117.Sherpa_221_NNPDF30NNLO_Zee_MAXHTPTV70_140_CVetoBVeto.deriv.DAOD_EXOT8.e5299_s3126_rXXXX_p4004

mc16_13TeV.364118.Sherpa_221_NNPDF30NNLO_Zee_MAXHTPTV70_140_CFilterBVeto.deriv.DAOD_EXOT8.e5299_s3126_rXXXX_p4004

mc16_13TeV.364119.Sherpa_221_NNPDF30NNLO_Zee_MAXHTPTV70_140_BFilter.deriv.DAOD_EXOT8.e5299_s3126_rXXXX_p4004

mc16_13TeV.364120.Sherpa_221_NNPDF30NNLO_Zee_MAXHTPTV140_280_CVetoBVeto.deriv.DAOD_EXOT8.e5299_s3126_rXXXX_p4004

mc16_13TeV.364121.Sherpa_221_NNPDF30NNLO_Zee_MAXHTPTV140_280_CFilterBVeto.deriv.DAOD_EXOT8.e5299_s3126_rXXXX_p4004

mc16_13TeV.364122.Sherpa_221_NNPDF30NNLO_Zee_MAXHTPTV140_280_BFilter.deriv.DAOD_EXOT8.e5299_s3126_rXXXX_p4004

mc16_13TeV.364123.Sherpa_221_NNPDF30NNLO_Zee_MAXHTPTV280_500_CVetoBVeto.deriv.DAOD_EXOT8.e5299_s3126_rXXXX_p4004

mc16_13TeV.364124.Sherpa_221_NNPDF30NNLO_Zee_MAXHTPTV280_500_CFilterBVeto.deriv.DAOD_EXOT8.e5299_s3126_rXXXX_p4004

mc16_13TeV.364125.Sherpa_221_NNPDF30NNLO_Zee_MAXHTPTV280_500_BFilter.deriv.DAOD_EXOT8.e5299_s3126_rXXXX_p4004

mc16_13TeV.364126.Sherpa_221_NNPDF30NNLO_Zee_MAXHTPTV500_1000.deriv.DAOD_EXOT8.e5299_s3126_rXXXX_p4004

mc16_13TeV.364127.Sherpa_221_NNPDF30NNLO_Zee_MAXHTPTV1000_E_CMS.deriv.DAOD_EXOT8.e5299_s3126_rXXXX_p4004

$Z \to \mu\mu$+jets:

mc16_13TeV.364100.Sherpa_221_NNPDF30NNLO_Zmumu_MAXHTPTV0_70_CVetoBVeto.deriv.DAOD_EXOT8.e5271_s3126_rXXXX_p4004

mc16_13TeV.364101.Sherpa_221_NNPDF30NNLO_Zmumu_MAXHTPTV0_70_CFilterBVeto.deriv.DAOD_EXOT8.e5271_s3126_rXXXX_p4004

mc16_13TeV.364102.Sherpa_221_NNPDF30NNLO_Zmumu_MAXHTPTV0_70_BFilter.deriv.DAOD_EXOT8.e5271_s3126_rXXXX_p4004

mc16_13TeV.364103.Sherpa_221_NNPDF30NNLO_Zmumu_MAXHTPTV70_140_CVetoBVeto.deriv.DAOD_EXOT8.e5271_s3126_rXXXX_p4004

mc16_13TeV.364104.Sherpa_221_NNPDF30NNLO_Zmumu_MAXHTPTV70_140_CFilterBVeto.deriv.DAOD_EXOT8.e5271_s3126_rXXXX_p4004

mc16_13TeV.364105.Sherpa_221_NNPDF30NNLO_Zmumu_MAXHTPTV70_140_BFilter.deriv.DAOD_EXOT8.e5271_s3126_rXXXX_p4004

mc16_13TeV.364106.Sherpa_221_NNPDF30NNLO_Zmumu_MAXHTPTV140_280_CVetoBVeto.deriv.DAOD_EXOT8.e5271_s3126_rXXXX_p4004

mc16_13TeV.364107.Sherpa_221_NNPDF30NNLO_Zmumu_MAXHTPTV140_280_CFilterBVeto.deriv.DAOD_EXOT8.e5271_s3126_rXXXX_p4004

mc16_13TeV.364108.Sherpa_221_NNPDF30NNLO_Zmumu_MAXHTPTV140_280_BFilter.deriv.DAOD_EXOT8.e5271_s3126_rXXXX_p4004

mc16_13TeV.364109.Sherpa_221_NNPDF30NNLO_Zmumu_MAXHTPTV280_500_CVetoBVeto.deriv.DAOD_EXOT8.e5271_s3126_rXXXX_p4004

mc16_13TeV.364110.Sherpa_221_NNPDF30NNLO_Zmumu_MAXHTPTV280_500_CFilterBVeto.deriv.DAOD_EXOT8.e5271_s3126_rXXXX_p4004

mc16_13TeV.364111.Sherpa_221_NNPDF30NNLO_Zmumu_MAXHTPTV280_500_BFilter.deriv.DAOD_EXOT8.e5271_s3126_rXXXX_p4004

mc16_13TeV.364112.Sherpa_221_NNPDF30NNLO_Zmumu_MAXHTPTV500_1000.deriv.DAOD_EXOT8.e5271_s3126_rXXXX_p4004

mc16_13TeV.364113.Sherpa_221_NNPDF30NNLO_Zmumu_MAXHTPTV1000_E_CMS.deriv.DAOD_EXOT8.e5271_s3126_rXXXX_p4004

$Z \to \tau\tau$+jets:

mc16_13TeV.364128.Sherpa_221_NNPDF30NNLO_Ztautau_MAXHTPTV0_70_CVetoBVeto.deriv.DAOD_EXOT8.e5307_s3126_rXXXX_p4004

mc16_13TeV.364129.Sherpa_221_NNPDF30NNLO_Ztautau_MAXHTPTV0_70_CFilterBVeto.deriv.DAOD_EXOT8.e5307_s3126_rXXXX_p4004

mc16_13TeV.364130.Sherpa_221_NNPDF30NNLO_Ztautau_MAXHTPTV0_70_BFilter.deriv.DAOD_EXOT8.e5307_s3126_rXXXX_p4004

mc16_13TeV.364131.Sherpa_221_NNPDF30NNLO_Ztautau_MAXHTPTV70_140_CVetoBVeto.deriv.DAOD_EXOT8.e5307_s3126_rXXXX_p4004

mc16_13TeV.364132.Sherpa_221_NNPDF30NNLO_Ztautau_MAXHTPTV70_140_CFilterBVeto.deriv.DAOD_EXOT8.e5307_s3126_rXXXX_p4004

mc16_13TeV.364133.Sherpa_221_NNPDF30NNLO_Ztautau_MAXHTPTV70_140_BFilter.deriv.DAOD_EXOT8.e5307_s3126_rXXXX_p4004

mc16_13TeV.364134.Sherpa_221_NNPDF30NNLO_Ztautau_MAXHTPTV140_280_CVetoBVeto.deriv.DAOD_EXOT8.e5307_s3126_rXXXX_p4004

mc16_13TeV.364135.Sherpa_221_NNPDF30NNLO_Ztautau_MAXHTPTV140_280_CFilterBVeto.deriv.DAOD_EXOT8.e5307_s3126_rXXXX_p4004

mc16_13TeV.364136.Sherpa_221_NNPDF30NNLO_Ztautau_MAXHTPTV140_280_BFilter.deriv.DAOD_EXOT8.e5307_s3126_rXXXX_p4004

mc16_13TeV.364137.Sherpa_221_NNPDF30NNLO_Ztautau_MAXHTPTV280_500_CVetoBVeto.deriv.DAOD_EXOT8.e5307_s3126_rXXXX_p4004

mc16_13TeV.364138.Sherpa_221_NNPDF30NNLO_Ztautau_MAXHTPTV280_500_CFilterBVeto.deriv.DAOD_EXOT8.e5313_s3126_rXXXX_p4004

mc16_13TeV.364139.Sherpa_221_NNPDF30NNLO_Ztautau_MAXHTPTV280_500_BFilter.deriv.DAOD_EXOT8.e5313_s3126_rXXXX_p4004

mc16_13TeV.364140.Sherpa_221_NNPDF30NNLO_Ztautau_MAXHTPTV500_1000.deriv.DAOD_EXOT8.e5307_s3126_rXXXX_p4004

mc16_13TeV.364141.Sherpa_221_NNPDF30NNLO_Ztautau_MAXHTPTV1000_E_CMS.deriv.DAOD_EXOT8.e5307_s3126_rXXXX_p4004

$Z \to \ell\ell$+jets t-channel:

mc16_13TeV.308092.Sherpa_221_NNPDF30NNLO_Zee2jets_Min_N_TChannel.deriv.DAOD_EXOT8.e5767_s3126_rXXXX_p4004

mc16_13TeV.308093.Sherpa_221_NNPDF30NNLO_Zmm2jets_Min_N_TChannel.deriv.DAOD_EXOT8.e5767_s3126_rXXXX_p4004

mc16_13TeV.308094.Sherpa_221_NNPDF30NNLO_Ztautau2jets_Min_N_TChannel.deriv.DAOD_EXOT8.e5767_s3126_rXXXX_p4004

$Z \to qq$+jets:

mc16_13TeV.304678.Herwigpp_UEEE5CTEQ6L1_Zjhadronic_280_500.deriv.DAOD_EXOT8.e4571_s3126_rXXXX_p4004

mc16_13TeV.304679.Herwigpp_UEEE5CTEQ6L1_Zjhadronic_500_700.deriv.DAOD_EXOT8.e4571_s3126_rXXXX_p4004

mc16_13TeV.304680.Herwigpp_UEEE5CTEQ6L1_Zjhadronic_700_1000.deriv.DAOD_EXOT8.e4571_s3126_rXXXX_p4004

mc16_13TeV.304681.Herwigpp_UEEE5CTEQ6L1_Zjhadronic_1000_1400.deriv.DAOD_EXOT8.e4571_s3126_rXXXX_p4004

mc16_13TeV.304682.Herwigpp_UEEE5CTEQ6L1_Zjhadronic_1400.deriv.DAOD_EXOT8.e4571_s3126_rXXXX_p4004

ZZ:

mc16_13TeV.363355.Sherpa_221_NNPDF30NNLO_ZqqZvv.deriv.DAOD_EXOT8.e5525_s3126_rXXXX_p4004

mc16_13TeV.363356.Sherpa_221_NNPDF30NNLO_ZqqZll.deriv.DAOD_EXOT8.e5525_s3126_rXXXX_p4004

WZ:

mc16_13TeV.363357.Sherpa_221_NNPDF30NNLO_WqqZvv.deriv.DAOD_EXOT8.e5525_s3126_rXXXX_p4004

mc16_13TeV.363358.Sherpa_221_NNPDF30NNLO_WqqZll.deriv.DAOD_EXOT8.e5525_s3126_rXXXX_p4004

WW:

mc16_13TeV.363359.Sherpa_221_NNPDF30NNLO_WpqqWmlv.deriv.DAOD_EXOT8.e5583_s3126_rXXXX_p4004

mc16_13TeV.363360.Sherpa_221_NNPDF30NNLO_WplvWmqq.deriv.DAOD_EXOT8.e5983_s3126_rXXXX_p4004

$W + \gamma$:

mc16_13TeV.364413.MadGraphPythia8EvtGen_WqqgammaNp0123_DP140_280.deriv.DAOD_EXOT8.e5969_s3126_rXXXX_p4004

mc16_13TeV.364414.MadGraphPythia8EvtGen_WqqgammaNp0123_DP280_500.deriv.DAOD_EXOT8.e5969_s3126_rXXXX_p4004

mc16_13TeV.364415.MadGraphPythia8EvtGen_WqqgammaNp0123_DP500_1000.deriv.DAOD_EXOT8.e5969_s3126_rXXXX_p4004

mc16_13TeV.364416.MadGraphPythia8EvtGen_WqqgammaNp0123_DP1000_2000.deriv.DAOD_EXOT8.e5969_s3126_rXXXX_p4004

mc16_13TeV.364417.MadGraphPythia8EvtGen_WqqgammaNp0123_DP2000_inf.deriv.DAOD_EXOT8.e5969_s3126_rXXXX_p4004

$Z + \gamma$:

mc16_13TeV.364418.MadGraphPythia8EvtGen_ZqqgammaNp0123_DP140_280.deriv.DAOD_EXOT8.e5969_s3126_rXXXX_p4004

mc16_13TeV.364419.MadGraphPythia8EvtGen_ZqqgammaNp0123_DP280_500.deriv.DAOD_EXOT8.e5969_s3126_rXXXX_p4004

mc16_13TeV.364420.MadGraphPythia8EvtGen_ZqqgammaNp0123_DP500_1000.deriv.DAOD_EXOT8.e5969_s3126_rXXXX_p4004

mc16_13TeV.364421.MadGraphPythia8EvtGen_ZqqgammaNp0123_DP1000_2000.deriv.DAOD_EXOT8.e5969_s3126_rXXXX_p4004

mc16_13TeV.364422.MadGraphPythia8EvtGen_ZqqgammaNp0123_DP2000_inf.deriv.DAOD_EXOT8.e5969_s3126_rXXXX_p4004

Dijet:

mc16_13TeV.364700.Pythia8EvtGen_A14NNPDF23LO_jetjet_JZ0WithSW.deriv.DAOD_EXOT8.e7142_s3126_rXXXX_p4004

mc16_13TeV.364701.Pythia8EvtGen_A14NNPDF23LO_jetjet_JZ1WithSW.deriv.DAOD_EXOT8.e7142_s3126_rXXXX_p4004

mc16_13TeV.364702.Pythia8EvtGen_A14NNPDF23LO_jetjet_JZ2WithSW.deriv.DAOD_EXOT8.e7142_s3126_rXXXX_p4004

mc16_13TeV.364703.Pythia8EvtGen_A14NNPDF23LO_jetjet_JZ3WithSW.deriv.DAOD_EXOT8.e7142_s3126_rXXXX_p4004

mc16_13TeV.364704.Pythia8EvtGen_A14NNPDF23LO_jetjet_JZ4WithSW.deriv.DAOD_EXOT8.e7142_s3126_rXXXX_p4004

mc16_13TeV.364705.Pythia8EvtGen_A14NNPDF23LO_jetjet_JZ5WithSW.deriv.DAOD_EXOT8.e7142_s3126_rXXXX_p4004

mc16_13TeV.364706.Pythia8EvtGen_A14NNPDF23LO_jetjet_JZ6WithSW.deriv.DAOD_EXOT8.e7142_s3126_rXXXX_p4004

mc16_13TeV.364707.Pythia8EvtGen_A14NNPDF23LO_jetjet_JZ7WithSW.deriv.DAOD_EXOT8.e7142_s3126_rXXXX_p4004

mc16_13TeV.364708.Pythia8EvtGen_A14NNPDF23LO_jetjet_JZ8WithSW.deriv.DAOD_EXOT8.e7142_s3126_rXXXX_p4004

mc16_13TeV.364709.Pythia8EvtGen_A14NNPDF23LO_jetjet_JZ9WithSW.deriv.DAOD_EXOT8.e7142_s3126_rXXXX_p4004

mc16_13TeV.364710.Pythia8EvtGen_A14NNPDF23LO_jetjet_JZ10WithSW.deriv.DAOD_EXOT8.e7142_s3126_rXXXX_p4004

mc16_13TeV.364711.Pythia8EvtGen_A14NNPDF23LO_jetjet_JZ11WithSW.deriv.DAOD_EXOT8.e7142_s3126_rXXXX_p4004

mc16_13TeV.364712.Pythia8EvtGen_A14NNPDF23LO_jetjet_JZ12WithSW.deriv.DAOD_EXOT8.e7142_s3126_rXXXX_p4004

A.3. Trigger names

Trigger Name	Year	p_{T} threshold	jet type
HLT_j460_a10r_L1SC111	2018	460 GeV	reclustered
HLT_j460_a10r_L1J100	2018	460 GeV	reclustered
HLT_j460_a10_lcw_subjes_L1SC111	2018	460 GeV	untrimmed
HLT_j460_a10_lcw_subjes_L1J100	2018	460 GeV	untrimmed
HLT_j460_a10t_lcw_jes_L1SC111	2018	460 GeV	trimmed
HLT_j460_a10t_lcw_jes_L1J100	2018	460 GeV	trimmed
HLT_j480_a10r_L1J100	2017	480 GeV	reclustered
HLT_j460_a10r_L1J100	2017	460 GeV	reclustered
HLT_j440_a10r_L1J100	2017	440 GeV	reclustered
HLT_j420_a10r_L1J100	2017	420 GeV	reclustered
HLT_j480_a10_lcw_subjes_L1J100	2017	480 GeV	untrimmed
HLT_j460_a10_lcw_subjes_L1J100	2017	460 GeV	untrimmed
HLT_j440_a10_lcw_subjes_L1J100	2017	440 GeV	untrimmed
HLT_j480_a10t_lcw_jes_L1J100	2017	480 GeV	trimmed
HLT_j460_a10t_lcw_jes_L1J100	2017	460 GeV	trimmed
HLT_j440_a10t_lcw_jes_L1J100	2017	440 GeV	trimmed
HLT_j420_a10t_lcw_jes_L1J100	2017	420 GeV	trimmed
HLT_j420_a10r_L1J100	2016	420 GeV	reclustered
HLT_j400_a10r_L1J100	2016	400 GeV	reclustered
HLT_j360_a10r_L1J100	2016	360 GeV	reclustered
HLT_j420_a10_lcw_L1J100	2016	420 GeV	untrimmed
HLT_j400_a10_lcw_L1J100	2016	400 GeV	untrimmed
HLT_j360_a10_lcw_L1J100	2016	360 GeV	untrimmed
HLT_j360_a10r_L1J100	2015	360 GeV	reclustered
HLT_j360_a10_sub_L1J100	2015	360 GeV	untrimmed

Table A.2.: List of used unprescaled single large-R jet triggers including the years of validity, the jet type and the trigger threshold.

Trigger name	Year	p_{T} threshold	mass threshold
HLT_2j330_a10t_lcw_jes_30smcINF_L1J100	2017	330 GeV	30 GeV (both)
HLT_2j330_a10t_lcw_jes_40smcINF_L1J100	2017	330 GeV	40 GeV (both)
HLT_2j330_a10t_lcw_jes_35smcINF_L1SC111	2018	330 GeV	35 GeV (both)
HLT_2j330_a10t_lcw_jes_35smcINF_L1J100	2018	330 GeV	35 GeV (both)
HLT_j360_a10t_lcw_jes_60smcINF_j360_a10t_lcw_jes_L1SC111	2018	360 GeV	60 GeV (lead)
HLT_j370_a10t_lcw_jes_35smcINF_j370_a10t_lcw_jes_L1SC111	2018	370 GeV	35 GeV (lead)

Table A.3.: List of used unprescaled multi large-R jet triggers including the years of validity and the trigger thresholds in jet p_{T} and mass.

Trigger name	Year	n_{jets}	p_{T} threshold	b-tagging
HLT_j175_bmedium	2015	1	175 GeV	medium
HLT_j225_bloose	2015	1	225 GeV	loose
HLT_j150_bmedium_j50_bmedium	2015	2	150 & 50 GeV	medium (both)
HLT_j175_bmv2c2040_split	2016	1	175 GeV	40%
HLT_j225_bmv2c2060_split	2016	1	225 GeV	60%
HLT_j275_bmv2c2070_split	2016	1	275 GeV	70%
HLT_j300_bmv2c2077_split	2016	1	300 GeV	77%
HLT_j360_bmv2c2085_split	2016	1	360 GeV	85%
HLT_j150_bmv2c2060_split_j50_bmv2c2060_split	2016	2	150 & 50 GeV	60% (both)
HLT_j175_bmv2c2060_split_j50_bmv2c2050_split	2016	2	175 & 50 GeV	60% & 50%
HLT_j175_gsc225_bmv2c1040_split	2017	1	225 GeV	40%
HLT_j225_gsc275_bmv2c1060_split	2017	1	275 GeV	60%
HLT_j225_gsc300_bmv2c1070_split	2017	1	300 GeV	70%
HLT_j225_gsc360_bmv2c1077_split	2017	1	360 GeV	77%
HLT_j150_gsc175_bmv2c1070_split_j45_gsc60_bmv2c1070_split	2017	2	175 & 45 GeV	70% (both)
HLT_j175_gsc225_bmv2c1040_split	2018	1	225 GeV	40%
HLT_j225_gsc275_bmv2c1060_split	2018	1	275 GeV	60%
HLT_j225_gsc300_bmv2c1070_split	2018	1	300 GeV	70%
HLT_j225_gsc360_bmv2c1077_split	2018	1	360 GeV	77%
HLT_j150_gsc175_bmv2c1060_split_j45_gsc60_bmv2c1060_split	2018	2	175 & 45 GeV	60% (both)

Table A.4.: List of used unprescaled b-jet triggers including the years of validity, the number of jets triggered on, the trigger threshold and b-tagging working point.

Trigger Name	Year	p_{T} threshold	ID	track isolation
HLT_e24_lhmedium_L1EM20VH	2015	24 GeV	medium	-
HLT_e60_lhmedium	2015	60 GeV	medium	-
HLT_e120_lhloose	2015	120 GeV	loose	-
HLT_e24_lhmedium_nod0_L1EM20VH	2016	24 GeV	medium	-
HLT_e24_lhtight_nod0_ivarloose	2016	24 GeV	tight	loose
HLT_e26_lhtight_nod0_ivarloose	2016-2018	26 GeV	tight	loose
HLT_e60_lhmedium_nod0	2016-2018	60 GeV	medium	-
HLT_e140_lhloose_nod0	2016-2018	140 GeV	loose	-
HLT_e300_etcut	2016-2018	300 GeV	-	-
HLT_mu20_iloose_L1MU15	2015	20 GeV	-	loose track
HLT_mu40	2015	40 GeV	-	-
HLT_mu24_ivarloose	2016	24 GeV	-	loose
HLT_mu24_ivarmedium	2016	24 GeV	-	medium
HLT_mu26_ivarmedium	2016-2018	26 GeV	-	medium
HLT_mu50	2016-2018	50 GeV	-	-

Table A.5.: List of used unprescaled single lepton triggers where the top set corresponds to single electron triggers and the bottom set to single muon triggers. The years of validity, the trigger threshold as well as identification and track isolation requirements on the leptons are also listed. For single electron triggers nod0 corresponds to no d_0 requirement on the triggered electron.

A.4. Window Cut Derivation

To take into account differences in variables resulting from the boosts the final state particles obtained from the masses of m_X and m_S, cuts on these variables are performed depending on the p_T of a related object. For example, if the variable of interest was the mass of the $H \to b\bar{b}$ candidate, the cut would depend on the p_T of the $H \to b\bar{b}$ candidate. Furthermore, not only a single cut is determined but a window corresponding to two cuts in between which the signal resides.

All windows are constructed by the following steps:

1. A two dimensional histogram consisting of the p_T and variable of interest is created for each relevant signal which are combined by simply adding all histograms such that the resulting histogram contains the information of all considered signals. To not miss any signal, the p_T range is set generously to $0\,\mathrm{GeV} \leq p_\mathrm{T} \leq 5000\,\mathrm{GeV}$ using bins with an initial bin width of 10 GeV. All considered events must pass the preselection defined in Section 5.4 and contain exactly one b-tagged TAR jet.

2. To ensure sufficient statistics in each p_T bin, neighbouring p_T bins are merged until the relative statistical uncertainty of the rebinned p_T bins is less than 5%.

3. In each resulting p_T bin, the smallest window around the median of the variable of interest containing a certain percentage of the signal events is constructed.

4. The determined upper and lower bounds for all p_T bins are then fitted by a suitable function to have a smooth definition of the bounds in p_T. The uncertainty on the p_T- variable bound points are assigned to be half of the p_T and variable bin width, respectively.

A.4.1. $H \to b\bar{b}$ mass window

The first window is constructed for the mass of the $H \to b\bar{b}$ candidate which depends on the p_T of the $H \to b\bar{b}$ candidate. Only signals corresponding to the HH production are considered. In Figure A.3, all signals peak around m_H but the shape of the peak varies depending on the mass of the resonance decaying to the $H \to b\bar{b}$. For low m_X, even a second very small peak can be observed in the low $m_\mathrm{TAR}^{H\to b\bar{b}}$ region. Furthermore, a clear correlation between m_X and the p_T of the $H \to b\bar{b}$ candidate is shown.

The function used to fit the bounds is a third order polynomial of $\log\left(p_\mathrm{T}^{H\to b\bar{b}}\right)$:

$$p_0 + p_1 \cdot \log\left(p_\mathrm{T}^{H\to b\bar{b}}\right) + p_2 \cdot \log\left(p_\mathrm{T}^{H\to b\bar{b}}\right)^2 + p_3 \cdot \log\left(p_\mathrm{T}^{H\to b\bar{b}}\right)^3, \tag{A.2}$$

where p_i denote the free fit parameters and $p_\mathrm{T}^{H\to b\bar{b}}$ is given in MeV.

The fit results for four different signal efficiencies can be found in Table A.6. The corresponding plots are displayed in Figure A.4. While the bulk of the points are well described by the function, both the lower and upper p_T tails are not fitted well. However, this is not a concern because the low tail is cut by the preselection. Thus, the dashed part

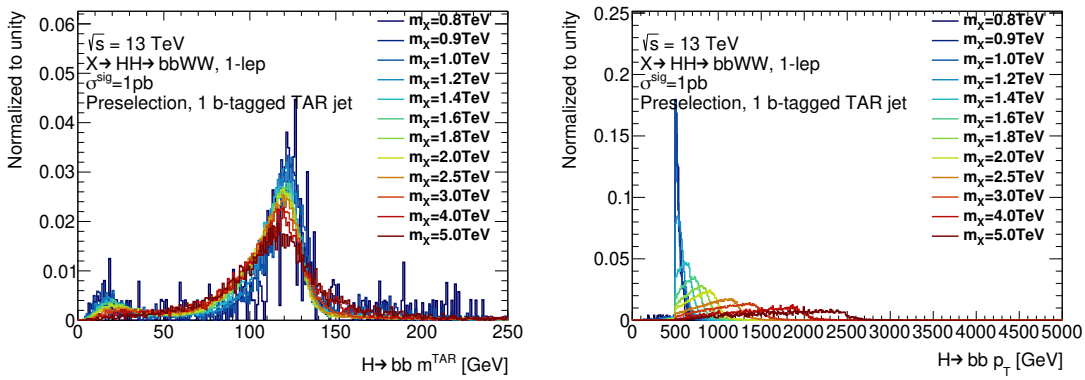

(a) $m_{\mathrm{TAR}}^{H\to b\bar{b}}$ **(b)** $p_{\mathrm{T}}^{H\to b\bar{b}}$

Figure A.3.: Normalised distributions of the mass and p_{T} of the $H \to b\bar{b}$ candidate for the individual signal samples. The preselection except the $p_{\mathrm{T}}^{H\to b\bar{b}} > 500$ GeV cut is applied. Furthermore, exactly one b-tagged jet in the event is required.

of the lines will not be considered in the analysis. Considering the high p_{T} tails, these are mainly populated by signal events and nearly no background events are expected in this region.

Efficiency	p_0 [GeV]	p_1 [GeV]	p_2 [GeV]	p_3 [GeV]
50%	-15 000	3 100	-210	4.5
	-78 000	17 000	-1 300	31
60%	-2 300	170	12	-0.9
	-60 000	13 000	-970	24
70%	-2 800	220	14	-1.0
	1 700	-110	-9	0.7
80%	-4 000	470	-5	-0.6
	-110 000	23 000	-1 700	42

Table A.6.: Fit parameter for the lower and upper bound on the $H \to b\bar{b}$ mass window for $p_{\mathrm{T}}^{H\to b\bar{b}}$ measured in MeV using anti-k_t ($R = 0.75$) TAR jets.

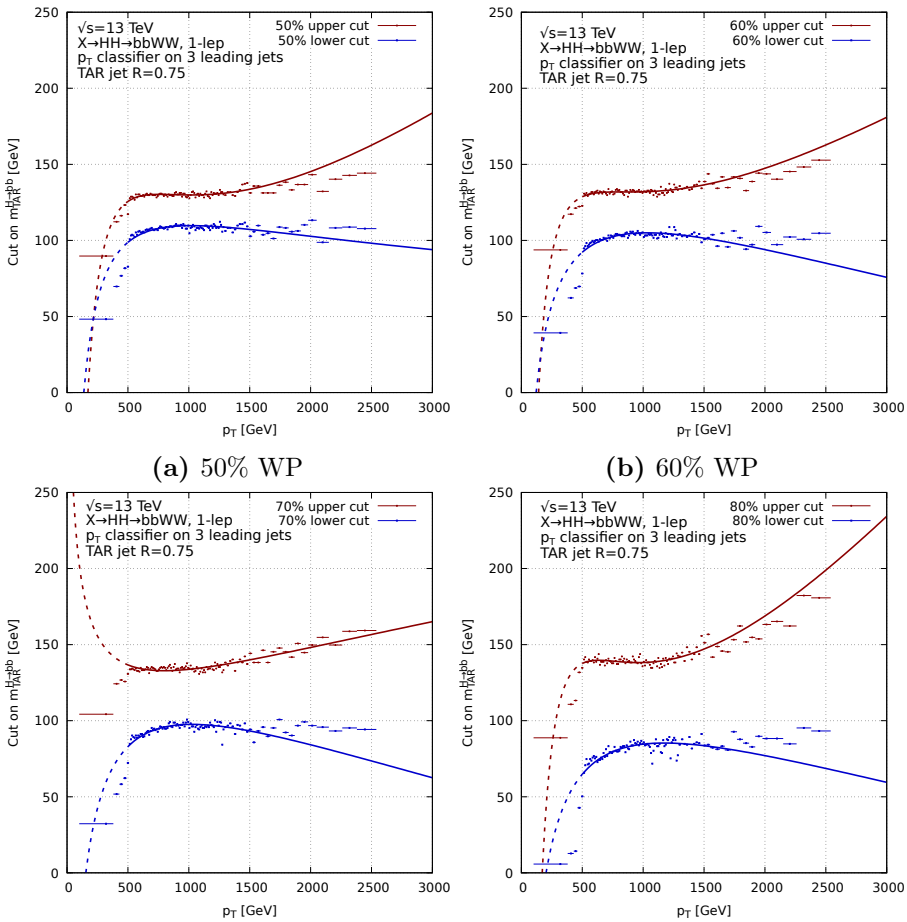

(a) 50% WP **(b)** 60% WP

(c) 70% WP **(d)** 80% WP

Figure A.4.: Mass windows of the $H \to b\bar{b}$ candidate depending on $p_{\mathrm{T}}^{H\to b\bar{b}}$ evaluated to contain a certain percentage of $X \to HH \to b\bar{b}WW^*$ and corresponding fits. The dashed part of the fit will not be used in the analysis due to the applied $p_{\mathrm{T}}^{H\to b\bar{b}} > 500$ GeV cut in the preselection (see Section 5.4).

A.4.2. $H \to b\bar{b}$ C_2 window

The second window to be constructed is for the substructure variable C_2 of the $H \to b\bar{b}$ candidate again depending on the p_{T} of the $H \to b\bar{b}$ candidate. The function to fit the bounds is

$$p_0 + \frac{p_1}{\sqrt{p_{\mathrm{T}}^{H\to b\bar{b}}}} + \frac{p_2}{p_{\mathrm{T}}^{H\to b\bar{b}}}. \tag{A.3}$$

Since there are differences between signals corresponding to HH and SH production, respectively, the bounds are determined separately for HH and SH signals. The results can be found in Tables A.7 (a) and (b), respectively, with the corresponding distributions shown in Figures A.5 and A.6.

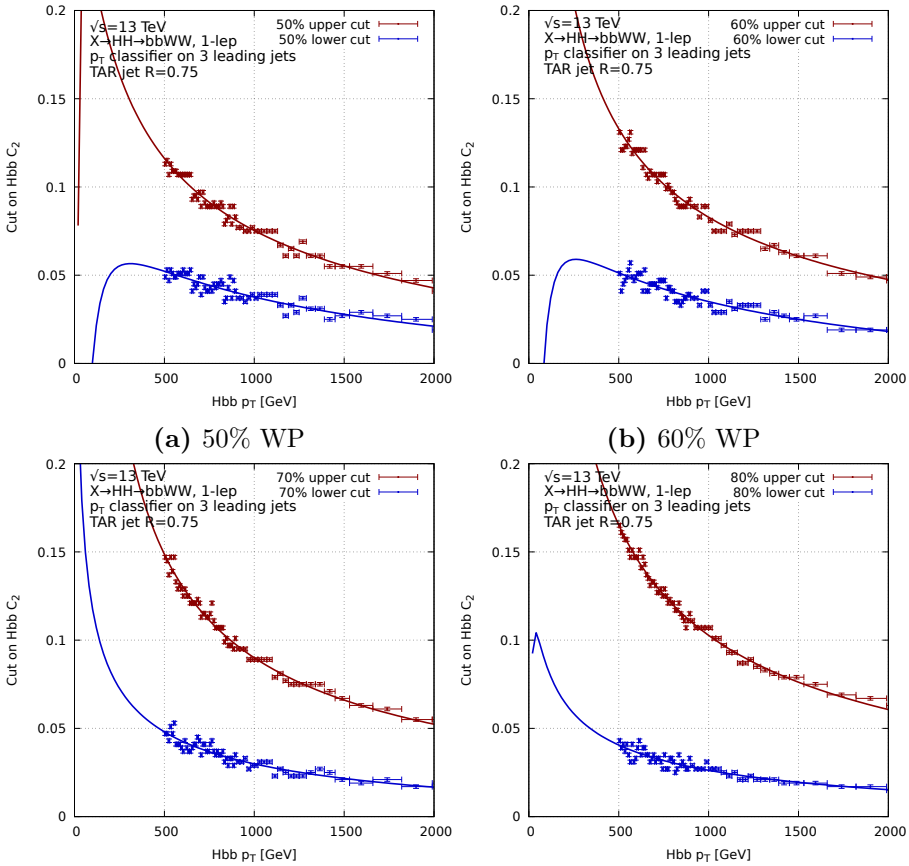

(a) 50% WP **(b)** 60% WP

(c) 70% WP **(d)** 80% WP

Figure A.5.: C_2 windows of the $H \to b\bar{b}$ candidate depending on $p_{\mathrm{T}}^{H\to b\bar{b}}$ evaluated to contain a certain percentage of $X \to HH \to b\bar{b}WW^*$ and corresponding fits.

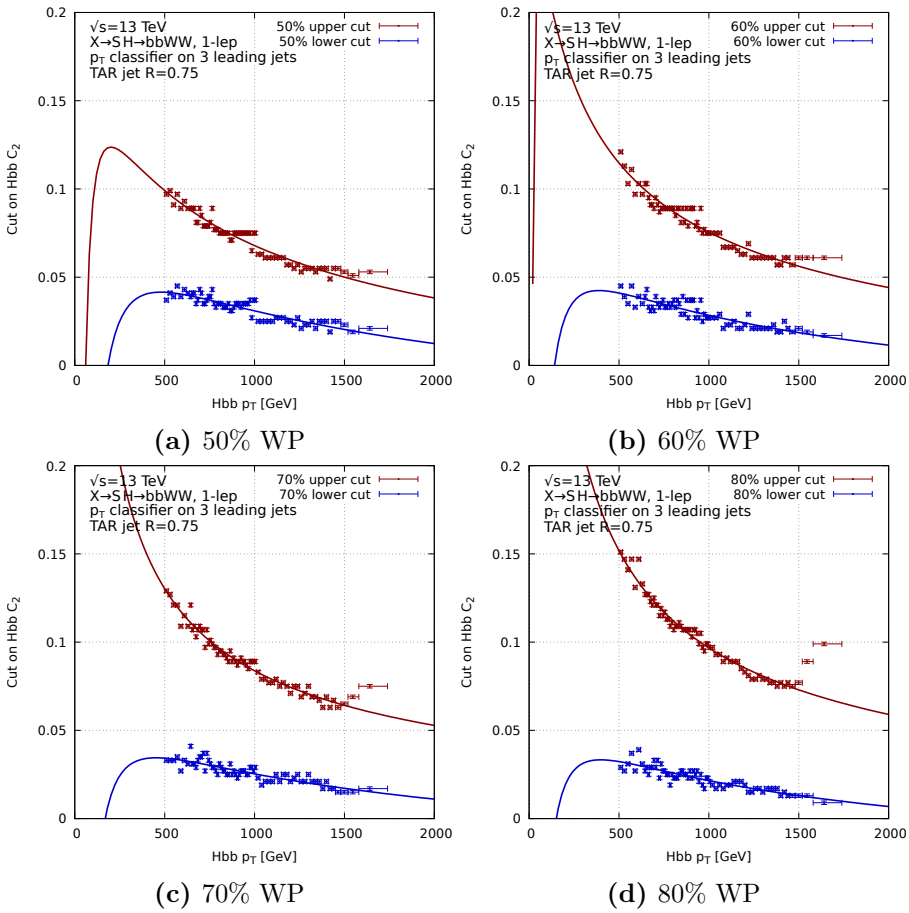

(a) 50% WP **(b)** 60% WP

(c) 70% WP **(d)** 80% WP

Figure A.6.: C_2 windows of the $H \to b\bar{b}$ candidate depending on $p_{\mathrm{T}}^{H\to b\bar{b}}$ evaluated to contain a certain percentage of $X \to SH \to b\bar{b}WW$ and corresponding fits.

Efficiency	p_0	p_1 [$\sqrt{\text{MeV}}$]	p_2 [MeV]
50%	-0.04	110	-30 000
	-0.05	140	-17 000
60%	-0.04	100	-26 000
	-0.04	120	600
70%	-0.02	48	-1 800
	-0.03	97	18 000
80%	-0.01	45	-4 200
	-0.03	130	10 000

(a) HH signals

Efficiency	p_0	p_1 [$\sqrt{\text{MeV}}$]	p_2 [MeV]
50%	-0.07	150	-53 000
	-0.06	160	-37 000
60%	-0.06	120	-38 000
	-0.04	140	-18 000
70%	-0.05	120	-39 000
	-0.02	90	9 200
80%	-0.05	110	-34 000
	-0.03	120	6 200

(b) SH signals

Table A.7.: Fit parameter for the lower and upper bound on the $H \to b\bar{b}$ C_2 window using anti-k_t ($R = 0.75$) TAR jets.

A.4.3. $\Delta R(\ell, W_{\text{had}})$ window

The third window in this analysis is constructed for $\Delta R(W_{\text{had}}, \ell)$ using HH signals. Since this variable depends on two objects, the W_{had} candidate and the lepton, the situation is more complex. Three potential transverse momenta can be considered: p_{T}^{ℓ}, $p_{\text{T}}^{W_{\text{had}}}$ and $p_{\text{T}}^{H_{\text{vis}}}$ where $H_{\text{vis}} = \ell + W_{\text{had}}$. The fit function is the same as for the $H \to b\bar{b}$ C_2 window:

$$p_0 + \frac{p_1}{\sqrt{p_{\text{T}}}} + \frac{p_2}{p_{\text{T}}}. \tag{A.4}$$

The bounds and corresponding fits depending the p_{T} of the different objects are shown for the 80% working point in Figure A.7. It can be seen that while all bounds have a falling behaviour, the fit does not work well when using the p_{T} of the W_{had} candidate. Comparing the p_{T} distributions themselves in Figure A.8, it becomes clear that the p_{T} of the H_{vis} is modelled the best. As it contains information on both relevant objects, it is used to determine the bounds. The fit results can be found in Table A.8 with the corresponding plots in Figure A.9.

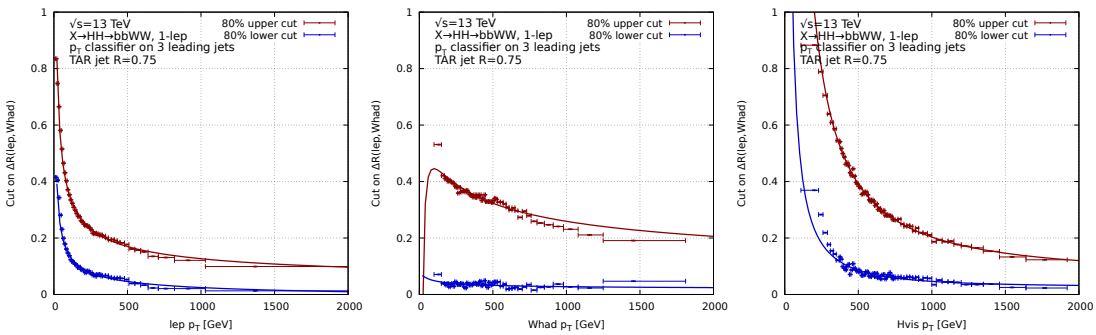

(a) lepton p_{T} **(b)** W_{had} candidate p_{T} **(c)** H_{vis} p_{T}

Figure A.7.: $\Delta R(W_{\text{had}}, \ell)$ windows containing 80% of $X \to HH \to b\bar{b}WW^*$ depending on the p_{T} of different contributing objects and corresponding fits.

Efficiency	p_0	p_1 [$\sqrt{\text{MeV}}$]	p_2 [MeV]
50%	0.11	-170	140 000
	0.09	-160	210 000
60%	0.10	-150	120 000
	0.11	-180	230 000
70%	0.07	-100	91 000
	0.14	-220	260 000
80%	0.05	-66	67 000
	0.09	-120	240 000

Table A.8.: Fit parameter for the lower and upper bound on the $\Delta R(W_{\text{had}}, \ell)$ window using anti-k_t ($R = 0.75$) TAR jets.

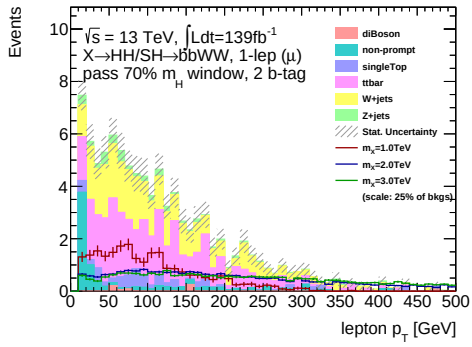

(a) lepton p_{T} in SRp2

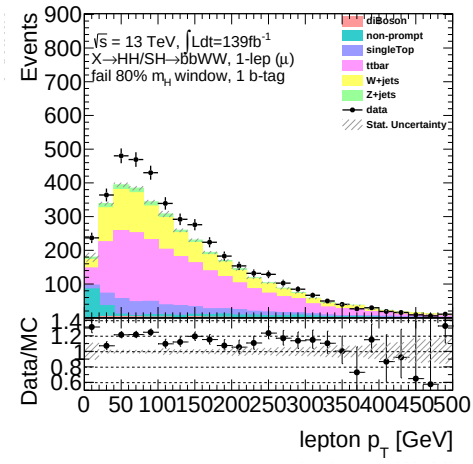

(b) lepton p_{T} in VRf1

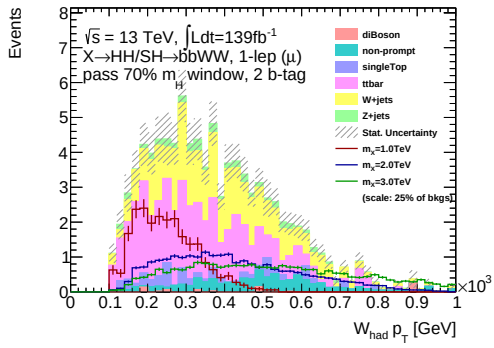

(c) W_{had} candidate p_{T} in SRp2

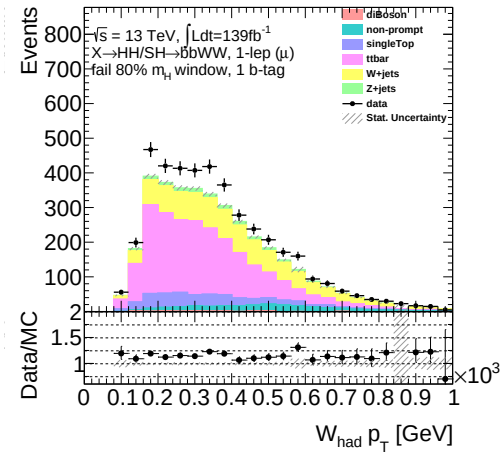

(d) W_{had} candidate p_{T} in VRf1

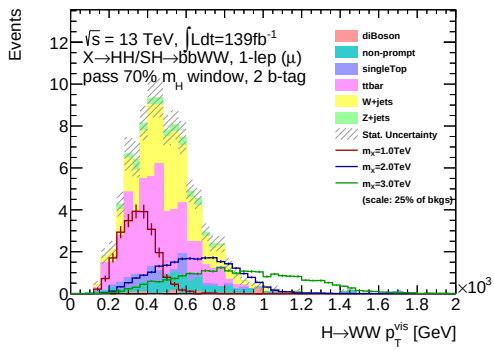

(e) H_{vis} p_{T} in SRp2

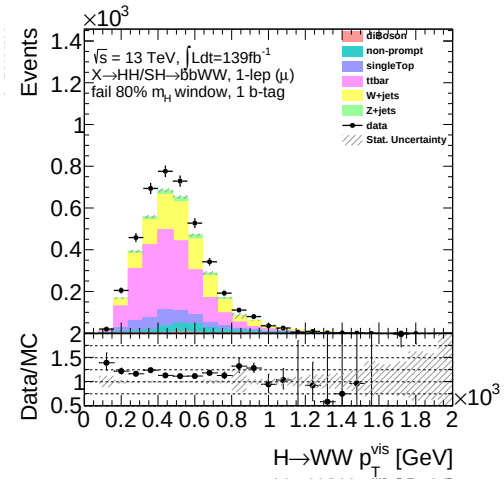

(f) H_{vis} p_{T} in VRf1

Figure A.8.: Distribution of the p_{T} of the different contributing objects to $\Delta R(W_{\mathrm{had}}, lep)$ in the most sensitive SR (top) and the VR (bottom). In the SR, the signal is scaled to 25% of the backgrounds integral.

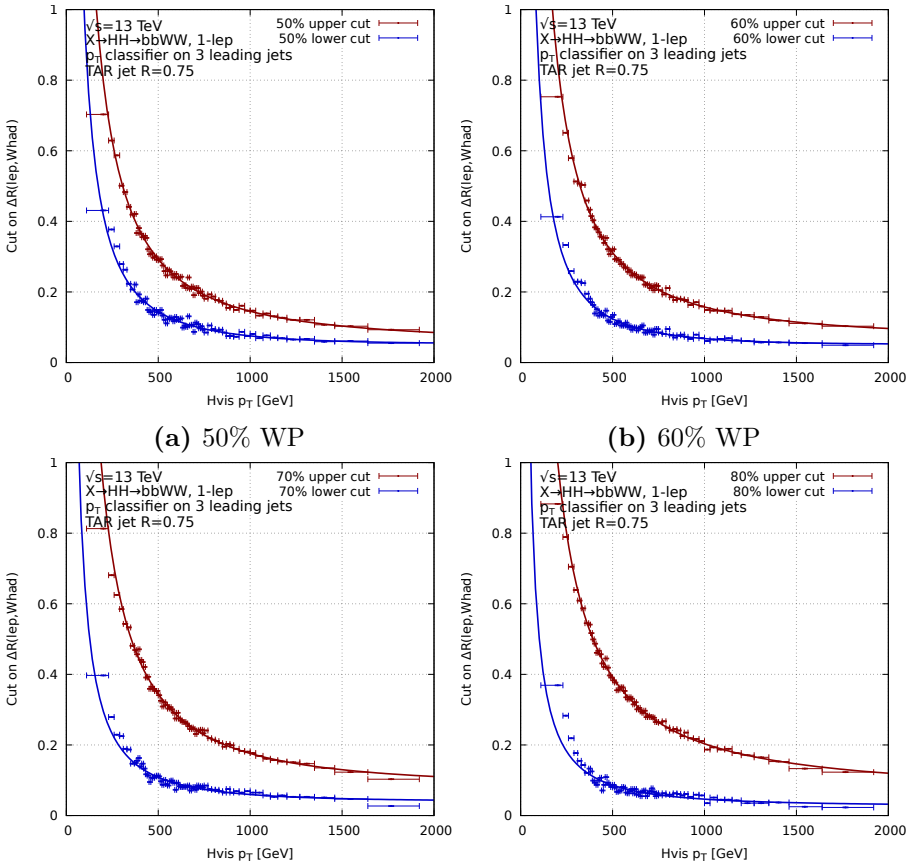

(a) 50% WP **(b)** 60% WP

(c) 70% WP **(d)** 80% WP

Figure A.9.: $\Delta R(W_{\text{had}}, \ell)$ windows depending on $p_{\text{T}}^{H_{\text{vis}}}$, where $H_{\text{vis}} = W_{\text{had}} + \ell$, evaluated to contain a certain percentage of $X \to HH \to b\bar{b}WW^*$ and corresponding fits.

A.4.4. W_{had} mass window

The last window is constructed for the mass of the W_{had} candidate depending on the p_{T} of the W_{had} candidate using SH signals. In contrast to the previous window cuts, this variable shows the shape of a Fermi-Dirac distribution:

$$p_0 + \frac{p_1}{1 + \exp(p_2 \cdot p_{\text{T}} + p_3)} \tag{A.5}$$

with $p_{\text{T}}^{W_{\text{had}}}$ and $m_{\text{TAR}}^{W_{\text{had}}}$ are given in MeV. The results can be found in Table A.9 with the corresponding plots in Figure A.10.

It can clearly be seen that for a low p_{T}, the mass window is in fact far away from the W boson mass and, thus, rather selects single quark jets as they appear in most of the backgrounds, e.g. the non-prompt lepton background, W+jets and also $t\bar{t}$ (see Section 5.6).

Efficiency	p_0 [GeV]	p_1 [GeV]	p_2 [GeV^{-1}]	p_3
50%	90	-70	0.14	-31
	64	-63	0.09	-22
60%	98	-78	0.06	-14
	61	-62	0.04	-10
70%	110	-100	0.03	-5
	59	-60	0.03	-8
80%	130	-160	0.01	-2
	53	-49	0.04	-14

Table A.9.: Fit parameter for the lower and upper bound on the $m_{\text{TAR}}^{W_{\text{had}}}$ window using anti-k_t ($R = 0.75$) TAR jets.

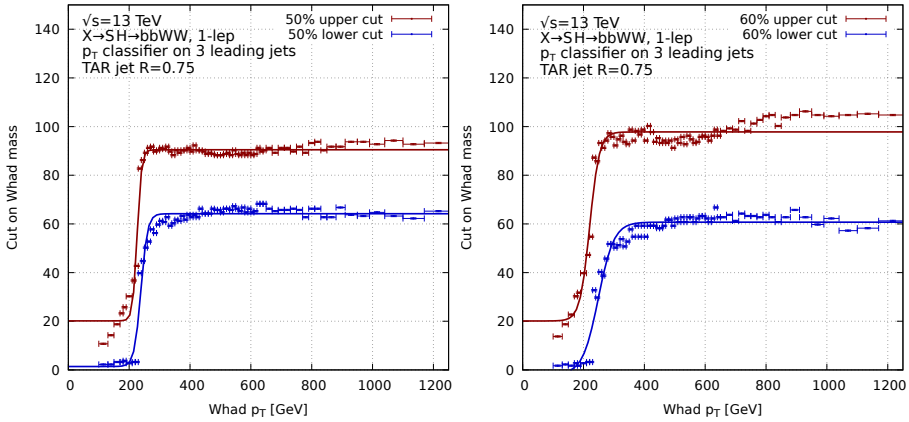

(a) 50% WP

(b) 60% WP

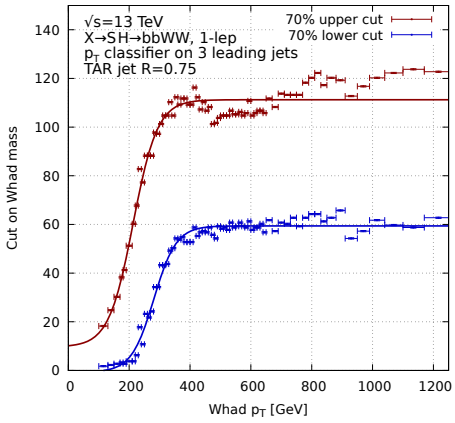

(c) 70% WP

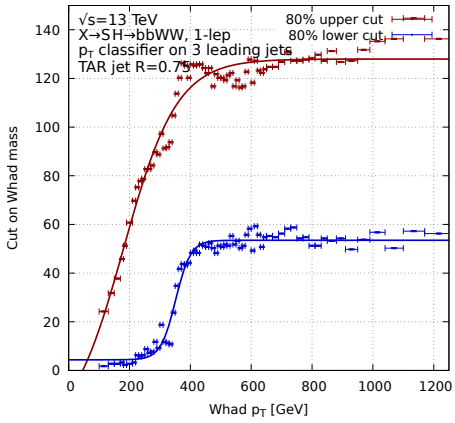

(d) 80% WP

Figure A.10.: Mass windows of the W_{had} candidate depending on $p_{\text{T}}^{W_{\text{had}}}$, evaluated to contain a certain percentage of $X \to SH \to b\bar{b}WW$ and corresponding fits.

A.5. Final Discriminant Options

As described in Section 5.9, four variables are investigated as final discriminant. The normalised distributions of these variables in SRf2 and SRp1 are displayed in Figures A.11 and A.12, respectively. While the invariant mass provides the best reconstruction of m_X also in SRf2 and SRp1, the necessity to calculate the neutrino p_z disfavours this variable. However, as for SRp2, a similarly good reconstruction can be achieved by using $m_{\text{vis+met}}$.

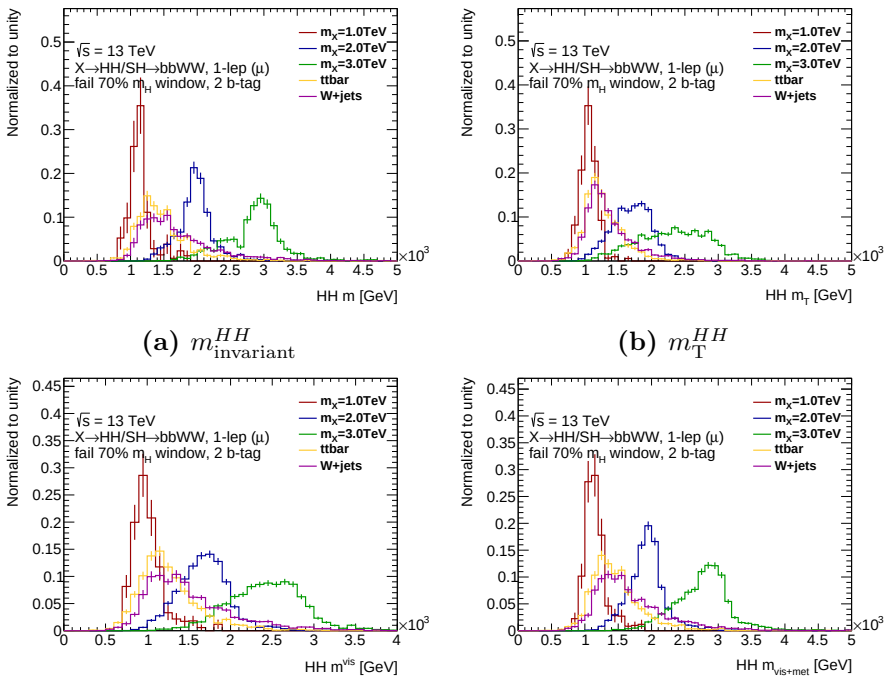

(a) $m^{HH}_{\text{invariant}}$ (b) m^{HH}_{T}

(c) m^{HH}_{vis} (d) $m^{HH}_{\text{vis+met}}$

Figure A.11.: Options considered as final discriminant for the boosted 1-lepton analysis in the SRf2 signal region.

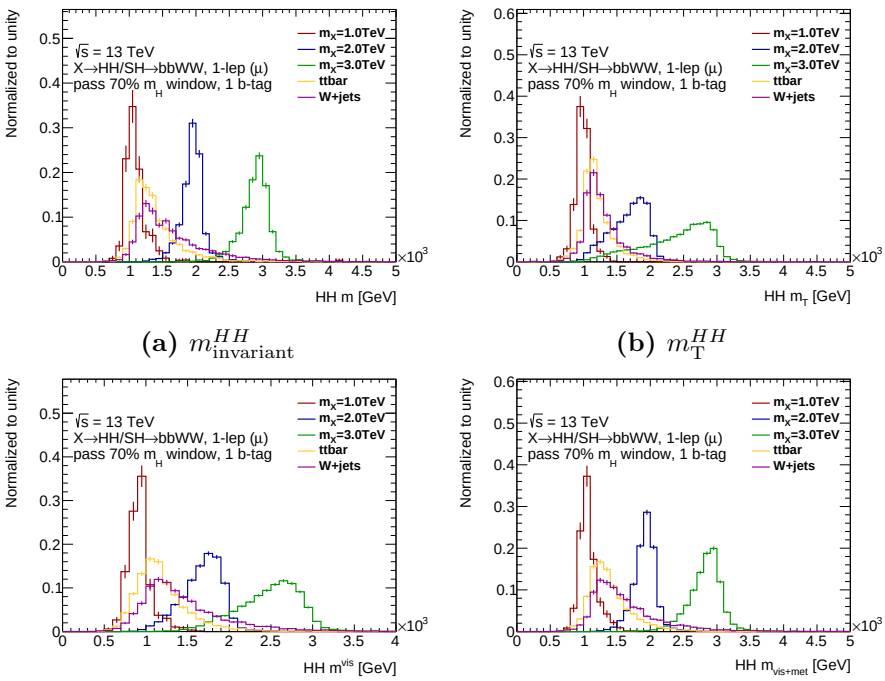

(a) $m^{HH}_{\text{invariant}}$ **(b)** m^{HH}_{T}

(c) m^{HH}_{vis} **(d)** $m^{HH}_{\text{vis+met}}$

Figure A.12.: Options considered as final discriminant for the boosted 1-lepton analysis in the SRp1 signal region.

A.6. Modelling in Control Regions

The distributions of

- $\boldsymbol{p_{\mathrm{T}}}$ of the lepton,
- $\boldsymbol{E_{\mathrm{T}}^{\mathrm{miss}}}$ as an approximate measure of the neutrino p_{T},
- $\boldsymbol{m_{\mathrm{TAR}}}$ of the $H \to b\bar{b}$ candidate,
- $\boldsymbol{\Delta R(W_{\mathrm{had}}, \ell)}$ defining the boosted phase space,
- $\boldsymbol{m_{\mathrm{vis+met}}}$ of the reconstructed HH or SH system, respectively, as final discriminant and, thus, probably the most important variable in this analysis.

are shown in Figures A.13–A.17 in the $t\bar{t}$ CR (a), W+jets CR (b) and QCD CR (c). A more extensive list of variables is presented in Appendix A.7.

Generally, there is only very small mismodelling in the $t\bar{t}$ CR showing that the kinematics of $t\bar{t}$ events are well described and only the normalisation needed to be corrected. In contrast, the modelling of the W+jets and the non-prompt lepton background in the W+jets and QCD CRs is not optimal. Despite the correction, the non-prompt lepton background appears to be underestimated while the W+jets background is slightly overestimated due to the anticorrelation between these two backgrounds.

While the lepton p_{T} is generally well modelled in all three CRs as can be seen in Figure A.13, the first bin in the QCD CR and in the W+jets CR features an underestimation of the background compared to data. Since this bin in the QCD CR is dominated by the non-prompt lepton contribution, the normalisation of the non-prompt lepton background appears to be underestimated. Other bins which have a larger W+jets contribution match the data better.

The same behaviour can be observed in the $E_{\mathrm{T}}^{\mathrm{miss}}$ distribution in Figure A.14 where the first bins show an underestimation of the backgrounds compared to data. This is also the case in the $t\bar{t}$ CR, where the effect is less dramatic and nearly covered by statistical uncertainties alone and, therefore, not considered to be problematic.

The distribution of the mass of the $H \to b\bar{b}$ candidate displayed in Figure A.15 features an overestimation of the backgrounds in the $t\bar{t}$ CR in the area of $m_{\mathrm{TAR}}^{H\to b\bar{b}} \lesssim 30\,\mathrm{GeV}$ and $m_{\mathrm{TAR}}^{H\to b\bar{b}} \approx 80\,\mathrm{GeV}$ which contain a significant contribution from the single top background. However, the mismodelling is nearly covered by the statistical uncertainties only. Due to the definition of the W+jets and QCD CR, the region around m_H is cut out and it is notable that for masses below this cut window, the background tends to overestimate the data, while above the cut window, the picture is reversed. Since the effect is small, the inclusion of systematic uncertainties is expected to cover the mismodelling.

The distribution of $\Delta R(W_{\mathrm{had}}, \ell)$ is shown in Figure A.16. In the QCD CR, this variable is used in determining the non-prompt lepton background (see Section 5.7). The modelling of this variable, however, does not reflect this. In Figure 5.24, the efficiency ϵ is relatively small for $p_{\mathrm{T}}^{\ell} < 50\,\mathrm{GeV}$ and $\min \Delta R(\ell, J) < 0.3$. At the same time the fake efficiency f is relatively large for $p_{\mathrm{T}}^{\ell} < 50\,\mathrm{GeV}$ and $\min \Delta R(\ell, J) > 0.2$ due to

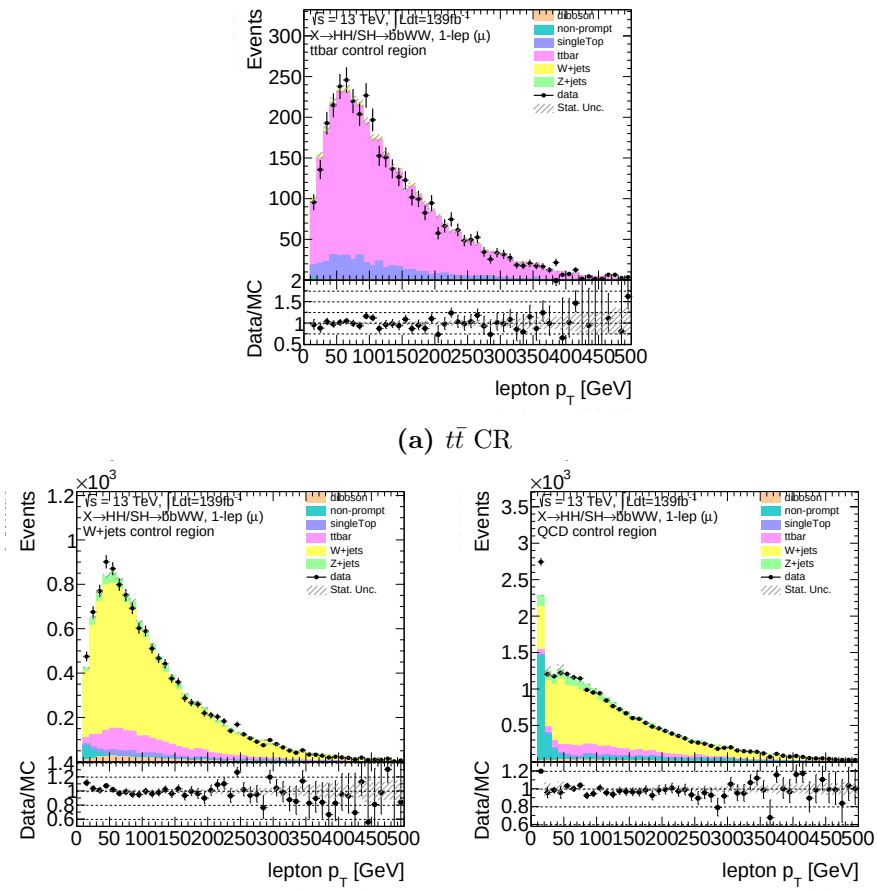

(a) $t\bar{t}$ CR

(b) W+jets CR

(c) QCD CR

Figure A.13.: Distribution of p_{T}^{ℓ} in the three CRs. The normalisation of the backgrounds is corrected.

the bins been merged to reduce the statistical uncertainty. This causes the two bins between $0.2 < \min \Delta R(\ell, J) < 0.3$ to overestimate the non-prompt lepton contribution and this mismodelling. The same argument holds for the underestimate of non-prompt lepton background at $\Delta R(W_{\mathrm{had}}, \ell) > 0.7$. It is noteworthy that the region with $0.2 < \Delta R(W_{\mathrm{had}}, \ell) < 0.3$ is well described in each selection applied to the VR.

Finally, the modelling of the final discriminant and thus, most important variable is investigated in Figure A.17. While the agreement between data and the background estimate is sufficient in the $t\bar{t}$ CR, since most deviations are covered by the statistical uncertainties, there is a clear mismodelling in the W+jets and QCD CRs resulting from the known inaccuracies in W+jets simulation if the lepton is produced collinear to a jet.

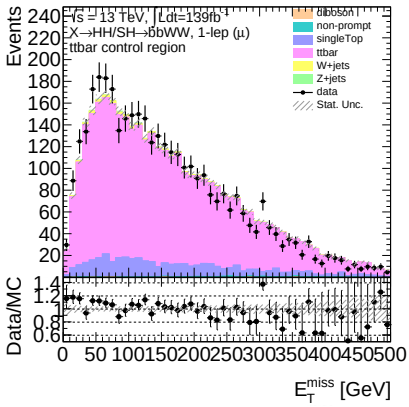

(a) $t\bar{t}$ CR

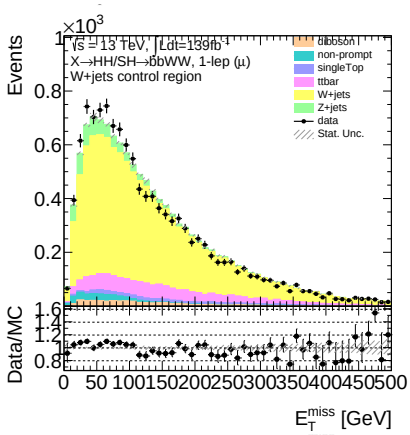

(b) W+jets CR

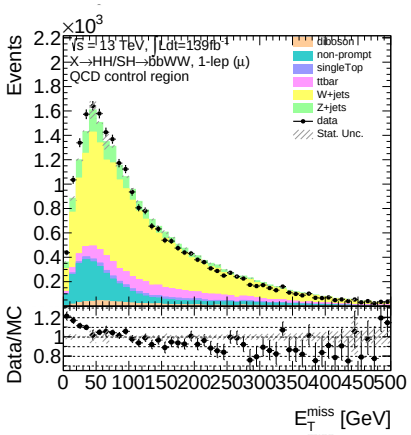

(c) QCD CR

Figure A.14.: Distribution of $E_{\mathrm{T}}^{\mathrm{miss}}$ in the three CRs. The normalisation of the backgrounds is corrected.

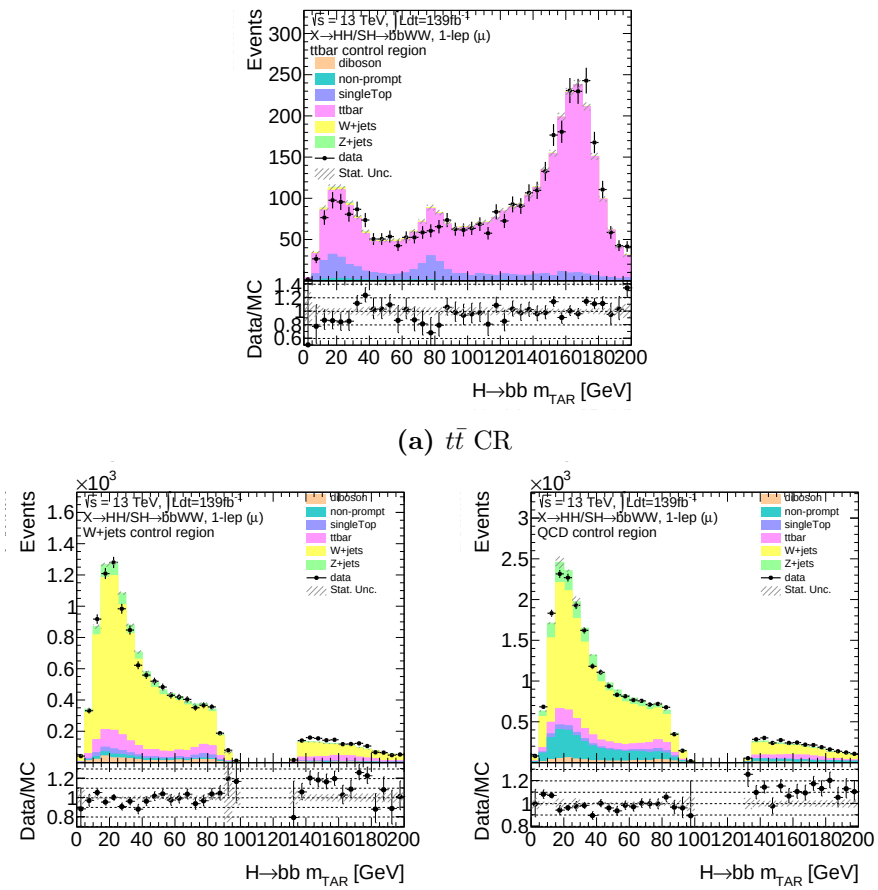

(a) $t\bar{t}$ CR

(b) W+jets CR

(c) QCD CR

Figure A.15.: Distribution of $m_{\mathrm{TAR}}^{H\to b\bar{b}}$ in the three CRs. The normalisation of the backgrounds is corrected.

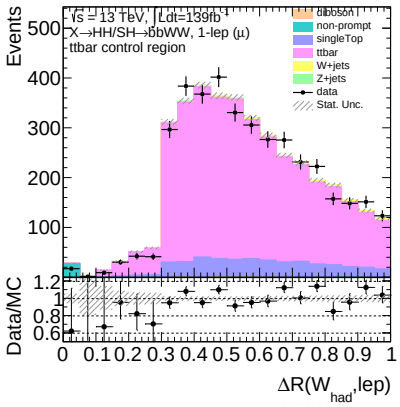

(a) $t\bar{t}$ CR

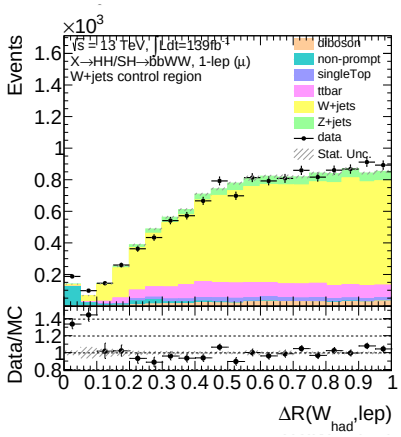

(b) W+jets CR

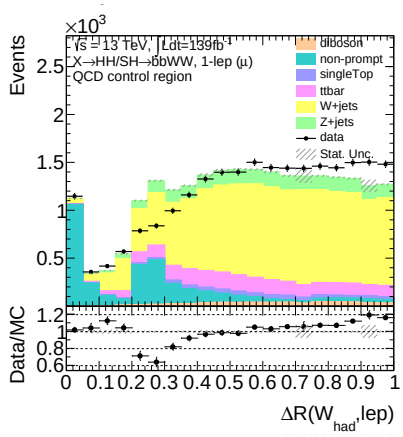

(c) QCD CR

Figure A.16.: Distribution of $\Delta R(W_{\text{had}}, \ell)$ in the three CRs. The normalisation of the backgrounds is corrected.

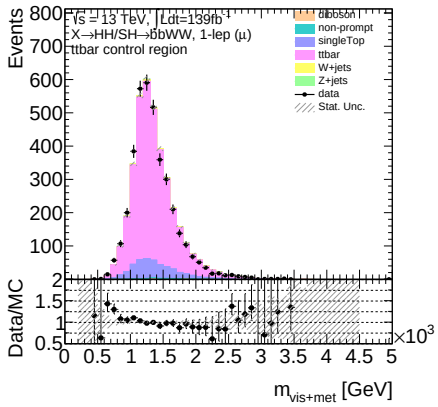

(a) $t\bar{t}$ CR

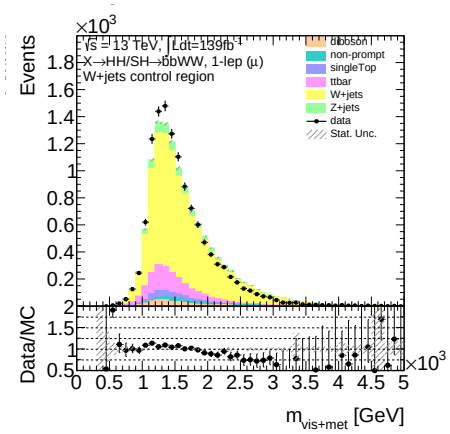

(b) W+jets CR

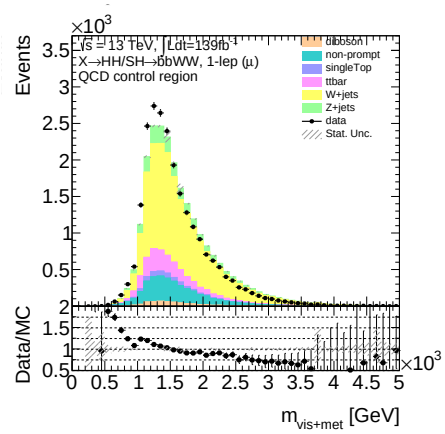

(c) QCD CR

Figure A.17.: Distribution of $m_{\text{vis+met}}$ in the three CRs. The normalisation of the backgrounds is corrected.

A.7. Control and Validation Region Plots

For convenience the definitions of the different regions are summarised again in Table A.10.

Preselection	single large-R jet trigger fired, $\geq$ 2 TAR jets, 1 signal muon, $\min \Delta R(\ell, J) < 1.0$ and $p_{\mathrm{T}}^{H\to b\bar{b}} > 500$ GeV
$t\bar{t}$ CR	preselection, 2 b-tagged TAR jets in the event, $m_{\mathrm{TAR}}^{W_{\mathrm{had}}} < 20$ GeV
W+jets CR	0 b-tagged TAR jets in the event, $H \to b\bar{b}$ candidate fails 70% m_H window, 60 GeV $< m_T^{W_{\mathrm{lep}}} <$ 120 GeV
QCD CR	preselection, 0 b-tagged TAR jets in the event, $H \to b\bar{b}$ candidate fails 70% m_H window, $m_T^{W_{\mathrm{lep}}} <$ 60 GeV or $m_T^{W_{\mathrm{lep}}} >$ 120 GeV
VRf1	preselection, 1 b-tagged TAR jet in the event, $H \to b\bar{b}$ candidate fails 80% m_H window, $H \to b\bar{b}$ candidate has 1 b-tag
SH selection	**in addition:** $H \to b\bar{b}$ candidate passes 80% C_2 window derived from SH samples
HH selection	**in addition:** $H \to b\bar{b}$ candidate passes 80% C_2 window derived from SH samples, event passes the 80% $\Delta R(W_{\mathrm{had}}, \ell)$ window

Table A.10.: Summary of the different region and selection definitions as discussed in Sections 5.5 and 5.6.

A.7.1. $t\bar{t}$ CR

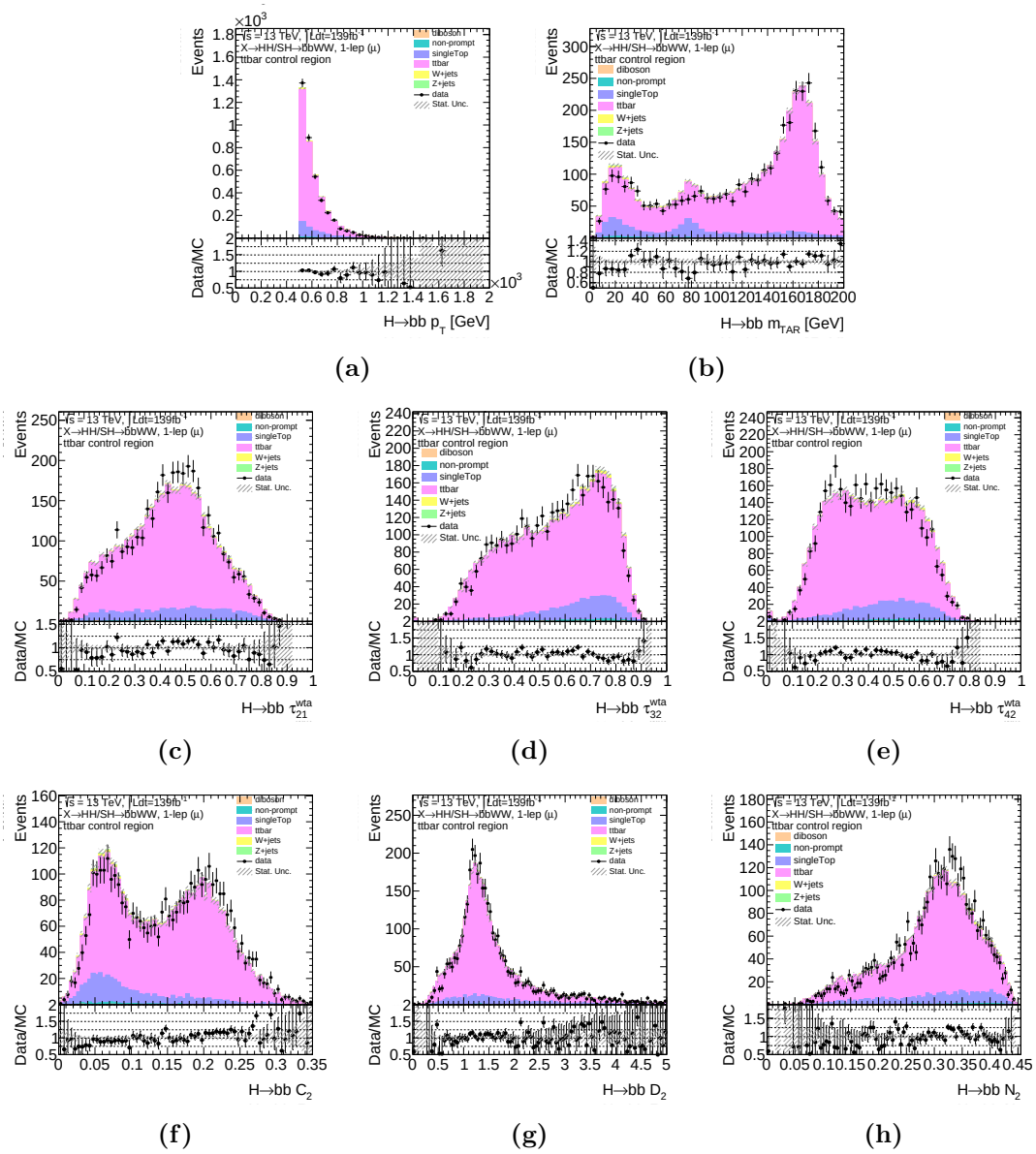

Figure A.18.: Plots related to the $H \to b\bar{b}$ candidate in the $t\bar{t}$ CR.

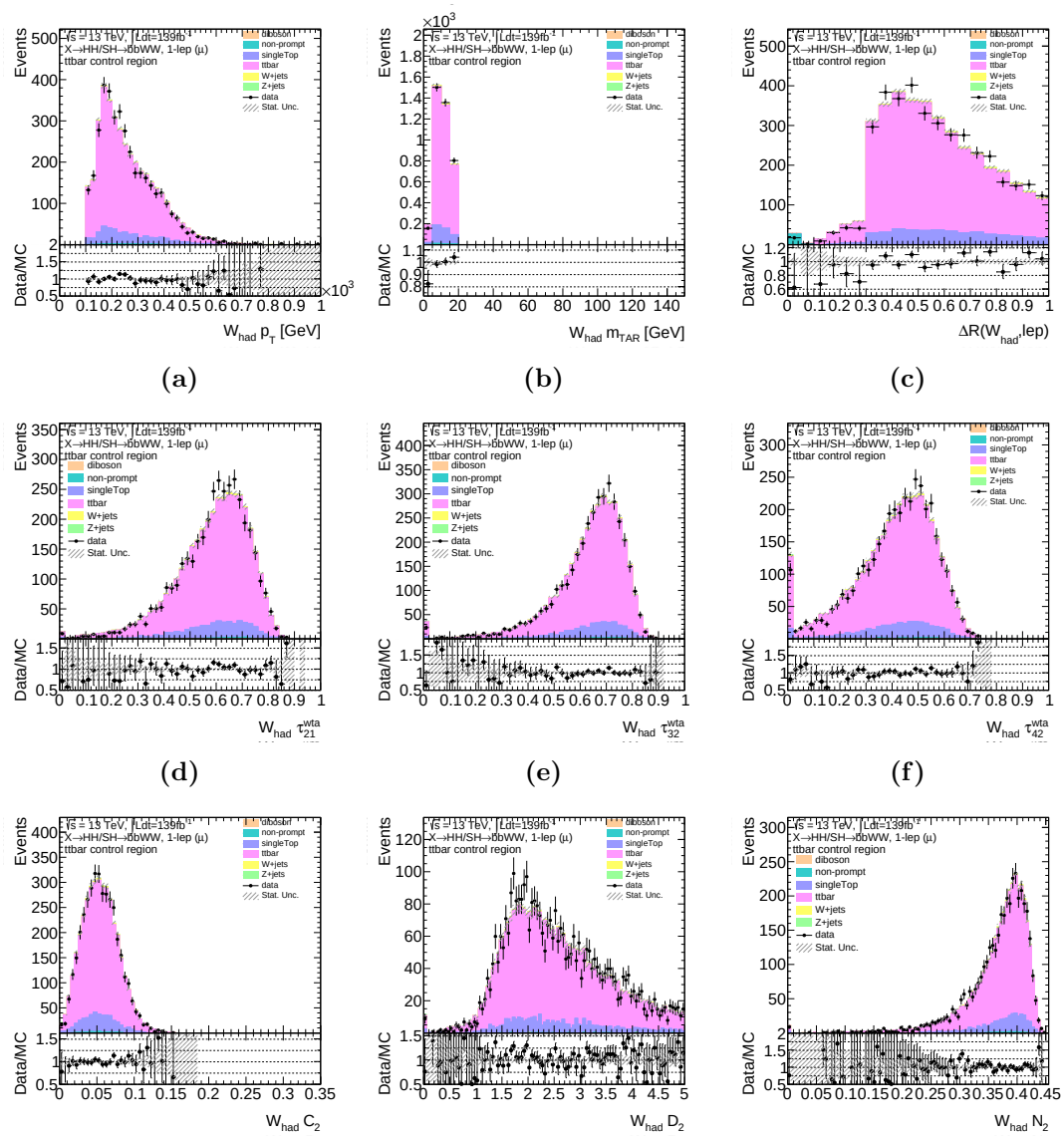

(a) (b) (c)

(d) (e) (f)

(g) (h) (i)

Figure A.19.: Plots related to the W_{had} candidate in the $t\bar{t}$ CR.

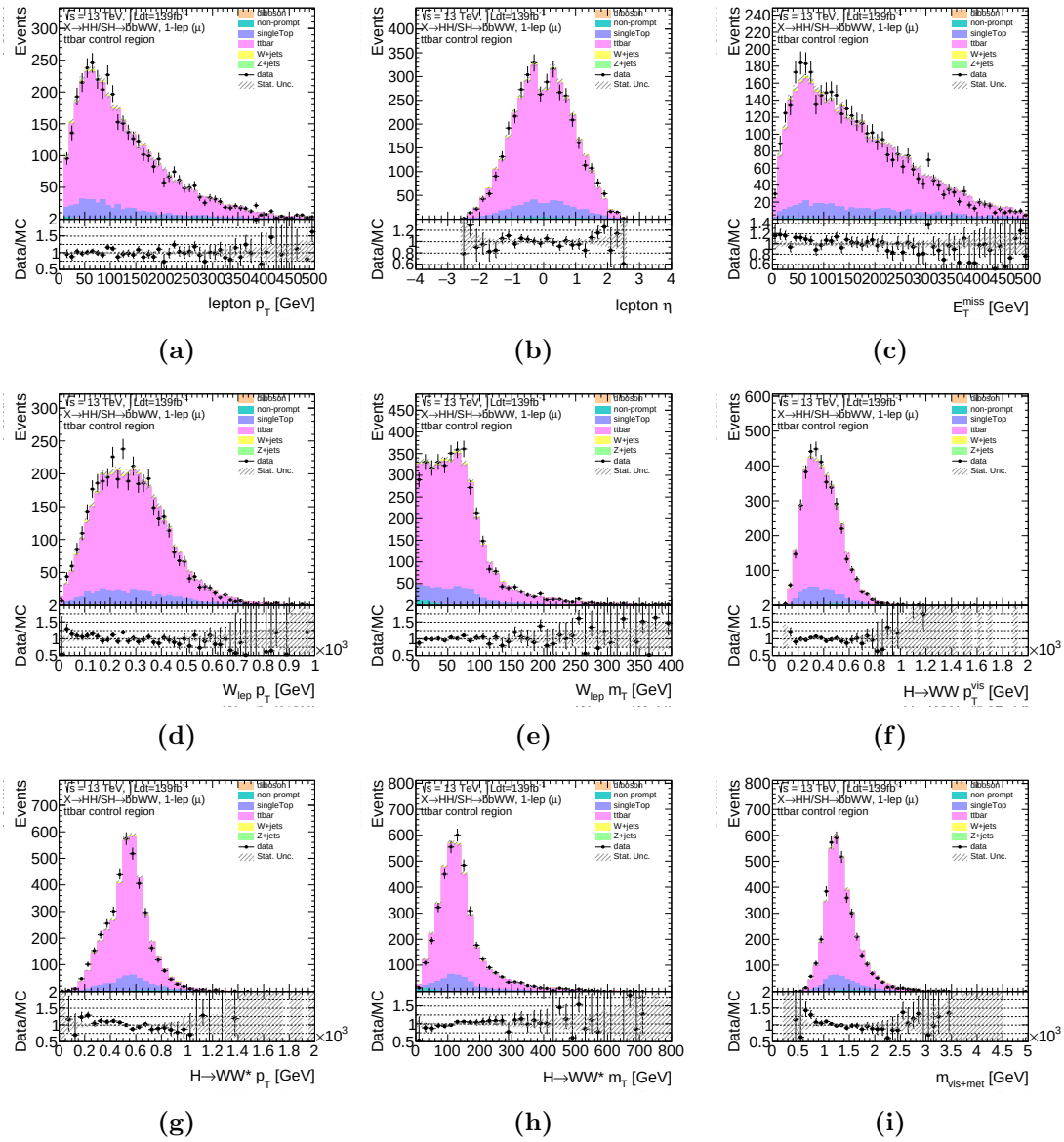

(a) (b) (c)

(d) (e) (f)

(g) (h) (i)

Figure A.20.: Plots related to the lepton, E_T^{miss} and combined objects in the $t\bar{t}$ CR.

A.7.2. W+jets CR

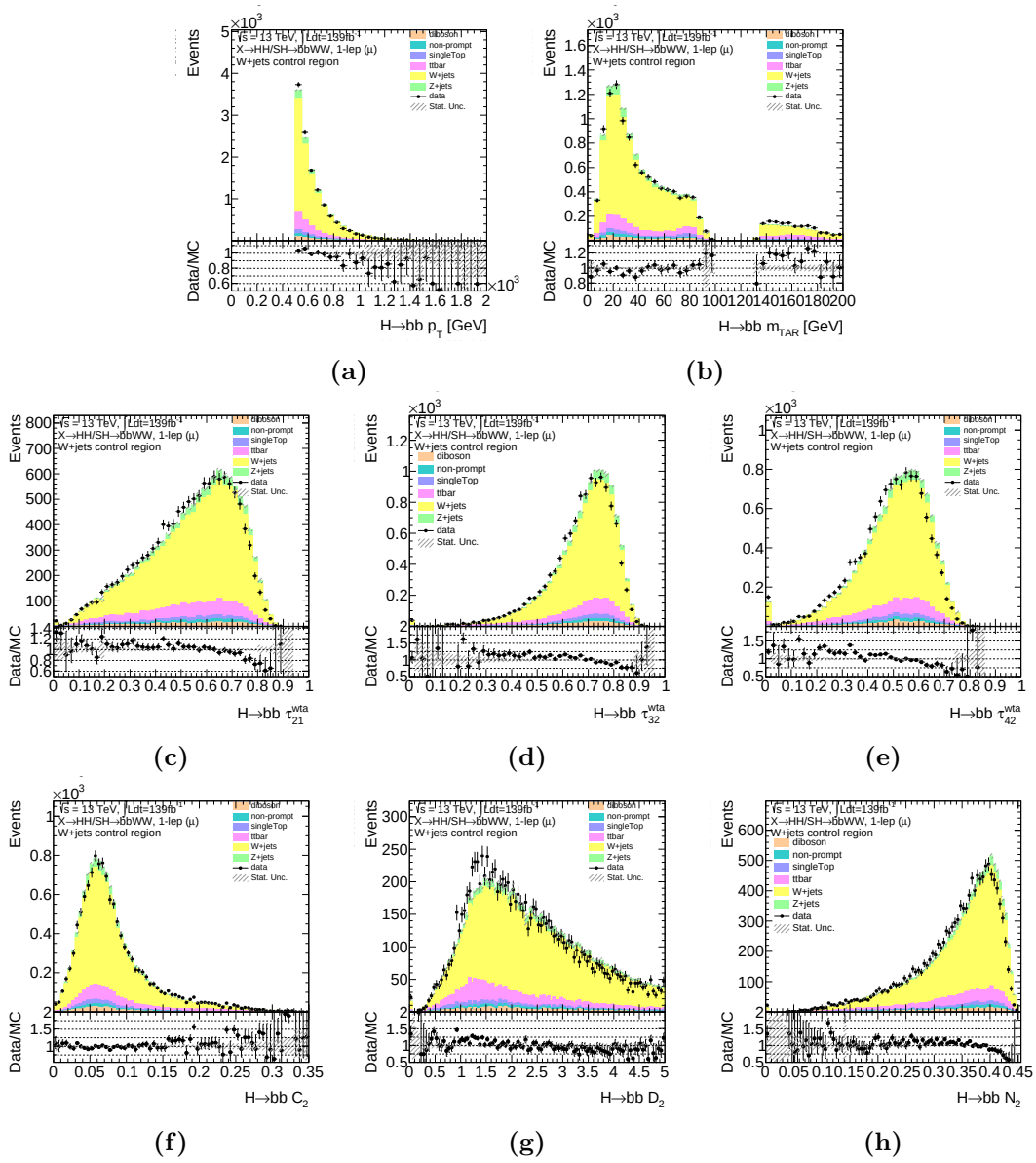

Figure A.21.: Plots related to the $H \to b\bar{b}$ candidate in the W+jets CR.

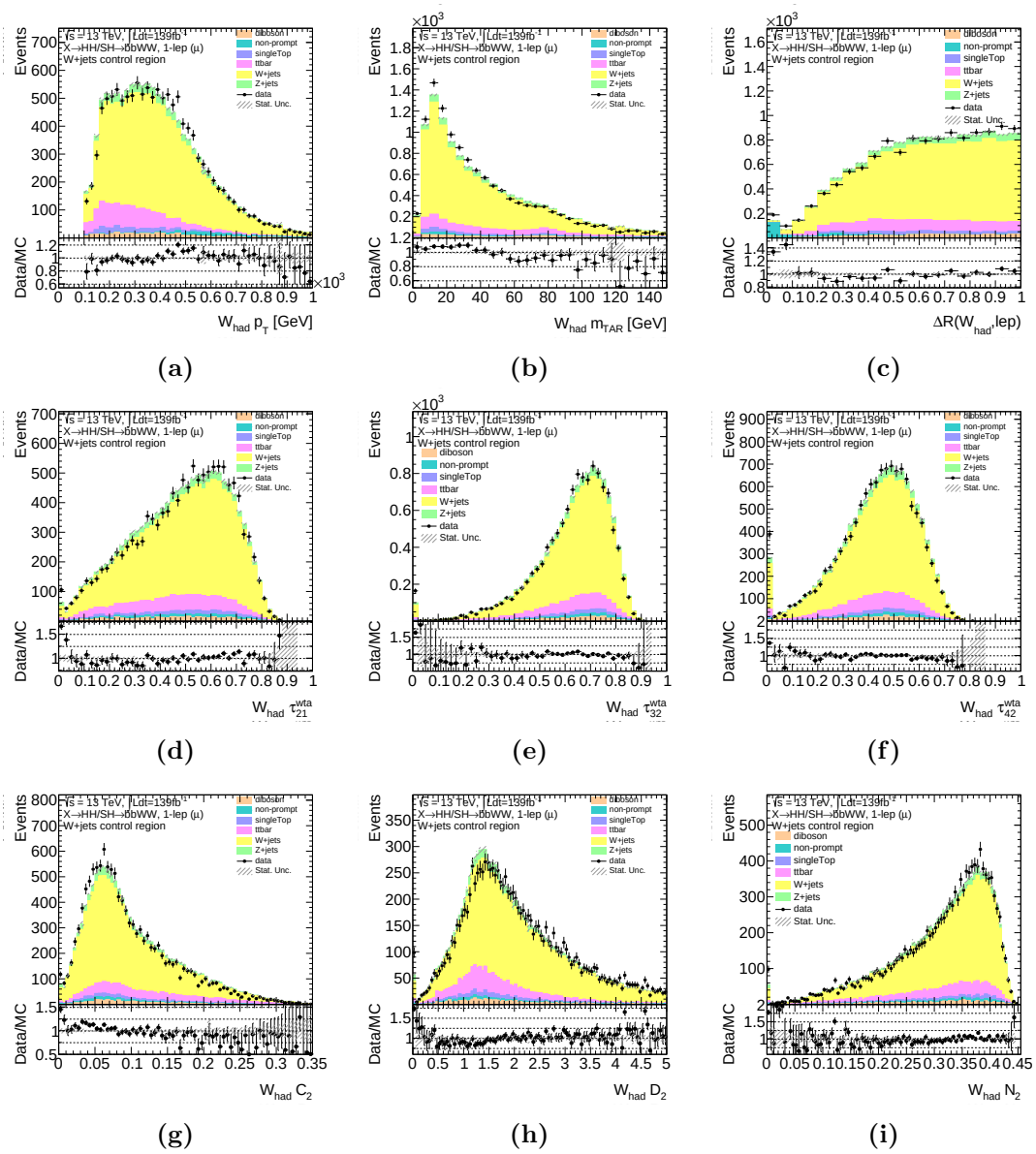

Figure A.22.: Plots related to the W_{had} candidate in the W+jets CR.

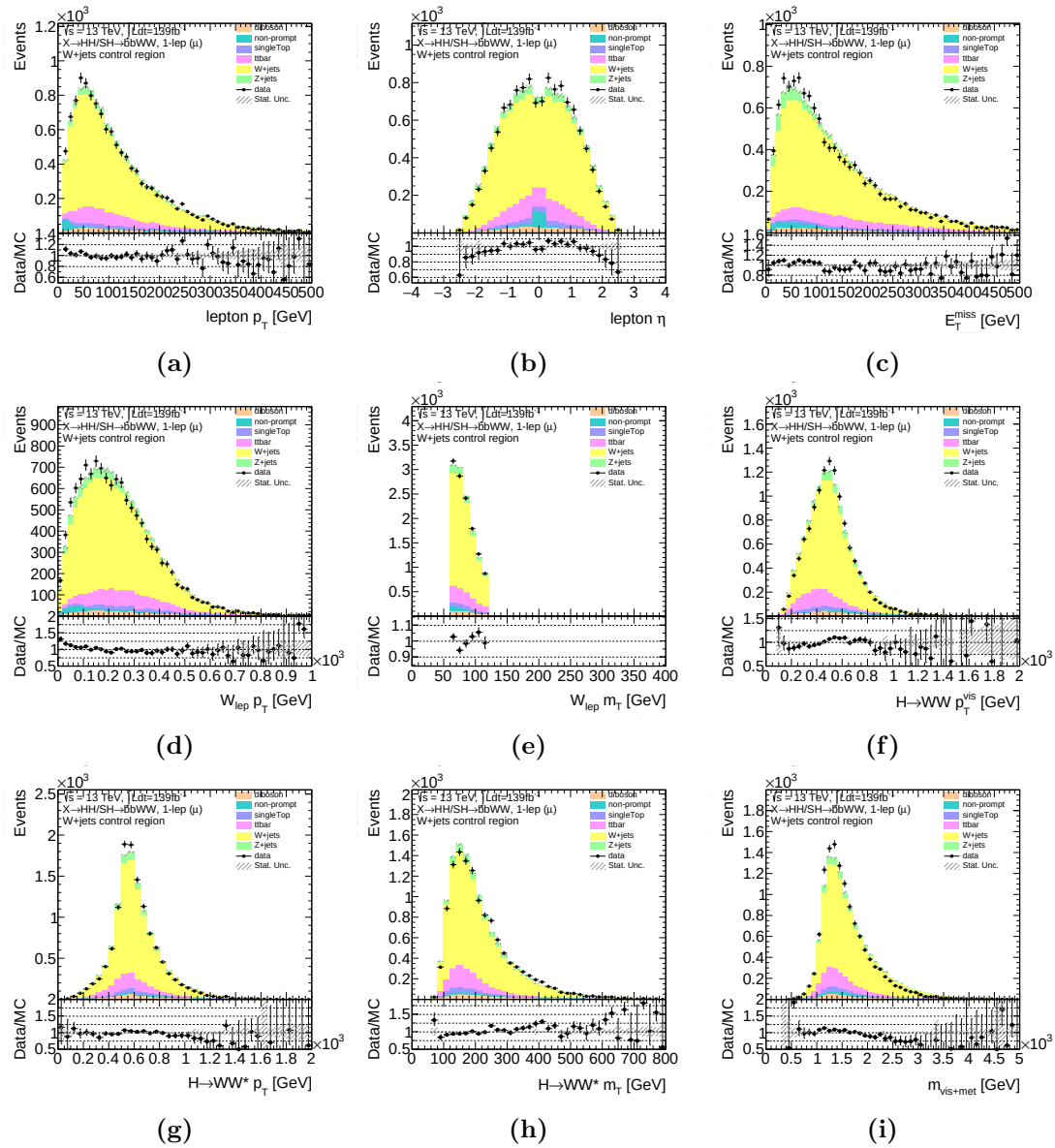

Figure A.23.: Plots related to the lepton, E_T^{miss} and combined objects in the W+jets CR.

A.7.3. QCD CR

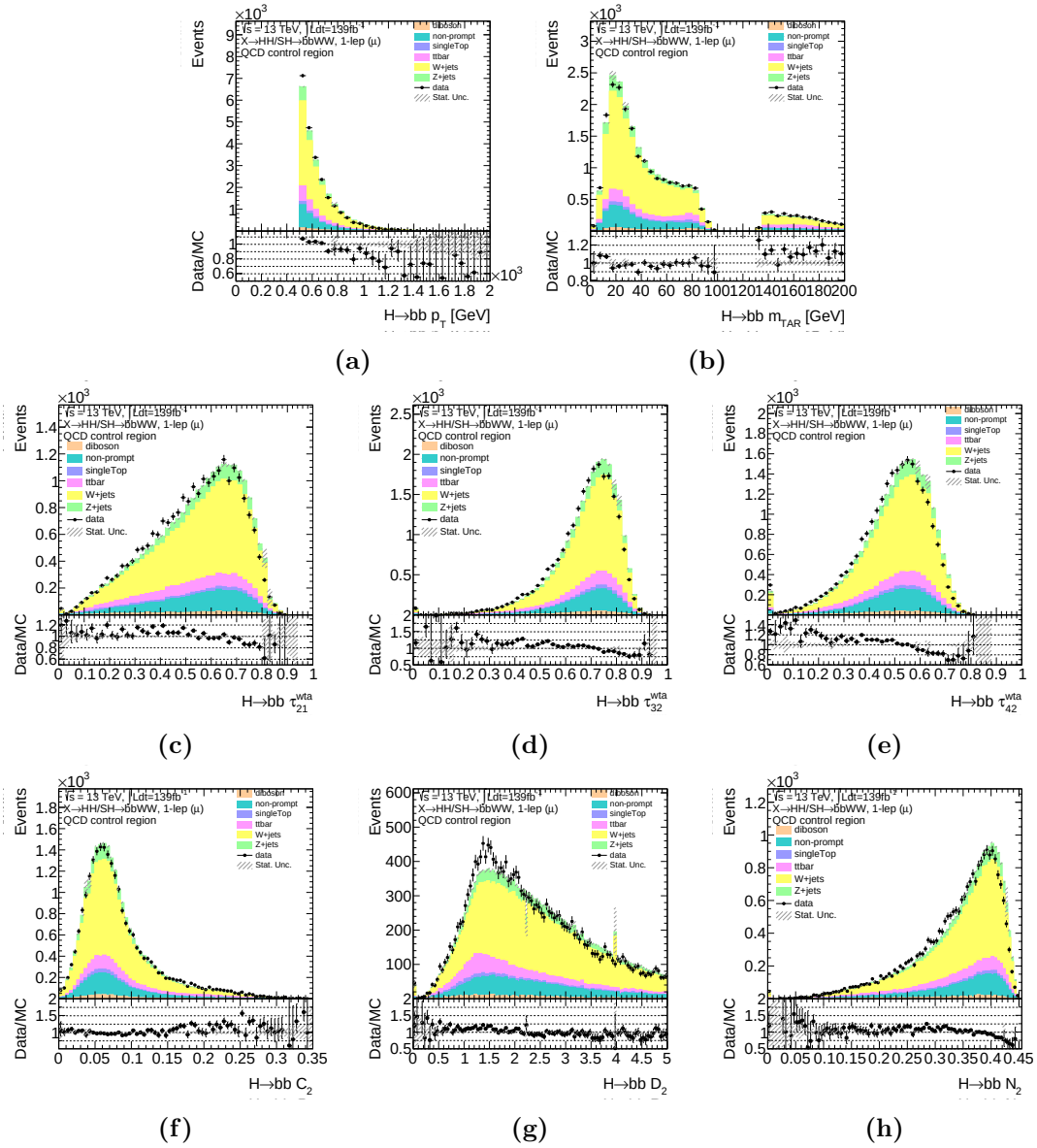

Figure A.24.: Plots related to the $H \to b\bar{b}$ candidate in the QCD CR.

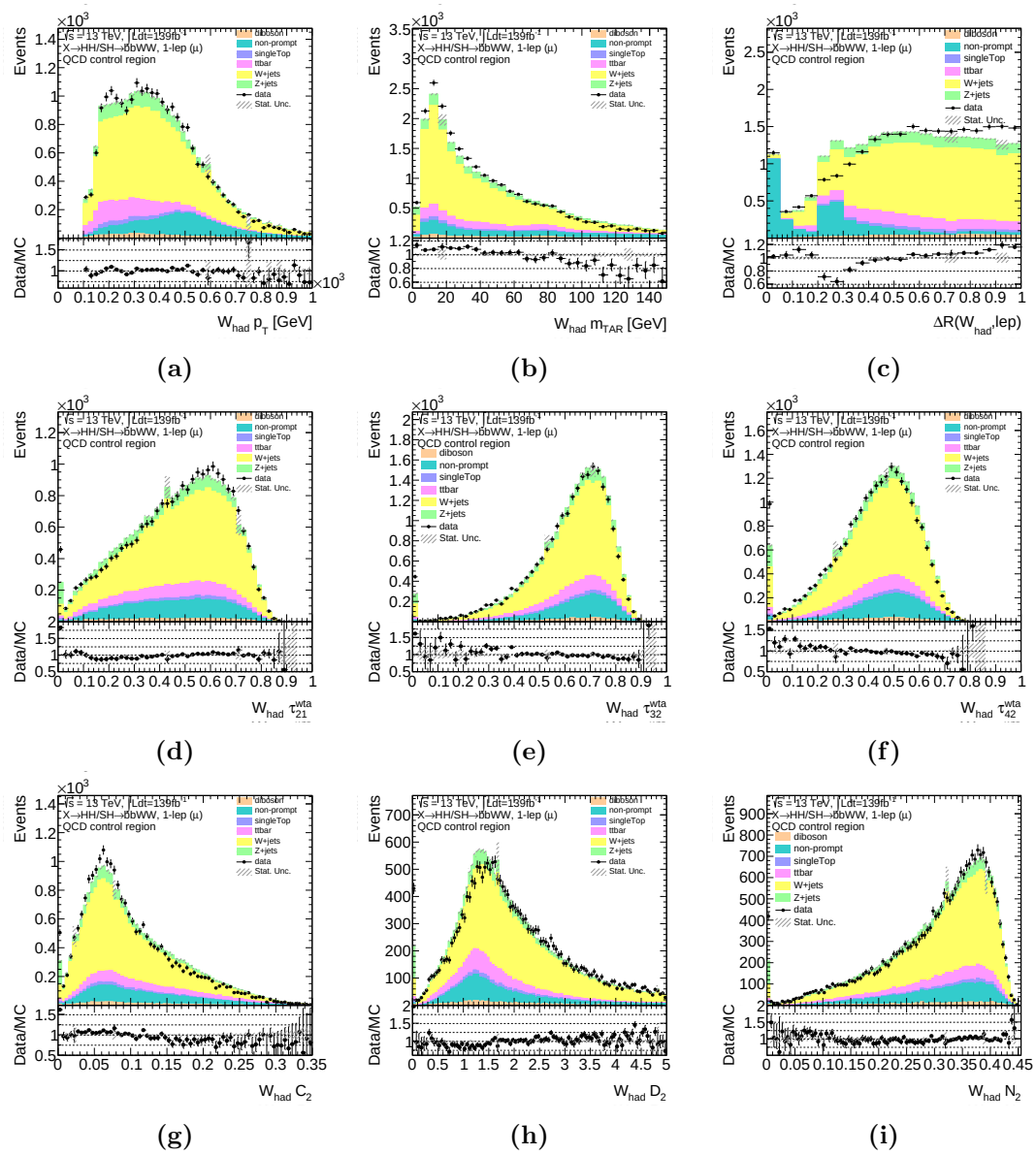

Figure A.25.: Plots related to the W_{had} candidate in the QCD CR.

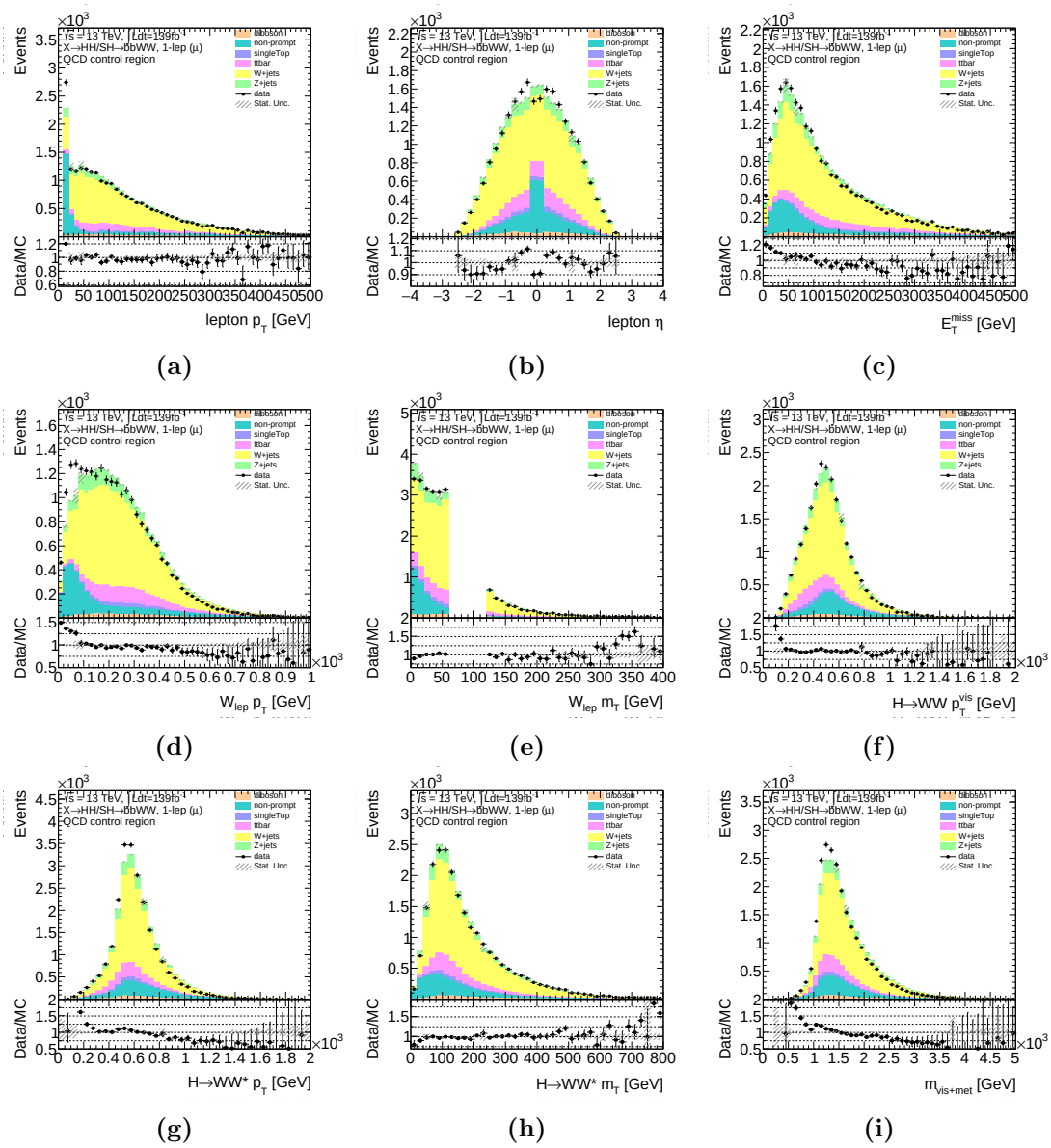

Figure A.26.: Plots related to the lepton, E_T^{miss} and combined objects in the QCD CR.

A.7.4. VRf1 with SH selection

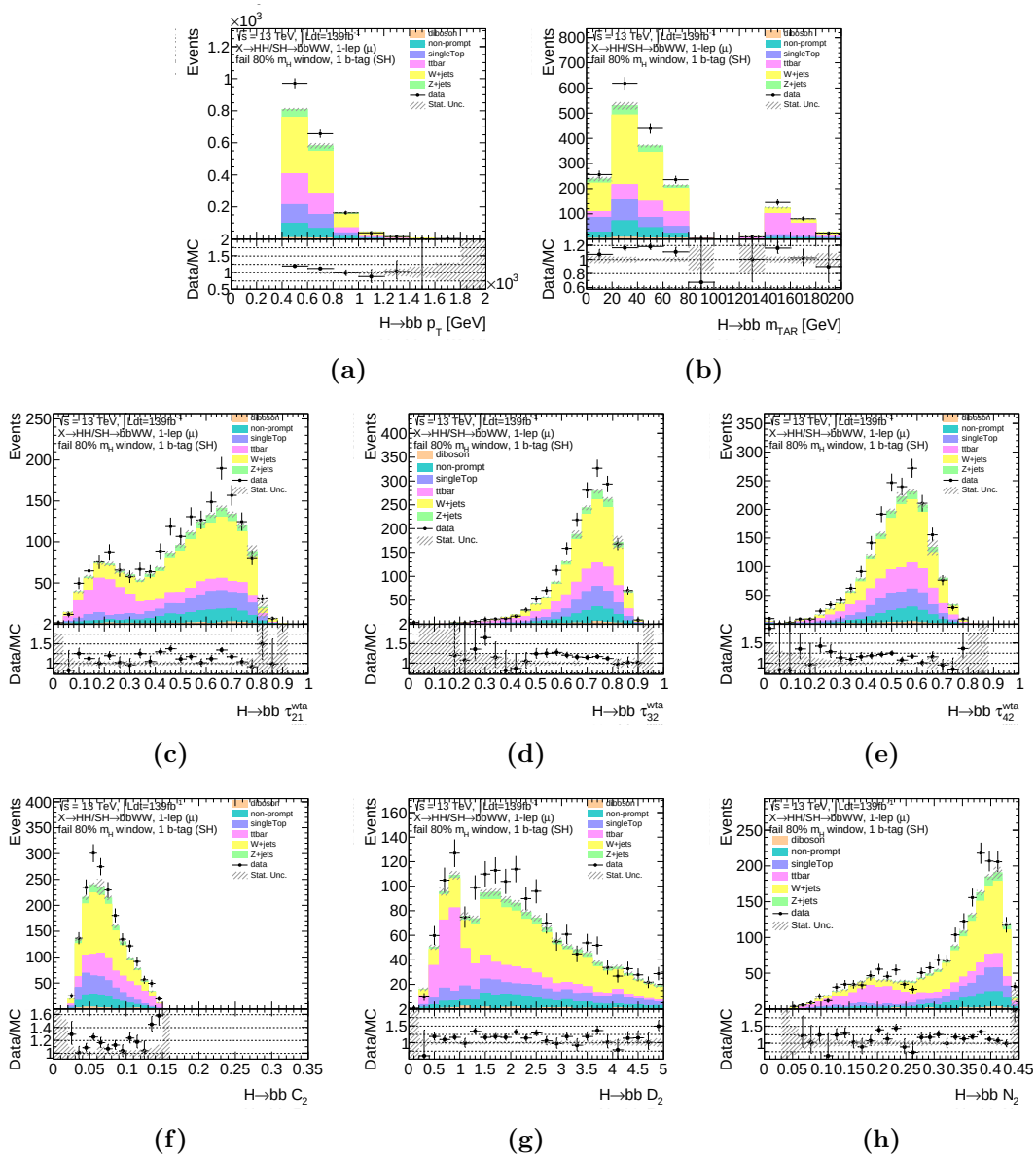

Figure A.27.: Plots related to the $H \to b\bar{b}$ candidate in the VRf1 with SH selection applied.

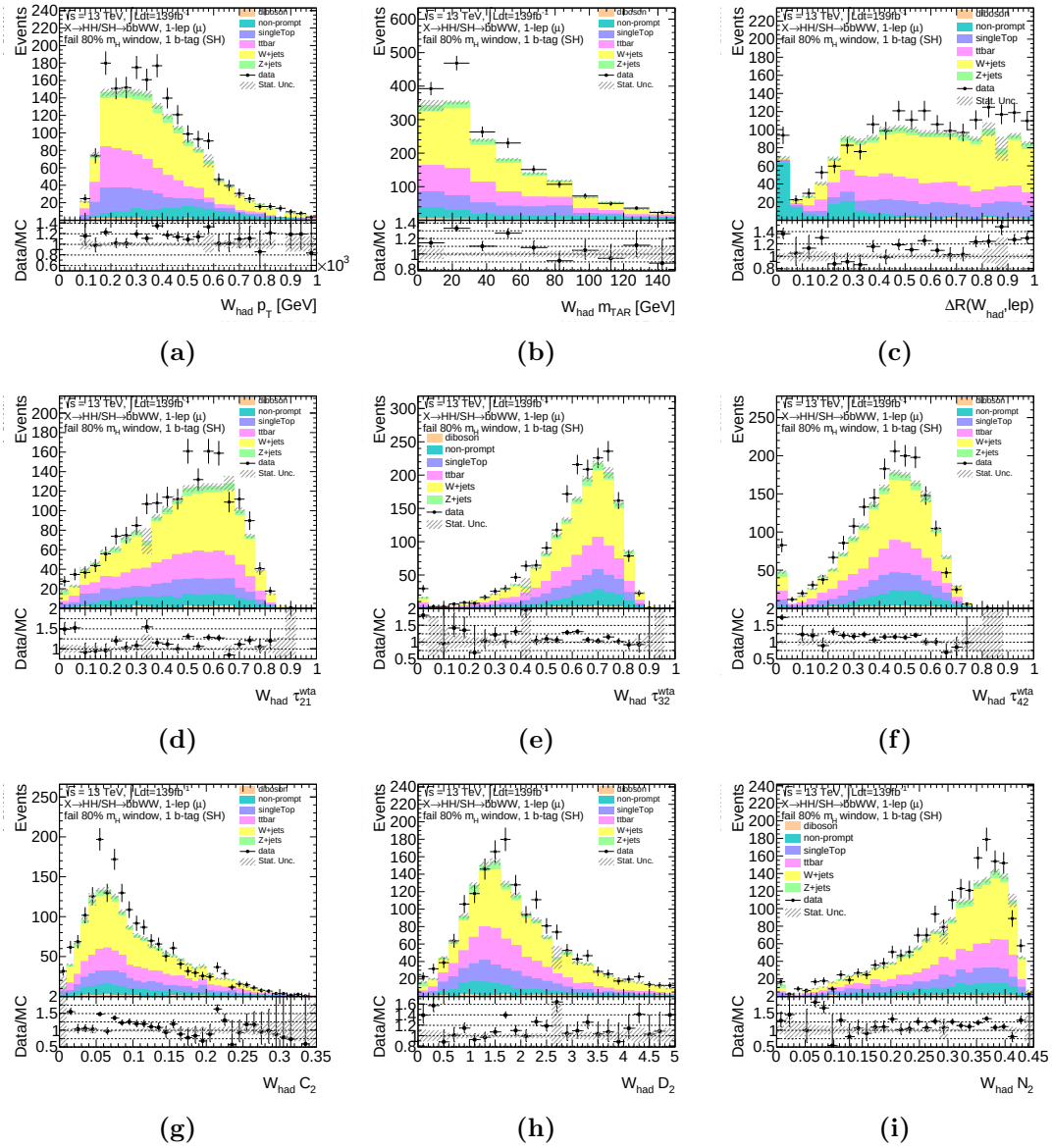

Figure A.28.: Plots related to the W_{had} candidate in the VRf1 with *SH* selection applied.

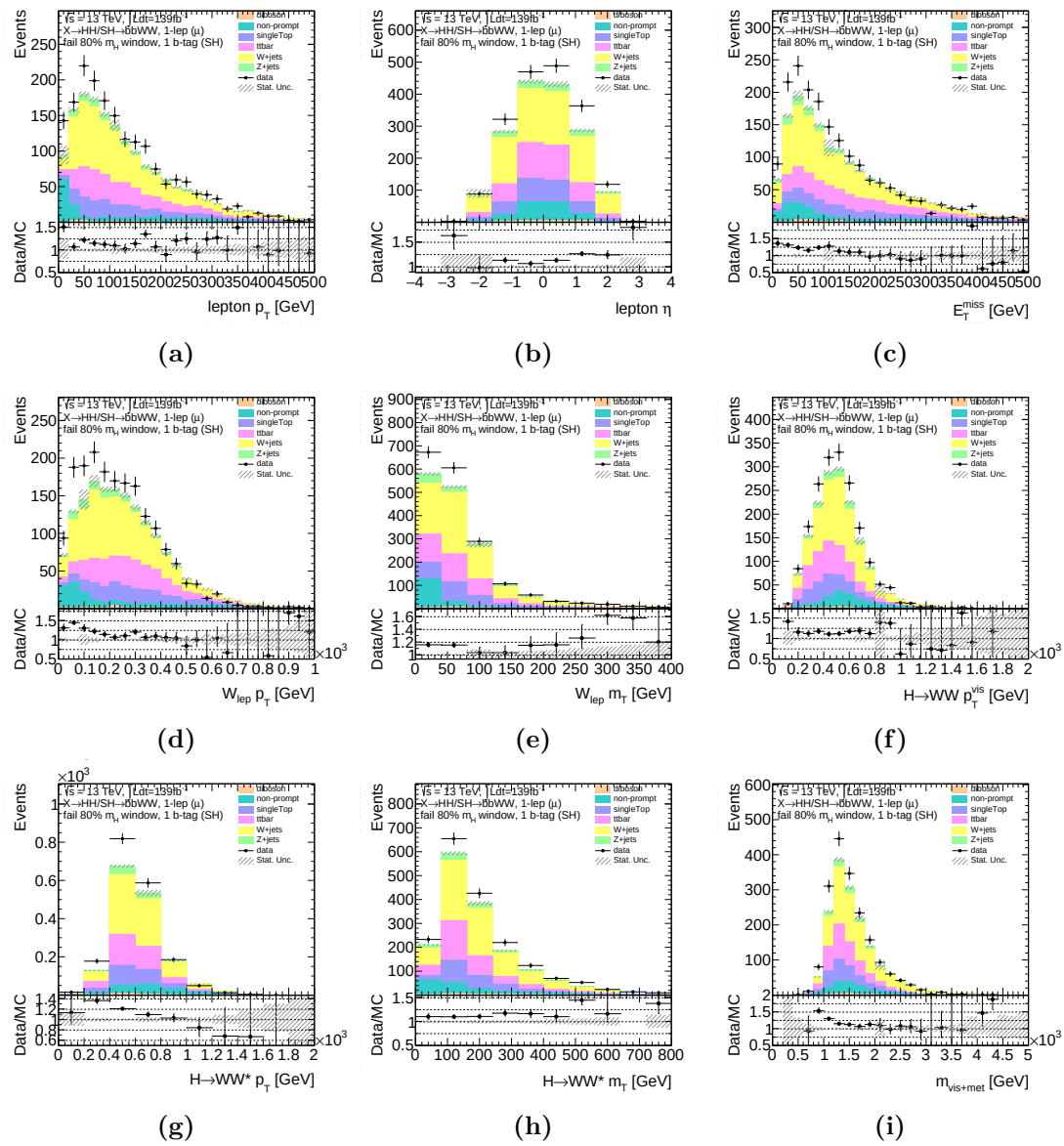

Figure A.29.: Plots related to the lepton, E_T^{miss} and combined objects in the VRf1 with SH selection applied.

A.7.5. VRf1 with HH selection

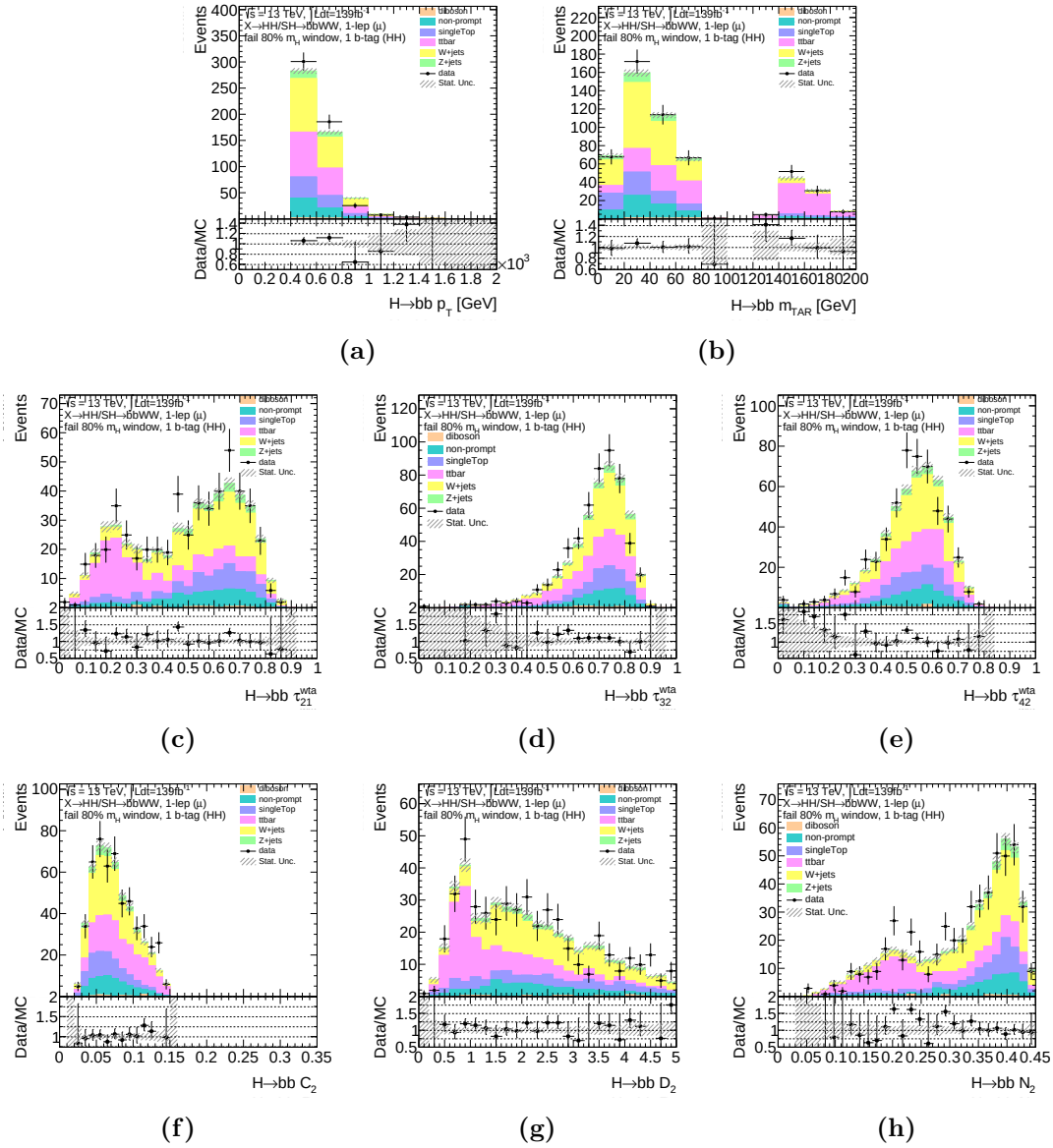

Figure A.30.: Plots related to the $H \to b\bar{b}$ candidate in the VRf1 with HH selection applied.

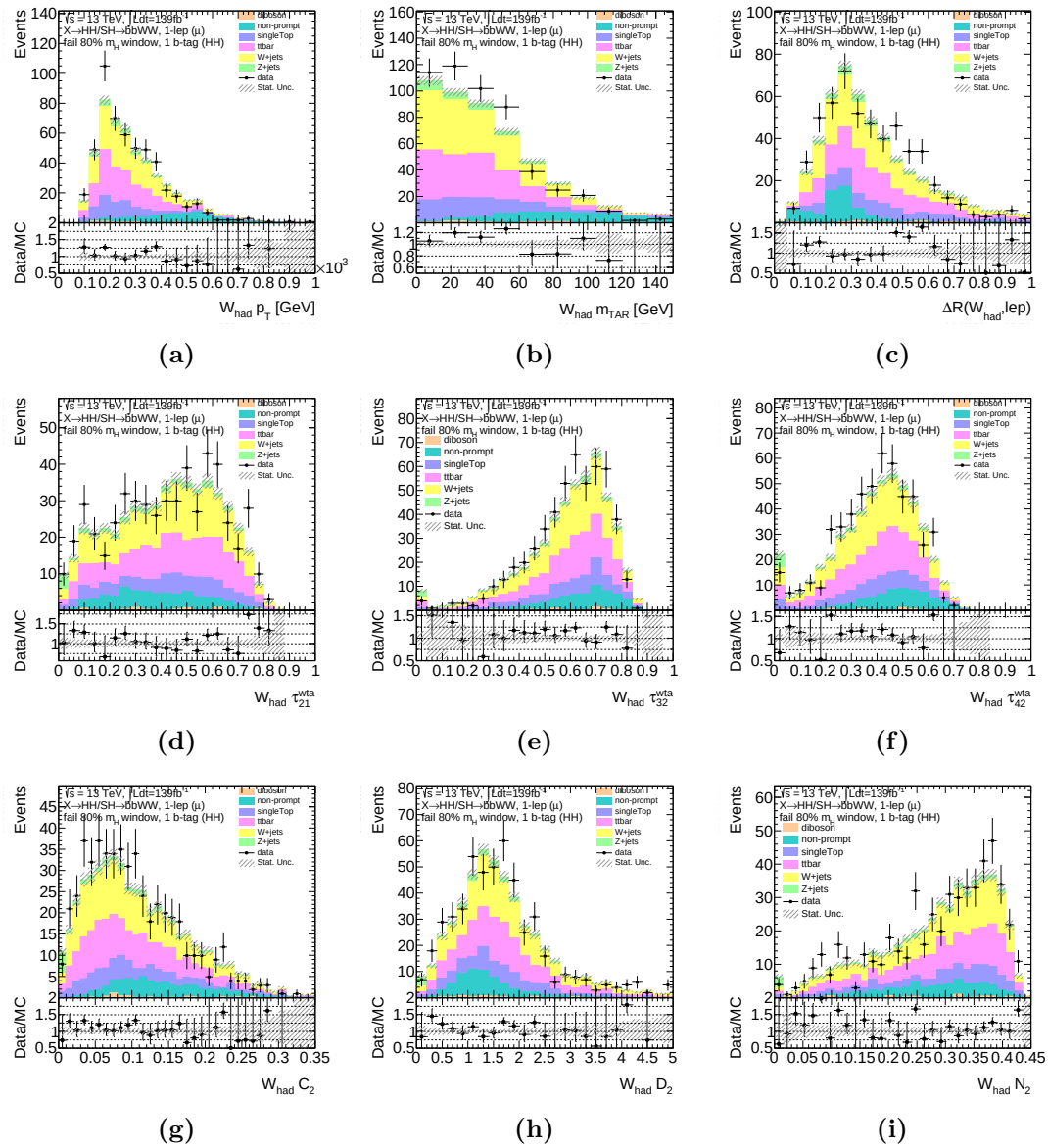

Figure A.31.: Plots related to the W_{had} candidate in the VRf1 with HH selection applied.

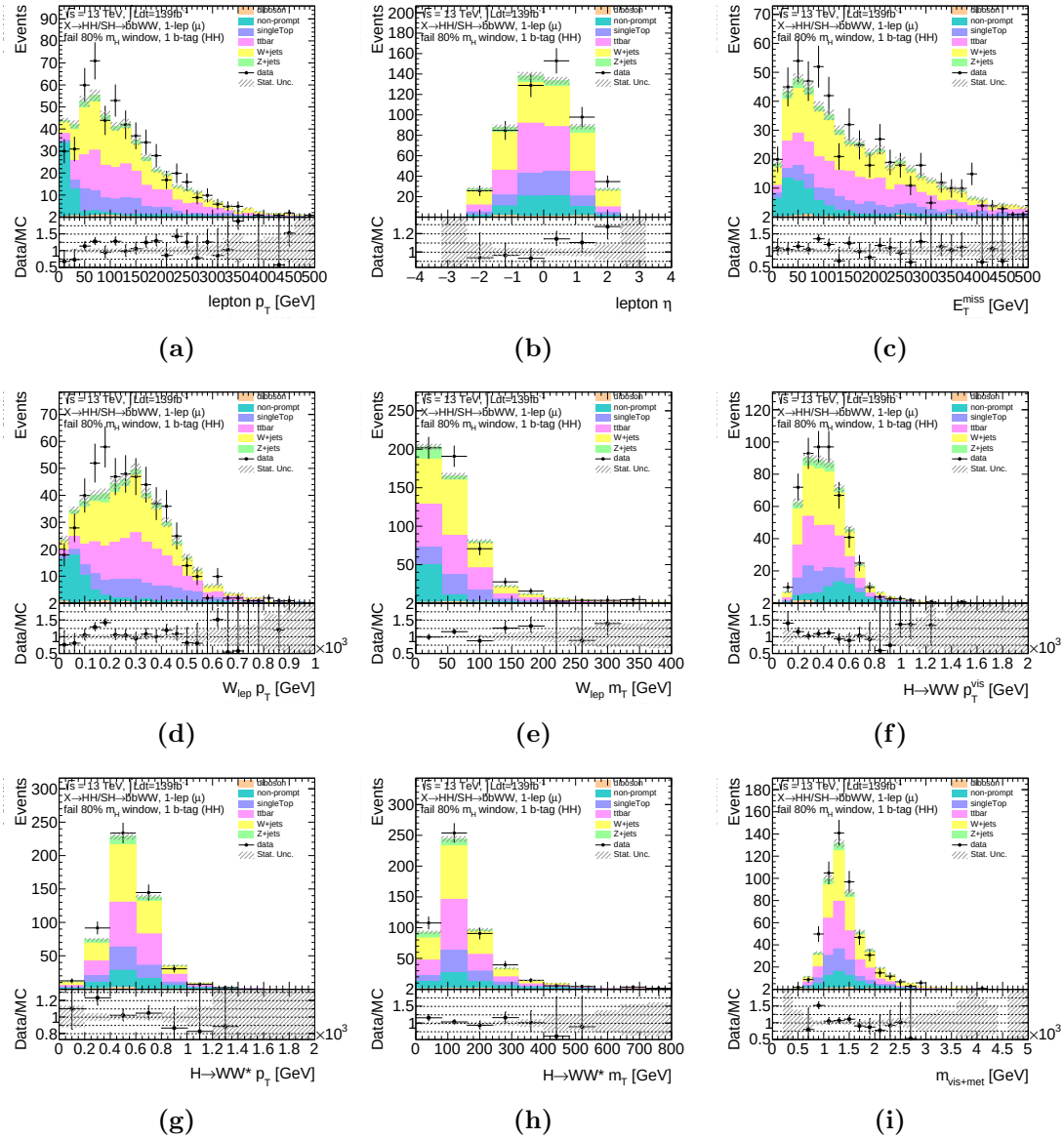

Figure A.32.: Plots related to the lepton, E_T^{miss} and combined objects in the VRf1 with HH selection applied.

A.8. Systematic Uncertainties

A.8.1. SRp2 with HH selection applied

ranking	nuisance parameter	δ^{avg}	δ^{max}
1	JER (effective 2)	3.14%	255.89%
2	JER (effective 3)	2.92%	219.74%
3	JER (effective 1)	2.86%	168.77%
4	JER (effective 4)	2.63%	96.01%
5	μ resolution (Muon Spectrometer)	2.17%	33.55%
6	μ resolution (Inner Detector)	1.69%	29.43%
7	JER (effective 5)	1.34%	103.61%
8	JER (effective 6)	1.31%	76.89%
9	JES (AFII)	1.02%	31.40%
10	JES (flavour response)	0.75%	65.41%
11	JES (mixed 1)	0.61%	101.63%
12	μ reconstruction efficiency (syst)	0.47%	39.06%
13	μ residual bias	0.43%	37.04%
14	JES (modelling 2)	0.33%	41.00%
15	JES (pileup $< \mu >$)	0.30%	29.52%
16	JES heavy flavour	0.30%	31.82%
17	JES (flavour composition)	0.28%	36.00%
18	JER (AFII)	0.27%	12.71%
19	JES (pileup ρ)	0.25%	33.45%
20	JES (stat 1)	0.25%	31.81%
21	JES (intercalibration modelling)	0.25%	20.18%
22	JES (pileup N_{PV})	0.21%	25.47%
23	JES (pileup p_{T}	0.15%	14.89%
24	JES (modelling 1)	0.12%	19.09%
25	b-tagging efficiency (c-jets 1)	0.11%	27.21%
26	JES (mixed 2)	0.09%	27.43%
27	JES (stat 3)	0.07%	17.63%
28	JES (stat 4)	0.07%	12.22%
29	b-tagging efficiency (b-jets 0)	0.06%	0.87%
30	JES (intercalibration stat)	0.06%	13.28%
31	JES (modelling 3)	0.05%	11.96%
32	JES (mixed 3)	0.05%	14.35%
33	μ TTVA efficiency (syst)	0.05%	6.64%
34	b-tagging efficiency (c-jets 0)	0.05%	8.03%
35	b-tagging efficiency (light jets 0)	0.04%	8.55%
36	JES (stat 5)	0.04%	9.66%
37	JES (modelling 4)	0.04%	7.38%

Table A.11.: $m_X = 2.0\,\text{TeV}$ continued on next page.

ranking	nuisance parameter	δ^{avg}	δ^{max}
38	μ scale	0.04%	11.78%
39	JES (detector 1)	0.03%	8.97%
40	b-tagging efficiency (light jets 1)	0.03%	7.39%
41	μ TTVA efficiency (stat)	0.03%	4.57%
42	μ reconstruction efficiency (stat)	0.03%	4.02%
43	b-tagging efficiency (light jets extrapolation)	0.03%	5.71%
44	b-tagging efficiency (c-jets 2)	0.03%	6.51%
45	JES (stat 2)	0.02%	10.51%
46	JES (intercalibration closure $\eta > 0$)	0.02%	7.18%
47	b-tagging efficiency (c-jet extrapolation)	0.02%	4.16%
48	JES (intercalibration closure $\eta < 0$)	0.01%	5.08%
49	b-tagging efficiency (b-jets 1)	0.01%	1.18%
50	JES (stat 6)	0.01%	7.38%
51	b-tagging efficiency (c-jets 3)	0.01%	1.24%
52	JES (punch through AFII)	0.00%	4.90%
53	b-tagging efficiency (light jets 2)	0.00%	0.67%
54	b-tagging efficiency (b-jets 2)	0.00%	0.64%
55	JES (detector 2)	0.00%	2.51%
56	b-tagging efficiency (light jets 3)	0.00%	0.26%
57	b-tagging efficiency (light jets 4)	0.00%	0.07%
58	e/γ scale	0.00%	0.00%
59	e/γ resolution	0.00%	0.00%
60	pileup reweighting	0.00%	0.00%
60	$e\gamma$ scale (AFII)	0.00%	0.00%
60	e ID efficiency	0.00%	0.00%
60	e isolation efficiency	0.00%	0.00%
60	e reconstruction efficiency	0.00%	0.00%
60	JES (intercalibration closure high E)	0.00%	0.00%
60	JES (JVT efficiciency)	0.00%	0.00%
60	JES (testbeams)	0.00%	0.00%
60	JES (fJVT efficiency)	0.00%	0.00%
60	μ isolation efficiency (stat)	0.00%	0.00%
60	μ isolation efficiency (syst)	0.00%	0.00%
60	μ interpolation	0.00%	0.00%
60	track d_0 bias	0.00%	0.00%
60	track residual bias	0.00%	0.00%
60	track z_0 bias	0.00%	0.00%
60	track efficiency	0.00%	0.00%
60	track efficiency (dense env)	0.00%	0.00%
60	track fake rate	0.00%	0.00%
60	track fake rate (dense env.)	0.00%	0.00%

Table A.11.: Summary of all nuisance parameters including their impact on $m_{\text{vis+met}}$ when considering the $m_X = 2.0\,\text{TeV}$ sample in SRp2 (HH) sorted in descending order in δ^{avg}. The up and down variations are symmetrised.

ranking	nuisance parameter	δ^{avg}	δ^{max}
1	JER (effective 3)	10.66%	244.90%
2	JER (effective 2)	10.66%	218.18%
3	μ resolution (Muon Spectrometer)	10.36%	77.97%
4	JER (effective 1)	10.27%	186.10%
5	JER (effective 5)	8.72%	213.33%
6	JER (effective 6)	8.57%	116.62%
7	μ resolution (Inner Detector)	7.99%	57.28%
8	JER (effective 4)	6.42%	227.29%
9	μ residual bias	5.95%	90.89%
10	JES (mixed 1)	4.66%	111.98%
11	JES (AFII)	2.58%	78.29%
12	JES (flavour response)	2.33%	114.90%
13	JES (flavour composition)	2.18%	87.58%
14	JES (pileup ρ)	2.06%	79.40%
15	JES (modelling 2)	1.98%	88.43%
16	JES (stat 1)	1.73%	63.71%
17	JES heavy flavour	1.71%	63.02%
18	μ reconstruction efficiency (syst)	1.22%	42.85%
19	JES (intercalibration modelling)	0.91%	52.28%
20	JES (modelling 1)	0.59%	46.25%
21	JES (pileup N_{PV})	0.51%	51.17%
22	JES (mixed 2)	0.39%	63.71%
23	JES (pileup $< \mu >$)	0.37%	47.68%
24	JES (stat 3)	0.35%	63.71%
25	JER (AFII)	0.33%	32.47%
26	JES (pileup p_{T}	0.26%	53.98%
27	JES (intercalibration stat)	0.22%	49.78%
28	b-tagging efficiency (c-jets 1)	0.18%	9.50%
29	μ scale	0.18%	36.11%
30	JES (modelling 3)	0.10%	31.21%
31	b-tagging efficiency (light jets extrapolation)	0.08%	6.12%
32	JES (stat 2)	0.06%	11.28%
33	b-tagging efficiency (light jets 0)	0.06%	3.52%
34	JES (intercalibration closure high E)	0.05%	27.00%
35	μ TTVA efficiency (syst)	0.05%	2.37%
36	b-tagging efficiency (light jets 1)	0.05%	3.86%
37	b-tagging efficiency (b-jets 1)	0.05%	0.54%
38	b-tagging efficiency (c-jets 2)	0.04%	2.49%
39	b-tagging efficiency (b-jets 0)	0.04%	0.47%
40	JES (testbeams)	0.04%	21.00%

Table A.12.: $m_X = 4.0\,\text{TeV}$ continued on next page.

ranking	nuisance parameter	δ^{avg}	δ^{max}
41	μ reconstruction efficiency (stat)	0.04%	1.48%
42	JES (mixed 3)	0.04%	19.94%
43	JES (stat 4)	0.03%	17.13%
44	μ TTVA efficiency (stat)	0.03%	1.62%
45	b-tagging efficiency (c-jets 0)	0.03%	1.90%
46	b-tagging efficiency (c-jet extrapolation)	0.02%	2.41%
47	JES (detector 1)	0.02%	9.26%
48	JES (modelling 4)	0.02%	9.25%
49	JES (punch through AFII)	0.02%	9.25%
50	b-tagging efficiency (b-jets 2)	0.01%	0.13%
51	b-tagging efficiency (c-jets 3)	0.01%	0.55%
52	b-tagging efficiency (light jets 2)	0.01%	0.32%
53	b-tagging efficiency (light jets 3)	0.00%	0.24%
54	b-tagging efficiency (light jets 4)	0.00%	0.04%
55	JES (stat 5)	0.00%	0.01%
56	JES (stat 6)	0.00%	0.00%
57	JES (intercalibration closure $\eta < 0$)	0.00%	0.01%
58	JES (detector 2)	0.00%	0.00%
59	JES (intercalibration closure $\eta > 0$)	0.00%	0.00%
60	pileup reweighting	0.00%	0.00%
60	e/γ resolution	0.00%	0.00%
60	$e\gamma$ scale (AFII)	0.00%	0.00%
60	e/γ scale	0.00%	0.00%
60	e ID efficiency	0.00%	0.00%
60	e isolation efficiency	0.00%	0.00%
60	e reconstruction efficiency	0.00%	0.00%
60	JES (JVT efficiciency)	0.00%	0.00%
60	JES (fJVT efficiency)	0.00%	0.00%
60	μ isolation efficiency (stat)	0.00%	0.00%
60	μ isolation efficiency (syst)	0.00%	0.00%
60	μ interpolation	0.00%	0.00%
60	track d_0 bias	0.00%	0.00%
60	track residual bias	0.00%	0.00%
60	track z_0 bias	0.00%	0.00%
60	track efficiency	0.00%	0.00%
60	track efficiency (dense env)	0.00%	0.00%
60	track fake rate	0.00%	0.00%
60	track fake rate (dense env.)	0.00%	0.00%

Table A.12.: Summary of all nuisance parameters including their impact on $m_{\text{vis+met}}$ when considering the $m_X = 4.0\,\text{TeV}$ sample in SRp2 (HH) sorted in descending order in δ^{avg}. The up and down variations are symmetrised.

A.8.2. SRp1 with HH selection applied

ranking	nuisance parameter	δ^{avg}	δ^{max}
1	μ resolution (Inner Detector)	4.00%	34.95%
2	JER (effective 1)	2.72%	182.30%
3	JER (effective 2)	2.72%	201.30%
4	μ resolution (Muon Spectrometer)	2.48%	29.21%
5	JER (effective 3)	2.44%	156.41%
6	JER (effective 5)	2.31%	108.34%
7	JER (effective 6)	2.15%	117.98%
8	JER (effective 4)	1.95%	94.32%
9	JES (flavour response)	1.26%	77.61%
10	JES (AFII)	1.02%	36.23%
11	JES (flavour composition)	0.92%	37.61%
12	JES (mixed 1)	0.89%	103.53%
13	μ residual bias	0.84%	27.56%
14	μ reconstruction efficiency (syst)	0.40%	31.91%
15	JES heavy flavour	0.33%	29.58%
16	JES (stat 1)	0.32%	32.47%
17	JES (modelling 2)	0.30%	42.00%
18	JES (pileup ρ)	0.28%	31.16%
19	JER (AFII)	0.25%	29.61%
20	JES (pileup p_{T}	0.19%	36.36%
21	b-tagging efficiency (c-jets 1)	0.18%	19.78%
22	JES (pileup N_{PV})	0.14%	34.54%
23	JES (mixed 2)	0.13%	18.82%
24	JES (intercalibration modelling)	0.12%	22.18%
25	JES (pileup $< \mu >$)	0.10%	10.38%
26	JES (modelling 3)	0.10%	14.83%
27	JES (stat 3)	0.10%	15.18%
28	μ scale	0.09%	14.45%
29	JES (mixed 3)	0.09%	12.55%
30	b-tagging efficiency (light jets extrapolation)	0.09%	12.19%
31	JES (modelling 1)	0.09%	23.49%
32	JES (stat 4)	0.08%	10.80%
33	JES (stat 5)	0.08%	8.10%
34	JES (stat 2)	0.08%	6.95%
35	JES (punch through AFII)	0.08%	5.00%
36	b-tagging efficiency (light jets 0)	0.05%	7.05%
37	b-tagging efficiency (c-jets 0)	0.04%	6.70%
38	JES (intercalibration stat)	0.04%	15.04%
39	b-tagging efficiency (c-jets 2)	0.04%	4.65%

Table A.13.: $m_X = 2.0\,\text{TeV}$ continued on next page.

ranking	nuisance parameter	δ^{avg}	δ^{max}
40	b-tagging efficiency (light jets 1)	0.04%	6.03%
41	μ TTVA efficiency (syst)	0.03%	4.89%
42	μ TTVA efficiency (stat)	0.02%	3.48%
43	b-tagging efficiency (b-jets 0)	0.02%	2.04%
44	b-tagging efficiency (c-jet extrapolation)	0.02%	4.91%
45	μ reconstruction efficiency (stat)	0.02%	3.07%
46	JES (stat 6)	0.02%	10.18%
47	b-tagging efficiency (c-jets 3)	0.01%	0.96%
48	JES (intercalibration closure $\eta > 0$)	0.01%	5.03%
49	JES (intercalibration closure $\eta < 0$)	0.01%	6.93%
50	b-tagging efficiency (b-jets 1)	0.01%	1.90%
51	b-tagging efficiency (light jets 2)	0.01%	0.51%
52	b-tagging efficiency (b-jets 2)	0.01%	0.75%
53	e/γ resolution	0.00%	4.86%
54	e/γ scale	0.00%	4.86%
55	JES (detector 2)	0.00%	2.25%
56	JES (detector 1)	0.00%	2.66%
57	b-tagging efficiency (light jets 3)	0.00%	0.20%
58	b-tagging efficiency (light jets 4)	0.00%	0.05%
59	JES (modelling 4)	0.00%	0.24%
60	pileup reweighting	0.00%	0.00%
60	$e\gamma$ scale (AFII)	0.00%	0.00%
60	e ID efficiency	0.00%	0.00%
60	e isolation efficiency	0.00%	0.00%
60	e reconstruction efficiency	0.00%	0.00%
60	JES (intercalibration closure high E)	0.00%	0.00%
60	JES (JVT efficiciency)	0.00%	0.00%
60	JES (testbeams)	0.00%	0.00%
60	JES (fJVT efficiency)	0.00%	0.00%
60	μ isolation efficiency (stat)	0.00%	0.00%
60	μ isolation efficiency (syst)	0.00%	0.00%
60	μ interpolation	0.00%	0.00%
60	track d_0 bias	0.00%	0.00%
60	track residual bias	0.00%	0.00%
60	track z_0 bias	0.00%	0.00%
60	track efficiency	0.00%	0.00%
60	track efficiency (dense env)	0.00%	0.00%
60	track fake rate	0.00%	0.00%
60	track fake rate (dense env.)	0.00%	0.00%

Table A.13.: Summary of all nuisance parameters including their impact on $m_{\text{vis+met}}$ when considering the $m_X = 2.0\,\text{TeV}$ sample in SRp1 (HH) sorted in descending order in δ^{avg}. The up and down variations are symmetrised.

ranking	nuisance parameter	δ^{avg}	δ^{max}
1	μ resolution (Muon Spectrometer)	8.38%	72.32%
2	μ resolution (Inner Detector)	7.58%	128.43%
3	μ residual bias	6.62%	82.39%
4	JER (effective 2)	5.72%	245.53%
5	JER (effective 3)	5.48%	335.00%
6	JER (effective 5)	5.17%	190.32%
7	JER (effective 1)	5.09%	185.86%
8	JER (effective 6)	4.32%	191.85%
9	JER (effective 4)	3.30%	156.08%
10	JES (AFII)	2.90%	60.23%
11	μ reconstruction efficiency (syst)	2.28%	79.75%
12	JES (flavour response)	2.12%	147.79%
13	JES (mixed 1)	1.73%	160.44%
14	JES (flavour composition)	1.52%	76.82%
15	JES (pileup ρ)	1.08%	120.16%
16	JES (intercalibration modelling)	0.89%	68.52%
17	JES (modelling 2)	0.86%	56.04%
18	JES (modelling 1)	0.73%	62.37%
19	JES (stat 1)	0.71%	50.36%
20	JES (testbeams)	0.67%	43.37%
21	JES (mixed 2)	0.66%	42.09%
22	μ scale	0.36%	35.76%
23	JES heavy flavour	0.31%	70.51%
24	JES (pileup $< \mu >$)	0.27%	55.03%
25	JES (pileup N_{PV})	0.25%	55.80%
26	JES (mixed 3)	0.24%	66.33%
27	JES (pileup p_{T}	0.23%	51.13%
28	JER (AFII)	0.19%	39.58%
29	b-tagging efficiency (c-jets 1)	0.16%	15.13%
30	JES (intercalibration stat)	0.14%	48.01%
31	JES (stat 3)	0.12%	45.49%
32	JES (modelling 3)	0.10%	45.49%
33	b-tagging efficiency (light jets extrapolation)	0.10%	16.49%
34	b-tagging efficiency (light jets 1)	0.07%	5.72%
35	JES (stat 4)	0.07%	33.92%
36	b-tagging efficiency (light jets 0)	0.06%	4.71%
37	μ TTVA efficiency (syst)	0.06%	4.08%
38	b-tagging efficiency (c-jets 0)	0.04%	3.23%
39	μ TTVA efficiency (stat)	0.04%	2.56%
40	b-tagging efficiency (c-jets 2)	0.04%	4.26%

Table A.14.: $m_X = 4.0\,\text{TeV}$ continued on next page.

ranking	nuisance parameter	δ^{avg}	δ^{max}
41	μ reconstruction efficiency (stat)	0.03%	2.35%
42	JES (modelling 4)	0.03%	19.41%
43	JES (punch through AFII)	0.03%	20.09%
44	JES (stat 5)	0.02%	11.05%
45	b-tagging efficiency (c-jets 3)	0.01%	0.93%
46	b-tagging efficiency (light jets 2)	0.01%	0.58%
47	b-tagging efficiency (c-jet extrapolation)	0.01%	2.16%
48	b-tagging efficiency (light jets 3)	0.00%	0.40%
49	b-tagging efficiency (b-jets 1)	0.00%	1.70%
50	b-tagging efficiency (b-jets 0)	0.00%	2.05%
51	b-tagging efficiency (b-jets 2)	0.00%	0.44%
52	b-tagging efficiency (light jets 4)	0.00%	0.06%
53	JES (stat 2)	0.00%	0.01%
54	JES (detector 1)	0.00%	0.01%
55	JES (stat 6)	0.00%	0.00%
56	JES (detector 2)	0.00%	0.00%
57	JES (intercalibration closure $\eta > 0$)	0.00%	0.01%
58	e/γ resolution	0.00%	0.01%
59	JES (intercalibration closure $\eta < 0$)	0.00%	0.00%
60	pileup reweighting	0.00%	0.00%
60	$e\gamma$ scale (AFII)	0.00%	0.00%
60	e/γ scale	0.00%	0.00%
60	e ID efficiency	0.00%	0.00%
60	e isolation efficiency	0.00%	0.00%
60	e reconstruction efficiency	0.00%	0.00%
60	JES (intercalibration closure high E)	0.00%	0.00%
60	JES (JVT efficiciency)	0.00%	0.00%
60	JES (fJVT efficiency)	0.00%	0.00%
60	μ isolation efficiency (stat)	0.00%	0.00%
60	μ isolation efficiency (syst)	0.00%	0.00%
60	μ interpolation	0.00%	0.00%
60	track d_0 bias	0.00%	0.00%
60	track residual bias	0.00%	0.00%
60	track z_0 bias	0.00%	0.00%
60	track efficiency	0.00%	0.00%
60	track efficiency (dense env)	0.00%	0.00%
60	track fake rate	0.00%	0.00%
60	track fake rate (dense env.)	0.00%	0.00%

Table A.14.: Summary of all nuisance parameters including their impact on $m_{\text{vis+met}}$ when considering the $m_X = 4.0\,\text{TeV}$ sample in SRp1 (HH) sorted in descending order in δ^{avg}. The up and down variations are symmetrised.

A.8.3. SRf2 with HH selection applied

ranking	nuisance parameter	δ^{avg}	δ^{max}
1	JER (effective 3)	3.08%	38.54%
2	μ resolution (Inner Detector)	2.59%	26.70%
3	JER (effective 2)	2.56%	76.68%
4	JER (effective 1)	2.35%	38.38%
5	μ resolution (Muon Spectrometer)	2.00%	21.68%
6	μ residual bias	1.75%	16.73%
7	JER (effective 5)	1.59%	30.36%
8	JER (effective 4)	1.57%	29.95%
9	JER (effective 6)	1.55%	24.86%
10	JES (flavour response)	0.84%	29.31%
11	JES (mixed 1)	0.69%	36.06%
12	JES (flavour composition)	0.69%	21.32%
13	JES heavy flavour	0.51%	12.90%
14	JES (modelling 2)	0.48%	10.19%
15	JES (stat 1)	0.41%	6.78%
16	JES (intercalibration modelling)	0.30%	21.25%
17	JES (AFII)	0.29%	24.99%
18	JES (pileup ρ)	0.26%	18.82%
19	μ reconstruction efficiency (syst)	0.25%	7.22%
20	JES (pileup $< \mu >$)	0.25%	13.72%
21	JES (modelling 1)	0.20%	12.74%
22	JES (pileup N_{PV})	0.14%	10.84%
23	b-tagging efficiency (c-jets 1)	0.13%	4.82%
24	JES (pileup p_{T}	0.08%	7.17%
25	JES (modelling 3)	0.08%	7.54%
26	JES (stat 3)	0.08%	11.50%
27	JER (AFII)	0.08%	13.74%
28	JES (mixed 2)	0.07%	7.54%
29	JES (intercalibration stat)	0.07%	5.06%
30	JES (stat 2)	0.06%	7.49%
31	JES (mixed 3)	0.06%	5.09%
32	b-tagging efficiency (c-jets 0)	0.05%	1.21%
33	JES (stat 4)	0.05%	5.09%
34	JES (stat 6)	0.05%	5.05%
35	JES (punch through AFII)	0.04%	5.05%
36	b-tagging efficiency (c-jet extrapolation)	0.04%	1.08%
37	JES (stat 5)	0.04%	5.05%
38	μ scale	0.04%	4.90%
39	b-tagging efficiency (light jets extrapolation)	0.04%	3.02%

Table A.15.: $m_X = 2.0\,\text{TeV}$ continued on next page.

ranking	nuisance parameter	δ^{avg}	δ^{max}
40	b-tagging efficiency (light jets 0)	0.03%	1.36%
41	b-tagging efficiency (c-jets 2)	0.03%	1.20%
42	μ TTVA efficiency (syst)	0.03%	1.22%
43	b-tagging efficiency (light jets 1)	0.03%	1.21%
44	JES (intercalibration closure $\eta < 0$)	0.02%	2.35%
45	JES (modelling 4)	0.02%	2.62%
46	μ TTVA efficiency (stat)	0.02%	0.77%
47	μ reconstruction efficiency (stat)	0.02%	0.67%
48	b-tagging efficiency (b-jets 1)	0.01%	0.69%
49	b-tagging efficiency (b-jets 0)	0.01%	0.66%
50	b-tagging efficiency (b-jets 2)	0.01%	0.57%
51	b-tagging efficiency (c-jets 3)	0.01%	0.23%
52	b-tagging efficiency (light jets 2)	0.00%	0.13%
53	b-tagging efficiency (light jets 3)	0.00%	0.05%
54	b-tagging efficiency (light jets 4)	0.00%	0.01%
55	JES (detector 1)	0.00%	0.00%
56	JES (detector 2)	0.00%	0.00%
57	JES (intercalibration closure $\eta > 0$)	0.00%	0.00%
58	pileup reweighting	0.00%	0.00%
58	e/γ resolution	0.00%	0.00%
58	$e\gamma$ scale (AFII)	0.00%	0.00%
58	e/γ scale	0.00%	0.00%
58	e ID efficiency	0.00%	0.00%
58	e isolation efficiency	0.00%	0.00%
58	e reconstruction efficiency	0.00%	0.00%
58	JES (intercalibration closure high E)	0.00%	0.00%
58	JES (JVT efficiciency)	0.00%	0.00%
58	JES (testbeams)	0.00%	0.00%
58	JES (fJVT efficiency)	0.00%	0.00%
58	μ isolation efficiency (stat)	0.00%	0.00%
58	μ isolation efficiency (syst)	0.00%	0.00%
58	μ interpolation	0.00%	0.00%
58	track d_0 bias	0.00%	0.00%
58	track residual bias	0.00%	0.00%
58	track z_0 bias	0.00%	0.00%
58	track efficiency	0.00%	0.00%
58	track efficiency (dense env)	0.00%	0.00%
58	track fake rate	0.00%	0.00%
58	track fake rate (dense env.)	0.00%	0.00%

Table A.15.: Summary of all nuisance parameters including their impact on $m_{\text{vis+met}}$ when considering the $m_X = 2.0\,\text{TeV}$ sample in SRf2 (HH) sorted in descending order in δ^{avg}. The up and down variations are symmetrised.

ranking	nuisance parameter	δ^{avg}	δ^{max}
1	JER (effective 2)	12.41%	68.43%
2	μ resolution (Inner Detector)	11.61%	52.32%
3	JER (effective 3)	10.19%	88.29%
4	μ resolution (Muon Spectrometer)	9.22%	32.05%
5	μ residual bias	7.07%	55.23%
6	JER (effective 1)	6.85%	65.53%
7	JER (effective 6)	5.62%	71.66%
8	JES (mixed 1)	4.62%	62.25%
9	JER (effective 4)	4.47%	50.49%
10	JER (effective 5)	4.31%	48.94%
11	JES (testbeams)	4.27%	22.61%
12	JES (flavour response)	2.94%	58.56%
13	JES (AFII)	2.51%	45.67%
14	JES (modelling 2)	2.29%	34.23%
15	JES (flavour composition)	2.10%	33.75%
16	JES (pileup ρ)	1.88%	27.21%
17	JES (stat 1)	1.63%	25.80%
18	JES (modelling 1)	1.56%	26.74%
19	μ reconstruction efficiency (syst)	1.39%	11.89%
20	JES heavy flavour	1.22%	23.13%
21	JES (mixed 3)	0.98%	13.13%
22	JES (intercalibration modelling)	0.86%	25.81%
23	JES (mixed 2)	0.86%	27.26%
24	JES (pileup N_{PV})	0.39%	12.91%
25	JES (pileup p_{T}	0.39%	20.94%
26	b-tagging efficiency (c-jets 1)	0.22%	2.71%
27	b-tagging efficiency (light jets extrapolation)	0.20%	14.80%
28	JES (pileup $< \mu >$)	0.15%	9.54%
29	JES (intercalibration closure $\eta < 0$)	0.10%	10.91%
30	b-tagging efficiency (c-jets 2)	0.06%	0.75%
31	b-tagging efficiency (light jets 1)	0.05%	0.62%
32	b-tagging efficiency (light jets 0)	0.05%	0.61%
33	b-tagging efficiency (c-jet extrapolation)	0.05%	0.95%
34	μ TTVA efficiency (syst)	0.04%	0.57%
35	μ reconstruction efficiency (stat)	0.03%	0.39%
36	b-tagging efficiency (c-jets 0)	0.03%	1.26%
37	μ TTVA efficiency (stat)	0.03%	0.37%
38	JES (intercalibration stat)	0.02%	1.97%
39	JES (stat 4)	0.02%	1.96%
40	JES (stat 3)	0.02%	1.96%

Table A.16.: $m_X = 4.0\,\text{TeV}$ continued on next page.

ranking	nuisance parameter	δ^{avg}	δ^{max}
41	b-tagging efficiency (c-jets 3)	0.01%	0.16%
42	b-tagging efficiency (b-jets 1)	0.01%	1.62%
43	b-tagging efficiency (light jets 2)	0.01%	0.12%
44	b-tagging efficiency (b-jets 0)	0.01%	1.36%
45	b-tagging efficiency (b-jets 2)	0.01%	1.34%
46	b-tagging efficiency (light jets 3)	0.00%	0.05%
47	JER (AFII)	0.00%	0.09%
48	b-tagging efficiency (light jets 4)	0.00%	0.01%
49	JES (stat 2)	0.00%	0.02%
50	JES (modelling 3)	0.00%	0.02%
51	JES (detector 1)	0.00%	0.01%
52	JES (intercalibration closure $\eta > 0$)	0.00%	0.01%
53	JES (stat 5)	0.00%	0.00%
54	JES (stat 6)	0.00%	0.00%
55	JES (modelling 4)	0.00%	0.00%
56	JES (detector 2)	0.00%	0.00%
57	JES (punch through AFII)	0.00%	0.00%
58	pileup reweighting	0.00%	0.00%
58	e/γ resolution	0.00%	0.00%
58	$e\gamma$ scale (AFII)	0.00%	0.00%
58	e/γ scale	0.00%	0.00%
58	e ID efficiency	0.00%	0.00%
58	e isolation efficiency	0.00%	0.00%
58	e reconstruction efficiency	0.00%	0.00%
58	JES (intercalibration closure high E)	0.00%	0.00%
58	JES (JVT efficiciency)	0.00%	0.00%
58	JES (fJVT efficiency)	0.00%	0.00%
58	μ isolation efficiency (stat)	0.00%	0.00%
58	μ isolation efficiency (syst)	0.00%	0.00%
58	μ interpolation	0.00%	0.00%
58	μ scale	0.00%	0.00%
58	track d_0 bias	0.00%	0.00%
58	track residual bias	0.00%	0.00%
58	track z_0 bias	0.00%	0.00%
58	track efficiency	0.00%	0.00%
58	track efficiency (dense env)	0.00%	0.00%
58	track fake rate	0.00%	0.00%
58	track fake rate (dense env.)	0.00%	0.00%

Table A.16.: Summary of all nuisance parameters including their impact on $m_{\text{vis+met}}$ when considering the $m_X = 4.0\,\text{TeV}$ sample in SRf2 (HH) sorted in descending order in δ^{avg}. The up and down variations are symmetrised.

A.8.4. $t\bar{t}$ CR

ranking	nuisance parameter	δ^{avg}	δ^{max}
1	JER (effective 2)	5.81%	4411.23%
2	JER (effective 3)	5.33%	3218.39%
3	JER (effective 6)	4.78%	3957.65%
4	JER (effective 1)	4.77%	3883.99%
5	JER (effective 4)	4.52%	3219.45%
6	JER (effective 5)	4.29%	2063.03%
7	JES (mixed 1)	0.85%	1039.20%
8	JES (flavour composition)	0.69%	680.47%
9	JES (flavour response)	0.66%	1135.97%
10	JES (pileup ρ)	0.60%	627.81%
11	JES (intercalibration modelling)	0.47%	995.59%
12	b-tagging efficiency (light jets extrapolation)	0.45%	1003.22%
13	b-tagging efficiency (b-jets 0)	0.37%	312.48%
14	b-tagging efficiency (b-jets 1)	0.34%	395.13%
15	JES (modelling 1)	0.34%	618.30%
16	b-tagging efficiency (light jets 0)	0.14%	272.97%
17	b-tagging efficiency (b-jets 2)	0.13%	223.29%
18	μ reconstruction efficiency (syst)	0.11%	109.76%
19	JES (modelling 2)	0.10%	488.23%
20	b-tagging efficiency (light jets 1)	0.06%	107.86%
21	JES (pileup $< \mu >$)	0.04%	327.40%
22	JES (pileup N_{PV})	0.04%	274.79%
23	JES (pileup p_{T}	0.03%	274.74%
24	b-tagging efficiency (c-jet extrapolation)	0.03%	48.73%
25	b-tagging efficiency (c-jets 1)	0.03%	62.99%
26	μ TTVA efficiency (syst)	0.02%	35.71%
27	b-tagging efficiency (c-jets 0)	0.02%	21.89%
28	μ reconstruction efficiency (stat)	0.02%	34.73%
29	JES heavy flavour	0.02%	110.42%
30	μ TTVA efficiency (stat)	0.02%	23.25%
31	b-tagging efficiency (light jets 2)	0.02%	32.51%
32	JES (mixed 2)	0.01%	110.27%
33	JES (intercalibration stat)	0.01%	110.49%
34	JES (detector 1)	0.01%	109.86%
35	JES (modelling 4)	0.01%	109.68%
36	JES (stat 3)	0.01%	109.58%
37	JES (stat 1)	0.01%	109.55%
38	μ resolution (Muon Spectrometer)	0.01%	109.35%
39	b-tagging efficiency (light jets 3)	0.01%	17.86%

Table A.17.: $t\bar{t}$ continued on next page.

ranking	nuisance parameter	δ^{avg}	δ^{max}
40	b-tagging efficiency (c-jets 2)	0.00%	8.33%
41	b-tagging efficiency (light jets 4)	0.00%	3.44%
42	b-tagging efficiency (c-jets 3)	0.00%	1.36%
43	μ resolution (Inner Detector)	0.00%	13.94%
44	JES (modelling 3)	0.00%	0.89%
45	JES (stat 4)	0.00%	0.91%
46	JES (stat 2)	0.00%	0.53%
47	JES (stat 6)	0.00%	0.83%
48	JES (stat 5)	0.00%	0.34%
49	JES (mixed 3)	0.00%	0.24%
50	JES (detector 2)	0.00%	0.24%
51	JES (intercalibration closure $\eta < 0$)	0.00%	0.27%
52	JES (intercalibration closure $\eta > 0$)	0.00%	0.17%
53	pileup reweighting	0.00%	0.00%
53	e/γ resolution	0.00%	0.00%
53	$e\gamma$ scale (AFII)	0.00%	0.00%
53	e/γ scale	0.00%	0.00%
53	e ID efficiency	0.00%	0.00%
53	e isolation efficiency	0.00%	0.00%
53	e reconstruction efficiency	0.00%	0.00%
53	JES (intercalibration closure high E)	0.00%	0.00%
53	JES (JVT efficiciency)	0.00%	0.00%
53	JES (testbeams)	0.00%	0.00%
53	JES (fJVT efficiency)	0.00%	0.00%
53	μ isolation efficiency (stat)	0.00%	0.00%
53	μ isolation efficiency (syst)	0.00%	0.00%
53	μ residual bias	0.00%	0.00%
53	μ interpolation	0.00%	0.00%
53	μ scale	0.00%	0.00%
53	track d_0 bias	0.00%	0.00%
53	track residual bias	0.00%	0.00%
53	track z_0 bias	0.00%	0.00%
53	track efficiency	0.00%	0.00%
53	track efficiency (dense env)	0.00%	0.00%
53	track fake rate	0.00%	0.00%
53	track fake rate (dense env.)	0.00%	0.00%

Table A.17.: Summary of all nuisance parameters including their impact on $m_{\text{vis+met}}$ when considering the $t\bar{t}$ sample in ttbar CR sorted in descending order in δ^{avg}. The up and down variations are symmetrised.

A.9. The Electron Channel

During the analysis, it became evident that the small gain in sensitivity of the electron channel (see Section A.9.4) is not worth the extra complexity added to the analysis. Therefore, it was deprioritised in the analysis but the studies conducted so far in this channel are documented within this section.

A.9.1. Lepton-in-Jet correction

The first complication arises from the topology itself, where the electron is expected to be very close or even inside a TAR jet. Due to the closeness of hadronic energy deposits the efficiency scale factors and uncertainties on the likelihood identification become invalid. Therefore, the scale factors centrally provided must be corrected by dedicated studies and an extra systematic uncertainty be derived.

In this analysis, the approach to use semileptonic $t\bar{t}$ decays is made. This results in several issues. For once, the $t\bar{t}$ CR is generally used to normalise the $t\bar{t}$ background in both the electron and muon channel. Thus, it is difficult to use this region to obtain the correction to the electron scalefactors as well. In addition, when using semileptonically decaying $t\bar{t}$ events, the jet closest to the lepton is in nearly all cases a b-jet introducing a possible bias because of the differences to light jets.

Due to the decision to not proceed using the electron channel in the analysis, this study was aborted without producing final results.

A.9.2. Region Definition

The region definitions introduced in Sections 5.4 and 5.6 are basically unchanged. The CRs defined in the muon channel are used in the same way also in the electron channel. The method to define the signal and validation regions also remains the same. Based on the $H \to b\bar{b}$ candidate passing or failing the m_H window and having one or two b-tags, four combinations are possible. As in the muon channel, the highest sensitivity is observed for the case where the $H \to b\bar{b}$ candidate passes the 70% m_H window and has two b-tags as can be clearly seen in Figure A.33 which is therefore defined to be a signal region (SRp2). In contrast to the muon channel, the other regions do not perform in any way compatible or complementary to SRp2. In particular, the region defined by the $H \to b\bar{b}$ candidate passing the 70% m_H window and having two b-tags is not able to recover the purity or signal efficiency at high m_X. Thus, the remaining three regions are used as validation regions. A summary of the region definitions are given in Table A.18. To reduce the signal contamination in the VRs, the 80% efficient m_H window is used in cases where the $H \to b\bar{b}$ candidate fails this window.

Taking into account that the muon channel only has one VR, having three VRs in the electron channel actually allows for additional cross checks. While in the muon channel, the assumption is made that extrapolating from VRf1 to all three signal regions SRf2, SRp1 and SRp2 does not introduce any biases, having three VRs in the electron channel allows to test this assumption. For once, the effect of changing the number of b-tags can

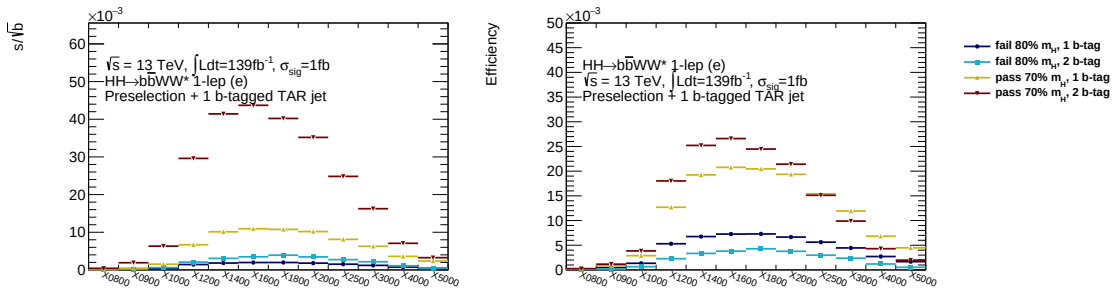

(a) signal purity **(b)** signal efficiency

Figure A.33.: Purity and efficiency of the four region definition options in the electron channel for the full range of HH production mass points. The expected signal cross section is set to 1 fb for all mass points.

region	name	mass window	number of b-tags
signal	SRp2	pass 70%	2
validation	VRp1	pass 70%	1
validation	VRf2	fail 80%	2
validation	VRf1	fail 80%	1

Table A.18.: Summary of the final signal and validation regions of the electron channel based on the mass window cut and the number of b-tags of the $H \to b\bar{b}$ candidate. Each region furthermore requires exactly one b-tagged TAR jet in the event.

be investigated by comparing VRf1 and VRf2. Additionally, comparing VRf1 and VRp1 allows to draw conclusions on the transition from failing to passing the m_H window even with changing the m_H window efficiency.

Due to the decision to deprioritise the electron channel, these studies have not been conducted.

A.9.3. Background estimate

As in the muon channel, the prompt-lepton backgrounds are estimated using events from MC simulations where the normalisation of the dominant backgrounds, W+jets and $t\bar{t}$, is corrected using the same iterative approach. However, including the electron channel in the background normalisation fit introduces three additional CRs. Due to lepton universality, there should be no fundamental difference between electrons and muons in the prompt lepton processes which could cause differences in the normalisation. Therefore, the NFs for the $t\bar{t}$ and W+jets backgrounds are shared between electron and muon channels. Considering non-prompt lepton events, these can indeed differ between electrons and muons since the non-prompt electron background also contains jets misidentified as electrons. Thus, one NF each is defined for the non-prompt electron

and non-prompt muon backgrounds. The obtained NFs are listed in Table A.19 and their effect can be seen in Figures A.34 and A.35 in the electron and muon channel, respectively.

Iteration	$\mathrm{NF}_{t\bar{t}}$	$\mathrm{NF}_{W+\mathrm{jets}}$	$\mathrm{NF}^{e}_{\mathrm{dijet/non\text{-}prompt}}$	$\mathrm{NF}^{\mu}_{\mathrm{dijet/non\text{-}prompt}}$
with dijet MC	0.72 ± 0.01	0.49 ± 0.01	0.49 ± 0.01	0.63 ± 0.03
with QCD estimate	0.73 ± 0.01	0.52 ± 0.01	0.32 ± 0.01	1.81 ± 0.11

Table A.19.: Normalisation factors for the $t\bar{t}$, W+jets and dijet/non-prompt backgrounds split in electron and muon channel obtained after the first and second iteration of the background normalisation fit [26]. The NFs for the dijet sample in the electron and muon channels in the first iteration are only listed for completion and will not be used in the analysis. The non-prompt electron estimate is based on efficiencies binned in $m_{\mathrm{vis+met}}$.

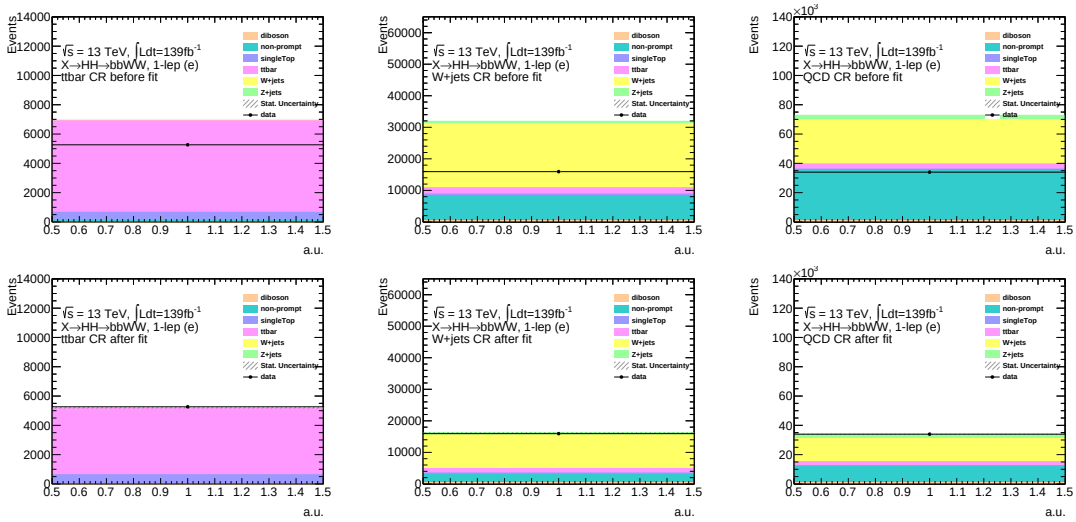

(a) $t\bar{t}$ CR **(b)** W+jets CR **(c)** QCD CR

Figure A.34.: Number of background events in the electron channel split into the different backgrounds in the $t\bar{t}$, W+jets and QCD CRs before (top) and after (bottom) performing the background normalisation fits. These plots correspond to the second iteration where the data driven non-prompt lepton estimate is included in the backgrounds.

The non-prompt lepton background estimate is still done using the Matrix Method. The corresponding definitions of loose and tight electron definitions are summarised in Table A.20. Due to the unique topology of this analysis, it has not been possible to find a binning of the efficiencies general lepton related variables that allowed a decent description of all other variables as well. The available amount of statistics is not sufficient

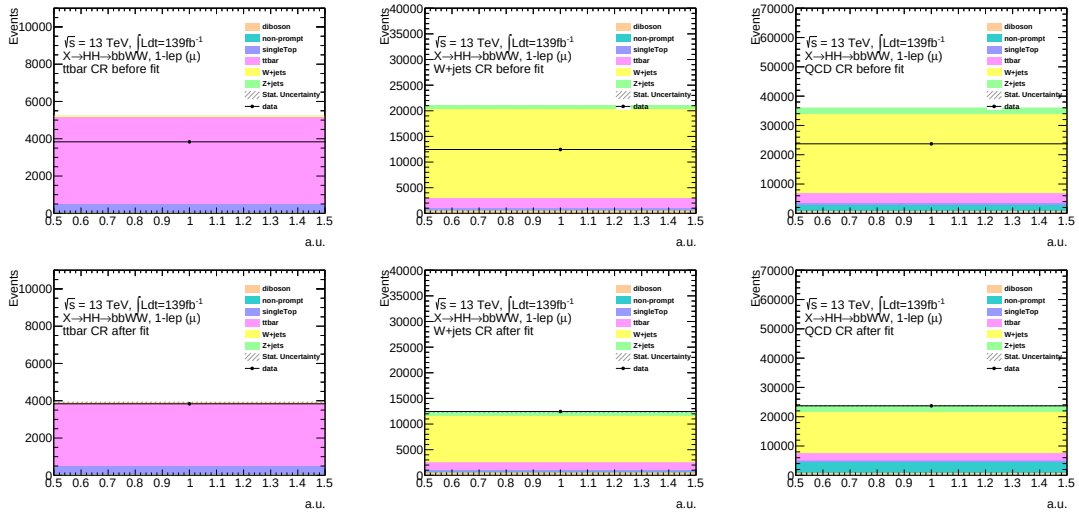

(a) $t\bar{t}$ CR **(b)** W+jets CR **(c)** QCD CR

Figure A.35.: Number of background events in the muon channel split into the different backgrounds in the $t\bar{t}$, W+jets and QCD CRs before (top) and after (bottom) performing the background normalisation fits. These plots correspond to the second iteration where the data driven non-prompt lepton estimate is included in the backgrounds.

to cope with the needed dimensions of the efficiency binning resulting in large statistical fluctuations.

Selection	ID	isolation
Loose	looseLH	-
Tight	mediumLH	TightTrackOnly

Table A.20.: Requirements on loose and tight electrons used in the non-prompt lepton estimate by the matrix method.

Therefore, a novel approach based has been tested. It is based on the assumption that the variable that the efficiencies are binned in is well modelled in the estimate later on. Thus, instead of binning the efficiencies in a large number of fundamental lepton quantities to describe more complex variables such as the final discriminant, the final discriminant is used to define the efficiencies, for example. Using this approach of one dimensional binnings in complex event variables solves the issue of large statistical uncertainties but at the same time ignores the theoretical principles of the matrix method. Therefore, an additional systematic uncertainty on the made assumption is assigned by comparing the distributions of variables used in the binning of the efficiencies to data in the VRs. The resulting distributions are shown in Figure A.36.

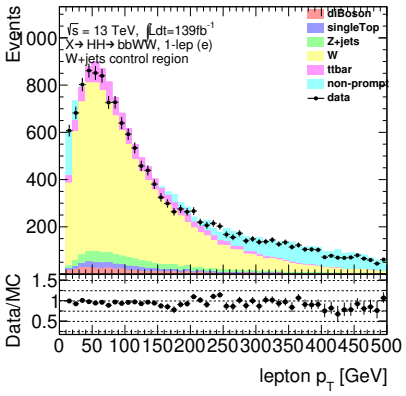

(a) p_{T}^{e}

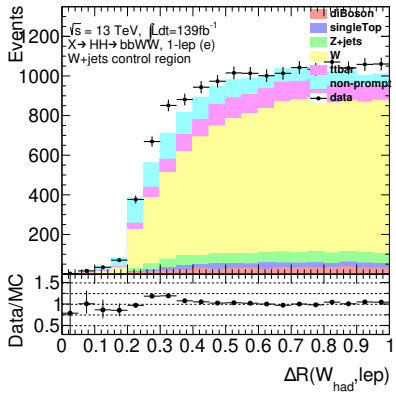

(b) $\Delta R(W_{\mathrm{had}}, e)$

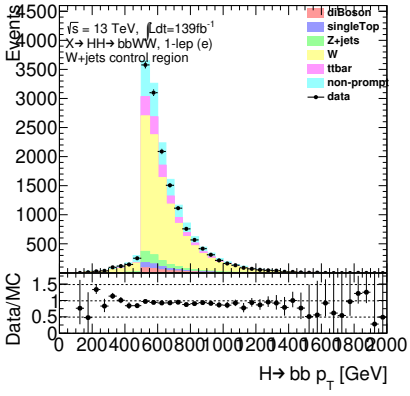

(c) $p_{\mathrm{T}}^{H\to b\bar{b}}$

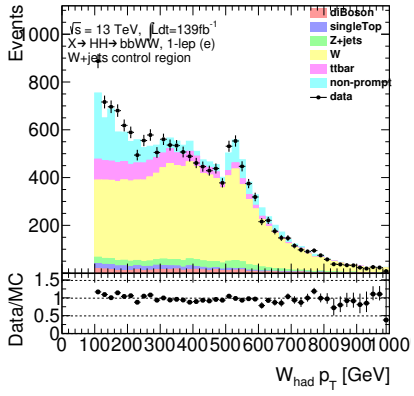

(d) $p_{\mathrm{T}}^{W_{\mathrm{had}}}$

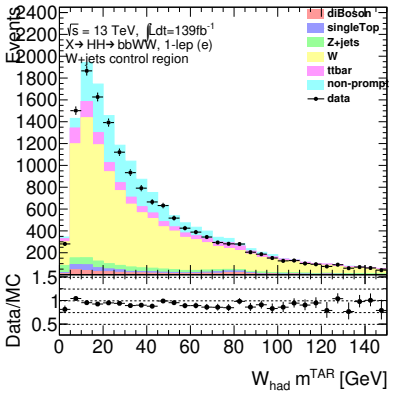

(e) $m_{\mathrm{TAR}}^{W_{\mathrm{had}}}$

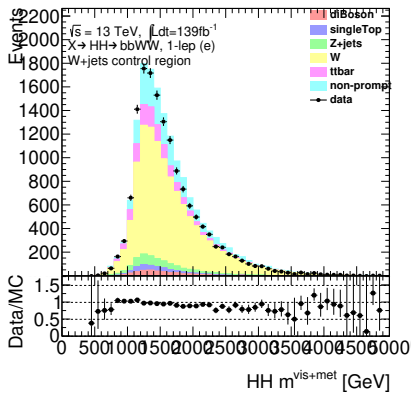

(f) $m_{\mathrm{vis+met}}$

Figure A.36.: Distributions of variables in the W+jets control region where the non-prompt lepton background estimate has been obtained from rates binned in the respective variable.

Apart from small discrepancies, the modelling of all variables the efficiencies have been binned in is sufficiently good in the W+jets CR, which due to its high W+jets contribution, is very prone to mismodelling. The attempt to assign an uncertainty on this approach is documented in Ref. [326].

A.9.4. Sensitivity

Given the extra complications introduced by the electron channel, only a benefit in the sensitivity would justify to extend the time schedule to include this channel in the analysis. Figure A.37 shows this is not the case. The red dashed line which correspond to the combined limit in the three muon SR together with SRp2 in the electron channel, while the black line with the error bands correspond to the three muon SRs only. In both cases, no HH selection is applied to any of the SRs. For $m_X > 2.5$ TeV, the sensitivity is purely driven by the muon channel with no benefit from the inclusion of the electron channel. The largest effect can be seen for $m_X \leq 1.2$ TeV where the analysis becomes generally insensitive such that the small increase in sensitivity is irrelevant compared to limits provided by the $HH \to b\bar{b}b\bar{b}$ analysis [12].

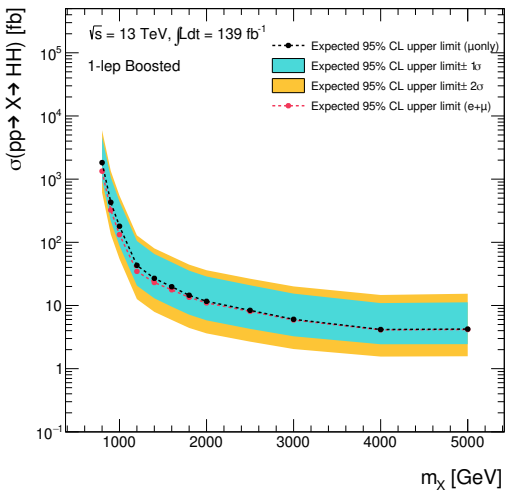

Figure A.37.: Expected upper limit using the three muon signal regions without applying the HH selection. For comparison, the expected exclusion limit also including the most sensitive signal region SRp2 in the electron channel is overlaid as dashed red line.

As shown in Figure A.38, including the second most sensitive region in the electron channel (VRp1) as a signal region also does not improve the limits significantly except for the very low m_X range where the analysis itself is not sensitive. On the other hand, removing the least sensitive signal region in the muon channel (SRf2) decreases the sensitivity in the more sensitive high m_X range.

The effect on the SH analysis has not been investigated.

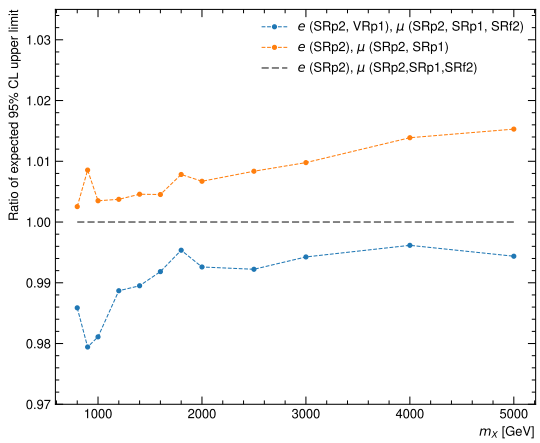

Figure A.38.: Comparison between limits obtained by using three muon SRs and one electron SR and limit obtained when including VRp1 as additional electron SR or removing SRf2 from the muon SRs. No HH selection is applied to any of the SRs.

APPENDIX B

ITK Simulation

The first technical design reports of the ATLAS Inner Tracker (ITK) were published in 2017 [192, 193]. Since then many changes to the planned layout have been made. This is particularly true for the ITK pixel detector and the different candidate layouts that have been considered are displayed in Figure B.1 [193, 327, 328]. The number of layers of barrel staves and endcap rings is consistently five regardless of the candidate layout, and layer 0 denotes the innermost layer, and layer 4 the outermost layer.

The design presented in the technical design report featured inclined sections in the barrel staves. Three types of modules were discussed:

- **single modules** which only carry one readout chip and are employed in the inclined section of the barrel layer 0,
- **dual modules** which carry two readout chips and are employed in the flat part of the barrel layer 0 and the inclined barrel sections in layers 2 to 4 and
- **quad modules** which carry four readout chips and are employed in the remaining detector parts.

All pixels considered possessed a size of $50 \times 50\,\mu\text{m}^2$.

After the technical design report was issued, the decision to include a High Granularity Timing Detector [194] in the Phase-II upgrade was made, resulting in less space available for the ITK components. Therefore, the size of the ITK in z-direction was reduced by 15 cm on each side. Additionally, the space accommodated for the service routing was found to be insufficient. Thus, the design was revisited. While the structure of five layers remained in the new design, the barrel now only consisted of flat staves and the first endcap rings in layers 2 to 4 were inclined instead. Furthermore, the dual modules were removed from the design. In the updated design, only the barrel layer 0 consisted of single modules. All other parts used quad modules.

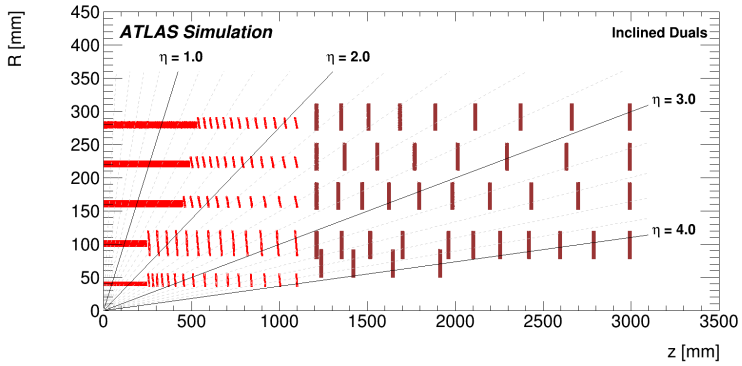

(a) Technical Design Report [193]

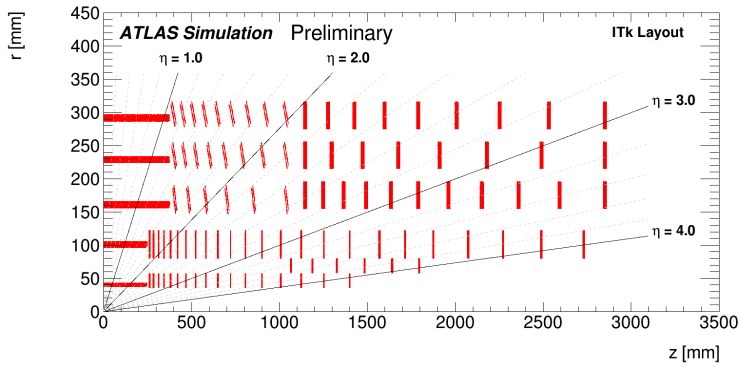

(b) Task Force II [327]

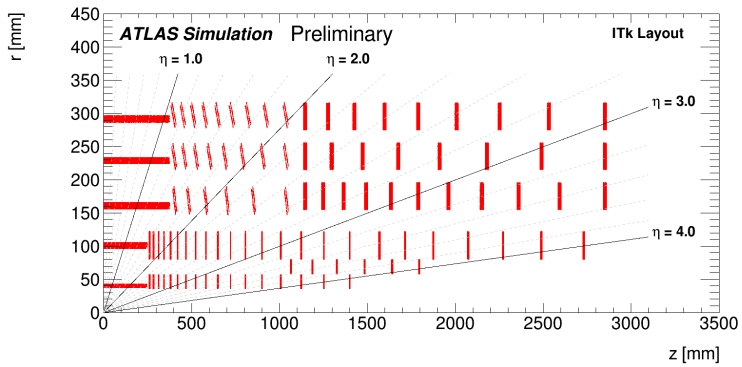

(c) Latest Updates [328]

Figure B.1.: Chronological development of the ITK pixel detector layout. These figures only display one quadrant and active material.

The inner radius of the ITK in this design was 39 mm in the barrel and 36 mm in the endcap part compared to the IBL of Inner Detector which has an inner radius of 31 mm. This resulted in a worse tracking performance of the ITK in the central region that is especially important for flavour tagging jets. Therefore, in the last adjustment

to the ITk pixel design, the inner radius was reduced to 34 mm in the barrel part and 33.2 mm in the endcaps improving the tracking and vertexing performance. Furthermore, this shift allowed to remove two staves from layer 0 and to rearrange the endcap disks while still covering the desired $|\eta| \leq 2.7$ range as shown in Figure B.1 (c). In the single modules, the pixel size was changed to $25 \times 100\mu\text{m}^2$.

Given the financial costs and time necessary to build such a new detector, it must be optimised before its construction is commissioned. A detailed simulation of the detector and the interaction between its materials and passing particles is crucial to find the best configuration and layout. However, the main challenge is to find the balance between accuracy, i.e. the detail in which the detector is described, and the computing power necessary to run the simulation, i.e. the resources necessary to load the layout and the time to simulate the interactions between particles and the detector material.

To avoid updating the entire simulation each time a detail in the detector layout is changed, the layout of the Atlas detector including its subcomponents is stored in a large database called geometry database (see Section B.1). Additionally, the conditions under which the detector is operated can change. While knowing the performance of the detector in perfect condition, its operation results in defects over time which need to be taken into account when evaluating the long time performance. More details on this are given in Section B.2.

B.1. Geometry Database

The geometry database [329] stores the layout of the entire Atlas detector in an advanced form of an SQL database as shown in Figure B.2. The structure of the detector is reflected by branches which correspond to the subcomponents such as the Inner Detector which can again be organised in branches such as pixel detector. The actual information are then stored in leaves which are classic SQL tables. The entries in the tables can either be integers, doubles or strings that can also point to another entry in the database.

A particular method to store information in the database is to use Character Large OBjects (CLOBs), which can be xml files. These store the layout of the ITk pixel detector, for example. While the strip detector layout of the Inner Detector is already stored as CLOB in the geometry database, the ITk pixel detector is the first pixel detector stored this way. Due to the description choice, the ITk pixel detector is actually represented by thirteen different xml files splitting the information into general geometry, the barrel staves, endcap rings, different services and also material specific information (see table in Figure B.2). In addition to the CLOB, an entry identifier as unique database key, a layout identifier (geotype), a version number and the name of the file stored as CLOB describe the respective parts of the ITk pixel detector. After moving to the GeoXMLmodel format, which is also used to describe the ITk strip detector, only one xml file containing all information remains.

The advantage of this setup compared to a usual SQL database is the possibility to create tags of the branches and leaves. Thus, several layouts can exist in parallel where

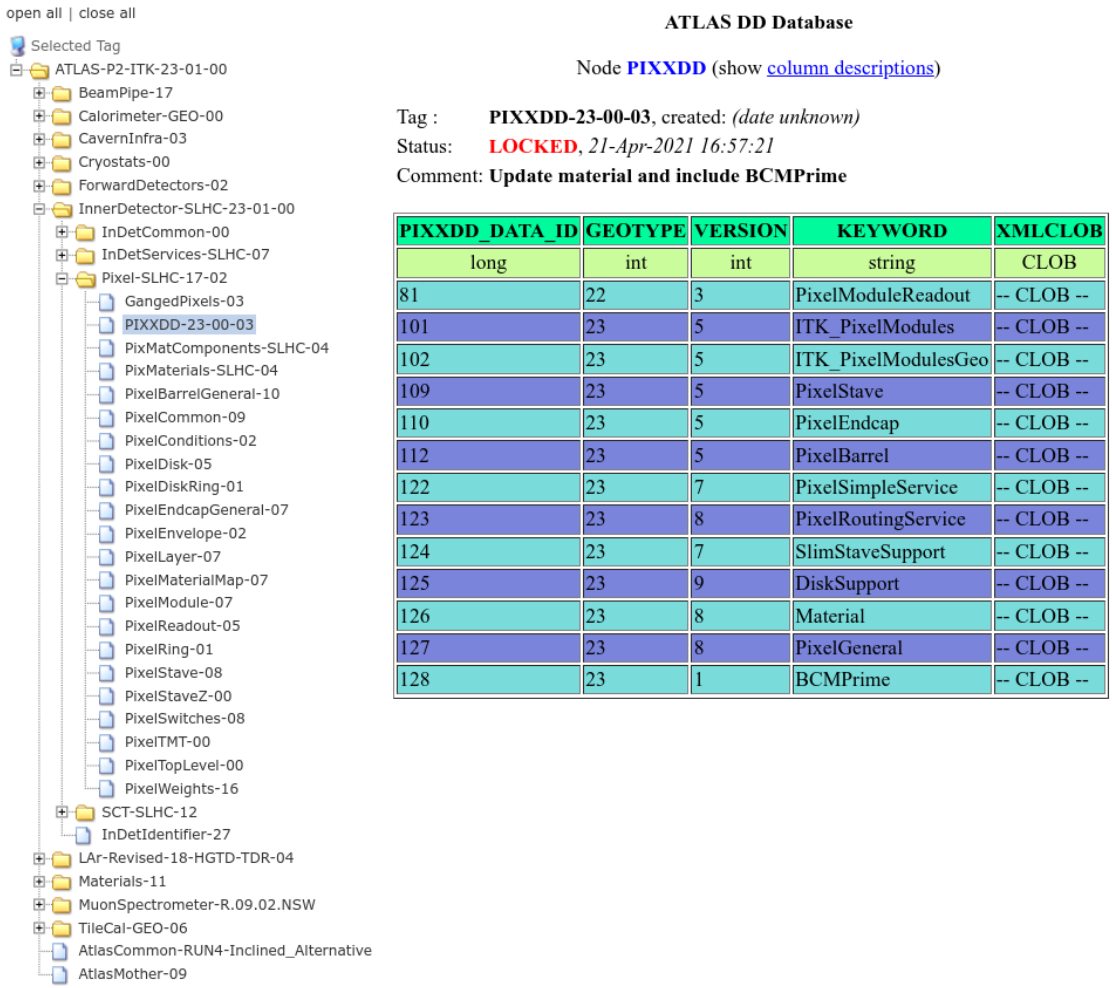

Figure B.2.: Excerpt of the geometry database showing the branch and leaf structure as well as the content of the leaf storing the ITK pixel layout as presented in Figure B.1 (c) [329].

the tagged branches and leaves only contain a selected fraction of information. This is also shown in Figure B.2. Each of the branches and leaves at the left-hand side is also labelled by a number, the tag. The table on the right-hand side contains only 13 entries although the entry identifier in the left most column shows that this table contains at least 128 entries.

This allows easy bookkeeping of different layouts. Furthermore, the option to reproduce various results or to compare different layouts by simply changing the ATLAS geometry tag in the simulation without the need to change anything in the database or simulation directly is made possible.

B.2. Simulating Defects in the Detector

With advancing age of the detector, pixels, readout chips or even entire modules start to fail. The term "defect" translates to active material becoming passive without changing any other properties of the detector except for the signal not being transmitted to readout. This effect becomes only visible in the digitisation step of the simulation.

The simulation of such defects can be done in two ways. Either the layout description stored in the geometry database is changed or a mask labelling certain modules or chips as inactive is overlaid. Given that changing geometry information in the xml files would result in complex modifications, the second option is pursued. This method is also used for the current Inner Detector.

A mask can be created in three ways:

Random: a tunable fraction of modules or chips is labelled as inactive. All modules and chips have thereby the same probability to be labelled inactive.

Random weighted: as in the previous case, a tunable fraction of the active material is labelled as inactive. Here, modules and chips in certain regions of the detector have a higher probability to be masked as others.

Deterministic: selected modules or chips are marked as defect. This can be useful for simulating power cuts and other systematic problems.

Figure B.3 shows the number of clusters reconstructed from 500 $t\bar{t}$ events without any pileup contributions when 15% of all modules and chips are randomly marked as defect normalised to the number of clusters when the detector is fully functioning. The random selection of defects is reflected in the plots where an overall decrease in reconstructed clusters is visible, but no region stands out. In Figure B.4, the track reconstruction yields the same picture. The resolution of the track parameters decreases overall without being dominant in any particular η region. Only the tracking efficiency suggests that the region around $|\eta| = 3.0$ is slightly more sensitive to defects than the rest of the detector. The largest decrease of the tracking efficiency in this region is approximately 5% compared to 1% to 2% elsewhere.

While these purely random defects can occur, it is more realistic that modules or chips that are exposed to a larger particle flux and a higher radiation dose are more likely to fail during the time of operation. The total ionisation dose for the layout introduced in the technical design report is calculated by the FLUKA framework [330] and displayed in Figure B.5. While layer 0 at high η is emitted with the highest radiation dose caused by elastic proton-proton scatterings, the outer parts of the ITk pixel detector are radiated by an order of magnitude less intensity. Assuming that the probability of a chip to become defect is proportional to the radiation dose for demonstrating purposes, the results for 15% of chips with defects are displayed in Figure B.6. In contrast to the purely randomly masked chips, barrel layer 0 is completely marked as defect while the endcaps of layer 1 retain a cluster fraction of 20% to 50%. Furthermore, the tracking efficiency at high $|\eta| \gtrsim 2.5$ worsens significantly to around 5% in the highest η bin.

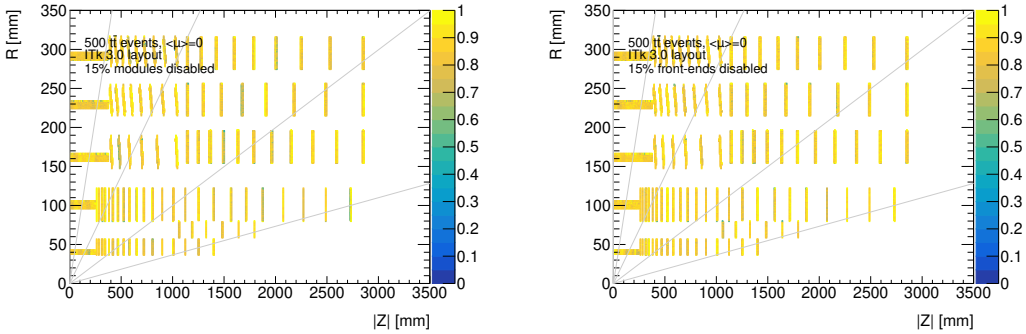

(a) 15% modules **(b)** 15% chips

Figure B.3.: Fraction of reconstructed pixel clusters after randomly introducing defects in 15% of all modules or in 15% of all chips present in the ITK pixel detector using the layout from Figure B.1 (b).

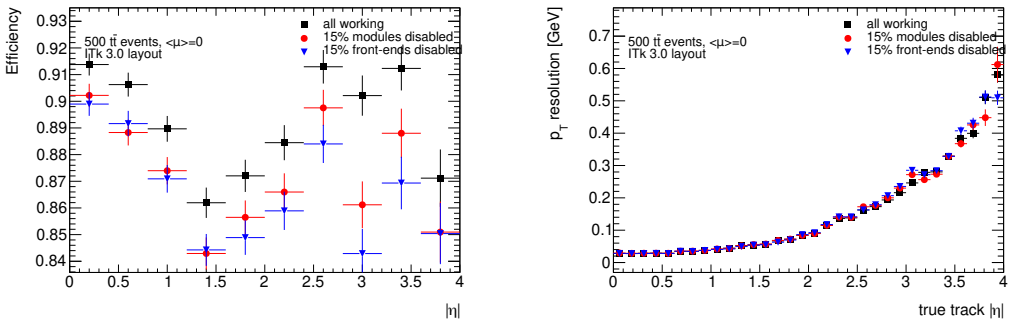

(a) tracking efficiency **(b)** track p_{T} resolution

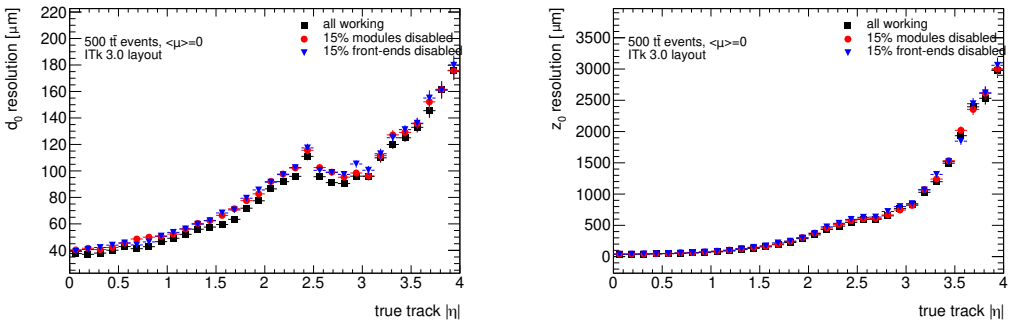

(c) track d_0 resolution **(d)** track z_0 resolution

Figure B.4.: Evolution of the tracking efficiencies as well as three track parameters when randomly introducing defects in 15% of all modules or in 15% of all chips present in the ITK pixel detector using the layout from Figure B.1 (b).

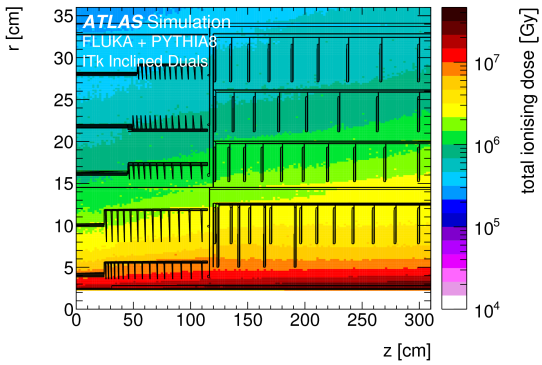

Figure B.5.: Expected total radiation dose after $\int \mathcal{L} dt = 4000\,\mathrm{fb}^{-1}$ data provided by the HL-LHC estimated by the FLUKA simulation. The layout introduced in the technical design report is used for these studies [193].

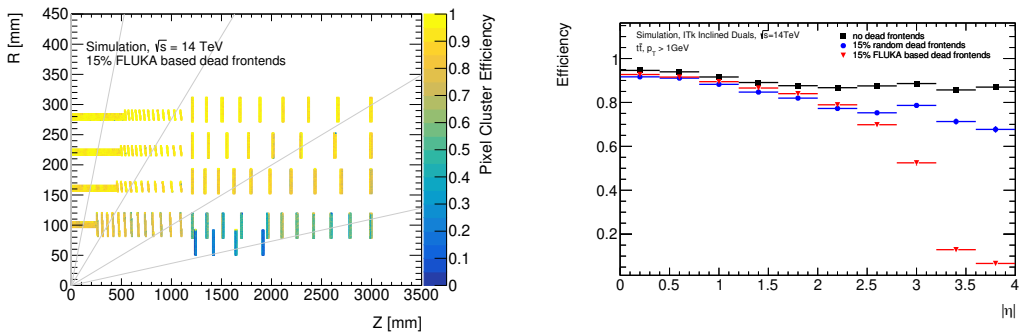

(a) fraction of pixel clusters

(b) tracking efficiency

Figure B.6.: Fraction of reconstructed pixel clusters and tracking efficiency after introducing defects in 15% of all chips present in the ITK pixel detector based on the total radiation dose of Figure B.5 using the layout from Figure B.1 (a).

Both masking methods have been demonstrated to work, while the exact probabilities of a module or chip to fail need to be revisited if being used to determine the ageing of the detector and the effect on its tracking performance.

APPENDIX C

Jet Energy Resolution of Small-R Jets

This section describes methods to measure the jet energy resolution (JER) of small-R jets which are reclustered from locally calibrated energy clusters using the anti-k_t algorithm with a size parameter of $R = 0.2$. As for any other jet collection, the correction of the JER is not the only necessary correction on jets in simulated events.

The jet energy scale (JES) needs to be corrected before the resolution is measured. The calibration of these jets is done in two stages. In the first stage, the energy of the jets is matched to the energy of jets reclustered using stable truth particles from the simulation, while in the second stage, *in situ* corrections to match the recorded data are applied to the jets reconstructed in simulation. To avoid repeating the full *in situ* calibration, a new approach is used where the small-R jets are geometrically matched to anti-k_t ($R = 0.4$) jets fully calibrated at the EM scale. This is called direct matching method [331].

The JER measurement discussed in this section is based on $\sqrt{s} = 13\,\text{TeV}$ proton-proton collisions recorded in 2015 and 2016 by the ATLAS experiment.

The relative JER can be parametrized in terms of the jet p_T by three independent terms:

$$\frac{\sigma_{p_T}}{p_T} = \underbrace{\frac{N}{p_T}}_{\text{noise}} \oplus \underbrace{\frac{s}{\sqrt{p_T}}}_{\text{stochastic}} \oplus \underbrace{C}_{\text{constant}} \tag{C.1}$$

called a NSC function.

The noise term results from electronic noise and pileup which both contribute directly to the energy measurement and can be considered as independent of the energy deposits of the showering particles. Therefore, the noise term for the relative JER scales with $1/p_\text{T}$ and contributes primarily in the low p_T range. The stochastic term has the largest impact in the mid p_T range of the JER and results from variations in the amount of

energy deposited by the showering particles. Thus, it scales with $1/\sqrt{p_{\mathrm{T}}}$. The last term collects contributions independent of the jet p_{T} such as energy deposits in the passive material of the ATLAS detector or the non-uniformity of the response across the calorimeter. This term dominates the JER in the high p_{T} range.

The two contributions to the noise term are approximately independent and can therefore be derived in two different measurements. The pileup contribution is derived by the random cones method in which energy deposits in circular areas matching the jet area are summed up using data events triggered by the zero-bias jet trigger. The electronic noise contribution is derived from special simulated events where the pileup is turned off. Both measurements are then combined in quadrature [332].

The stochastic and constant terms are derived together using the direct balance method on dijet events which have a large cross section and are theoretically well understood. Based on the fact that pure dijet events are balanced in their transverse momenta, any deviations in this balance result from the experimental resolution. In reality, initial or final state radiation and the event selection used in the measurement have to be taken into account as well. To reduce the effect of radiation, dijet events must fulfil

- $\Delta\phi(j_1, j_2) \geq 2.7$ to force a back to back topology in the transverse plane and
- $p_{\mathrm{T}}^{j_3} < \max(25\,\mathrm{GeV}, 0.25 \cdot p_{\mathrm{T}}^{\mathrm{avg}})$ with $p_{\mathrm{T}}^{\mathrm{avg}} = (p_{\mathrm{T}}^{j_1} + p_{\mathrm{T}}^{j_2})/2$ being the average p_{T} of the two leading jets to reduce the impact of events where part of the energy is consumed by initial and final state radiation.

Furthermore, the impact of pileup is reduced by requiring that the jets pass the medium JVT working point. Since no optimised JVT is available for jets with a size parameter of $R = 0.2$, the small-R jets are matched to anti-k_t ($R = 0.4$) jets which use the EM scale (EMTopo) using a condition on the angular distance.

C.1. Asymmetry Fits

The balance between a probe and a reference jet can be quantified by the asymmetry

$$\mathcal{A} = \frac{p_{\mathrm{T}}^{\mathrm{probe}} - p_{\mathrm{T}}^{\mathrm{ref}}}{p_{\mathrm{T}}^{\mathrm{avg}}} \tag{C.2}$$

where $p_{\mathrm{T}}^{\mathrm{ref}}$ is the p_{T} of a reference jet which must be in the well calibrated detector area $0.2 \leq |\eta| < 0.7$, while $p_{\mathrm{T}}^{\mathrm{probe}}$ is the p_{T} of the probe jet which is allowed to be in the full calorimeter range $|\eta| < 4.5$. The average p_{T} of both jets is used to normalise the asymmetry.

The corresponding resolution of the asymmetry is then expressed in terms of the relative energy resolutions of the probe and reference jets

$$\sigma_{\mathcal{A}} = \left(\frac{\sigma_{p_T}}{p_T}\right)^{\mathrm{ref}} \oplus \left(\frac{\sigma_{p_T}}{p_T}\right)^{\mathrm{probe}} \Leftrightarrow \left(\frac{\sigma_{p_T}}{p_T}\right)^{\mathrm{probe}} = \sigma_{\mathcal{A}} \ominus \left(\frac{\sigma_{p_T}}{p_T}\right)^{\mathrm{ref}} \tag{C.3}$$

Fitting the asymmetry with a convoluted Gaussian function, it is possible to extract $\sigma_{\mathcal{A}}$ from asymmetry measurements, which are affected by physical effects such as multiple parton interactions, radiation or hadronisation on an event-by-event basis that are corrected using true asymmetry resolution $\sigma_{\mathcal{A}}^{\text{truth}}$. Additionally, the asymmetry is split in $p_{\text{T}}^{\text{avg}}$ and η^{probe} bins to account for differences in the detector and energy range. Two examples of asymmetry fits for each simulated and recorded data events are shown in Figure C.1.

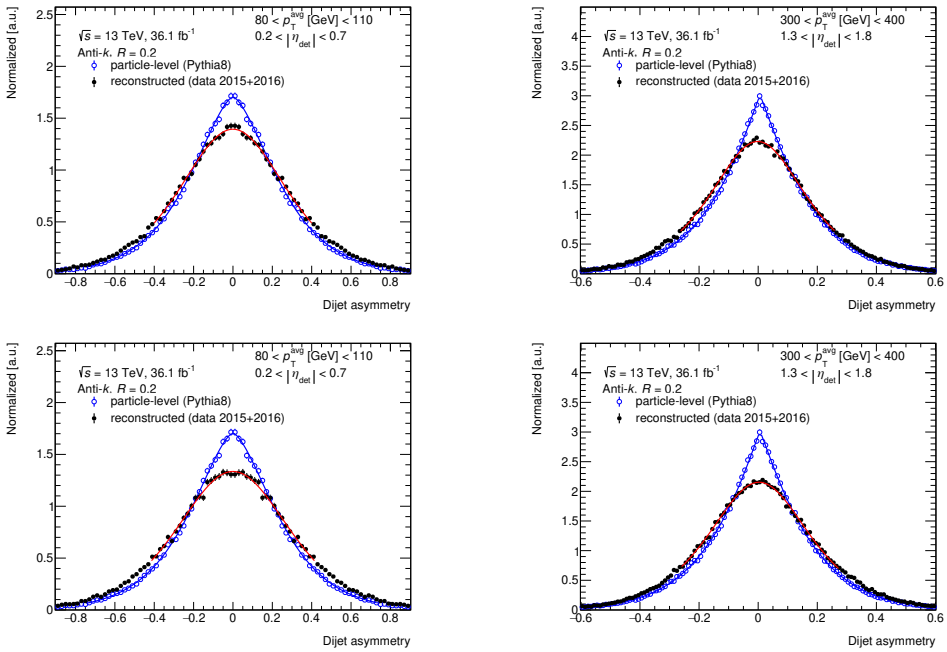

(a) $80\,\text{GeV} \leq p_{\text{T}}^{\text{avg}} < 110\,\text{GeV}$, $0.2 \leq |\eta^{\text{probe}}| < 0.7$

(b) $300\,\text{GeV} \leq p_{\text{T}}^{\text{avg}} < 400\,\text{GeV}$, $1.3 \leq |\eta^{\text{probe}}| < 1.8$

Figure C.1.: Asymmetry fits in two representative p_{T} and η bins for simulated (top) and recorded data (bottom) events. The true asymmetry shown in blue is the same for MC and data events. The asymmetry in all bins can be found in Ref. [331].

The relative resolution of the reference can then be obtained from requiring both the reference and probe jet to be within $0.2 \leq |\eta| < 0.7$. The derived relative resolutions of the probe jet are combined by minimising

$$\chi^2 = \sum_{i=1}^{n} \frac{(O_i - E_i)^2}{E_i}, \tag{C.4}$$

where O_i are the observed measurements and E_i are the corresponding expected values defined by the NSC function of Eq. C.1. The index i denotes one of the seven η bins. Two example relative JER determinations as a function of $p_{\text{T}}^{\text{reco}}$ in different η bins are displayed in Figure C.2 using events in data. Since the noise term has been measured

independently, it is constrained in the fit to the measured value and its uncertainty is neglected for this purpose.

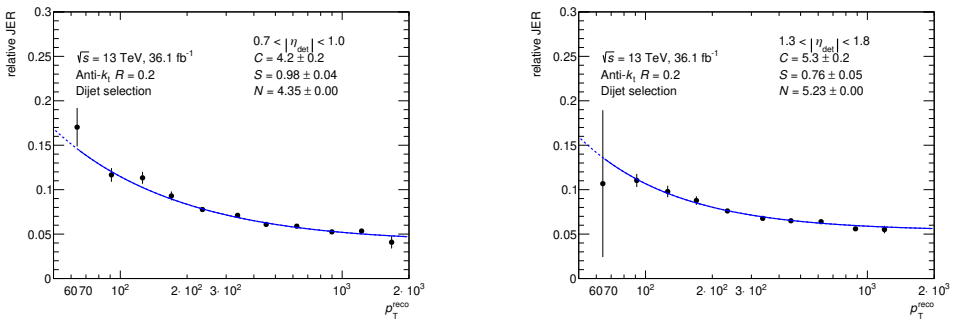

(a) $0.2 \leq |\eta| < 0.7$ **(b)** $0.2 \leq |\eta| < 0.7$

Figure C.2.: *NSC* fits in two representative η bins. All bins can be found in Ref. [331].

To stabilise the measured resolutions against statistical fluctuations, the root mean square of one hundred simulated toy datasets called bootstraps [333] is used as statistical uncertainty.

C.2. JER Uncertainties

The uncertainty on the relative JER measurement can be grouped into four sources:

- **noise term**, a measurement independent of the direct balance method which is explained in detail in Ref. [331].
- **direct balance method**, making several assumptions and selections which can influence the JER.
- **small-R JES uncertainties**, also affecting the JER since energy scale and energy resolution are correlated.
- **anti-k_t $R = 0.4$ JES uncertainties** must be propagated due to the matching between small-R jets and anti-k_t ($R = 0.4$) jets in the JES and JER determination.

In the following, the systematic uncertainties are represented in the form

$$\delta\mathcal{R} = \frac{\mathcal{R}^{\text{var}} - \mathcal{R}^{\text{nom}}}{\mathcal{R}^{\text{nom}}} \tag{C.5}$$

where $\mathcal{R}^{\text{var}}$ corresponds to the systematically varied relative JER while $\mathcal{R}^{\text{nom}}$ is the nominal relative JER as shown in the previous section. This ratio is built for all bootstrapped datasets. There are cases where the asymmetry resolution has an imaginary part due to the detector resolution being smaller than the particle-level resolution. This results in very significant deviations from the average asymmetry resolution. Therefore, the

bootstrap events are cleaned from these cases before the root mean squared (RMS) is calculated and used as uncertainty on the ratio. The ratios are then rebinned to reduce the statistical uncertainty further by combining bins which do not differ significantly. Here, a deviation of two standard deviations or more is considered significant.

The results in this thesis will only be shown in one representative η bin. The results in other η bins are discussed in Ref. [331] where the largest uncertainty is around 10% overall.

C.2.1. Uncertainties of the direct balance method

The uncertainties on the direct balance method can be divided according to the different selections applied. Starting with the dijet topology whose selection is to a certain degree arbitrary, the bias introduced by this choice is estimated by tightening the selection to

- $\Delta\phi(j_1, j_2) \geq 2.9$ and
- $p_{\mathrm{T}}^{j_3} < \max(20\,\mathrm{GeV}, 0.20 \cdot p_{\mathrm{T}}^{\mathrm{avg}})$

and also loosening it to

- $\Delta\phi(j_1, j_2) \geq 2.5$ and
- $p_{\mathrm{T}}^{j_3} < \max(30\,\mathrm{GeV}, 0.30 \cdot p_{\mathrm{T}}^{\mathrm{avg}})$.

The resulting relative uncertainty on the JER is shown in Figure C.3.

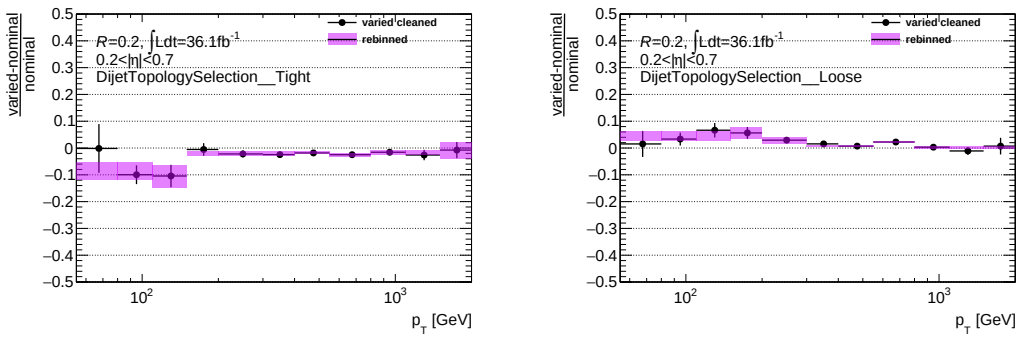

(a) tightened selection **(b)** loosened selection

Figure C.3.: Effect on the JER when systematically varying the dijet topology selection in the $0.2 \leq |\eta| < 0.7$ bin. The purple boxes show the uncertainties as they are used in the recommendation.

For the same reason, the JVT working point applied to the matched anti-k_t ($R = 0.4$) jet is tightened with the relative uncertainty on the JER being presented in Figure C.4 and showing a significantly smaller effect.

Another choice that has been made is the MC generator used to estimate the true uncertainty. In particular, the choice of the parton shower can affect the JER significantly.

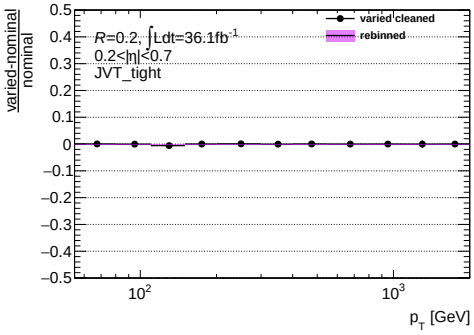

Figure C.4.: Effect on the JER when systematically varying the JVT working point on the matched anti-k_t ($R = 0.4$) jets in the $0.2 \leq |\eta| < 0.7$ bin. The purple boxes show the uncertainties as they are used in the recommendation.

Nominally, the simulated events are generated by PYTHIA which uses the string model for hadronisation. To quantify this effect, the generator is replaced by SHERPA which uses the cluster model for hadronisation. The corresponding relative uncertainty on the JER is displayed in Figure C.5 with large deviations being visible in the low p_{T} range.

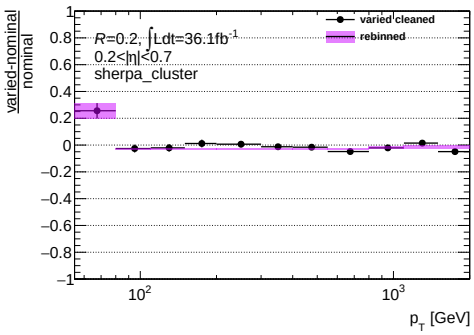

Figure C.5.: Effect on the JER when systematically varying the simulated events by using samples simulated by SHERPA instead of PYTHIA in the $0.2 \leq |\eta| < 0.7$ bin. The purple boxes show the uncertainties as they are used in the recommendation.

Furthermore, a closure test on the method itself performed by comparing the response of the simulated events which is defined as $p_{\mathrm{T}}^{\mathrm{reco}}/p_{\mathrm{T}}^{\mathrm{truth}}$ with the JER obtained *in situ* by the direct balance method. The result is shown in Figure C.6 and is consistently below 10%.

The last uncertainty related to the direct balance method is obtained from the differences observed between data and simulated events. Typically, simulated events have a better JER. In this case, the JER is smeared by a Gaussian with a mean of one and a width of

$$\sigma_{\mathrm{smear}} = (\sigma_{\mathrm{nom}} + |\sigma_{\mathrm{NP}}|)^2 - \sigma_{\mathrm{nom}}^2, \tag{C.6}$$

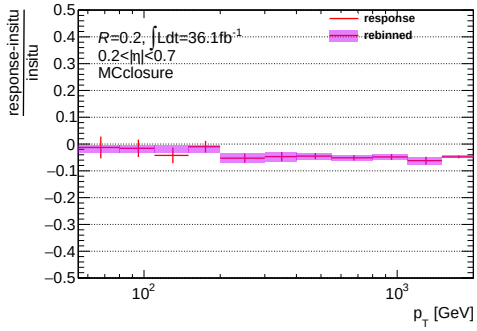

Figure C.6.: Effect on the simulated JER when using the true resolution in the $0.2 \leq |\eta| < 0.7$ bin. The purple boxes show the uncertainties as they are used in the recommendation.

where σ_{nom} is the nominal JER of the sample to be smeared and σ_{NP} is the standard deviation of the evaluated variation. If $\sigma_{\text{NP}} > 0$, the smearing is applied to the simulation, otherwise the data is smeared to ensure that the distributions agree.

In certain regions of the phase space, it is also possible that the simulated events have a worse JER. Then, the difference between simulated and data events is taken as systematic uncertainties.

The differences between simulation and data can be seen in Figure C.7. In the shown η bin, no additional systematic uncertainty needs to be assigned.

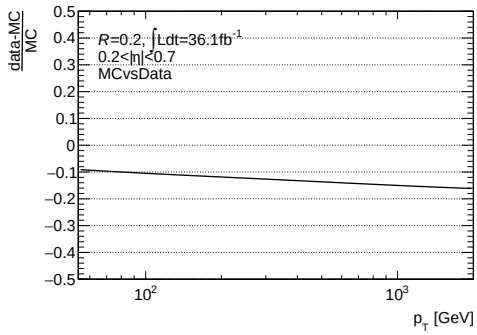

Figure C.7.: Effect on the JER when comparing the data to simulation in the $0.2 \leq |\eta| < 0.7$ bin. Whenever the resolution in data is better than the resolution in simulation it is used as a systematic uncertainty while smearing is applied otherwise.

C.2.2. Uncertainties of the small-R JES

Uncertainties on the JES also affect the JER and are therefore propagated to the results. There are five sources of uncertainties considered for the JES, namely

- **statistical uncertainty** from the finite number of events used to measure the

JES

- **ΔR cut** between the reference and the probe jet to ensure a high purity of the selected topology as well as
- **isolation requirement** of the probe jet for the same reason,
- **JVT efficiency** of matched anti-k_t ($R = 0.4$) jets and
- **physics modelling** due to the choice of MC generator.

Since the JES has been obtained using Z+jet events for the low p_{T} range and dijet events for the high p_{T} range, these uncertainties have to be evaluated for both samples. The results can be found in Figures C.8 and C.9, respectively. Compared to the uncertainties associated with the direct balance method, they are small and mostly flat across the whole p_{T} range.

C.2.3. Uncertainties of the anti-k_t ($R = 0.4$) JES

Finally, the uncertainties on the JES of the matched anti-k_t ($R = 0.4$) jets must be taken into account. Since the uncertainties are comparably small with regards to the uncertainties on the method itself and all nuisance parameters affect the small-R JER measurement in the same way, the global reduction scheme is applied to the anti-k_t ($R = 0.4$) JES, resulting in 7 nuisance parameters. The propagated effects on the JER are displayed in Figure C.10 and are well below 10%.

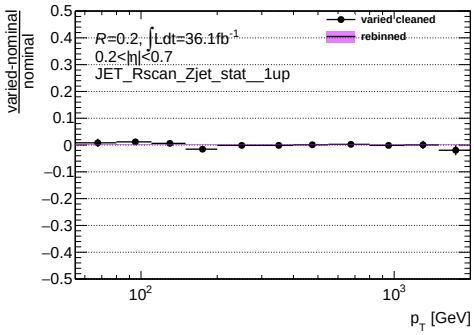

(a) statistical uncertainty

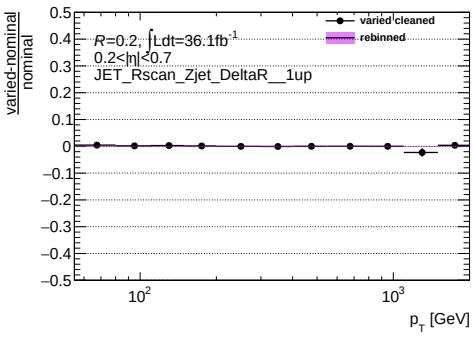

(b) ΔR cut

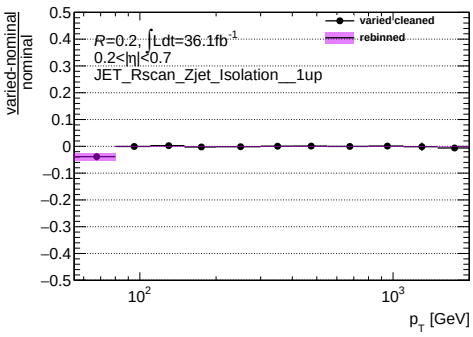

(c) isolation requirement

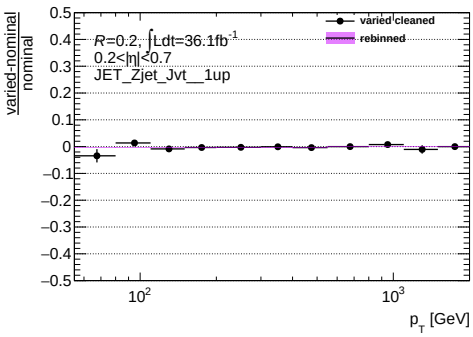

(d) JVT

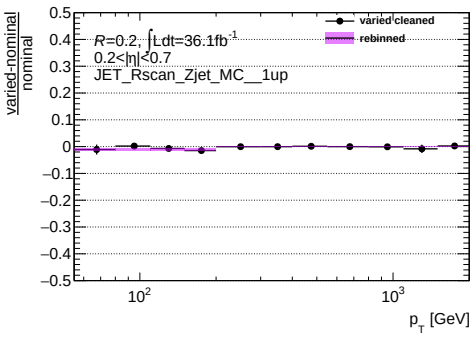

(e) physics modelling

Figure C.8.: Effect on the JER when systematically varying nuisance parameters identified in the JES calculation using the Z+jet topology in the $0.2 \leq |\eta| < 0.7$ bin. The purple boxes show the uncertainties as they are used in the recommendation.

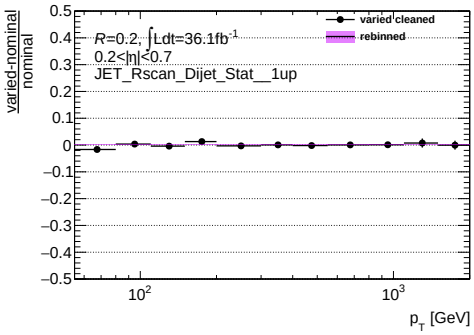

(a) statistical uncertainty

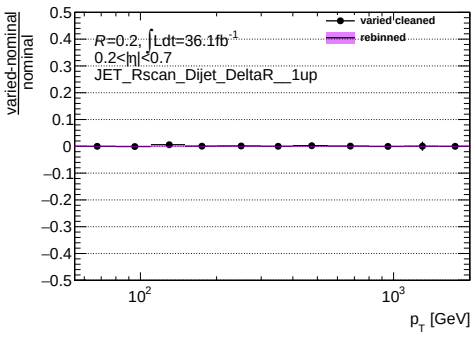

(b) ΔR cut

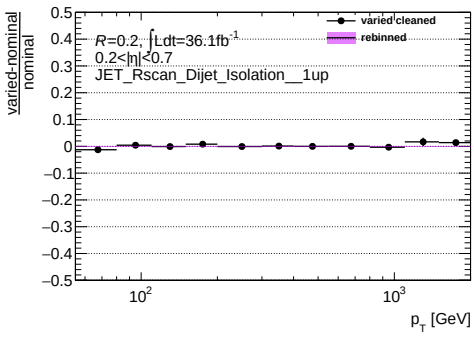

(c) isolation requirement

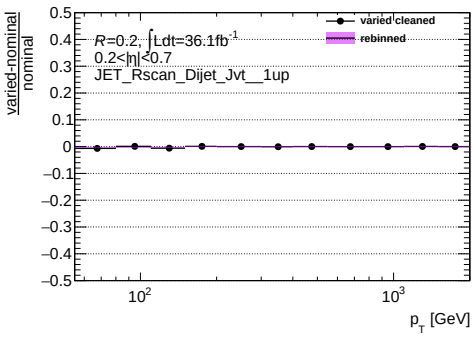

(d) JVT

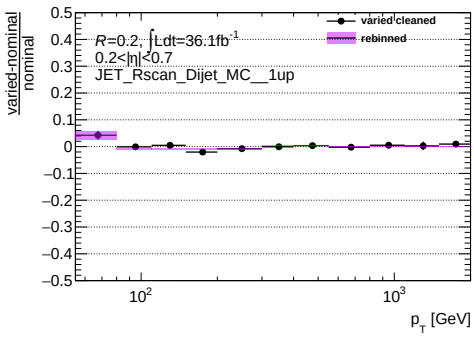

(e) physics modelling

Figure C.9.: Effect on the JER when systematically varying nuisance parameters identified in the JES calculation using the dijet topology in the $0.2 \leq |\eta| < 0.7$ bin. The purple boxes show the uncertainties as they are used in the recommendation.

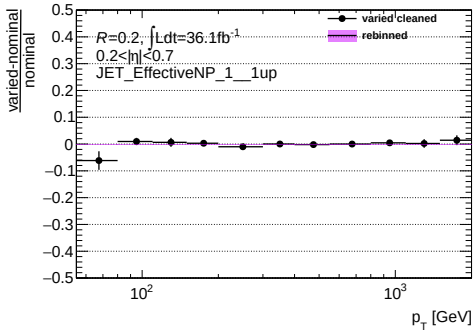

(a) nuisance parameter 1

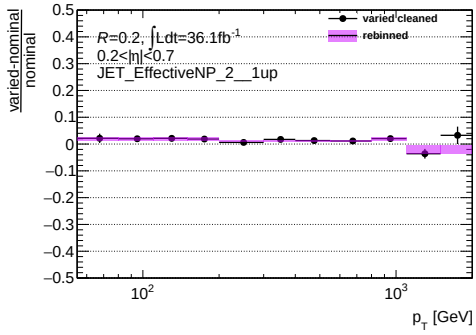

(b) nuisance parameter 2

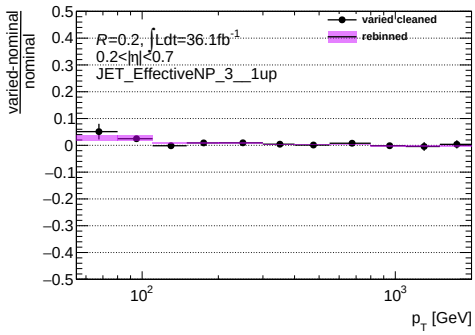

(c) nuisance parameter 3

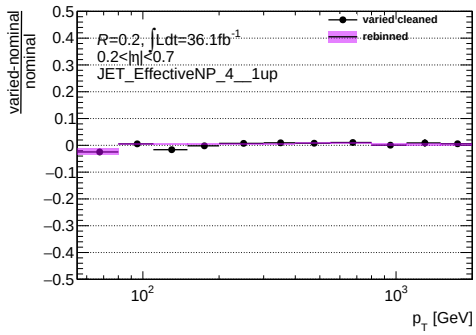

(d) nuisance parameter 4

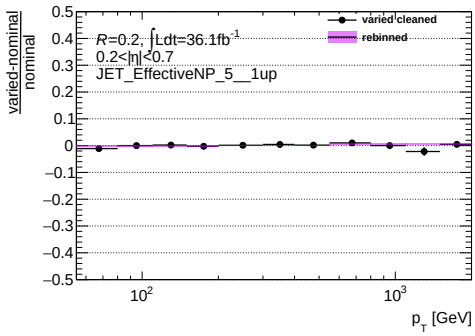

(e) nuisance parameter 5

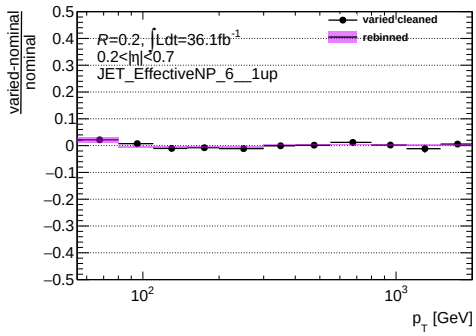

(f) nuisance parameter 6

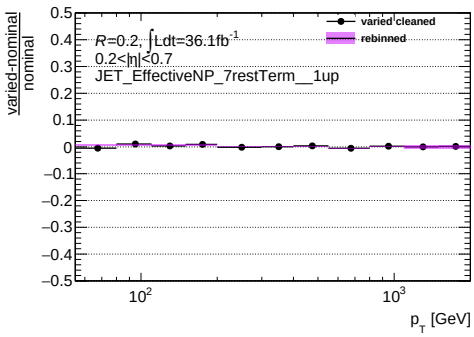

(g) nuisance parameter 7

Figure C.10.: Effect on the JER when systematically varying nuisance parameters associated to the anti-k_t ($R = 0.4$) JES in the $0.2 \leq |\eta| < 0.7$ bin. The purple boxes show the uncertainties as they are used in the recommendation.

C.3. Recommendations

The aforementioned uncertainties are translated into 101 nuisance parameters (NPs) which are all treated as correlated across the p_{T} and η bins and correspond to the following sources:

- **2 NPs** from the noise term: central ($|\eta| \leq 2.5$) and forward ($|\eta| > 2.5$)
- **17 NPs** from the JES measurements
- **4 NPs** from the dijet topology selection
- **77 NPs** from the statistics in the p_{T}-η bins
- **1 NP** from the comparison between data and simulation if the JER in data is smaller than the JER in simulation.

Additional correlations between the uncertainties corresponding to the dijet MC modelling and the JVT working point choice must be taken into account. The total uncertainties on the relative JER measurement for representative η values are shown in Figure C.11. It is evident that the uncertainty is larger at small p_{T}, where the uncertainty on the noise term dominates. Furthermore, the uncertainty increases for increasing η where the largest increase is observed between the central and forward detector regions.

To avoid the need to consider 101 NPs, an eigenvector decomposition of the total covariance matrix is performed to account for correlations between all listed NPs except the difference between data and simulation which is kept separate due to its special treatment.

Two reduction schemes are evaluated using effective NPs corresponding to the largest eigenvalues of the covariance matrix. In the full scenario, the NPs are reduced to 16 effective NPs and a rest term which corresponds to the remaining eigenvectors added in quadrature. Thus, the full scenario is reduced to 18 NPs, while the maximum difference between the original correlation matrix and the one built from effective NPs is in the order of 10^{-4}. This corresponds to a negligible loss of correlation information.

In the simple scenario, the correlation difference is allowed to be around 0.3, which is still achieved when reducing the number of effective NPs to ten and the rest term. Furthermore, independent of the sign of the difference between data and simulation, simulated events are always smeared.

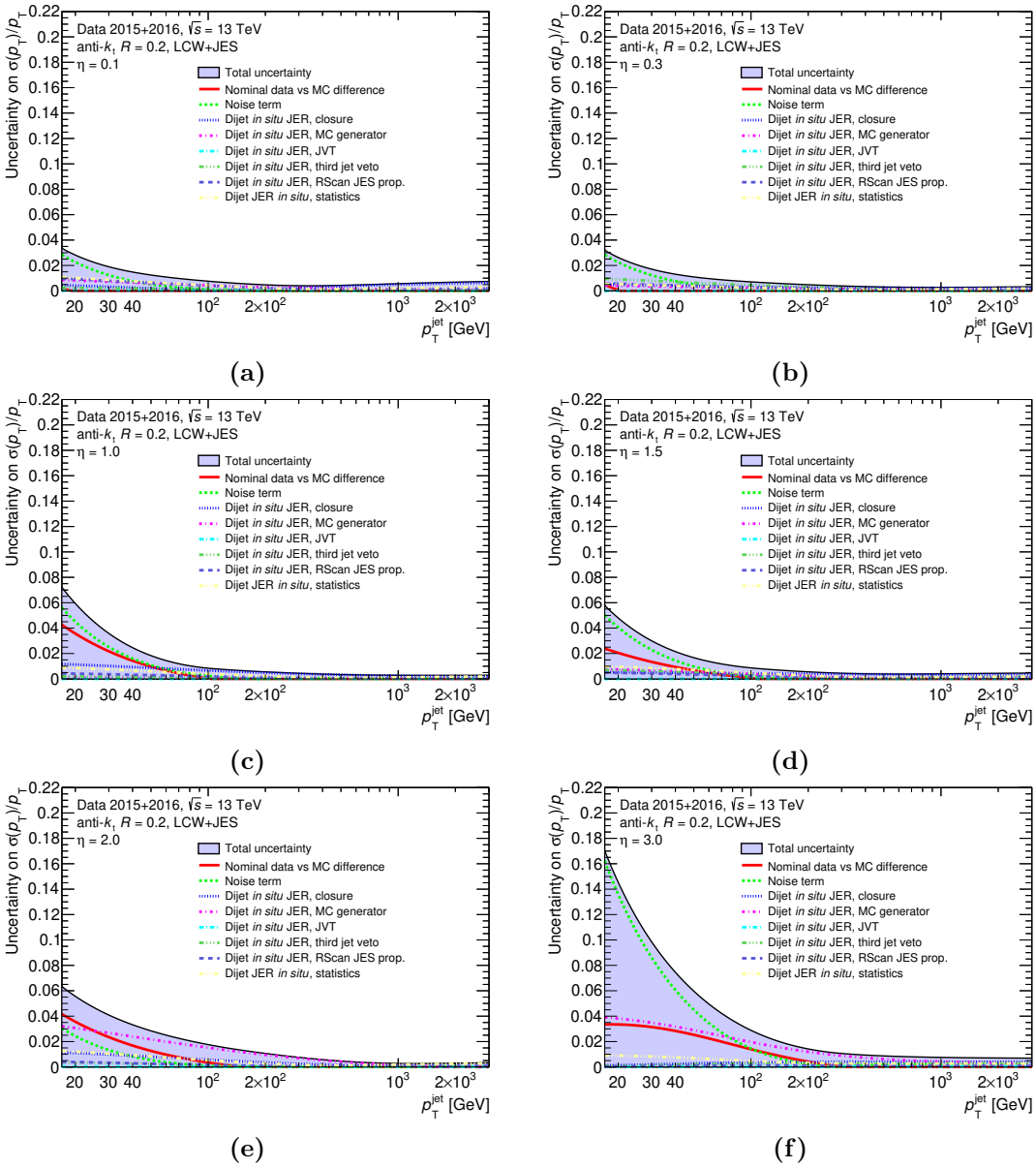

Figure C.11.: Total relative uncertainty on the relative JER measurement and the contribution of the most dominant components for representative η values [331].